INVESTIGATIONS OF PHOTOPLETHYSMOGRAPHY IN THE ASSESSMENT OF HAEMODYNAMICS, VASCULAR MECHANICS AND HAEMORHEOLOGY

A thesis submitted for the degree of doctor of philosophy

at City University of London

by Haneen Njoum

Research Centre for Biomedical Engineering

Department of Electrical and Electronic Engineering

School of Mathematics, Computer Science and Engineering

City University of London, London EC1V 0HB

March 2017

Table of Contents

Acknowledgement

This work would not have been possible without the support and guidance of my supervisor and mentor, Professor Panayiotis Kyriacou. He provided advice and encouragement throughout the project. I am truly grateful for his trust and belief in my vision to take alternative approaches. I also would like to thank Dr Justin Phillips for his advice and support always made available.

I would like to thank all members of the Biomedical Engineering Research Centre for creating the educational hub that I have enjoyed within the last few years. I thank Dr Victor Rybynok, for his generous advice always made available, Dr Kamran Shafqat for allowing me to acknowledge the power of Matlab, Dr Meha Qassem for sharing her expertise in spectrometry and her support, Tomas Ysehak Abay for his invaluable support during all times, Karthik Buddiha for always being a great companion since we first joined the centre. I also thank Dr Iasonas Triantis and Mario Bejarano for our interesting discussions and collaborations.

I would like to express my thanks to Mark Turmaine at UCL and Prof. Sarah Stallebrass at City University of London for making their resources available

I would like to thank all the volunteer participants for their valuable contribution.

I thank Prof. Rosemary Hollis for her support and advice since my arrival in London and all my friends especially Layaly, Ziat, Chris, Nitzan, Konrad, Marwan and Anfisa.

I am grateful for Tim Schubert, for his love and support along the way, and I am thankful to Heike, Juergen, and Uwe.

I'm indebted for my parents, Ismail and Nadia, who nourished my curiosity and empowered me to dream, Nadine and Ibrahim for being the loving and supportive siblings they are.

To Jonathan Bashir, the light of my life

Abbreviations

APV- Adjusted Pulse Volume

AS-Arterial Stiffness

ATH- Atherosclerosis

BP-Blood Pressure

BV-Blood Viscosity

CPT - Cold Pressor Test

CVD- Cardiovascular Disease

E_v- Volume Elastic Modulus

Hb- Haemoglobin

Hct- Haematocrit

HDL-High-density Lipoprotein

IMT- Intima Media Thickness

IR-InfraRed

LDL-Low-Density Lipoprotein

NPV-Normalised Pulse Volume

NVS-Normalised Volumetric Strain

PPG-Photoplethysmography

RBC-Red Blood Cells

RMSE - Root Mean Square Error

R-Red

SaO_2- Blood Oxygen Saturation

SpO_2- Pulse Oximeter Blood Oxygen Saturation

SSE - Sum Square Error

Abstract

Real-time cardiovascular assessment is vital for monitoring patients at an early stage of cardiovascular diseases (CVDs), at risk of reoccurrence of heart attacks and strokes and during pharmacological and non-pharmacological treatments. Blood Pressure (BP), Arterial Stiffness (AS) and Blood Viscosity (BV) are three essential parameters that can provide a reliable assessment of hypertension, atherosclerosis, and hyperviscosity associated with the development and progression of cardiovascular pathologies to complex stages. The currently available methods designed for evaluation of such parameters incur limitations and challenges that stand as an obstacle to the development of non-invasive, portable and reliable all-in-one device intended for personal use. This project engaged in novel fundamental and rigorous *in vivo* and *in vitro* investigations in an effort to shed more light on the photoplethysmographic signals (AC and DC) during induced changes of BP, AS, and BV. The underlying hypothesis is to show for the first time that Photoplethysmography (PPG) has the potential to non-invasively assess, in a qualifying and quantifying manner, the above parameters. Positives outcomes from such approach will establish the potential of the PPG as a preferential monitoring (screening and possible diagnosis) technique for the assessment of CVDs.

Novel miniature PPG sensors were developed along with a state of the art PPG processing unit, a data acquisition system and a customised manuscript for offline signal analyses. ECG and temperature processing systems were also designed and developed for use in the *in vivo* investigations. State of the art *in vitro* experimental rig was developed to mimic the human circulation under a wide range of flow conditions. A pilot volunteer investigation highlighted the effect of a cold pressor test in one hand on the PPG signals from both hands. The results indicated that there are changes in flow regulation mechanisms and hemodynamics besides the expected vasoconstriction effects of local cooling. These findings led to the controlled *in vitro* experiments. The *in vitro* investigations were completed in four stages where the potential of the PPG to provide a measure of blood pressure values, volume elastic modulus (E_v) and to detect fluid viscosity and haemorheological changes.

Results from the *in vitro* investigations highlighted that Adjusted Pulse Volume (APV) was found to be the optimum method for measuring BP values using Red (R) and Infrared (IR) wavelengths as validated under a range of BP values simulating hypotensive to hypertensive scenarios. The correlation was significant with Rsquare ranging between 0.96 and 0.99 for different arterial models and circulating fluids. Moreover, a proposed mathematical derivation allowed the PPG to provide a direct measure of AS using E_v. The method showed strong agreement with the gold standard measurement of material testings, the Instron device, with a percent error of 0.26% and 1.9% for different arterial models. Furthermore, the PPG signals also responded to changes in rheological characteristics in relation to fluid viscosities, the presence of the red blood cells, changes in shear rates and blood clotting.

These results strongly suggest that PPG has the potential to be used as a non-invasive and continuous method for the assessment of cardiovascular disease markers such as blood pressure, arterial stiffness and blood viscosity.

Chapter 1
INTRODUCTION

1.1 Introduction

Cardiovascular Diseases (CVD) are the leading cause of morbidity and mortality from early childhood to old age globally (Laslett et al., 2012). In 2013, CVDs resulted in 17.3 million deaths (31.5%) compared to 12.3 million (25.8%) in 1990 (Townsend et al, 2014). The most interesting fact reported in the literature is that 90% of CVDs are preventable (McGill et al., 2008). On this ground, this project will focus on the potential and limitations of Photoplethysmography (PPG) as a non-invasive and continuous device for cardiovascular assessment. There are three major determinants of CVD at an early stage; hypertension, atherosclerosis, and hyperviscosity. The three parameters have been associated with the progression of CVD and morbid events (Coull et al., 1991; Hansen et al., 2006; Hirai et al., 1989; Jan et al., 1975; Turczyński et al., 2002). They have been identified as the earliest determinants of the preclinical CVD. Hypertension, atherosclerosis, and hyperviscosity can be assessed with measurement of Blood Pressure (BP), Arterial Stiffness (AS) and Blood Viscosity (BV), respectively. The three parameters interact together, and it is only plausible to study them combined. An abnormal value or behaviour in one of those parameters tend to result in a positive feedback loop of plaque formation, increased vascular resistance, blood aggregation, and heart overload. This loop may stabilise, but sometimes it accelerates and eventually leads to catastrophic events of thrombosis, heart attacks, strokes, and anginas.

There is no currently available medical device designed for practical, non-invasive, continuous personal use at an affordable price for full cardiovascular assessment. The available techniques are used to perform measurements or estimations of the parameters separately.

A variety of methods is available for non-invasive Blood pressure (BP) measurement. However, these methods are mostly intermittent, which incurs limitations due to the unavailable data during the time between the two measurements. Continuous blood pressure measurements and estimations include the vascular unloading method and the

pulse wave velocity. Both are not considered reliable to replace classical methods of blood pressure measurements and are not available for personal use.

Arterial stiffness (AS) has been recognised as an independent predictor of atherosclerosis and cardiovascular risk mainly through Pulse wave velocity and ultrasound measurement methods. However, a host of indices is found in the literature that provides an indirect estimation of AS. None of these methods is capable of providing a direct measure of the elastic modulus for accurate quantification of AS for clinical or personal use. Moreover, some studies have questioned the reliability of these indices due to the low correlation between them, especially when the study groups are adjusted for age and gender (Jerrard-Dunne et al., 2008).

Elevated blood viscosity values, or hyperviscosity, have been associated with increased cardiovascular risk (Coull et al., 1991; Fossum et al., 1997; Lowe et al., 1997; Turczyński et al., 2002). However, the parameter received little attention in the development of diagnostic methods and is virtually non-existent in the Photoplethysmograph. Currently available commercial devices for measurement of blood viscosity are limited to industrial devices and are not particularly designed for clinical use. Photoplethysmography (PPG) has been widely applied in the pulse oximeter for the estimation of blood oxygen saturation. However, beyond this application, the PPG signal is believed to contain information related to the blood circulation (Shelley, 2007). Nonetheless, most studies rely on the assumption that the PPG is purely a resultant of volume changes in the vascular bed, and only a limited amount of studies have addressed the possibility of other factors affecting the PPG signal, such as haematocrit values (Ochoa and Ohara, 1980) and wall stiffness (Kamshilin et al., 2015).The main focus of this project is to investigate the AC and DC components of the PPG and the potential of the technique to be used as a diagnostic method for cardiovascular assessment. More specifically this work focuses in the utilising of PPG in the measurement of BP, AS, and BV. This is achieved through original investigations of the PPG as a technique addressing fundamental-based questions such as:

1. To what extent does the fluid volume contribute to the generation of the AC and DC components of the PPG signal?
2. How are the AC and DC PPG signals affected by radial pressure (stress on inner walls)?
3. How does wall elasticity affect both components of the PPG signal?

4. How do pumping frequency and stroke volume affect the signal in conjunction with other factors, such as fluid volume, geometry, and arterial stiffness?
5. What is the role of fluid viscosity in the generation of both components of the PPG signal?
6. Does blood rheology affect both components of the PPG signal?

   These questions resulted in the design of a series of *in vivo* and *in vitro* investigations that consider these factors and lead to address the application-based questions:

7. What are the limitations of the PPG technique as a diagnostic medical for a general and reliable method for cardiovascular assessment, including blood pressure measurements, arterial stiffness and blood viscosity?

1.2 Chapters Overview

Chapter 2 covers the basic physiological background of the cardiovascular system with emphasis on blood pressure and flow regulation methods and blood rheological properties. The chapter also describes the major cardiovascular diseases that are known to develop at early stages (before the occurrence of heart attacks, strokes, and anginas) such as, atherosclerosis, hypertension, and hyperviscosity. This is followed by a brief overview of some of the basic principles of the physics of blood flow.

Chapter 3 describes the current state of the art in the assessment of cardiovascular risks and provides an overview of the available methods and devices for measurement of blood pressure, estimation of arterial stiffness. The chapter also covers current methods for clinical testing of blood viscosity and possible methods that are being investigated in the research community.

Chapter 4 provides an in-depth overview of the principles of light properties, pathways, and interaction in biological tissues. The chapter also highlights results obtained from optical interactions with skin, blood mediums and the major chromophores.

Chapter 5 is dedicated to an overview of Photoplethysmography. The chapter covers the basic principles of the technique, modes of operation and early and recent history of the origin of the technique. The chapter highlights the most common applications of the PPG and the associated limitations.

Chapter 6 describes the incremental design and development of the PPG probes that will be utilised in the *in vivo* (finger probes) and *in vitro* (tube probes) investigations. The chapter includes the design considerations, the chosen components and their

specifications and the manufacturing procedure. This chapter also describes the design and development of the temperature measurement system which will be used for the evaluation of the finger probes and later on in the *in vivo* investigation. A section for the evaluation of the fabricated finger and tube probes will be presented.

Chapter 7 covers the design and development of the hardware and software used for processing, recording and analysing the PPG signals. The design of the dual channel, dual wavelength PPG processing system includes the mechanical, electrical descriptions of the system along with an evaluation of the system's performance. The design and development of the ECG system are also included. The chapter includes a description of the designed data acquisition system along with the chosen acquisition cards and the development of the virtual instrument in LabVIEW for the *in vivo* and *in vitro* investigations. A description of the custom written Matlab script used for offline analysis of the collected PPG and ECG signals is also included.

Chapter 8 describes the first *in vivo* investigation of PPG, ECG and temperature signals in healthy volunteers undergoing a cold pressor test in one hand. The study motivation, protocol, data acquired, and the statistical analysis is presented. The study highlights the response of AC amplitudes and DC levels of the PPG signals in both hands and underlines the need for controlled *in vitro* investigations.

Chapter 9 describes the development of the *in vitro* setup. The setup was designed to mimic human blood circulation and allows investigations of the PPG signals under controlled scenarios of flow conditions while acquiring pressure and flow velocity signals. A summary of the *in vitro* investigations protocol is listed. The chapter covers the evaluation of the developed system by observing flow patterns in the arterial models.

Chapter 10 presents the first *in vitro* investigation of PPG, pressure and flow signals in an arterial model under varied conditions of flow and pressure. This is achieved by control of stroke volumes and pumping frequencies in two arterial models with different cross-sectional areas. A proposed method for measurement of systolic pressure values using normalised and adjusted pulse volumes is validated.

Chapter 11 addresses the effect of wall stiffness on the PPG signal by acquiring PPG, pressure and flow signals from the *in vitro* setup from two arterial models with different wall stiffness properties. A proposed method for measurement of the elastic Modulus is validated with the standard gold method. The method shows strong agreement and proposes that PPG can be used for direct measurement of wall elastic modulus.

Chapter 12 reports on the effect of fluid viscosity on the PPG components. The study acquires PPG, pressure, and flow signals from the *in vitro* setup while circulating two fluids with similar optical properties and different viscosities. The chapter motivation, protocol, data acquired, and statistical analysis are presented. This chapter highlights that both components of the PPG signal are sensitive to fluid viscosity.

Chapter 13 presents the results highlighting the role of blood rheology on the PPG signal. It addresses the role of the presence of the vesicle-shaped red blood cells, the effect of different shear rates and finally the influence of thromboplastin activation on the AC and DC components of the PPG signals.

Chapter 14 discusses results and observations made in previous chapters (8, 10,11,12 and 13) and presents final conclusions, remarks, limitations, and suggestions for future work.

Chapter 2
BASIC PRINCIPLES AND PHYSIOLOGY OF BLOOD CIRCULATION

2.1 Introduction

The main focus of this project is the applications of Photoplethysmography (PPG) in the assessment of cardiovascular health, primarily, the interaction of the photoplethysmographic signal with blood flow. Previous studies since the 1930s have recorded and observed the synchronised PPG signal with the heartbeat from a skin surface. Therefore, it is essential to develop an understanding of the main contributors to the pulsatile signal in blood circulation from an anatomical, physiological and physical point of view.

Blood flow and pressure are regulated by the cooperation of multiple systems in the human body; the nervous system, the respiratory system, the circulatory system, and the urinary system as seen in **Figure 2-1**. This Chapter will present a brief overview of the role of the nervous system in blood flow and pressure regulation, a physiological and anatomical description of the cardiovascular system. A brief description of cardiovascular diseases and their symptoms of hypertension, atherosclerosis and hyperviscosity will also

be presented. We will also provide some fundamentals of the physics of the flow in elastic arteries.

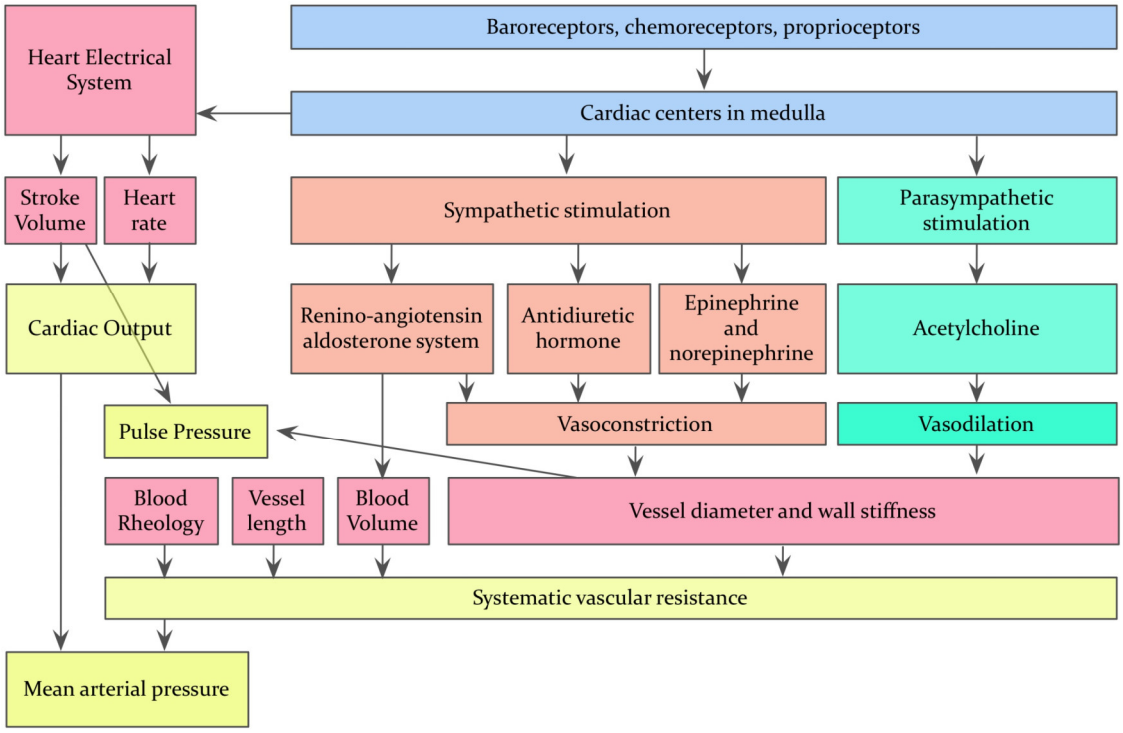

Figure 2-1
Block diagram demonstrating the main contributors to blood pressure and blood flow regulation.

2.2 The Nervous-Cardiovascular Interaction

The autonomic nervous system (ANS) is the component of the peripheral nervous system that controls cardiac muscle contraction, visceral activities, and glandular functions of the body. Specifically, the ANS can regulate heart rate, blood pressure, the rate of respiration, body temperature, sweating, gastrointestinal motility and secretion, as well as other visceral activities that maintain homoeostasis (Rhoades and Bell, 2012). The ANS functions continuously without conscious effort and is controlled by centres located in the spinal cord, brain stem, and hypothalamus. Those centres receive signals from different receptors in the body as summarised in **Figure 2-2.**

The ANS has two interacting systems: the sympathetic and parasympathetic systems. Sympathetic and parasympathetic neurones exert antagonistic effects on the heart. The sympathetic system prepares the body for energy expenditure, i.e. fight or flight. Conversely, the parasympathetic system is more active under restful conditions. The parasympathetic counteracts the sympathetic system after a stressful event and restores the body to a restful state. The sympathetic system releases norepinephrine (NE) while the parasympathetic nervous system releases acetylcholine (Ach). At any given time, the

effect of the ANS on the heart is the net balance between the opposing actions of the sympathetic and parasympathetic systems (Shusterman and Barnea, 2005). In relation to the circulatory system, the stimulation of the sympathetic system causes an increase in heart contractility (inotropic effects) of both atriums and ventricles, blood vessel constriction and enhancement of conduction (dromotropic effects) by increasing the AV conduction velocity. The parasympathetic stimulation decrease heart rates (negative chronotropic effect), decrease conduction velocity (negative dromotropic effects) and it is a matter of debate if this stimulation affects myocardial contractility. However, it is suggested that it can cause a decrease in heart contractility (Brahme, 2014).

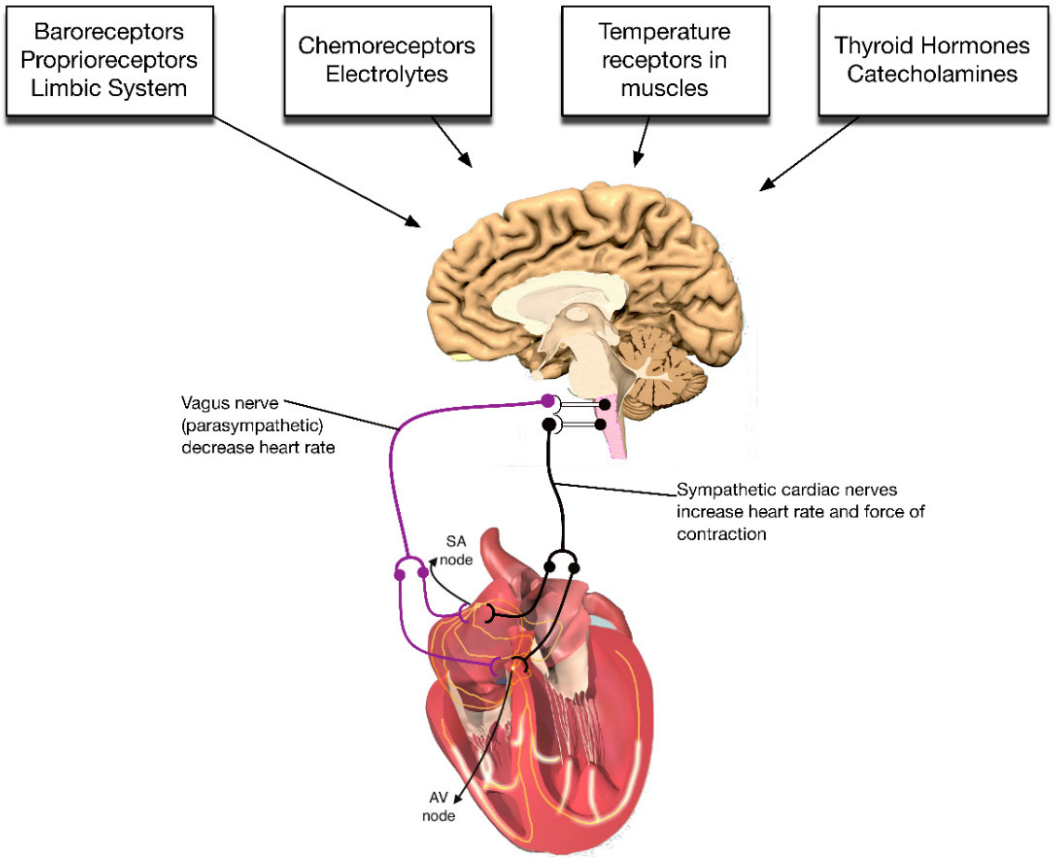

Figure 2-2
The autonomic nervous system role in heart regulation and the main receptors that sense changes throughout the body, showing the location of the sinoatrial (SA) node cells and the AtrioVentricular (AV) node cells in the walls of the right atrium (Primal Pictures).

2.3 The Cardiovascular System

The cardiovascular system comprising the heart, blood vessels, and blood is responsible for supplying nutrients and metabolic products to every living cell in the human body, which is to be estimated approximately at 10^14 cells (Zamir, 2005).

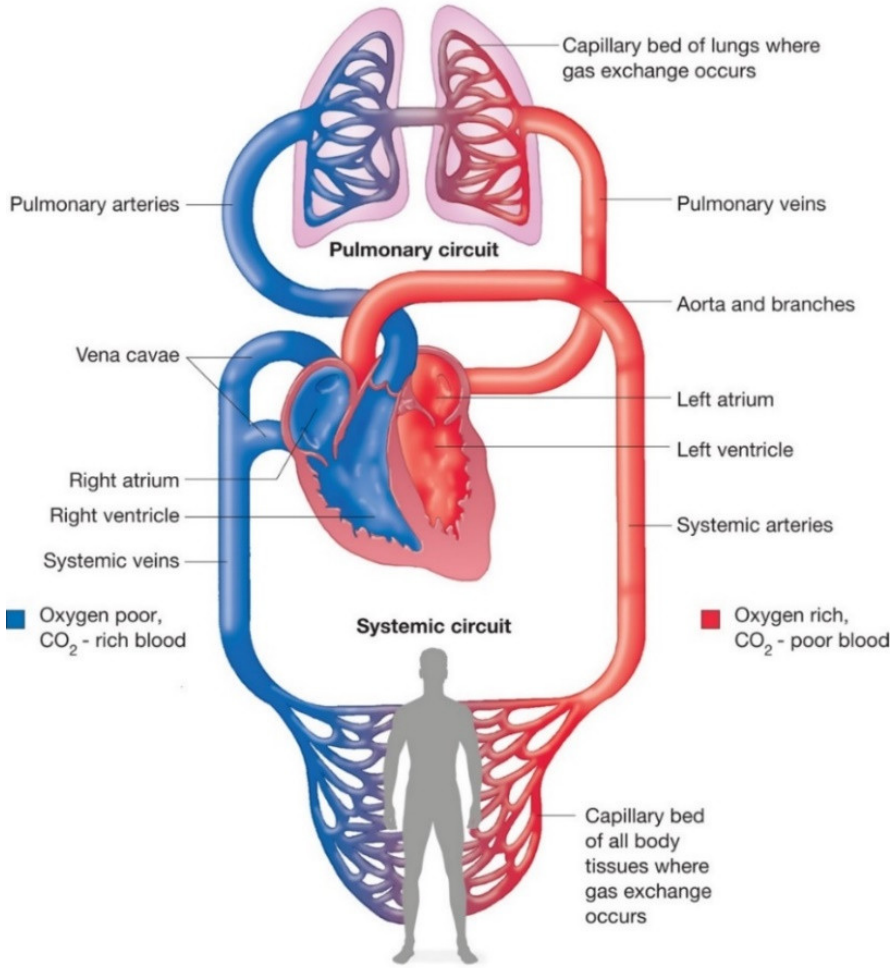

Figure 2-3
Illustration of human heart anatomy showing the systematic and pulmonary circulations (Tortora and Derrickson, 2008).

2.3.1 The Heart

The heart consists of four chambers as illustrated in **Figure 2-3**: Two ventricles and two atria, which contract and relax rhythmically. The two ventricles eject blood, and both atria act as receiving chambers for returning blood. In the pulmonary circuit, blood that is high in carbon dioxide and low in oxygen flows from the right heart to the lungs. In the capillaries of the lungs, blood takes on oxygen and offloads carbon dioxide. Oxygenated blood then flows from the lungs to the left heart. In the systemic circuit, oxygenated blood flows from the left heart to the systemic tissues. Systemic capillaries are the site of exchange of nutrients and wastes. The blood offloads oxygen to the tissues

and picks up carbon dioxide wastes. Deoxygenated blood then flows from the systemic tissues to the right heart, completing the circuit (Iaizzo, 2010).

The pulmonary arterial system starts at the pulmonary valves. The main pulmonary artery (pulmonary trunk), like the aorta, has sinuses behind the valve cusps. In humans the trunk is 5–6 cm in length and 2.5–3.0 cm in diameter, and it passes upwards and backwards, as shown in **Figure 2-3**, to lie beneath the aortic arch, where it divides into the right and left main pulmonary arteries. These pass towards the corresponding lungs, but before entering them, they divide into several branches, which supply the different lobes (Iaizzo, 2010; Tortora and Derrickson, 2008).

2.3.1.1 Pacemaker Cells

The heart is the pump that drives that circulation. It pumps continuously by contracting and relaxing in a rhythmic pattern initiated by electrical impulses, the rate which those impulses spark, controls the heart rate. Those impulses are originated in the pacemakers' cells in the heart. Under normal conditions, pacemakers are responsible for initiating their own potentials, and they are the source of current that flows through the heart, causing depolarization and contraction of the cardiac myocytes. Pacemaker cells are present in the SinoAtrial node (SA node) and the AtrioVentricular node (AV) (Courneya, 2010).

Action potentials that originate in the SA node spread to the myocardial cells of the atria through gap junctions between cells. Depolarization of the atria stimulates contraction of the atrial myocardium. Action potentials cannot directly spread from the atrial myocardium to the ventricular myocardium due to the presence of the non-conducting fibrous skeleton that separates them. Rather, the impulse travels to the ventricles through a system of specialised cells called the conduction system (Aaronson et al., 2012).

2.3.1.2 The Conduction System

The conduction system consists of the atrioventricular node (AV node), Bundle of His, bundle branches and Purkinje fibres. After the action potential has spread across the atria, it travels to the AV node. At the AV node, the impulse is delayed for a brief period of time to allow the ventricles to fill with blood before ventricular contraction occurs. The impulse travels from the AV node into the Bundle of His and then moves into both bundle branches. The impulse travels to the apex of the heart before travelling into the ventricular walls through Purkinje fibres. The impulse then spreads throughout the ventricular myocardium by way of gap junctions between myocardial cells.

Depolarization of the ventricles causes contraction of the ventricular myocardium (Marieb, 2000).

2.3.1.3 The Fluid Heart

The heart does not only function as a mechanical pump. Many investigators have pointed out that the pattern of the fluid movement as it is ejected from the heart plays a major role in the ability of the fluid to propagate along the blood vessels in the body. The fluid movement in the body emerges from the myocardium; which forms most of the heart and consists of muscle fibres. The outer muscle fibre starts at the upper part of the heart and sweeps down in counterclockwise curves to the tip (apex) of the heart. At that point, they loop around and form the heart vortex (vortex cordis), they loop more to form the vortex pattern, some of those fibres spread around the papillary muscles that move the atrioventricular valves (Pedrizzetti et al., 2015; Peskin and McQueen, 1992).

Most muscle consists of about 75% water. The looping pattern of the heart fibres, including the vortex, forms an image of fluid movement as illustrated in **Figure 2-4**. On the events of the contraction of the myocardium, the blood that streams through the heart also creates loops and vortices. This movement drawn by the spiralling fibres of the heart is very intricate (Lipowsky, 2005; Wong et al., 2008; Kocica et al., 2006).

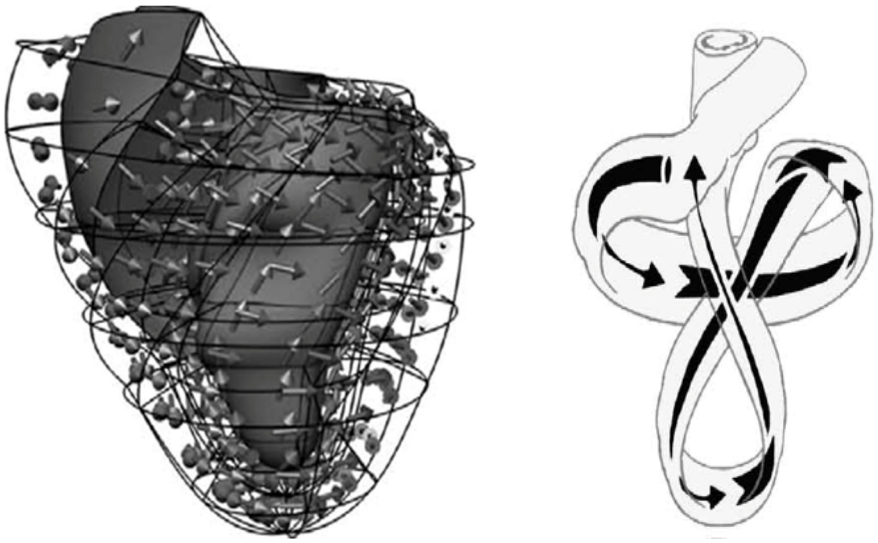

Figure 2-4
Modelling of the forces within the ventricular mass. on the right, the developed forces in various directions within the ventricular mass are conducted to the blood flow, where the tissue structure merge(Kocica et al., 2006).

This energy that is delivered to the blood, part of it dissipates through viscosity, another part is stored in the elastic structure, and the remainder is stored in the kinetic energy of the blood. Though some of that elastic energy is stored in the fluid during the initiation

of flow due to the elastic properties of red blood cells, its presence is hidden from observation when the flow reaches a steady state. This means the steady flow measurements reflect only the rate of energy dissipation. Because early studies of blood flow were carried using quiescent fluid model only –it was not possible to provide the complete basis of understanding pulsatile flow in the circulation (How, 1996).

2.3.2 Blood Vessels: Anatomical and Mechanical Properties

Blood is transported around the body in three different types of blood vessels: arteries, capillaries, and veins. Each blood vessel is composed of three layers of tissue. From inside in they are the *tunica intima*, *tunica media*, and *tunica external* (Ethier and Simmons, 2007)**.** An illustration of blood vessel types labelled with tissue layers is presented **Figure 2-5**. Tissue layers are labelled in reference to **Table 2-1**(Primal Pictures, 2015)**.**

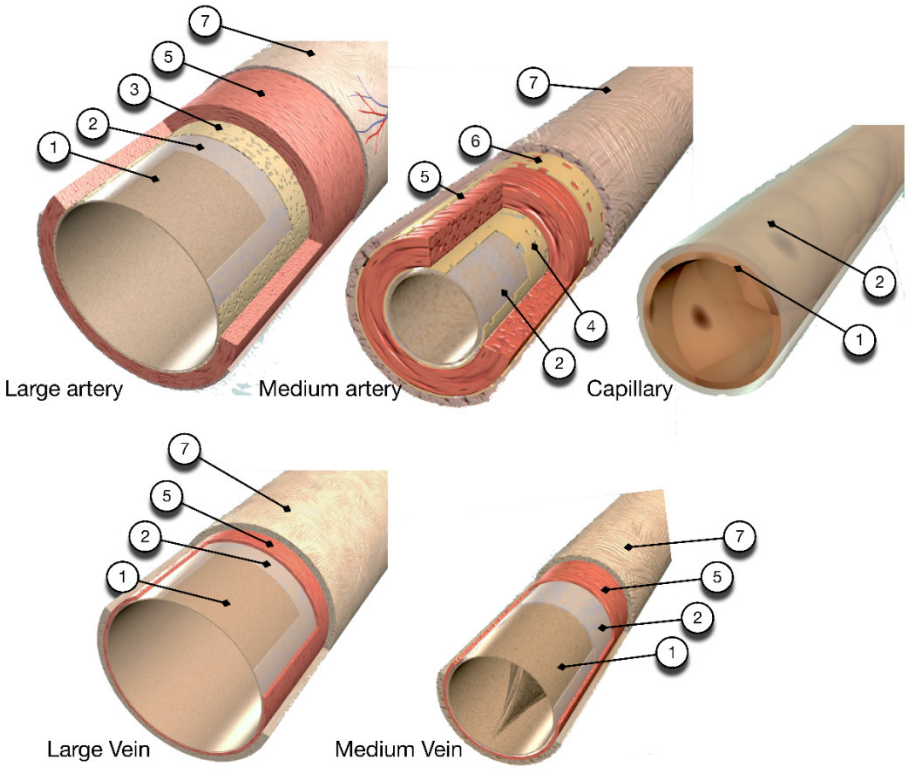

Figure 2-5
Types of blood vessels showing larger artery, medium artery, capillary and a large and a medium vein. Tissue layers are labelled in reference to Table 2-1. Modified Illustrations (Primal Pictures).

Table 2-1

Label No.	Tissue Type	Description
Tunica intima		
1	Endothelium	A layer of simple squamous epithelial cells that is in direct contact with the blood. It is permeable to certain materials in the bloodstream. It regulates the diffusion of substances, prevents cells sticking to its walls and contracts to prevent blood flow.
2	Basement membrane	A framework of collagen fibres provides a firm supportive base and anchorage for the endothelial lining to the lamina propria while retaining an elasticity great enough to ensure a vessel's ability to stretch and recoil. The basement membrane also regulates molecular movement, playing an important role in tissue repair of blood vessel walls.
3	Lamina propria	A layer of loose connective tissue or dense irregular connective tissue, which lies beneath the epithelium and together with the epithelium constitutes the mucosa.
4	Internal elastic lamina	A thin sheet of elastic fibres that helps the vessel recoil after is has been stretched by an increase in blood pressure. It contains window-like openings that facilitate diffusion between the tunica internal and tunica media.
Tunic media		
5	Smooth muscle	Most smooth muscle is of the single-unit variety, that is, either the whole muscle contracts or the whole muscle relaxes, but there is the multiunit smooth muscle in the large elastic arteries. Single unit smooth muscle, however, is most common and lines blood vessels (except large elastic arteries).
6	External elastic lamina	Helps the artery to recoil after it has been stretched by the increase in blood pressure experienced during each heartbeat.
Tunica Externa		
7	Tunica Externa	A loose, thick layer of connective tissue consisting of elastic and collagen fibres. It contains a network of tiny nerves, lymphatics, and capillaries that supply the vessel wall.

2.3.2.1 Arteries

Arteries carry blood away from the heart to other organs. Their size and wall thickness vary depending on their vicinity to the heart, i.e., large arteries with thick elastic walls carry blood being pumped directly from the heart, and arteries smaller in diameter with thinner walls deliver blood to the extremities (Ethier and Simmons, 2007). Arteries have all three layers of a typical blood vessel. Their tunica media exhibits a greater muscular

and elastic thickness than in veins, enabling their walls to stretch easily with a small increase in blood pressure (high compliance) (Ethier and Simmons, 2007).

Three main types of arteries are defined: elastic arteries, muscular arteries, and arterioles.

Elastic arteries

Elastic arteries are also referred to as conducting arteries, are large and conduct blood from the heart to muscular arteries. They have well defined internal and external elastic laminae, and their tunica media is thick and full of elastic fibres (elastic lamellae), enabling their walls to stretch easily with an increase in blood pressure (high compliance), as seen during systole. They propel blood from the heart during ventricular diastole (Iaizzo, 2010). Their elastic properties are essential to accommodate the volume of blood created when blood is expelled from the heart. As they stretch, elastic fibres store mechanical energy, which is converted into kinetic energy as the elastic fibres recoil and force the blood away from the heart such as the aorta, subclavian, common iliac, and common carotid arteries (Ethier and Simmons, 2007).

Muscular (medium) arteries

Muscular arteries are also referred to as distributing arteries, as they repeatedly branch until reaching their target organs. They are less elastic than the conducting arteries as they do not have to deal with the same degree of pressure changes. They have well-defined internal but thin external elastic laminae. Depending on the size of the artery, the thick tunica media is made up of 3-40 concentrically arranged layers of smooth muscle cells (Courneya and M.D, 2010; Iaizzo, 2010). The tunica externa is often thicker than the tunica media, consisting of longitudinally oriented fibroblasts, collagen fibres, and elastic fibres. The loose arrangement of these cells enables arteries to alter their diameter. The lack of elastic fibres in the walls of muscular arteries means that recoil does not propel the blood as in elastic arteries. Instead, smooth muscle cells maintain a state of partial contraction or vascular tone, ensuring that vessel pressure and efficient blood flow are sustained and enable efficient adjustment of the rate of blood flow by vasoconstriction and vasodilation (Safar et al., 2014).

Arterioles

Arterioles also referred to as resistance vessels, are numerous, microscopic arteries that feed blood into capillary networks. Vessel diameter varies from 15-300 μm depending on the location, and their wall thickness is about half the total diameter. The tunica interna is thin, with a porous internal elastic lamina that diminishes as the arteriole tapers

towards its terminal end and continues as a capillary (Aaronson et al., 2012). The muscular tunica media is made up of one to two concentrically arranged layers of smooth muscle cells. A smooth muscle cell forming the precapillary sphincter demarcates the junction and controls the flow of blood between a metarteriole and its adjoining capillary. The tunica externa contains unmyelinated sympathetic nerves and loose connective tissue. Along with local chemical mediators, the sympathetic nerve supply of the arteriole triggers vasoconstriction and vasodilation, regulating the rate of blood flow, blood pressure, and vascular resistance. The smaller the vessel diameter, the higher the vascular resistance and the slower the rate of blood flow (Safar et al., 2014).

2.3.2.2 Capillaries

Capillaries are short, branched, interconnecting vessels that form networks within nearly every structure of the body, bridging the gap between arterioles and venules. A micro-circulation exists as blood flows from a metarteriole, through capillaries, into a postcapillary venule. Structurally, capillaries lack both tunica media and tunica externa. Their thin, one layer epithelial structure and vast surface area make for rapid exchange of small molecules, such as glucose, and the diffusion of gases, such as oxygen and carbon dioxide, between blood and cellular interstitial fluid (Iaizzo, 2010). Capillaries also referred to as exchange vessels, have a diameter varying between 5-10 μm. Red blood cells, 8 μm in diameter, must, therefore, deform in order to fit through smaller capillaries. A capillary wall is approximately 0.2 micrometres (0.02 mm) thick and is composed of a single layer of endothelial cells adhered to a basement membrane. Capillary networks provide a large surface area in contact with tissues throughout the body (Aaronson et al., 2012).

2.3.2.3 Veins

The systemic veins begin at the venules, where the capillaries join together and end where the venae cavae enter the right atrium. They carry blood back to the heart from the extremities and organs of the body. Their size varies from about 0.5 mm in diameter to 3 cm, depending on their proximity to the heart. Veins generally have very thin walls in relation to their diameter. Their thin walls and ability to unfold contribute to their high distensibility. In certain regions, veins can be seen to widen, forming vascular or venous sinuses, structurally different from regular veins (Caro, 2012). They have thin endothelial walls, with a complete lack of smooth muscle, leaving them reliant upon surrounding connective tissue for support. Veins are more numerous than arteries and often appear as pairs. Superficial veins spread throughout the subcutaneous layer, deep

to the skin, and deep veins run between skeletal muscles. Connections exist between the two, called anastomotic veins (Aaronson et al., 2012).

Venules

Venules, like arterioles, are numerous and microscopic. However, their walls are much thinner. Postcapillary venules are continuous with capillary networks. They are small in diameter, 10-50 μm, and have gaps between the endothelial cells that make up their walls. As venules extend further from their capillary networks, they become larger in diameter, 50-200 μm, and more muscular with more layers of concentrically arranged smooth muscle cells (Caro, 2012). Venules drain blood from the capillary networks and feed the return flow of blood to the veins. Postcapillary venules function as an exchange unit, however, the larger, thicker walled venules do not (Ethier and Simmons, 2007).

Medium veins

Medium veins are around 1 cm in diameter. They have all three layers of a typical blood vessel: the tunica externa is the thickest layer, consisting of collagen and elastic fibres; the tunica media, lacking in smooth muscle and elastic fibres, is thin along with the tunica interna (Caro, 2012). They do not have internal or elastic laminae and therefore are not able to withstand high pressure. With blood pressure in veins being relatively low, they rely somewhat on the contraction of surrounding skeletal muscle and the pumping action of the heart to boost venous return. Many medium veins contain valves, small extensions or infoldings of the tunica internal into the lumen, creating flap-like cusps. The valves function to boost venous return by preventing backflow of blood due to gravity. Examples of medium veins are the Renal, internal carotid, ulnar, splenic, and popliteal veins (Iaizzo, 2010).

Large veins

Large veins can be up to 3 cm in diameter. They have a thick tunica externa, similar to that of medium veins, but they lack valves. Large veins drain from their tributaries into the heart. Examples of the large veins are the superior vena cava, internal jugular veins, and common iliac veins (Caro, 2012).

Normal values for canine cardiovascular parameters are presented in **Table 2-2**.

Table 2-2
Normal values for canine cardiovascular parameters (Caro, 2012).

Site		Aorta				Carotid artery	Arteriole	Capillary	Venule	Inferior vena cava	Main pulmonary artery
		Ascending	Descending	Abdominal	Femoral						
Internal diameter d_i	cm	1.5 1.0–2.4	1.3 0.8–1.8	0.9 0.5–1.2	0.4 0.2–0.8	0.5 0.2–0.8	0.005 0.001–0.008	0.0006 0.0004–0.0008	0.004 0.001–0.0075	1.0 0.6–1.5	1.7 1.0–2.0
Wall thickness h	cm	0.065 0.05–0.08		0.05 0.04–0.06	0.04 0.02–0.06	0.03 0.02–0.04	0.002	0.0001	0.0002	0.015 0.01–0.02	0.02 0.01–0.03
h/d_i		0.07 0.055–0.084		0.06 0.04–0.09	0.07 0.055–0.11	0.08 0.053–0.095	0.4	0.17	0.05	0.015	0.01
Length	cm	5	20	15	10	15 10–20	0.15 0.1–0.2	0.06 0.02–0.1	0.15 0.1–0.2	30 20–40	3.5 3–4
Approximate cross-sectional area	cm^2	2	1.3	0.6	0.2	0.2	2×10^{-5}	3×10^{-7}	2×10^{-5}	0.8	2.3
Total vascular cross-sectional area at each level	cm^2	2	2	2	3	3	125	600	570	3.0	2.3
Peak blood velocity	$cm\ s^{-1}$	120 40–290	105 25–250	55 50–60	100 100–120		0.75 0.5–1.0	0.07 0.02–0.17	0.35 0.2–0.5	25 15–40	70
Mean blood velocity	$cm\ s^{-1}$	20 10–40	20 10–40	15 8–20	10 10–15						15 6–28
Reynolds number (peak)		4500	3400	1250	1000		0.09	0.001	0.035	700	3000
α (heart rate 2Hz)		13.2	11.5	8	3.5	4.4	0.04	0.005	0.035	8.8	15
Calculated wave speed c_0	$cm\ s^{-1}$	580		770	840	850				100	350
Measured wave speed c	$cm\ s^{-1}$	500 400–600		700 600–750	900 800–1030	800 600–1100				400 100–700	250 200–330
Young's modulus E	$N\ m^{-2} \times 10^5$	4.8 3–6		10 9–11	10 9–12	9 7–11				0.7 0.4–1.0	6 2–10

From C. G. Caro, T. J. Pedley and W. A. Seed (1974). Mechanics of the circulation. Chapter 1 of *Cardiovascular Physiology* (ed. A. C. Guyton). Medical and Technical Publishers, London.

2.3.3 Blood

A detailed approach to investigate the PPG technique and the resulting pulsating signal, by highlighting the importance of blood as the main absorber and variable during the recording has not been sufficiently investigated before. This section will address blood properties. The human body is a complex multicellular organism that comprises trillions of cells working together as tissues, organs, and systems. These cells require a continuous and unfaltering supply of oxygen and nutrients in order to function. They also need an efficient and fast means of delivery of these substances as well as a means of removing waste byproducts. This demand cannot be met by simple diffusion alone. Therefore, a more sophisticated system of supply exists in the human body (Aaronson et al., 2012). The cardiovascular system performs part of this function, transporting a specialised connective tissue, the blood, which has the following functions (Rhoades and Bell, 2012):

- Transport: It carries nutrients, oxygen, and water to the cells of the body as well as carrying away waste products and carbon dioxide. It also transports hormones to target cells throughout the body.
- Regulation: It helps regulate body temperature, pH, the ion composition of interstitial body fluids, and cell water content.
- Protection: It plays an important role in immune and inflammatory responses, protecting the body against disease and infection. It also protects the body against excessive blood loss through clotting.

2.3.3.1 Blood Components

From a biological point of view, the blood can be considered a tissue composed of various types of cells (i.e. Red blood cells, white blood cells, and platelets) and a liquid intercellular material (i.e. Plasma). **Figure 2-6** presents a summary of blood components and their major function.

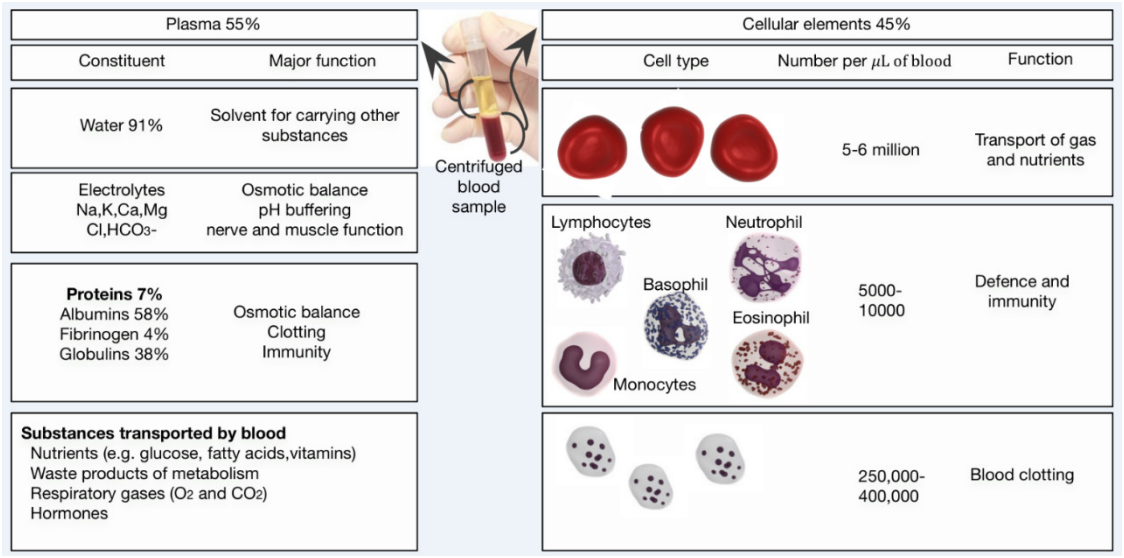

Figure 2-6
Blood constituents. An overview of blood constituents, their concentrations and major function.

From a rheological point of view, blood can be considered a two-phase liquid: it can also be considered as a solid-liquid suspension with the cellular elements being the solid phase. About 40-45% of the blood volume is occupied by the cellular elements; this volume percentage is termed haematocrit. Given the ratio 1000:60:1 for red blood cells (RBCs), platelets, and White Blood Cells (WBCs), leaves RBCs 99% as the main cellular elements of blood. The plasma or the liquid phase include the macroions, electrolytes, as well, it contains 8g of protein per 100 ml. Plasma also contains fibrinogen, a soluble protein that during the clotting process, is converted to insoluble, polymerised form called fibrin. This is an important factor of the flow behaviour of blood, as this protein is responsible for the reversible aggregation of RBC, another property of the blood that will be discussed (Cokelet, 2011; Rhoades and Bell, 2012; McArdle et al., 2006).

Therefore, we will focus attention on the erythrocytes, or red blood cells (RBCs) because they are the only cells which significantly influence the mechanical properties of blood due to being the main cellular element When RBCs are suspended unstressed in plasma, or isotonic fluid, RBCs are highly flexible biconcave discs with the shape and dimensions shown in **Figure 2-6**.

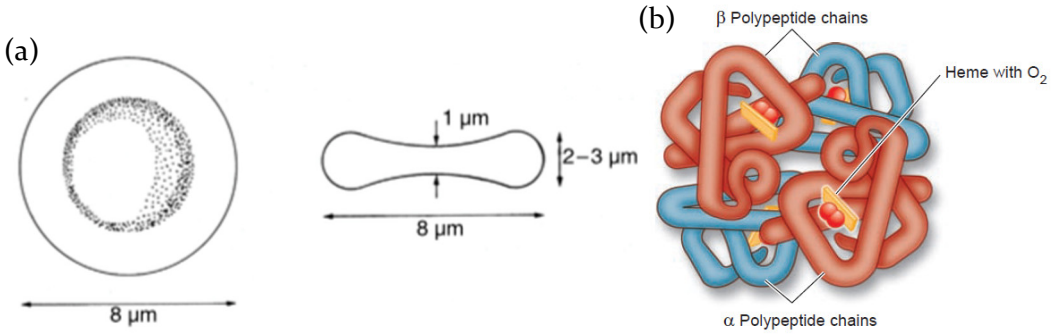

Figure 2-7
Erythrocytes. (a) Showing dimensions of unstressed erythrocyte and average dimensions of a human cell, erythrocytes contain hundreds of haemoglobin molecules. (b) Diagram of the structure of haemoglobin which consists of four polypeptide chains (two alpha and two Beta), with each containing iron bound to its heme group (McArdle et al., 2006).

2.3.3.2 Haemorheology background

Biorheology deals with the flow and deformation behaviour of biofluids. In this study, the focus is around blood rheology or haemorheology. Its purpose is to study blood flow in interaction with its surrounding environment, in both macro and micro circulation.

From a rheological point of view, fluids can be divided into two main groups: *Newtonian liquids;* in which the viscosity is independent of variations in shear rate or shear stress and stated as a constant value, *and Non-Newtonian fluids*, in which the apparent viscosity is variable but rather depends on the magnitude of the shear stress or shear rate. This viscosity of a non-Newtonian fluid may decrease (shear thinning behaviour), or increase (shear thickening behaviour) as the shear rate is increased. The flow behaviour of such liquids may also be time-dependent. Also, the viscosity of all liquids varies with temperature (Baskurt, 2007; How, 1996; Lipowsky, 2005).

2.3.3.3 Viscous properties of blood

Deformation in rheology is defined as, the relative displacement of material points within the body. Solid reacts by deforming if the solid is elastic, the deformation is proportional to the applied force, and the original shape is spontaneously recovered when the force is removed. While fluids continuously deform, or in other means, flow due to the applied forces. Blood and some other materials exhibit viscoelastic properties, which is a combination of fluid-like and solid-like behaviour.

To study the degree of deformation, the force applied per unit area needs to be considered. The deforming force termed stress may have several components: Shear stress; the force per unit area acting parallel to the surface, and normal stress; the force

per unit area acting perpendicular to the surface, or the liquid pressure. The degree of deformation is termed strain. The strain also has various components; for example, shear stress results in shear strain termed shear rate, in which the layers of material move parallel to each other in a progressive manner.

The major field of interest is blood viscosity and elasticity, which is determined by plasma haematocrit, erythrocyte deformability, aggregability and orientation (How, 1996). Moreover, factors such as vessel diameter and temperature can directly affect blood viscosity.

Haematocrit

Haematocrit (Hct) is the relationship between the cellular volumes as compared with the total blood volume, the normal expected values are between 40 and 45% and differ according to gender. It provides valuable information about the changes in the number and the dimensions of RBCs as well as about the volume of the blood plasma.

It is found that the viscosity measured at shear rates of 10 s^{-1} are strongly dependent on haematocrit, with a weaker dependence on plasma viscosity, platelets and plasma proteins (fibrinogen, albumin, and cholesterol) (Friebel et al., 2006).

Under laminar flow conditions, the presence of cellular elements disturbing the flow streamlines is the primary reason why blood viscosity is higher than plasma viscosity. The contribution of this disturbance to the magnitude of blood viscosity can be appreciated by calculating the relative viscosity of blood (i.e. blood viscosity divided by plasma viscosity). The degree of disturbance of flow streamlines and consequently the viscosity of blood is strongly dependent on the concentration of the cellular elements. As shown, there is an exponential relationship between the haematocrit value and blood viscosity, such that at higher levels of haematocrit, blood viscosity becomes increasingly sensitive to haematocrit alterations. At medium to high shear rates, there is about a 4% increase of blood viscosity per unit increase of haematocrit (Ku, 1997).

Cell Deformation

Blood flows only because the RBCs are deformable, and can be reoriented to slide the low viscosity plasma. The elastic deformability of cells means that energy can be stored in and recovered from the RBCs to its original shape. It is affected by the alternations in the properties and associations of the skeletal membrane proteins, together with cell volume and cytoplasmic viscosity alternations as a result of fluid-electrolyte imbalance (Chien et al., 1967; Cokelet, 2011; Fujii et al., 1999; How, 1996).

The primary element responsible for blood viscoelasticity is erythrocytes. Without cell deformation, calculations have shown, erythrocytes give a haematocrit of 58%. On the other hand, in the range of normal haematocrits, there is little plasma space for free cell motion without deformation (McDonald, 1960) .

Observations of the stretching of the erythrocytes and the recovery of the initial shape have been recorded. Also, their significance to the circulation has promoted many studies to assess erythrocyte deformability (Bitbol, 1986; Higgins and Fronek, 1986; Mofrad and Kamm, 2006).

Erythrocyte aggregation

Another important rheological property of RBCs is their tendency to reversible aggregation (the reversible clumping of these cells under low shear forces) (Baskurt, 2007). At low shear forces, the RBCs aggregate in a special way that resembles stacks of coins, forming rouleaux, this has a considerable effect on the blood viscosity at those levels of shear. The degree of the RBC aggregation is widely accepted as a very important determinant of this behaviour is the presence of fibrinogen and other plasma proteins (Baskurt et al., 2011). Each species has its own rheological fingerprint, and the value of aggregation range from hyper aggregating in a group of animals (equine, rhinoceros), to medium type (elephants, rabbits, primates…) and to no aggregation in others (cow, sheep, camelids, rodents) (Cokelet, 2011, Windberger et al., 2003).

Erythrocyte Orientation

It has been known that RBCs in a shear field can orient themselves almost parallel to the flow direction (Fischer, 2007; Fujii et al., 1999; Miller and Jones, 1993). In the presence of the tank-treading motion of the membranes around the cell content which enables the erythrocyte to take a stable orientation. The transition threshold of the RBC from a flipping motion to a definite orientation has been demonstrated to depend on both viscosity ratio and the erythrocyte elongation. The flipping and tank-treading motion are not the only possible influences. Higher shear rates affect RBCs orientation to be more aligned with the vorticity axis, where the cells exhibit spin without angular rotation (Cokelet, 2011; Fischer, 2007; Fujii et al., 1999).

Figure 2-8 shows a representation of the RBC deformation during the change of orientation. When RBCs exhibits unsteady tumbling-rotating motion, the biconcave RBC rotates and flips accompanied with periodical shape deformation as seen in **Figure 2-8(a)**. On the other hand, when RBC is located in a more viscous fluid, it displays a tank-

treading movement with a stationary flattened and stretched shape as seen in **Figure 2-8(b)**.

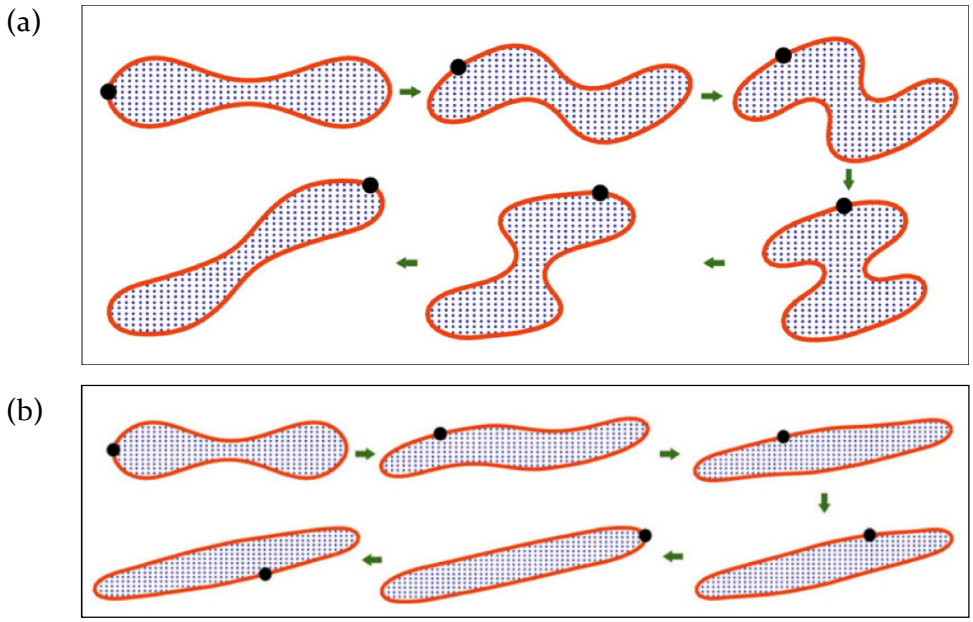

Figure 2-8
Illustration representing the rotation behaviour of RBCs. (a) The RBC tumbling behaviour under shear flow. (b) The RBC tank-trading behaviour under shear flow.

Vessel Diameter and Shear rate

In a study investigating the relationship between vessel diameter and shear rate, it is mentioned that knowledge of the instantaneous volume flow rate of blood through that vessel is a must (Ercan and Koksal, 2003). This relationship varies according to the shear rate. However, a vessel's diameter may remain fixed over time while the blood flow rate may change over time through the same vessel (Cokelet, 2011; Ercan and Koksal, 2003). The shear rate is dependent on viscosity, yet the vessel diameter is not and there is no direct relationship between shear rate and vessel diameter (Ercan and Koksal, 2003).

Temperature

Previous studies have suggested that increased blood temperature, results in decreased blood viscosity related to an increased blood flow rate, decreased local concentration of coagulation factors per volume per time and vasodilation effects (Cokelet, 2011; How, 1996; Valant et al., 2011). Inversely, an increase in blood viscosity due to decreased blood temperatures, higher concentrations of coagulation factors per volume per time and vasoconstriction effects (Valant et al., 2011). Also, other factors were recorded to affect blood viscosity, mental stress in relation to the Autonomic Nervous system (Reims et al.,

2005). Further investigations need to include blood flow velocity in relation to the rheological properties of the blood (Cokelet, 2011).

2.4 Cardiovascular Diseases

Cardiovascular diseases (CVDs) are the leading cause of death globally. CVDs include coronary artery diseases (CAD) such as angina and myocardial infarction (commonly known as a heart attack). Other CVDs are a stroke, hypertensive heart disease, rheumatic heart disease, cardiomyopathy, heart arrhythmia, congenital heart disease, valvular heart disease, carditis, aortic aneurysms, peripheral artery disease, and venous thrombosis (Members et al., 2012).

This project is primarily focused on the investigation of Photoplethysmography for the non-invasive assessment of factors that are altered at an early stage of cardiovascular disease. Hence, the major concern is pathologies that develop at an early stage, i.e. preclinical stages and prior to the occurrence of heart attacks or anginas. Such pathologies are atherosclerosis, hypertension, and hyperviscosity. All of these factors interact with each other to cause a positive feedback loop that drives the growth of the atherosclerotic plaque, increased arterial stiffness, microvascular resistance and overloading the heart muscle. In some cases, this process may stabilise, or sometimes accelerate. Hence, it is only plausible to study these factors together as they are part of the pathological mechanism that essentially drives the progression of cardiovascular diseases at an early stage.

2.4.1 Atherosclerosis

Atherosclerosis (ATH) is primarily an arterial disorder, classically characterised by lipid deposition in the vessel intima, and associated with inflammation, scarring, and calcification (Kwak et al., 2014). Eventually, these lesions cause luminal stenosis and potentially culminate in thrombotic occlusion and/or embolism. Since the manifestations of ATH –including coronary artery disease, peripheral vascular disease, and abdominal aortic aneurysm, renal artery stenosis, and carotid artery stenosis- account for a significant fraction of worldwide morbidity and mortality (Asakura and Karino, 1990; Kwak et al., 2014). The earliest visible lesion of ATH is the fatty streak, which is an accumulation of lipid-laden macrophages in the vascular intima as seen in **Figure 2-9**. These lipid-laden macrophages are often referred to as foam cells because of their foamy appearance and are believed to derive from the ingestion of lipids by macrophages within the intima .

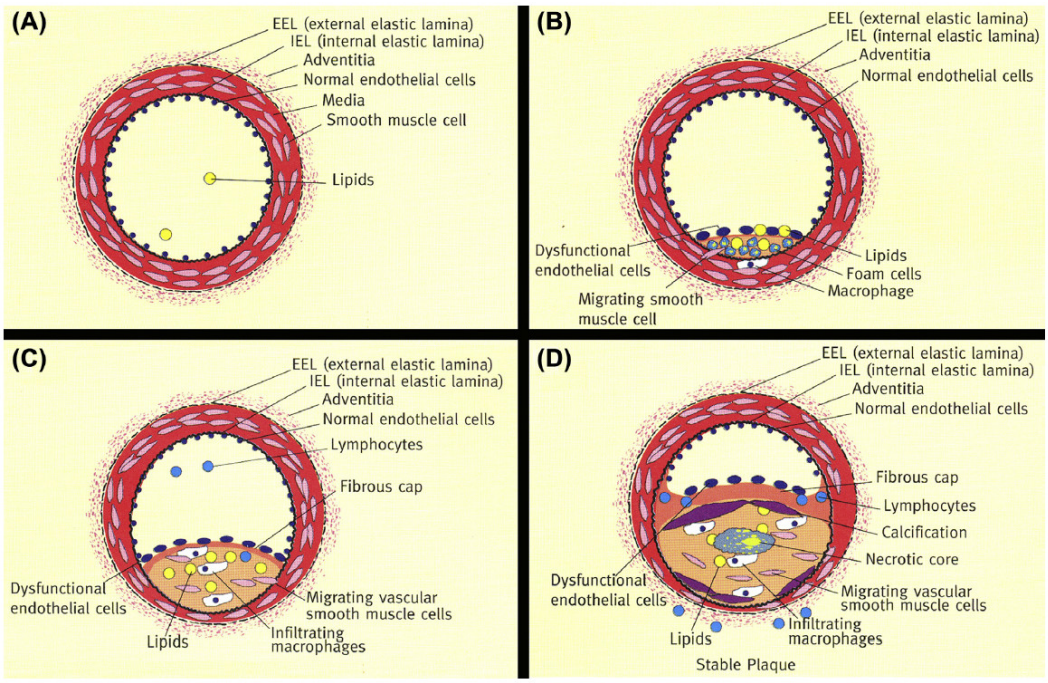

Figure 2-9
Progression of atherosclerotic plaques.(a) the normal vessel is characterised by a lack of inflammation, non-activated endothelium and balanced levels of circulating lipids.(B) The fatty streak develops in the context of local endothelial dysfunction, lipid accumulation in the intima, and recruitment of monocytes that differentiate into macrophages and the development of foam cells.(C) plaque progression shows continued accumulation of lipid, macrophages, and smooth muscle cells, with the recruitment of other inflammatory cells such as lymphocytes.(D) The stable fibro-atheromatous plaque is characterised by a fibrous cap composed of smooth muscle cells and relatively dense extracellular matrix.(Wang et al., 2012, pp. 461–467).

The atherosclerotic process starts early in life and proceeds silently over a long period of time before clinical manifestations. Research into the mechanisms leading to the formation of early ATH lesions is still ongoing, but clearly, a number of factors play important roles. In the current understanding of atherogenesis, the three most important factors, all interacting with each other, appear to be altered lipid metabolism, vascular cell activation, and inflammation (Wang et al., 2012).

Lipids in ATH

Circulating lipids, essential for biological functions, accumulate in the tissue of the blood vessel without ever reaching the intended target cells. This accumulation is promoted by increased levels of lipids in the bloodstream, and in particular, increased levels of cholesterol (Packard and Rader, 2005). Cholesterol circulates in the blood as multiple distinct forms of lipoprotein particles. In particular, low-density lipoprotein (LDL)-associated cholesterol (so-called bad cholesterol) promotes ATH development. In contrast, the high-density lipoprotein (HDL) particles are so-called the good cholesterol and promote the reverse cholesterol transport by removing cholesterol from the vessel

wall. LDL cholesterol can thus be viewed as the fuel for the development of ATH. There is no critical threshold level of LDL that will trigger the development of ATH, and since all humans have LDL, all who live until adulthood will develop ATH to some extent (Packard and Rader, 2005). However, the degree to which the atherosclerotic lesions in any one person will progress is impacted by the concentration of LDL in the blood of that person (Expert Panel on Detection, Evaluation, and Treatment of High Blood Cholesterol in Adults, 2001; Packard and Libby, 2008; Wang et al., 2012).

Endothelial Activation

ATH results in large part from the interaction of lipoproteins with the vessel wall. Thus, changes in the cells of the vessel wall play an important role in the formation of atherosclerotic lesions. Activation of the endothelial cells and vascular smooth muscle cells is a relatively general response to diverse stimuli. It is the endothelium that largely determines the specific section of an artery that will first develop ATH (Naghavi, 2010). Endothelial cells are responsive to biomechanical stimuli imparted by blood flow. Steady laminar shear stress promotes an 'atheroprotective state' in the endothelial cells. However, distributed blood flow that might exhibit some turbulent behaviour or high shear rates, i.e. near branch sites in the vasculature, causes endothelial changes that promote ATH (Naghavi, 2010).

Activated endothelial cells become less efficient in promoting vasodilation, and preventing platelet aggregation, and in suppressing coagulation. The shift toward such endothelial dysfunction is associated with increased reactive oxygen species production (e.g. superoxide and hydrogen peroxide) and a decreased generation of nitric oxide (Shoenfeld et al., 2001).

Inflammation in ATH

Inflammatory responses play important roles in the development of ATH (Packard and Libby, 2008). In ATH, there is abnormal activation of inflammatory cells, which are largely directed towards the lipid deposited in the vascular wall. In general, the greater the systemic inflammatory response, the more likely there will be vascular –associated inflammatory reactions (Shoenfeld et al., 2001). Thus, ATH is amplified by a number of chronic inflammatory conditions including periodontal disease and rheumatoid arthritis.

In ATH, the leukocytes in the circulation are recruited in the vascular wall at the sites of lipid accumulation. Initially, the leukocytes are monocytes, which are activated to form tissue macrophages. The lipid loading of these macrophages can trigger cell death that

contributes to more build-up of thrombogenic material within the intima, including phospholipid and tissue factor (Naghavi, 2010; Packard and Libby, 2008).

2.4.2 Hypertension

Elevated blood pressure, also known as hypertension, affects ~30% of the adult population in both developed and developing countries and is a major cause of morbidity and mortality (Sliwa et al., 2011). There is a positive and continuous correlation between blood pressure and the risk of cardiovascular disease, kidney disease, and stroke, even in the normal range of blood pressures. In middle-aged groups and the elderly, this correlation is more robust for systolic blood pressure than with diastolic blood pressure (Chobanian AV et al., 2003).

The main reasons for the development of hypertension include hereditary reasons, factors that affect the physiological control of blood pressure as described in **Figure 2-1** including the cardiac output, peripheral resistance, the sympathetic nervous system, the kidneys, and homoeostasis. These factors are discussed in further depth hereunder.

2.4.2.1 Genetics of hypertension

Primary hypertension clusters in families. Individuals with two or more first-degree relatives with hypertension younger than 55 years have an almost four times greater risk of developing hypertension before 50 years of age. Family studies clearly demonstrate a significant heritability component for blood pressure (Members et al., 2012).

2.4.2.2 Cardiac output and hypertension

Cardiac output is the product of stroke volume and heart rate. Accordingly, increased the pre-load or cardiac contractility or heart rate to neural simulations are important. Patients with established hypertension usually have a lower blood volume and total exchangeable sodium when compared to normotensive individuals. This was attributed to increased translocation of fluid across the capillary bed into the interstitial space and possibly to increased intracellular fluid volume. Increased heart rates have been attributed to increased sympathetic activity and/or decreased parasympathetic activity (Safar et al., 2014).

2.4.2.3 The sympathetic nervous system and hypertension

Increased sympathetic activity plays a major role in hypertension, particularly in the early stages (Tank et al., 2003). This is evidenced by elevated plasma norepinephrine levels, increased heart rate and blood pressure variability, increased alpha-adregnic vasoconstriction and increased vascular reactivity to norepinephrine. Changes in other

neurotransmitters (e.g. adenosine and dopamine) may also reflect sympathetic nervous system involvement (Reims et al., 2004).

2.4.2.4 Renal function and hypertension

The link between abnormal renal function and hypertension has been long established. The kidney increases urinary sodium excretion in response to elevated blood pressure, and reduce blood volume and normalise blood pressure. It has been suggested that a reduction in the filtration surface in the kidney (due to reduced number or efficiency of nephrons) may limit renal sodium excretion. Also, excess dietary salt intake induces hypertension by increasing fluid volume and cardiac output. Sodium excess may also increase blood pressure by influencing vascular reactivity and tone (Courneya and M.D, 2010; Rhoades and Bell, 2012).

2.4.2.5 The vascular system and hypertension

Small arteries are responsible for blood pressure control and regional distribution of blood flow through effects on vascular resistance. According to Poiseuille law, a slight change in lumen size results in significant changes in resistance. The lumen diameter of resistance arteries is a function of vasomotor tone via the vasoconstriction and vasodilation processes and the mechanical properties of the vessel wall (Safar et al., 2014).

Vascular contraction

Vascular smooth muscle cell contraction is a major factor regulating the vascular tone. It is increased in experimental and clinical hypertension. Non-invasive diagnostic approaches including vascular ultrasound, pulse wave analysis and peripheral tone studying the endothelial function and human vascular tone have demonstrated that patients with hypertension exhibit impaired endothelium-dependant vasodilation, increased vascular reactivity, and increased contractility (Barac et al., 2007).The vascular contraction is primarily regulated by the increased levels of calcium ions (Baker, 2000).

Vascular ageing and hypertension

Age-associated changes in blood vessels are known to occur in healthy individuals (Mancia et al., 2007). These changes include increased arterial wall thickness, reduced compliance, increased stiffness, and decreased lumen diameter. All of these features cause the increase in flow resistance and hence, overloading the workload on the heart, and hence they are commonly associated with hypertension. The structural changes are also related to the endothelial dysfunction, caused by the change in the chemical content of the vessel wall. Arterial ageing is a predominant risk factor for the occurrence of CVDs,

such as hypertension, and is associated with increased vascular stiffness, intima-media thickening, calcification, and inflammation (Mancia et al., 2007).

2.4.2.6 Other factors

Other factors include the Renin-Angiotensin system which can be described as a haemodynamic regulator the increases blood pressure temporarily by vasoconstriction and chronically through aldosterone-mediated volume expansion. Moreover, the reactive oxygen species and oxidative stress also play a role in hypertension. Reactive oxygen species are signalling molecules important in the regulation of many physiological processes including defence, ageing, and cellular hemostasis.

2.4.3 Hyperviscosity

We have previously defined blood viscosity and the associated rheological properties of RBCs. Patients with acute and chronic CVDs may have abnormalities involving blood viscosity, plasma viscosity, red cell deformability, red cell aggregation and fibrinogen (Cho et al., 2014; Coull et al., 1991; Dintenfass, 1964). Medically, it is possible to find abundant evidence throughout the literature that blood viscosity can be a significant indicator of cardiovascular diseases at an early stage. A strong link has been reported in thrombosis (Dintenfass, 1964), hypertension (Letcher et al., 1983; Pop et al., 2002), myocardial infarction (Jan et al., 1975; Turczyński et al., 2002), cardiovascular complications (Cho et al., 2014; Lowe et al., 1997) and acute stroke(Coull et al., 1991; Gusev et al., 2008). Hyperviscosity is also linked with CVD risk factors such as increased cholesterol levels (Crowley et al., 1994), diabetes (Irace et al., 2013), obesity (Safar et al., 2006) and tobacco exposure (Shimada et al., 2011).

2.5 The Physics of Blood Flow

It is essential to develop an understanding of the physical factors and laws that govern the movement of blood in the cardiovascular system for an overall understanding of its function. This section is dedicated to cover some of the most relevant concepts related to cardiac fluid mechanics. For simplification purposes, we will represent flow movement in a cylindrical vascular model as seen in **Figure 2-10**.

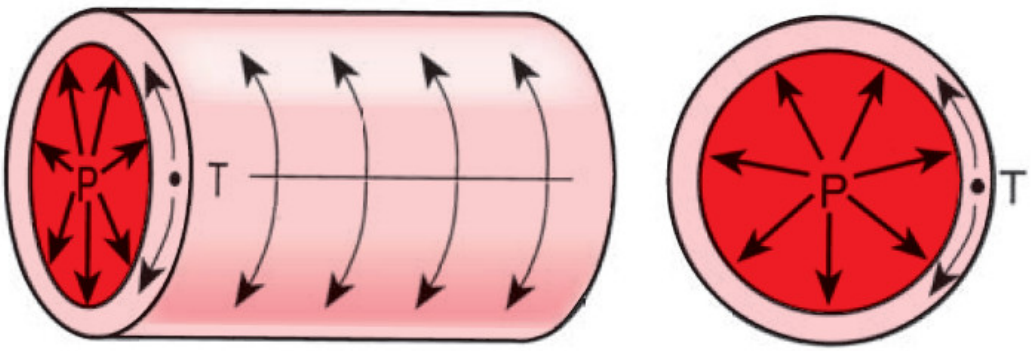

Figure 2-10
Pressure and tension in a cylindrical blood vessel. The tension is the force that would pull the vessel apart along line along the length of the vessel. Tension in the vessel wall is related to the law of Laplace. P, pressure, tension(Rhoades and Bell, 2012) .

The volume contained in arteries and veins is a function of the pressure difference across their wall, called the *transmural pressure,* and the degree of stiffness within the vascular wall. Transmural pressure (P_T) is defined as the difference in pressure inside versus the outside of a hollow structure cylinder (Caro, 2012; Rhoades and Bell, 2012). The change in volume (V) for a given change in transmural pressure is called the *compliance* (C)*;* which is defined *as* the property of a material undergoing elastic deformation or change in volume when subjected to an applied force. It is equal to the reciprocal of stiffness and is given by the equation

$$C = \Delta V / \Delta P_T \qquad (2.1)$$

Where Δ signifies the before/after a change of volume or pressure. The outside pressure is taken to be atmospheric pressure, which is always given at the baseline value of zero in normal physiologic systems. As will be highlighted later, vascular compliance and stiffness are critical determinants of the performance of the heart, workload placed on the heart, and the amount of oxygen consumption for normal functionality.

It is important to note that arterial compliance or stiffness are not constants within the cardiovascular system (e.g. as P increases, C decreases). Moreover, arterial compliance decreases with age at any given transmural pressure as seen in **Figure 2-11** and is reduced by contraction of the smooth muscle within arteries or veins. This is an important component of haemostasis control in individuals.

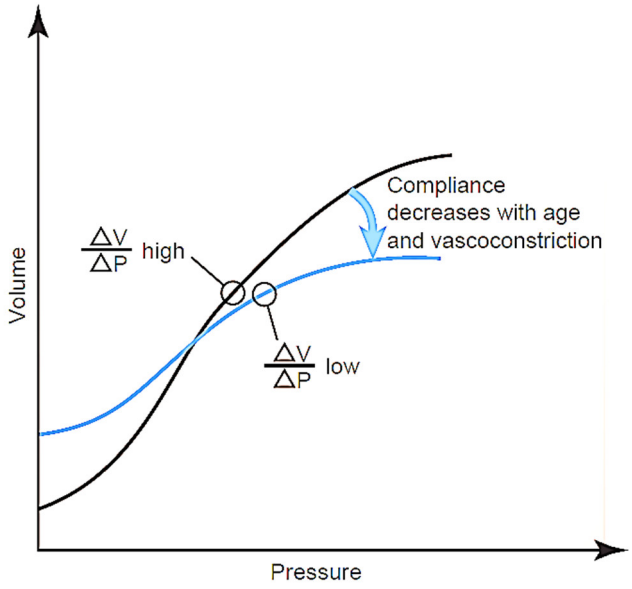

Figure 2-11
The relationship between volume and transmural pressure in arteries and the effect of age on the relationship (Rhoades and Bell, 2012).

Any transmural pressure within an artery or vein exerts distributed forces on the inner surface of the vessel wall as illustrated in **Figure 2-10**. Such forces are balanced with the opposing forces supplied by the muscle and connective tissue of the vessel wall, termed as *Tension* (T). For cylinders with thin walls in comparison to the tube radius (commonly agreed ratio of 10-20), tension is represented with *Law of Laplace* which relates the vessel radius (r) with P_T through the relationship $T = P_T.r$ (Rhoades and Bell, 2012). However, such conditions do not apply to most blood vessels, the walls of arteries and veins are sufficiently thick, and in reality, tension is proportional to *wall stress* (S) and is expressed with the relationship $S = P_T.r / w$, where w is the wall thickness. Tension and stress are important determinants of energy requirements of the contraction of blood vessels, as they need to be overcome for the vessels to contract.

2.5.1 Reynolds' Observations: Laminar and Turbulent flow

After the middle of the 19th century, collected experimental data revealed that in a liquid flowing at a slow rate, the pressure drop is proportional to the speed of flow. Under these

conditions, it has been observed that the liquid parts move smoothly adjacent to the parallel tube wall, known as *Laminar* flow. In the case of increasing flow rates, there is a tendency for the liquid flow to become irregular, as the fluid move in swirls and random patterns. This type of chaotic flow is termed *Turbulent*.

Reynolds found (King, 1916) that the onset of turbulence depends on the average flow velocity through the tube Reynolds number was introduced as a dimensionless quantity to help predict similar flow patterns in different fluid flow situations. It is defined as the ratio of inertial forces to viscous forces and is represented by the following equation:

$$\mathrm{Re} = \rho vL \Big/ \mu = vL \Big/ \eta \qquad (2.2)$$

Where v is the maximum velocity of the fluid in m/s, L is the characteristic linear dimension, for a flow in a pipe, L is the hydraulic diameter of the pipe, μ is the dynamic viscosity of the fluid (N s/m² or kg/(m.s)), ρ is the density of the fluid (kg/m³) and η is the kinematic viscosity (m²/s).

The typical Reynolds number range of blood flow in the body varies from 1 in small arterioles to approximately 4000 in the largest artery, the aorta. Thus, the flow spans a range in which viscous forces are dominant on one end, and inertial forces are more important on the other.

2.5.2 Poiseuille Law

In the 1840s, Louis Poiseuille conducted experiments that resulted in a mathematical relationship that describes flow in a cylindrical tube (Ku, 1997; McDonald, 1960). This is known as Poiseuille law and states that:

$$Q = \pi r^4 \Delta P / 8\mu l \qquad (2.3)$$

Where Q is the flow, ΔP is the pressure difference between a point at the entrance of the tube and the end, l is the tube length and μ is fluid viscosity. The term $8\mu l / \pi r^4$ is the *resistance* (R) to the flow and in physiology is expressed in mmHg/ml and is known as *peripheral resistance*. Hence in the cardiovascular system, this relationship can be rewritten as

$$\Delta P = Q.R \qquad (2.4)$$

This relationship indicates that flow is proportional to the pressure difference between the entrance and the exit points of the tube and inversely proportional to the resistance

of the cardiovascular system, ''the end of the tube'' is considered the right atrium where the pressure is known to be about 2 mmHg. This is usually eliminated from the equation, so the difference in the pressure becomes simply P, as is taken as the mean pressure within an artery or vein. Consequently, the Poiseuille law reduces to

$$P = Q.R \tag{2.5}$$

This law indicates that the mean pressure is the product of the flow output of the heart, called *cardiac output*, and the resistance to flow provided by all blood vessel and blood viscosity is total peripheral vascular resistance (TPR).

2.5.2.1 The applicability of Poiseuille equation to the circulation

The conditions under which the Poiseuille's equation applies should be considered in more details (McDonald, 1960):

1. The fluid is homogenous, and its viscosity is the same at all rates of shear: Blood is a non-Newtonian fluid. However, it has been assumed that in tubes with large internal diameter compared with the size of the erythrocytes, blood behaves as a Newtonian fluid.
2. The liquid does not slip at the wall. This was the assumption that velocity is zero in fluid layers adjacent to the wall. This theory is held to be universally true for liquids.
3. The flow is laminar, and the liquid is at all points moving parallel to the walls of the tube. Turbulence might occur in the largest blood vessels, but the laminar flow is expected to be present in all the vessels.
4. The rate of flow is steady, where the flow is not subject to deceleration or acceleration. If the velocity is altered, the pressure gradient is partly utilised in communicating kinetic energy to the liquid. Blood flow is markedly pulsatile, and Poiseuille laws do not apply.
5. The tube is long compared with the region being studied. Near the inlet of the tube, flow is not yet developed into the parabolic velocity profile of laminar flow. In the circulation, there is never the condition of a stationary reservoir leading to steady laminar flow.
6. The tube is rigid, and the diameter does not vary with the internal pressure. Blood vessels are viscoelastic structures, and their diameter is a function of transmural pressure. However, Baez et al. demonstrated that the diameter of capillaries varied very little with changes in the internal pressure in the range of 20-100

mmHg. Similar observations led Fung et al. to postulate that the extracellular fluid has a gel-like structure that effectively strengthens the wall(Fung et al., 1966).

The assumptions underlying the Poiseuille equation discussed above can be only be applied approximately in living circulation. Such assumptions can compensate the reality of the pulsatile flow in the circulation and the role of wall elasticity, fluid viscosity and the most basic phenomena that are essential to describe blood pulsatile flow. A more comprehensive and inclusive mathematical approach is the Navier-stokes equation discussed below.

2.5.3 Navier-Stokes Equations in Tubes

The Navier-Stokes equations are the basic governing equations for a viscous, heat conducting fluid. The initial work was conducted by Navier in 1827. However, this was not completely successful and was later developed by Poisson in 1831. Both of which relied on assumptions of intramolecular forces that are now considered unrealistic. Stoke reworked the entire problem in 1845, and the resulting equations are known as Navier-Stoke equations. It is a vector equation obtained by applying Newton's Law of motion to a fluid element and is also called the momentum equation. It is supplemented by the mass conservation equation, also called continuity equation and the energy equation. Usually, the term Navier-Stokes equations are used to refer to all of this equation (Zamir, 2000).

By applying Navier-Stokes equations to cylindrical coordinates and when the tube wall is nonrigid, there presents radial velocity (u), and both axial and radial velocities are dependent on the displacement (x) even away from the tube entrance. Using Navier-Stokes equations, and assuming only axial symmetry leads to,

$$\rho\left(\frac{\partial u}{\partial t}+u\frac{\partial u}{\partial x}+v\frac{\partial u}{\partial r}\right)+\frac{\partial p}{\partial x}=\mu\left(\frac{\partial^2 u}{\partial t^2}+\frac{\partial^2 u}{\partial r^2}+\frac{1}{r}\frac{\partial u}{\partial r}\right) \tag{2.6}$$

$$\rho\left(\frac{\partial v}{\partial t}+u\frac{\partial v}{\partial x}+v\frac{\partial v}{\partial r}\right)+\frac{\partial p}{\partial r}=\mu\left(\frac{\partial^2 v}{\partial t^2}+\frac{\partial^2 v}{\partial r^2}+\frac{1}{r}\frac{\partial v}{\partial r}-\frac{v}{r^2}\right) \tag{2.7}$$

Where ρ is density, u is axial velocity, v is radial velocity, t is time, and r is tube radius. An input oscillatory pressure propagates down the tube, and there is wave motion within the tube, where, the pressure gradient and the two velocities are functions of both x and t. u and v are functions of x.

While in a rigid tube, it is possible to postulate a fully developed region away from the tube entrance where the flow is independent of *x*. Thus, derivatives of *u*, *v* with respect to x are zero. The equation of continuity combined with the boundary condition *v*=0 at the tube wall then leads to *v* being identically zero and the governing equations reduce to

$$\rho\frac{\partial u}{\partial t}+\frac{\partial p}{\partial x}=\mu(\frac{\partial^2 u}{\partial r^2}+\frac{1}{r}\frac{\partial u}{\partial r}) \tag{2.8}$$

Where the pressure gradient is a function of *t* only, not of *x* and the velocity *u* is then a function or *r* and *t* only, not of *x*. For an oscillatory pressure gradient, the velocity *u* then oscillates with the same frequency, and since it is not a function of x, it will represent the velocity at every cross section of the tube. The fluid is expected to oscillate in bulk, and no wave motion is expected to be present when the tube is rigid. An illustration representing the flow profiles in a rigid (top) and an elastic tube (bottom) are presented in **Figure 2-12**.

The speed of which the wave propagates down the tube depends on the elasticity of the tube wall. If the wall thickness is small compared to the tube radius, and if the effects of viscosity can be neglected, the wave speed is given approximately by the Moen-Korteweg formula (Zamir, 2000, p. 115).

$$PWV=\sqrt{\frac{Eh}{\rho d}} \tag{2.9}$$

The Moens–Korteweg equation states that pulse wave velocity (PWV) is proportional to the square root of the incremental elastic modulus, (*E*), of the vessel wall given constant ratio of wall thickness, h, to vessel diameter, d, and blood density, ρ, assuming that the artery wall is isotropic and experiences isovolumetric change with pulse pressure.

Applying Navier-stoke equations to blood flow in arteries usually requires making some assumption to simplify the equations. The equations are non-linear partial differential equations that require powerful computers to provide a solution. One of the simplified dimensional analysis of the equations is Womersley number.

2.5.4 Womersley Number

A dimensional analysis of the unsteady Navier-Stokes equations leads to a non-dimensional number commonly referred to as the Womersley or Witzig parameter:

The Womersley number (α) is a dimensionless expression of the pulsatile flow frequency in relation to viscous effects. It is named after John R. Womersley (1907–1958) for his work with blood flow in arteries and is represented by the following relationship:

$$\alpha^2=\rho\omega r^2/\mu \qquad (2.10)$$

where r is the tube radius, ω is the angular frequency, and μ is the kinematic viscosity (Womersley, 1955). This parameter is used in the similarity transform developed in the well-known Stokes' Second Problem, in which flow is induced by an oscillating flat plate.

The Womersley parameter α can be interpreted as the ratio of the unsteady forces to the viscous forces. When the Womersley parameter is low, viscous forces dominate, velocity profiles are parabolic in shape, and the centerline velocity oscillates in phase with the driving pressure gradient (McDonald, 1960; Womersley, 1955). For Womersley parameters above 10, the unsteady inertial forces dominate, and the flow is essentially one of piston-like motion with a flat velocity profile. The amplitude of motion decreases at the higher frequencies, and there is a 90° phase difference between the pressure gradient and flow, as in a low-pass filter.

In contrast to unsteadiness, several features of biological flows tend to be neglected in some situations as secondary in importance. These properties include vessel wall elasticity, non-Newtonian viscosity, slurry particles in the fluid, body forces, and temperature. Although each is physiologically relevant, the analysis is greatly simplified when these can be justifiably neglected.

2.5.5 Velocity Profiles

Vascular biologists are currently more concerned with the local haemodynamic conditions in a given artery or branch than simply the flow waveform. A detailed local description of these pulsatile flows is needed. The fluid-wall shear stress in a blood vessel for a given pulsatile flow situation often needs to be determined. Fully developed pulsatile flow in a straight or tapered tube can be expressed analytically (Hale et al., 1955; Womersley, 1955). A physiologic pressure or flow waveform can be expanded as a Fourier series, and the harmonic components of velocity can be summed to yield the unsteady velocity profiles. **Figure 2-12** shows an example of velocity profiles for pulsatile flow in a rigid and non-rigid tube wall.

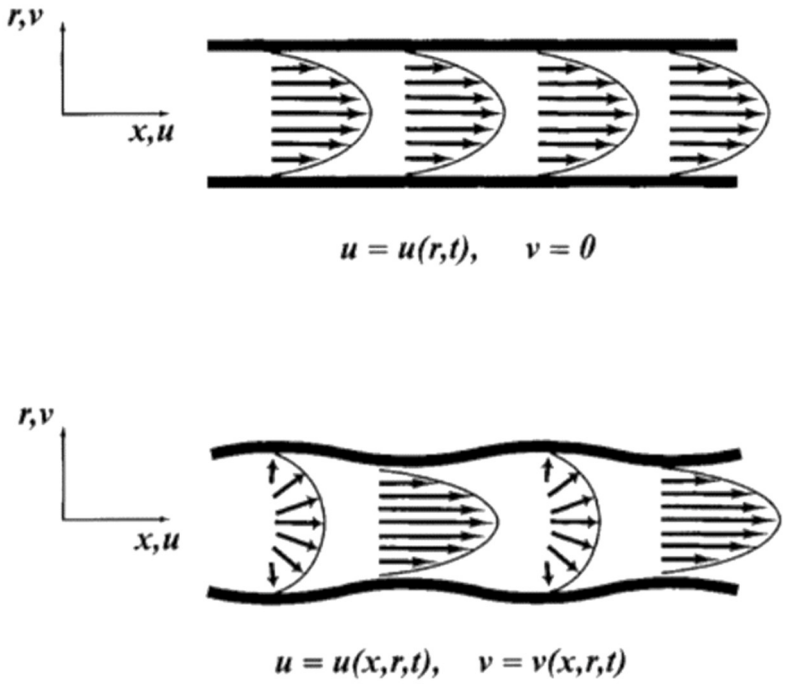

Figure 2-12
Pulsatile flow in a rigid wall (top) and in a nonrigid wall (bottom) (Zamir, 2000).

The Womersley solution for velocity can be used to generate excellent approximations for shear stress as long as secondary and separated flows are not present. Analytical solutions have also been obtained for flow through arteries that translate or change their radius of curvature, such as coronary arteries, which ride on the moving heart surface (Delfino et al., 1994).

2.5.6 Entrance Regions

Flow from the heart comes from a large pressure reservoir into successively smaller tubes. The flow is not fully developed near some of the origins of arteries. Flow in these regions is similar to an entrance flow with a potential core and a developing boundary layer at the wall. The velocity profiles are blunt near the centre, and the centerline velocity accelerates as the boundary layer retards velocity near the wall (Zamir, 2000).

Unsteady flow through the entrance region depends on the Womersley parameter as well as the Reynolds number. For low Womersley parameters, the maximum unsteady entrance length is approximately the same as the steady entrance length for the peak flow and is primarily dependent on the Reynolds number. For high Womersley parameters, the Stokes boundary layer growth is faster, and the entrance length is more uniform

during the cycle. For $\alpha \geq 12.5$, the pulsatile entrance length is approximately the same length as the entrance length of the mean flow. At all α, the wall shear rate converges to its fully developed value at about half the length at which the centerline velocity converges to its fully developed value. Thus, the upstream flow conditions leading to a specific artery may or may not be fully developed and can be predicted by the magnitudes of the Reynolds number and Womersley parameter (He and Ku, 1994)

Although a Womersley-type analysis is useful to gain a general understanding of the relevant forces, the nonlinear convective term is important to many flows at arterial branches. Likewise, the flow in most arteries is subject to viscous forces that cannot be neglected. For a medium-sized artery, the Reynolds number is typically on the order of 100 to 1000, and the Womersley parameter ranges from 1 to 10 (Caro, 2012). These conditions allow for few simplifications of the unsteady Navier-Stokes equations. Arteries have a high degree of stiffness that does allow for a long wavelength approximation. In most cases, the effects of elasticity are considered to be very small, and analytics are based on an assumption of rigid tube flow. Most studies of artery haemodynamics use experimental measurements, potential flow theory, or computational fluid mechanics. The three-dimensional (3D) nature of many of these unsteady flows is a serious obstacle to computational methods because the computational time required is enormous.

2.5.7 Fluid Viscosity

On the molecular level, fluids exert forces of attraction on each other. When the fluid flows over a surface, the layer adjacent to the surface may become attached to it, where the rest of the layers are moving. Therefore, a shearing force takes place between the layers of the fluid. Shear stress is the force applied to a layer of fluid to cause it to slide past other layers. The rate of shear is the velocity gradient between 2 parallel planes in a flowing liquid that occurs as a result of the force (Feireisl, 2003). The viscosity of a fluid is defined as a ratio of shear stress to the rate of shear. The unit of viscosity in the metric system is the Poise, named after Jean Poiseuille. Generally, the poise is expressed in CGS (centimeter-gram-second). In the MKS system, poise is replaced with the Pascal.second (Pa.s).

For most fluids, such as plasma or serum, the viscosity of a liquid is an inherent property of the liquid itself. The measured viscosity is the same regardless of the shear rate. Such fluids are called Newtonian fluids; Newtonian fluids are generally homogeneous.

On the other hand, fluids that change viscosity in accordance with varying shear rates are called non-Newtonian fluids. Many mathematical models are available to describe the nonlinear ''shear stress versus deformation-rate'' relationship of non-Newtonian fluids (Waite and AccessEngineering, 2007). But no general model can describe the constitutive equation of all kind of non-Newtonian fluids. However, the mathematical model for describing the mechanistic behaviour of a variety of commonly used non-Newtonian fluids is the Power-Law model which is also known as Ostwald-de Waele model where

$$\tau = K(\partial u / \partial y)^n \qquad (2.11)$$

Where τ is the shear stress, K is the flow consistency index, $\partial u / \partial y$ is the shear rate or velocity gradient perpendicular to the plane of shear in s^{-1}, and n is a dimensionless parameter termed the flow behaviour index.

Power-law fluid can be subdivided into three different types of fluids based on the value of their flow behaviour index; where n=1 is a pseudoplastic fluid, n=1 is a Newtonian fluid and at n>1 is a dilatant fluid.

Pseudoplastic or *shear-thinning* fluids have a lower apparent viscosity at higher shear rates and are usually solutions of large, polymeric molecules in a solvent with smaller molecules (Viswanath et al., 2007). It is generally supposed that the large molecular chains tumble at random and affect large volumes of fluid under low shear, but that they gradually align themselves in the direction of increasing shear and produce less resistance. Dilatant or *shear-thickening* fluids increase in apparent viscosity at higher shear rates. They are rarely encountered.

Whole blood behaves as a non-Newtonian fluid. This property is related to the behaviour of the erythrocytes and their known viscoelastic properties that were discussed earlier. Even that such factors can be heavily affected by chemical content, they are reflected in the mechanical behaviour of red blood cells and of blood as a whole. Studies have shown that blood behaves like observed in **Figure 2-13** under varying shear rates. The factors affecting whole blood viscosity have been discussed earlier in this chapter.

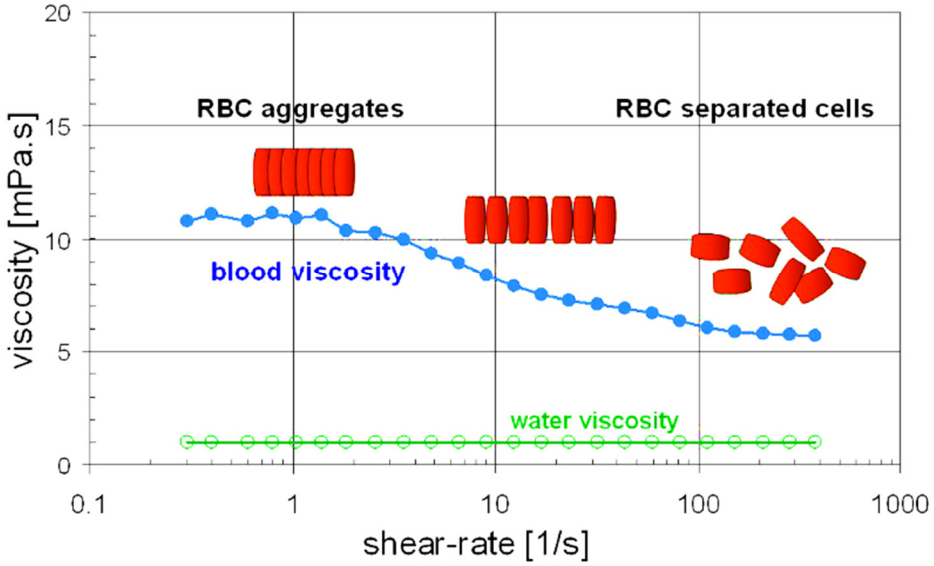

Figure 2-13
Whole blood behaves as a non-Newtonian fluid and its viscosity is dependent on the amount shear rate exposed to the sample as described by Somer and Meiselman (Somer and Meiselman, 1993).

SUMMARY

This chapter discussed the fundamentals of the cardiovascular system from a physiological and anatomical point of view considering the role of the nervous system in blood pressure and flow regulation and the function of the heart, arteries and blood as the main organs of the cardiovascular system. Briefly, we have overviewed cardiovascular diseases and the main three preclinical parameters that contribute to the progression of the disease; hypertension, atherosclerosis, and hyperviscosity. We also overviewed the basic physical principles known in blood flow theories and their applicability to the human blood circulation.

Chapter 3
CURRENT STATE OF THE ART OF BLOOD PRESSURE, ARTERIAL STIFFNESS AND BLOOD VISCOSITY MEASUREMENTS

3.1 Introduction

Cardiovascular Diseases (CVDs) are the leading cause of morbidity and mortality from infancy to old age globally. It is estimated that 90% of CVD is preventable (McGill et al., 2008). CVDs are associated with many risk factors. These include hereditary reasons that cannot be influenced and other risk factors that can be treated or controlled. These include hypertension, tobacco exposure, hypercholesterolemia, obesity, physical inactivity, diabetes, unhealthy diets and harmful use of alcohol. These are useful predictors of morbid atherosclerosis and hypertensive events, and their control variably reduces the incidence of morbid events.

National health policy panels have recommended active treatment of hypertension and hyperlipidemia when clinical measurements of blood pressure and cholesterol fall outside the predefined normal limits (Chobanian AV et al., 2003; Expert Panel on Detection, Evaluation, and Treatment of High Blood Cholesterol in Adults, 2001). Yet

epidemiologic data indicate that most cardiovascular events occur among individuals with moderate levels of risk factors (Hulley et al., 1992). Therefore, there is a need for more accurate early-stage monitoring/screening where preclinical parameters that can predict future morbid events in patients, especially those with asymptomatic CVD can be readily available using noninvasive technologies.

This project will focus on the three major determinants of cardiovascular health at an early stage: blood pressure (BP), arterial stiffness (AS) and blood viscosity (BV).Our interest in those three parameters stems from their importance in the cardiovascular circulation and the amount of literature that reports on hypertension, increased arterial stiffness and hyperviscosity as major risk factors at the very early stages of preclinical and asymptomatic CVD and their role in the progression of atherosclerosis to more complex stages and the development of strokes (Coull et al., 1991; Hansen et al., 2006), anginas (Taniguchi et al., 2014; Yoneda et al., 1989), and heart attacks (Hirai et al., 1989; Jan et al., 1975; Turczyński et al., 2002). Hence, they can be considered, as the source of the progression and development of cardiovascular diseases.

In this chapter, we present an overview of the most commonly used invasive and non-invasive methods for measurement or estimation of BP, AS, and BV whether commercially available for clinical assessments and personal devices or methods that are being investigated by researchers.

3.2 Blood Pressure Measurements

Arterial blood pressure is a key measurement of haemodynamic status and is a marker of adequate organ perfusion and tissue flow. The monitoring of blood pressure is one of the minimal mandatory standards required in anaesthetic practice. The accurate measurement of a patient's arterial blood pressure is vital as it enables clinicians to deliver safe and appropriate care. Currently available methods for blood pressure measurements include continuous invasive methods and non-invasive intermittent and continuous methods and are discussed in this section (Marini and Wheeler, 2012).

3.2.1 Invasive Continuous Methods

The direct measurement of arterial pressure uses an indwelling cannula and is considered to be the most accurate, real-time method of monitoring blood pressure. An intra-arterial cannula is hydraulically coupled via a column of saline to a diaphragm and transducer assembly (Chung et al., 2013). The transducer is usually a bonded wire strain gauge. Changes in pressure produce very small movements of the diaphragm that in turn alters

the length of the strain gauge wire and its electrical resistance. The strain gauge is incorporated into the four-resistor arrangement of a Wheatstone bridge containing a null deflection galvanometer (Chung et al., 2013). The changes in electrical resistance mirror the changes in arterial pressure. The arterial pressure waveform is a periodic complex wave which may be considered to be the sum of a series of overlapping sine waves of different frequencies, amplitudes, and phase relationships. Using Fourier analysis, the waveform is converted into its sine wave components. The fundamental frequency (*f*) is the most basic sine wave component and is equal to the heart rate (1-2 Hz). Subsequent harmonics are integer multiples of the fundamental frequency (*2f, 3f, 4f.*). As the harmonics increase, their amplitude decreases. Thus, higher order harmonics contribute least to the shape of the arterial pressure wave, and the pressure wave can be reliably reconstructed from the first ten harmonics (Marini and Wheeler, 2012).

This method incurs some disadvantages that can be summarised as:

- The invasive nature of this method makes it less appealing for regular or fast assessments.
- A non-feasible method for personal devices and home healthcare.
- There are two sources of error in this method: resonance, which can be avoided using wide tubes and less dense fluid, and damping, which emerges from bubbles and clots in the system.
- It requires experienced staff to connect the device and provide the readings.

3.2.2 Non-invasive Intermittent Methods

3.2.2.1 Manometry

A pneumatic cuff connected to a liquid filled manometer is inflated, occluding the arterial flow to a limb and then deflated. The pressure measured is the height of the fluid column when the pulse returns distally to the cuff. It is detected by digital palpation or auscultation for Korotkoff sounds. The cuff may be used on the upper arm, forearm or leg and the width should be 40% of the mid-circumference of the limb, covering two-thirds of the limb length. Aneroid gauges or electronic pressure transducers are now more commonly used (Marini and Wheeler, 2012).

3.2.2.2 Oscillometry

Devices employing oscillometric principles include the DINAMP (Device for non-INvasive Automatic Mean Arterial Pressure). These devices allow automatic hands-free blood pressure measurement at a user defined frequency (Chung et al., 2013). They are

designed to be more user-friendly and come in different sizes and configurations (See **Figure 3-1**).

A pneumatic cuff occludes the arterial flow which is then deflated automatically at different steps coupled with the patient's heart rate. As the arterial flow returns, the vessel wall vibrates causing variations in cuff pressure, which are sensed by a pressure transducer. The signal is digitised and a microprocessor presents a numerical display. Mean arterial pressure (MAP) is the point of maximal oscillations and the most accurate measurement. Systolic blood pressure (SBP) and diastolic blood pressure (DBP) are calculated as the fastest rate of increase and decrease in oscillation amplitude respectively).

Figure 3-1
Oscillometry manometer (Grahamfield, 2016).

Early oscillon tonometers (Von Recklinghausen, 1931) used two cuffs. The proximal cuff with adjustable bleed valve occludes arterial flow. The distal cuff senses when pulsations return by means of two aneroid chambers which are connected to a dial via a mechanical linkage. A rotating valve determines interconnections between the cuffs, inflating mechanism, bleed valves, and aneroids (Marini and Wheeler, 2012).

Non-invasive intermittent methods are simple to use and require minimal training however inaccuracies may arise from:

- Inappropriate cuff size can cause misreadings; a small cuff can cause over readings and under-reading with a large cuff
- Limb movement
- External compression
- Hypotension
- Arrhythmias (atrial fibrillation)
- The cuff may cause tissue or nerve damage and patient discomfort

- The delay between readings is the major drawback with intermittent techniques and can be overcome by using continuous monitoring devices.

3.2.3 Non-invasive Continuous Methods

3.2.3.1 Ultrasound

Doppler ultrasound measures change in blood velocity in the large arteries. Velocity profiles and distension waveforms may be measured using a brightness mode (B-mode or 2D mode) ultrasound device; allowing local Pulse Wave Velocity (PWV) to be estimated mathematically (Beulen et al., 2011). The PWV values are then used to convert distension waveforms to pressure waveforms with good correlation to reference pressure traces.

The main drawbacks of this method are:

- It requires extreme precision to the placement and securing of the ultrasound transducer directly over the artery. Dislocation of the transducer from the arterial site leads to sudden loss of information which might cause confusion for the operator if the loss of information is due to an emergency or the dislocation of the sensor.
- The ultrasound technique is not suitable for measurement of diastolic BP.
- The method is not practical for personal use or home healthcare devices and has limitations for providing the desired continuous, reliable readings of blood pressure.

3.2.3.2 Applanation tonometry

Tonometry is widely used in ophthalmology for measuring intraocular pressure and for the assessment of glaucoma and its response to treatment. The method was first applied to the determination of arterial pressure waves by Pressman and Newgard in 1963 (Pressman and Newgard, 1963). A pressure transducer is applied directly over and partially flattens the radial artery or other sites. The resultant waveform is used to calculate systolic, diastolic and mean arterial pressures. An algorithm allows the calculation of pressure values such as central systolic pressure, pulse wave velocity and ejection time.

Requirements for effective applanation of the arterial wall by a tonometry sensor include:

- The artery at the measurement site runs shallow beneath the skin and is fixed on a hard tissue such as a bone.

- The sensor is always smaller than the applanted area of the arterial wall along the cardiac cycle.
- The sensor's position is exactly fixed and is not affected by physical motion during the measurement.

Difficulties associated with the method include:

- Under optimal conditions for applantation, the pressure wave measured non-invasively is virtually identical to that recorded with a high fidelity transducer with the artery (Kelly et al. 1989, Somer and Meiselman, 1993). In practice, the pressure required to applanate the artery and compress the overlying structure does vary, so that the absolute values of systolic and diastolic pressure cannot be determined reliably. The signal is very position-sensitive, and the transducer needs to be situated directly in the centre of the artery.
- The carotid artery has an additional difficulty, which is movement in the surrounding tissues due to respiration.
- The probe can cause mechanical stimulation of the baroreceptor which might induce BP fluctuations during the measurement.
- The theory only applies when a small part of the arterial wall is flattened. This, of course, will not apply if the sensor is not applied directly over the artery, neither if a large sensor is applied over the artery and adjoining structures. Most sensors need to be calibrated against an intra-arterial pressure to confirm accuracy.
- With radial tonometry, strict adherence to standard processes is necessary to ensure that clinically sound data are obtained. This method requires trained staff to acquire reliable measurements and hence, the method is not feasible for personal healthcare devices.

3.2.3.3 Photoplethysmography:

Photoplethysmography (PPG) is an optical technique commonly known to detect changes in blood volume from skin surfaces. The technique will be discussed in more detail in Chapter 5 as it is the main focus of this project.

The PPG has been utilised for blood pressure measurements in two methods: the vascular unloading method and the Pulse Wave Velocity (PWV) method or Pulse Transit Time (PTT).

Figure 3-2
Demonstration of the non-invasive beat-to-beat blood measurement system, CNAP monitor 500 as obtained from the manufacturer.

The vascular unloading technique uses Infrared (IR) transmission PPG to provide 'raw' continuous pressure readings in commercial devices such as the Finapres (Finapres Medical Systems B.V., Netherlands), the CNAP (cnsystems, US) (seen in **Figure 3-2**), and Nexfin (ClearSight System, Edwards Lifesciences, US). Finger-IR PPG detects changes in blood volume and is used in conjunction with a finger cuff and servo-controlled pump which adjusts cuff pressure to maintain a constant finger blood volume. The Finapres considers that the cuff pressure needed to maintain light intensity equals the arterial blood pressure. However, this assumption might encounter inaccuracies due to: (1) The effective cuff pressure may not equal the cuff pressure due to the lack of uniform distribution of cuff pressure. (2) The cuff pressure at which the maximum amplitude of variation in transmitted light is observed may not equal the mean arterial pressure. (3) The Finapres assumes that the only blood under the cuff is in the artery. However, blood continues to pass through the artery during the measurement, leading to an increase in blood volume in the capillaries at the end of the finger (Chung et al., 2013). Consequently, the pressure there begins to rise and venous pressure will become comparable with arterial pressure, at which point blood will flow back along the vein. The implications of this flow on the Finapres readings are not well understood (Nm et al., 1991; Stokes et al., 1991). The CNAP overcomes this by alternating the readings between two nearby finger cuffs and provide comparable accuracy to invasive intra-arterial pressure measurements in normotensive conditions (Jeleazcov et al., 2010), however, the device is less accurate

during hypotension events or at alternating vascular tone (Ilies et al., 2012). Other limitations include the potential for patient discomfort due to the need for repeated calibration with the brachial artery pressure using an oscillometric cuff. The Nexfin monitor uses similar vascular unloading techniques to produce a brachial arterial pressure waveform. The Nexfin can reliably detect changes in arterial pressure, however, reduced precision during periods of haemodynamic instability makes it an unsuitable alternative to direct pressure monitoring (Weiss et al., 2014). Moreover, the three available commercial devices come with a high price tag and are not well suited for personal or home use.

Pulse Wave Velocity (PWV) is the speed of a pressure pulse propagating along the arterial wall and can be calculated from pulse transit time (PTT). PTT is the time between two pulse waves propagating on the same cardiac cycle from two arterial sites (Gesche et al., 2012). This method has been investigated using a combination of ECG and PPG signals (Ahlstrom et al., 2005; Foo and Lim, 2006, 2006). While few studies consider the method to be reliable (Ahlstrom et al., 2005; Gesche et al., 2012), some question the reliability of this approach as a clinical device (Jerrard-Dunne et al., 2008; Payne et al., 2006). Investigation in a large number of subjects showed that age, BP, gender and cardiovascular risk factors significantly influence PWV (Foo and Lim, 2006; Yamashina et al., 2002). Studies suggest that PWV can only be used for measurement of relative BP changes and may encounter errors due to the effect of BP on the measurement and the variability of arterial elasticity from one individual to another or due to neurohormonal factors.

3.3 Assessment of arterial stiffness

The stiffness of large arteries has been shown to be an independent predictor of cardiovascular mortality, especially in hypertensive subjects. More specifically, aortic stiffness has been shown to be a predictor of primary coronary events (Mattace-Raso et al., 2006) and of fatal stroke (Laurent et al., 2003) in hypertensive patients. Arterial stiffness (AS) was also reported as an independent risk factor for recurrent acute coronary events in patients with ischemic heart disease (Stefanadis et al., 2000) or a predictor of cardiovascular mortality in patients with end-stage renal disease (Blacher et al., 1999). Type-2 diabetes has also been shown to be associated with increased stiffness (Catalano et al., 2013), which is believed to be a major cause of the increased general cardiovascular risk related to diabetes (Alvim et al., 2013). Moreover, AS has also been associated with risk factors of CVDs, such as obesity (Safar et al., 2006). In all these cases, knowledge of

arterial stiffness represents a valuable indicator for diagnosis, prognosis and therapy assessment of patients.

Measuring arterial stiffness has been recommended as an additional test for hypertension management in a Task Force study appointed by the European Society of Hypertension and the European Society of Cardiology (Members et al., 2013). The underlying reason for the correlation between arterial stiffness and cardiovascular risk is commonly related to changes in the cardiac work resulting from arterial stiffening, leading eventually to cardiac hypertrophy, alteration of perfusion and of metabolic demand, and increased systolic dysfunction (Gatzka et al., 1998; Kass et al., 1996)

Reliable methods capable of estimating arterial stiffness represent therefore significant clinical interest. In this section, we present an overview of the currently available methods for the assessment of arterial stiffness.

3.3.1 Arterial Stiffness Terminology

There are different methods of assessing arterial stiffness, some of which are more widely applicable in the clinical setting than others. Several techniques give information on systemic arterial stiffness while others only give information on local stiffness of the vessel being studied. Terms used in the field of arterial stiffness are often used interchangeably when in fact they have slightly different meanings. In simple terms, arterial stiffness describes the rigidity of the arterial walls. Other terms used to describe the properties of vessel walls are defined in **Table 3-1**.

Table 3-1
Indices of arterial stiffness

Term	Definition	Methods of measurement
Elastic modulus**	The pressure change required for theoretical 100% stretch from the resting diameter. Also reported as Peterson's Modulus $(\Delta P \times D)/\Delta D$ (mmHg)	Ultrasound* MRI
Young's modulus**	Elastic modulus per unit area $(\Delta P \times D)/(\Delta D \times h)$ (mmHg/cm)	Ultrasound* MRI
Arterial distensibility**	Relative change in diameter (or area) for a given pressure change; inverse of elastic modulus $\Delta D/(\Delta P \times D)$ ($mmHg^{-1}$)	Ultrasound* MRI
Arterial compliance**	Absolute diameter (or area) change for a given pressure step $\Delta D/\Delta P$ (cm/mmHg) (or cm^2/mmHg)	Ultrasound* MRI
Pulse wave velocity	Velocity of travel of the pulse along a length of artery Distance/Δt (cm/s)	Pressure waveform* Volume waveform Ultrasound MRI
Augmentation index	The difference between the second and first systolic peaks as a percentage of pulse pressure	Pressure waveform*
Stiffness index (β)**	Ratio of ln (systolic/diastolic pressures) to (relative change in diameter)	Ultrasound*
Capacitative compliance	Relationship between pressure change and volume change in the arteries during the exponential component of diastolic pressure decay $\Delta V/\Delta P$ (cm^3/mmHg)	Pressure waveform*
Oscillatory compliance	Relationship between oscillating pressure change and oscillating volume change around the exponential pressure decay during diastole $\Delta V/\Delta P$ (cm^3/mmHg)	Pressure waveform*

P, pressure; D, diameter; V, volume; h, wall thickness; t, time; v, velocity; s, systolic; d, diastolic. *Most common method of measurement; **Also requires pressure measurements.(Mackenzie et al., 2002)

3.3.2 Pulse Pressure for Estimation of AS

Pulse pressure can be measured using a standard sphygmomanometer. It is one of the simplest measures of arterial stiffness, and easily practicable in the clinical setting (Nichols and M.D, 2011). The pulse pressure is the difference between systolic and diastolic pressures and depends on the cardiac output, large-artery stiffness and wave

reflection. In 1922, Bramwell and Hill identified that pulse pressure as a good indicator of arterial stiffness (Bramwell and Hill, 1922). Both systolic and diastolic blood pressures tend to increase with age (Franklin et al., 1997). However, beyond the age of 50–60 years, there is no further increase in diastolic blood pressure and, in many cases, it actually declines. **Figure 3-3** shows the change in systolic and diastolic pressure values with age. However, some oscillometric sphygmomanometers may be unreliable in older subjects (Popele et al., 2000). Moreover, pulse pressure alone is inadequate to assess arterial stiffness accurately. Problems include the 'normal' amplification of the pressure wave as it travels from the aorta to the periphery, although this effect becomes less pronounced with increasing age. Thus, measurements of pulse pressure made in the periphery, for example in the upper arm, do not always accurately reflect the actual central pulse pressure (Pauca et al., 1992).

Indeed, there can be differences of up to 20 mmHg between central pressures of patients with identical brachial blood pressure readings. Interestingly, exaggerated amplification is thought to account for the phenomenon of pseudo-hypertension in the young (O'Rourke et al., 2000).

Central pressure may, therefore, be a more accurate predictor of risk than peripheral blood pressure. Moreover, it is the central pressure that contributes most to the development of left ventricular hypertrophy, itself an independent predictor of cardiovascular mortality, and changes in left ventricular geometry (Boutouyrie et al., 1999). Also, carotid intimal medial thickness, a marker of cardiovascular risk (Matsushima et al., 2004; Zureik et al., 2002) is dependent on carotid but not brachial pulse pressure.

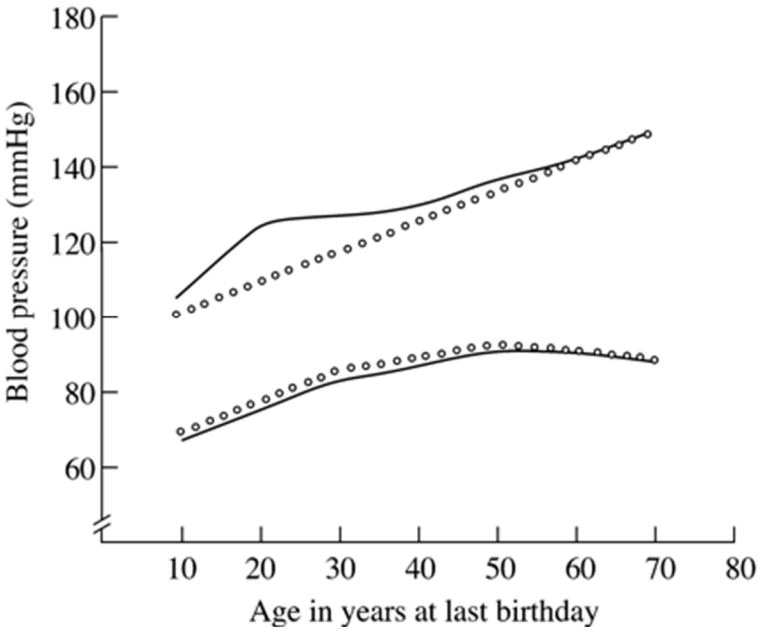

Figure 3-3
Changes in systolic and diastolic blood pressure with age (Nichols, 2011).

3.3.3 Pulse Wave Velocity for AS Estimation

Pulse wave velocity is the speed at which the forward pressure wave is transmitted from the aorta through the vascular tree. It is calculated by measuring the time taken for the arterial waveform to pass between two points a measured distance apart, and involves taking readings from the two sites simultaneously, or gating separate recordings to a fixed point in the cardiac cycle (e.g. the R-wave of the ECG, the PPG signal, pressure or flow signals, or a combination of both). Various different methods have been used, both invasive and non-invasive, and can be applied to either flow or pressure waves (Naidu et al., 2005; Padilla et al., 2006; Sutton-Tyrrell et al., 2005). The important point is the reference point on the waveforms. Indeed, the foot-to-foot methodology is usually used, as it avoids the confounding influence of wave reflection (Hermeling et al., 2008).

The relationship between PWV and arterial stiffness is described by the Moens Korteweg equation (Korteweg, 1878; Moens, 1878):

$$PWV = \sqrt{E \times h / 2r\rho} \tag{3.1}$$

where E=Young's modulus of elasticity of wall material, the h=wall thickness of vessel, the r=inside radius of vessel and ρ=density of blood).

Another version of this equation is the Bramwell and Hill equation, which relates PWV to distensibility:

$$PWV = \sqrt{\Delta P.V / \Delta V \rho} = \sqrt{1 / \rho D} \quad (3.2)$$

where $\Delta PV/\Delta V$=relative volume elasticity of vessel segment, ρ=density of blood, and D=distensibility.

The technique of pulse wave velocity is valid and reproducible and has been widely applied in both normal volunteers and patients in the research setting (Ben-Shlomo et al., 2014; Blacher et al., 1999; Sutton-Tyrrell et al., 2005; Takashima et al., 2014).The principle is relatively simple and the technique can be learned fairly easily. While, some studies data show that pulse wave velocity is an independent predictor of cardiovascular risk in both hypertensive patients and patients with the end-stage renal disease, other studies showed weak correlations between PWV and cardiovascular risks and consider the method unreliable for measurement of arterial stiffness (Jerrard-Dunne et al., 2008; Payne et al., 2006; Pereira et al., 2015)

Some limitations of this technique include:

- The inaccessibility of the central arteries, necessitating compromise by using the nearest superficial arteries.
- There can also be some difficulty in estimating the actual arterial distance between recording sites using only surface measurements. The pulse wave velocity becomes less accurate if the recording points are very close together, and the technique is, therefore, limited to use on the larger arteries.
- As stated earlier, PWV is a parameter that is highly affected by blood pressure, arterial geometry and fluid density, and therefore, a change in PWV might be due to other factors apart from AS. For that reason, some studies have considered the method to be unreliable with the weak correlation between PWV and cardiovascular risks to a point where there is no correlation when data was adjusted for gender and age.

3.3.4 Ultrasound-derived Indices for AS Estimation

Ultrasound can be readily used to measure arterial stiffness (distensibility and compliance), but its use is limited to the larger and more accessible arteries. Hence, this technique has been used mainly on the brachial, femoral and carotid arteries and the abdominal aorta. Several images of the vessel wall are obtained per cardiac cycle, and the maximum and minimum areas of the vessel are calculated by wall tracking and computerised edge-finding software. Distensibility and hence compliance (inverse of

stiffness) can be calculated using the following formulae if blood pressure is also recorded:

$$Distensibility = \Delta V / \Delta P.V \tag{3.3}$$

Where ΔV=change in volume, ΔP=change in pressure, and V=volume.

Problems associated with the use of ultrasound to assess arterial stiffness include:

The limited resolution can make the detection of very small changes in vessel diameter difficult. The technique also relies heavily on the ability of the operator to image the walls of the vessel being studied accurately, and there have been some concerns about the reproducibility of the technique, although with an experienced operator this can be improved. The technique can be made less operator-dependent by introducing measures such as fixing the ultrasound transducer in a robotic arm, and maintaining the arm of the subject in a fixed position using a groove or brace (Lee et al., 1992).

It is necessary to measure blood pressure simultaneously to measure the elastic modulus. This is usually done in the brachial artery or finger, which may not be appropriate if distensibility is being assessed in a more central artery, for example, the aorta, due to the normal phenomenon of pressure wave amplification towards the periphery. Moreover, finger blood pressure is not necessarily a reliable measure of brachial blood pressure. It is unclear whether information obtained from one particular site can be generalised to the rest of the vasculature.

Although ultrasound has the advantage of being non-invasive, the imaging equipment required is not yet integrated in wearable devices and is expensive. Thus, the use of ultrasound in determining arterial stiffness has been largely confined to the research setting to date.

3.3.5 MRI-derived Indices for AS Estimation

Magnetic resonance imaging (MRI) techniques have been used to measure vascular distensibility and compliance. Most of the human studies have been based on measurements of the aorta. MRI has been used to demonstrate the inverse relationship between aortic distensibility and age, that arterial stiffness is increased in hypertensive patients (Resnick et al., 1997), and that arterial compliance is reduced in patients with coronary artery disease but increased in athletes (Mohiaddin et al., 1989). Although MRI has the advantage of being non-invasive, it remains very expensive, and the availability

of scanning facilities is limited. Therefore, the place of this technique in clinical practice is doubtful, and it is completely unfeasible for personal healthcare devices.

3.3.6 The Arterial Waveform for AS Estimation

The arterial pressure waveform is a composite of the forward pressure wave created by ventricular contraction and a reflected wave. Waves are reflected from the periphery mainly at branch points or sites of impedance mismatch. Therefore, the arterial waveform varies throughout the arterial tree (Nichols and M.D, 2011). The velocity at which the pressure wave travels through the vasculature is influenced by the stiffness of the vessel walls—the stiffer the walls, the higher the velocity. In the elastic vessels, the reflected wave tends to arrive back at the aortic root during diastole, serving to augment diastolic pressure and hence improve coronary artery perfusion. In the case of stiff arteries, the reflected wave arrives back at the central arteries earlier, causing augmentation of the systolic pressure and a consequent decrease in diastolic pressure. High central systolic pressure accelerates the development of left ventricular hypertrophy, whereas low diastolic pressure reduces coronary artery perfusion. The amplitude of the reflected wave also increases as the arterial stiffness increases, further augmenting central systolic pressure.

The O'Rourke Pulse Wave Analysis (PWA) system is a simple and non-invasive method of measuring arterial stiffness. Applanation tonometry is used to record pressures at the radial or carotid artery, and a validated generalised transfer factor is then applied to derive the corresponding central waveform. From this, the augmentation index (AIx), which is the difference between the first and second systolic peaks expressed as a percentage of the pulse pressure, and a measure of systemic stiffness, can be derived. It is also possible to estimate the central arterial pressure from the peripheral waveform (O'Rourke et al., 2001). The estimation of augmentation index using this technique is more reproducible than blood pressure as assessed by some automated sphygmomanometers. The tonometer is easily portable and, therefore, useful in both hospital and clinic settings. However, the method is not feasible for personal healthcare devices and the limitations related to applanation tonometry as mentioned above are not overcome.

Pressure pulse contour analysis is another method which has been used to estimate arterial stiffness non-invasively. This technique involves tonometry at the radial artery, but the compliance is derived differently, using a modified Windkessel model of the circulation and an assessment of diastolic pressure decay (Rietzschel et al., 2001). This

method calculates large-vessel and peripheral compliance. Augmentation index and peripheral compliance, as calculated by pulse contour analysis, are related but augmentation index more accurately reflects drug-induced haemodynamic changes. Pressure pulse contour analysis requires estimation of cardiac output from an algorithm. The technique does not provide any information on central pressures or augmentation index. Also, it may be less accurate than the technique described above, as the theoretical model depends on the diastolic component of the waveform, which tends to be less reliably recorded than the systolic component. Most of the wave reflection occurs in systole rather than diastole. Also, the point at which diastole is assumed to start and the point in diastole from which the exponential decay is calculated may be affected by the reflected wave, leading to further inaccuracies.

3.3.7 Photoplethysmography in the Assessment of AS

Photoplethysmography has been used to record the digital volume pulse. This technique resembles that of pulse oximetry, and measures the transmission of infrared light through the finger, thus detecting changes in flow and producing a volume waveform. It has been used to develop a stiffness index and a reflection index that are thought to reflect systemic arterial stiffness. Problems include the damping of the peripheral pulse and temperature-dependant changes in the peripheral circulation. A study that compared Photoplethysmography of the digital volume pulse with pulse wave velocity found that pulse wave velocity correlated more closely with the expected influences on vascular compliance, namely age and atherosclerosis. According to Mackenzie: “the technique has the advantages of being relatively simple and easily portable. If it were to be validated, it would have potential uses in the clinical setting”(Mackenzie et al., 2002). Photoplethysmography also has been used as a pulse transducer to measure aortic femoral PWV (Loukogeorgakis et al., 2002; Wowern et al., 2015).

Pressure waveform analysis has also been performed more distally on the digital artery using a servo-controlled pressure cuff. One such example is the Finapres system (Millasseau et al., 2000) which has been successfully used to measure the arterial waveform. However, there are some reservations mentioned above about this method, and that the recorded waveform may be significantly damped and, therefore, any derivations of central pressure may be less accurate.

3.4 Assessment of Blood Viscosity

Blood viscosity is the thickness and stickiness of blood. It is a direct measure of the ability of blood to flow through the vessels. Blood viscosity is non-Newtonian that inhibits shear-thinning properties, the factors that contribute to an increase or drop in blood viscosity have been discussed in more details in the previous chapter. Medically, it is possible to find abundant evidence throughout the literature that blood viscosity can be a significant indicator of cardiovascular disease. A strong link has been reported in thrombosis (Dintenfass, 1964), hypertension (Letcher et al., 1983; Pop et al., 2002), myocardial infarction (Jan et al., 1975; Turczyński et al., 2002), cardiovascular complications (Cho et al., 2014; Lowe et al., 1997) and acute stroke (Coull et al., 1991; Gusev et al., 2008). Elevated blood viscosity (hyperviscosity) is also associated with cardiovascular risk factors, such as diabetes (Irace et al., 2013), obesity (Solá et al., 2007) and smoking (Shimada et al., 2011).

Viscosity is classically measured in one of two ways: by determining the rate of fluid flow as a result of applying a predefined force or by measuring the amount of force required to achieve a predefined rate of fluid flow.

To measure the viscosity of a sample, modern viscometers generally measure the rate of fluid flow at a specified force or, conversely, the amount of force required to achieve a predefined rate of flow. It does not matter which method is used for plasma and serum viscosity measurement. The result should be the same because plasma and serum are Newtonian fluids. However, the latter method is most appropriate for measuring whole blood viscosity because whole blood is a non-Newtonian fluid. The viscosity of whole blood varies depending on the rate of flow. Therefore, the rate of flow (proportional to shear rate) ideally should be precisely measured.

The viscosity of fluids is most frequently measured by instruments that fall into one of two categories, either rotational or tube instruments.

3.4.1 Viscosity Measurement Methods

3.4.1.1 Capillary viscometers

Capillary viscometers are available in different designs as seen in **Figure 3-4**. Measurements using capillary viscometers are based on the relation between viscosity and time. They use gravity as the driving force; therefore, the results are kinematic viscosity values. The main advantage of this method is that gravity is a highly reliable driving force(Lauda GmbH, 2016).

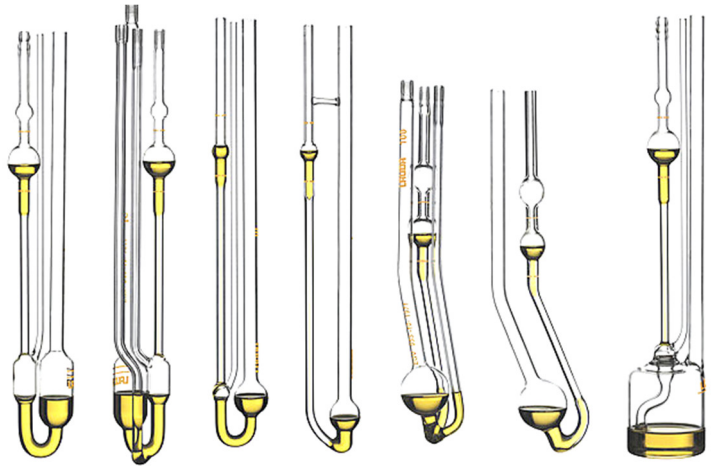

Figure 3-4
Illustrations of the range of capillary viscometer designs available from the LAUDA manufacturer (Lauda DR R. Wobser GmBH, Germany) (Lauda GmbH, 2016).

There are direct-flow or reverse-flow capillaries available. In direct-flow capillaries the sample reservoir is located below the measuring marks; in reverse-flow types, the reservoir sits above the marks. Reverse-flow capillaries allow the testing of opaque liquids and can have a third measuring mark. Having three measuring marks provides two subsequent flow times and can define the measurement's determinability.

Viscosity values are obtained using the following relationship

$$\mu = K_C.t_f \qquad (3.4)$$

Where μ is kinematic viscoisty (mm^2/s), K_C is the capillary factor (mm^2/s^2) and t_f is the sample flow time (s).

While capillary viscometers might be suitable for measurement of plasma viscosity such as the commercially available BV200, its principles do not apply to non-Newtonian fluids, such as blood.

3.4.1.2 Rotational viscometers

Rotational viscometers consist of one stationary element and one rotary element separated by a thin layer of fluid. As the rotary element is spun, the viscous forces of the fluid interact with both the rotating body and the stationary body, having the net effect of impeding the motion of the rotating body. Rotational viscometers can be further divided into one of two types, co-axial cylinder, and cone-plate viscometers.

Coaxial Cylinder Viscometers

The co-axial rotating cylinder viscometer consists of a cylinder, which houses a concentrically mounted solid cylinder. The fluid is placed between the outer and inner

cylinders. The inner cylinder (Searle type viscometer) or the outer cylinder (Couette type viscometer) are capable of forced rotation. The viscous drag created by the fluid between the outer and inner cylinders is measured as a function of the angular displacement of the inner cylinder (Viswanath et al., 2007).

Cone-plate Viscometers

The cone-plate viscometer (see **Figure 3-5**) operates in a similar fashion to the coaxial cylinder viscometers. A cup with a flat bottom serves as both the vessel, which contains the fluid, and the plate at which the fluid builds a viscous resistance (Cokelet, 2011).

A rotating cone with the large angle at the apex transmits a torque on the system. The drag exerted by the interaction between the viscosity of the fluid and the stationary and rotating surfaces is measured by the deflection of a spring mounted on the shaft between the cone and the motor.

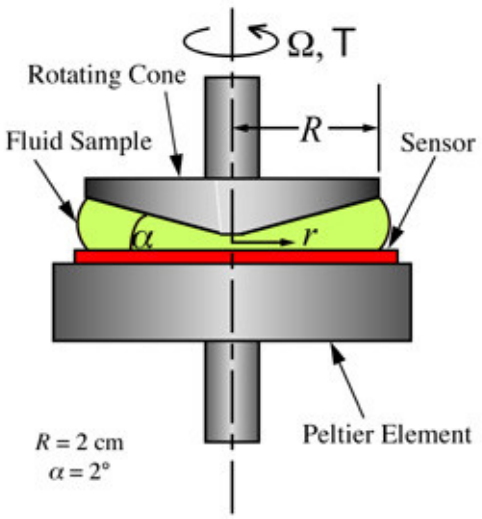

Figure 3-5
Illustration of the Cone-plate viscometer chamber ("Cone and Plate Chamber," 2008).

In the cone-plate, the viscosity is measured form the following equations:

$$\dot{\gamma} = \omega / \sin\theta \tag{3.5}$$

$$\tau = M / \frac{2}{3}\pi r^3 \tag{3.6}$$

Where $\dot{\gamma}$ is shear rate (s^{-1}), θ is the cone angle (degrees), ω is angular velocity (rad/s), τ is shear stress (N/m^2), M is the measured torque (Nm) and r is the cone radius. The dynamic viscosity, η (poise) is then calculated from (3.6) and (3.5) as the following:

$$\eta = \dot{\gamma} / \tau \qquad (3.7)$$

3.4.1.3 Rolling ball viscometers

Rolling-ball viscometer operating concept is seen in **Figure 3-6** measures the rolling time of a ball through transparent and opaque liquids according to Hoeppler's falling ball principle (Viswanath et al., 2007).

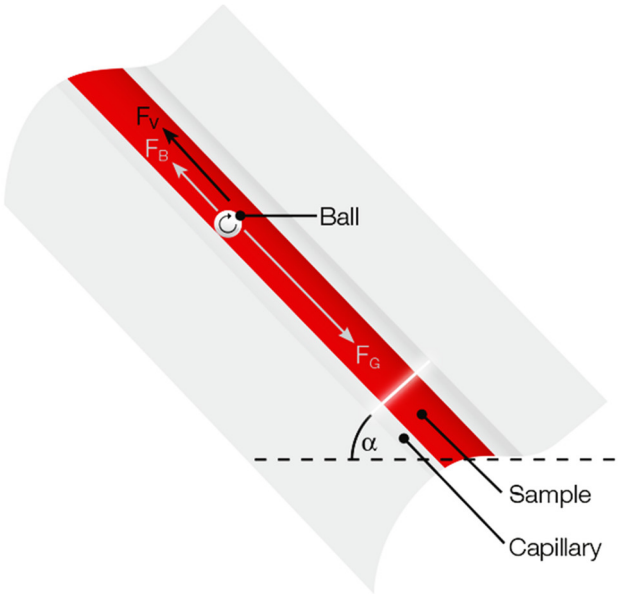

Figure 3-6
Illustration of the Rolling ball viscometer principle. F_G is the effective component of gravity, F_B is the effective component of buoyancy and F_v is the viscous force (Viscopedia, 2016).

The rolling-ball principle uses gravity as the driving force. A ball rolls through a closed capillary filled with sample fluid which is inclined at a defined angle. The time it takes the ball to travel a defined measuring distance is a measure of the fluid's viscosity. The inclination angle of the capillary permits the user to vary the driving force. If the angle is too steep, the rolling speed causes turbulent flow. For calculating the viscosity from the measured time, the fluid's density, and the ball density needs to be known.

Instruments that perform at inclination angles between 10° and 80° are rolling-ball viscometers. If the inclination angle is 80° or greater, the instrument is referred to as a falling-ball viscometer. Apart from balls as falling objects, there are other viscometers

which use rods or needles. Another variety of this principle is the bubble viscometer, which registers the rising time of an air bubble in the sample over a defined distance. The oscillating piston viscometer (ASTM D 7483) is an exception: It does not rely on gravity as the driving force but uses electromagnetic force to pull a magnetic cylinder through the sample (Viswanath et al., 2007).

As seen in **Figure 3-6**, a number of force components affect this type of measurement. F_G is the component of gravitational force as the gravity pulls the ball downwards, F_B is the effective component of buoyancy where the buoyancy inside the liquid and the liquid's viscosity oppose the gravitational force (Viswanath et al., 2007). And finally, F_v is the viscous force of the liquid which causes the friction to the rolling ball. To calculate the ball's viscosity from the rolling time, the gravitational and buoyancy influence have to be considered. While the influence of gravity (F_G) depends on the ball's density and volume, an object's buoyancy depends also on the liquid's density as can be described with Newton's second law:

$$F_G = m.g = \rho.V.g \tag{3.8}$$

Where m is mass in kg, g, is gravitational acceleration (m/s²) and ρ is density (kg/m³). The dynamic viscosity η (mPa.s) can be calculated from the following relationship:

$$\eta = K.(\rho_b - \rho_s).t_r \tag{3.9}$$

Where K is the proportionality constant, ρ_b is the ball density (g/cm³), ρ_s is the sample density (g/cm³) and t_r is the ball rolling time (s).

3.4.2 Challenges in Blood Viscosity Measurement in the Clinical Setting

There has been no evidence that blood viscosity measurement is implemented in regulatory assessments of cardiovascular patients in the US or the UK. However, some private clinics have adopted these tests more recently. However, regulatory assessment of plasma viscosity is common for diagnosis purposes for patients with hyperviscosity syndrome (HVS), multiple myelomas and Waldenstrom Macroglobulinaemia (WM) with symptomatic hyperviscosity.

Although hyperviscosity syndrome is caused by hyperviscous blood, clinical laboratories generally only measure the serum or plasma component. The methods used for the measurement of serum or plasma viscosity in patients have changed little since Waldenström's use of a capillary viscometer in 1944 (Waldenström, 1944). College of

American Pathologists (CAP) data for 2010 reveal that approximately 75% of clinical laboratories use a capillary viscometer (Mancia et al., 2007). In the UK the BV200 capillary Viscometers (Benson Viscometers Ltd, UK) are widely common in the clinical setting for plasma viscosity measurements. In the case of Polycythaemia, where blood viscosity is evident to increase, only full blood count is a regulatory test in the UK. Other measurements used for general health screening is erythrocyte sedimentation rate using Starrsed ESR (Mechatronics International, Netherlands). Bleeding disorders are commonly assessed using the clotting Screen by assessing prothrombin time (PT), fibrinogen, activated partial thromboplastin time (APTT), thrombin time and D-Dimer, using the ACL Top (Werfen company, US) and is part of the regulatory tests in the National Health Services in the UK (Chee et al., 2008).

The simplicity of the tube method for viscosity measurement encounter a lack of standardisation and subtle risks for imprecision. Laboratories using the Ostwald and pipette methods report their data as ratios rather than in units of viscosity, such as centipoise (cp). The results are reported as the ratio of time for a patient sample to pass through the tube relative to the time for a reference fluid (eg, water). Consequently, commercial viscosity controls traceable to a National Institute of Standards and Technology standard, reported in centipoise, are not directly applicable. The Ostwald and pipette methods lack the kind of standardised commercial calibrators and controls that are commonplace for other haematology or chemistry assays. The Ostwald tube remains a simple, reliable method for measuring relative serum viscosity in patients. In a study where 499 serum viscosity determinations were performed, 297 (59.5%) of which were elevated (Stone, 2009). A total of 60% of these specimens were reproducible to ± 5% and usually available within 3 hours.

Commercially available viscosity instrumentation generally does not focus on the clinical laboratory. Instead, viscosity instrumentation is sold primarily for industrial applications, which represent much larger markets. Industrial applications for viscosity measurement include measuring the viscosity of paint, solvents, oil and petrochemicals, resins, and polymers. The US Food and Drug Administration classifies viscometers as class I devices (21 CFR 862.2920), requiring only establishment registration before product distribution in the United States. Comapnies registered under that classification do not market viscometers to clinical laboratories. The LV2000 micro-viscometer (Anton Paar, Austria) relies on the rolling-ball concept and provides a point-of-care whole blood viscometer, currently labelled for research use only. Coulter (Miami, FL, US) manufactured and

marketed a viscometer to the clinical laboratory almost two decades ago. The line was discontinued after a few years, and none is marketed currently primarily to the clinical laboratory. Therefore, clinical laboratory professionals must choose among instruments that are not intended primarily for clinical laboratory use but are easily adaptable with proper validation.

The most common method used in recent research studies for blood viscosity measurement is the cone/plate type such as the DV-III Brookfield Rheometer (Wells-Brookfield, Stoughton, MA) (Irace et al., 2013; Solá et al., 2007) or the MCR301 Rheometer (MCR series, Anton Paar) (Forsyth et al., 2011). However, CAP data reveal that only 7% of clinical laboratories use the cone/plate type of viscometer (Stone and Bogen, 2012). Most validation studies linking HVS to a particular serum or plasma viscosity were performed using the Ostwald tube. Consequently, the viscosity ratios (normalised to water at 20°C) may not exactly match the viscosity measured by an automated method, expressed in centipoise.

3.4.3 Non-invasive Methods for BV Measurement (Research Investigations)

There have been few investigations for ex-vivo optical measurements of blood viscosity. One of these method report on a contact-free optical viscosity measurement technique using a laser-induced capillary wave (Muramoto and Nagasaka, 2011). Two pulsed YAD laser beams of equal wavelength and intensities intersect on a weak absorbing sample surface at a specified crossing angle. They generate an intensity distribution within the volume grating interference pattern with the grating period between 80 and 100 μm. The temperature distribution of the thermal grating creates a spatially modulated displacement on the liquid surface driven by the thermal expansion and the temperature dependencies the surface tension. By solving the Navier-stokes equation, the continuity equation, and the heat conduction equation with appropriate boundary conditions using the Laplace transformation, viscosity, and surface tension can be both determined. This method brings the benefit of a contact-free method, high-speed measurement and high spatial resolution, small sample volume and a wide range of viscosity.

Recently, an *in vivo* blood viscosity monitoring method was suggested using a central venous catheter using electrical impedance (Pop et al., 2013). The method showed agreement with *in vitro* blood viscosity measurements using the coaxial viscometer (Contraves LS 300 instrument, proRheo GmbH, Germany).

SUMMARY

Assessment of cardiovascular mechanics is vital for the diagnosis and monitoring of cardiovascular health, especially in the early stages of hypertension and atherosclerosis for prevention of further complications. In this chapter, the source of CVD progression and development in the preclinical and asymptomatic CVD patients is narrowed to the three major parameters documented in the literature; blood pressure, arterial stiffness and blood viscosity. A range of methods are available for measurement of arterial BP, however, these methods endure limitations due to reliability, discomfort, portability, and cost efficiency. A variety of indices are used for the assessment of AS, however, there is a disparity in the reliability of measurement of cardiovascular risks especially after adjustment for age and gender. Currently available methods for measurement of blood viscosity are invasive methods and the assessment of BV is limited to measurement of plasma viscosity only, this might be due to the lack of specially designed technique for clinical instruments.

Photoplethysmography is an optical technique that has the benefits of being non-invasive, it provides a continuous pulse wave signal and requires no specialised practitioner to obtain the signal and can be manufactured at low-cost. Therefore, we aim to investigate the PPG and its potential and limitations in providing a measure of vascular mechanics, by assessing its capability in the quantification of BP and AS and its sensitivity to BV.

Chapter 4
LIGHT-TISSUE INTERACTIONS

4.1 Introduction

Photoplethysmography (PPG) is an optical technique and therefore, it is important to provide a thorough background of light interactions with biological tissue. Once the light reaches the skin, part of it is absorbed, part is reflected or scattered, and part is further transmitted. The understanding of the factors related to the light-tissue interaction is essential for understanding PPG. For that reason, we will only investigate the light characteristics that are relative to this application.

Long established laws, observations and definitions relevant to the quantification and measurement of light absorption and scattering are presented in this chapter. Biological tissue is inhomogeneous, therefore, light propagation within such a tissue depends on the scattering and absorption properties of its components: cells, cell organelles, and various fibre structures. The optical properties of refractive index, scattering and absorption coefficients; and the polarisation states of the incident light all play important roles in the propagation of light in tissues (Tuchin, 2007).

A review of how light propagates in the skin layers, RBCs, and the relevant chromophores will be discussed by presenting the relevant optical parameters in tissue components.

4.2 Light

For thousands of years, light has captured the imagination of humankind and fascinated scientists to attempt to assemble a complete picture for this remarkable phenomenon. Light has also played an important role in medicine. In prehistoric times, the healing

power of light was often attributed to mythological, religious, and supernatural powers. The history of light therapy dates back to the ancient Egyptians, Persian, Hindus, Romans, and Greeks, all of whom created temples to worship the therapeutic powers of light, especially sunlight, for healing the body as well as the mind and the soul (Bohren and Huffman, 2007).

Today, light is studied as optics, a branch of physics. Where, this science deals with the nature of light and the phenomenon exhibited by it (Bohren and Huffman, 2007). For a glimpse of the evolution of light theories, Newton in his corpuscular theory (1675 AD) assumed that light consists of very small particles, which he named corpuscles. Those corpuscles are emitted from a luminous source and travel with high speed. Using this theory, only rectilinear propagation of light (reflection and refraction) can be explained. However, the theory was unable to explain interference, diffraction and polarisation. Huygens' wave theory of light (1678 AD) considered light to consist of periodic disturbance transmitted through a medium in the form of longitudinal waves. Where the source of light creates periodic disturbances that behave as waves. This theory can explain reflection, refraction, interference and diffraction (Bohren and Huffman, 2007). In the nineteenth century, Maxwell's electromagnetic theory (1873), which assumed light to be electromagnetic in nature, has arrived to rule out the concept of elastic ether[1], as no material medium is required for the propagation of light. Max Plank proposed, the quantum theory of light, in which light consists of small particles in the form of discrete bundles of energy called photons (Splinter and Hooper, 2007).

The energy of a photon is equal to hf, where *f* is its frequency and h is the Planck's constant.

$$E=hf \tag{4.1}$$

Today, the present understanding of light is that it possesses dual characteristics. Where sometimes it manifests its wave nature (reflection, refraction, diffraction, polarisation), while in other times, it manifests its particle nature as in photoelectric effect, Raman effect and Compton effect (Jha, 2009).

[1] "Treatise of light" the assumption that light propagates as an elastic impulse in a special medium - ether filling all the space

The most relevant optical properties applicable to Photoplethysmography are light absorption,scattering, and refraction. The following section will introduce definitions and principles related to those properties.

4.2.1 Light Absorption

Light absorption refers to the loss of photonic energy during interaction with electrons, atoms, and molecules. The energy lost by photons is converted into either heat or light of longer wavelengths (Splinter and Hooper 2007).

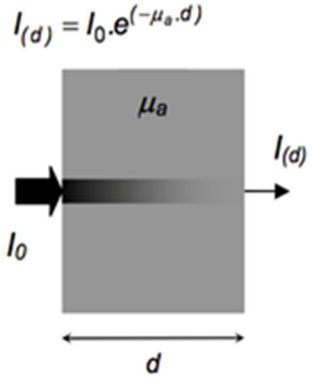

Figure 4-1
Attenuation of light through a non-scattering medium.

In the 18th century, the Beer-Lamber-Bouguer law or as commonly known as Lambert-Beer law was introduced to describe the logarithmic attenuation of light travelling through an absorbing medium. In a substance consisting of different layers of equal thicknesses, each absorbs the same fraction of an incident beam of light. The first layer will absorb ½ of the incident light, the second will absorb ¼ the incident light and only 1/8 will emerge from the next layer.

A collimated beam of light of Intensity I_o at the wavelength λ will attenuate across a homogenous and non-scattering medium of thickness d with the given equation:

$$dI/I = d.\mu_a \qquad (4.2)$$

Which describes how each successive layer of d of the medium absorbs the same fraction dI/I of the incident intensity I for a constant μ_a . The latter is known as the absorption coefficient of a medium in mm^{-1} for a given wavelength λ, and it represents the probability of the photon being absorbed through one unit of length in that medium.

For an incident intensity I_o , the transmitted intensity I_d through a distance d will be

$$I_d = I_o.e^{-d.\mu_a} \qquad (4.3)$$

Where, μ_a is the absorption coefficient of a medium in mm^{-1} for a given wavelength, λ, and it represents the probability of the photon being absorbed through one unit of length in that medium. The reciprocal of the absorption coefficient, known as the absorption length m is the distance required for the intensity of the beam to fall to e^{-1} of the initial intensity. Expressing the previous equation in base 10 logarithms:

$$I_d = I_o.10^{-\alpha d} \tag{4.4}$$

Where α is the specific absorption coefficient of the compound (mm/molar).

The absorbance of the medium A, or the dimensionless light attenuation, given in optical density units (OD) is defined as the $\log_{10}$ ratio of the incident and transmitted intensities

$$A = log_{10}(I_o / I_{d)} \tag{4.5}$$

In the 19th Century, August Beer derived a law stating that the optical density of a non-absorbing medium, with an absorbing substance dissolved in it, is proportional to the concentration ([C], molars) of the absorbing substance.

The combination of the two laws is commonly known as the Beer-Lambert Law and can be written as:

$$A = log_{10}(I_o / I_{d)} = \mathcal{E}.[C].d \tag{4.6}$$

Where, $\mathcal{E}$ is the specific extinction coefficient or the absorptivity of the compound (mm/molar) and the distance (d) crossed by the light through the solution.

In the case where the medium contains several different compounds, the above equation can be extended to consider the contribution of each compound. (For instance, in a blood solution, the different compounds are oxy-haemoglobin, deoxy-haemoglobin, water, etc.)

$$A(\lambda) = \mathcal{E}_1(\lambda).[C_1].d + \mathcal{E}_2(\lambda).[C_2].d + \ldots\mathcal{E}_n(\lambda).[C_n].d$$

$$A(\lambda) = \sum_n \mathcal{E}_n(\lambda).[C_n].d \tag{4.7}$$

$$log_{10}(I_o / I_d) = \alpha_1(\lambda).[C_1].d + \alpha_2(\lambda).[C_2].d + \ldots\alpha_n(\lambda).[C_n].d$$

$$log_{10}(I_o / I_d) = \sum_n \alpha_n(\lambda).[C_n].d \tag{4.8}$$

Transmittance T can also be defined by the following ratio,

$$T = I_d / I_o \tag{4.9}$$

The Beer-Lambert law is only valid under certain limited conditions: the light entering the medium must be monochromatic and perfectly collimated, and the medium itself

must be purely and uniformly absorbing. Therefore, certain errors will arise when applying the law to practical measurements since, for example, even lasers are not perfectly monochromatic. The consequences on experimental measurements of the limitations imposed by the Beer-Lambert law will be highlighted at a later stage.

4.2.2 Light Scattering

The fundamentals of the theory behind light scattering and its definitive parameters are introduced. This discussion will highlight elastic scattering, in which there is no loss in energy of the scattered light, on the grounds that non-linear scattering in tissue is generally not as significant in the used wavelengths for Photoplethysmography monitoring.

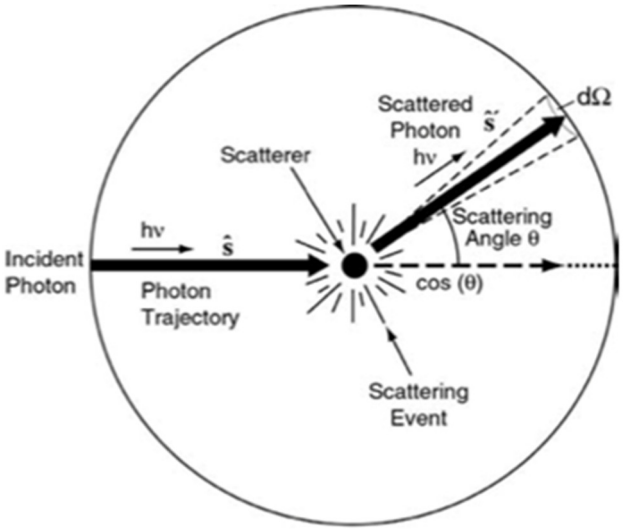

Figure 4-2
Distribution of the scattered light relative to the incident light. The incident photon travels along the direction $\hat{s}$ and the scattered photon exits in $\hat{s}'$ direction (Vo, 2003).

Light scattering can be elastic or inelastic. In the event of elastic scattering, the photons experience a change in direction without any loss of energy and this is more frequent than the inelastic scattering such as Raman scattering, where photons can both gain and lose energy. Scattering of a photon can even be treated as absorption of the photon followed by the immediate emission of a new photon (Ball, 2001; Hecht, 2002).

Scattering is mostly described by considering the incident light as a plane wave; a wave of uniform amplitude in any plane perpendicular to the direction of propagation, at least over a size scale larger than the scattering particle. Scattering is quantified by the scattering cross section. For a monochromatic plane wave that has a given intensity I_o encountering the medium, some amount of power P_{scat} gets spatially scattered. The ratio

of the scattered energy to the incident intensity is *the scattering cross section* (σ_s) as illustrated in **Figure 4-2.**

$$\sigma_s(\hat{s}) = P_{scatt}/I_o \tag{4.10}$$

where $\hat{s}$ is the propagation direction.

The angular distribution of the scattered radiation is given by the differential cross section $\frac{d\sigma_s}{d\Omega}(\hat{s}, \hat{s}')$, where $\hat{s}'$ defines the axis of a cone of solid angle dΩ originating at the scatterer.

Assuming that the scattering section is independent of the light orientation of the incident light and the scatterer, which leave us with $\sigma_s(\hat{s}) = \sigma_s$ and hence,

$$\frac{d\sigma_s}{d\Omega}(\hat{s}, \hat{s}') = \frac{d\sigma_s}{d\Omega}(\hat{s}, \hat{s}') \tag{4.11}$$

The differential cross section, which represents the angular distribution of the scattered light depends on the polarisation states of the incoming and outgoing waves, as with the scattering cross section.

A medium containing a uniform distribution of identical scatterers is characterised by the scattering coefficient μ_s and the cross-sectional area for scattering per unit volume of medium.

$$\mu_s = \rho\sigma_s \tag{4.12}$$

where ρ is the density of scatterers.

The scattering mean free path d_s which represent the average distance a photon travels between consecutive scattering events.

$$d_s = 1/\mu_s \tag{4.13}$$

The light which is absorbed is dissipated as thermal energy, and light which is scattered keeps its intensity but travels in another direction (Martelli et al., 2010). Therefore, it is convenient to describe the angular distribution of scattered light by defining an angular probability function of a photon to be scattered by an angleθ. If all scatter directions are equally probable, the scattering is isotropic. Otherwise, scattering is anisotropic.

In elastic scattering, when a photon is scattered from its original direction S, a measure of the anisotropy of scattering is given by the coefficient of anisotropy g, which represents the average value of the cosine of the scattering angle. This can be expressed as

$$g = \int_{-1}^{1} cos\,\theta. \qquad (4.14)$$

Light scattering can be classified into three modes of light-particle interaction: Rayleigh scattering, Mie scattering, and Raman scattering. The occurrence of Rayleigh or Mie scattering is determined principally be the ratio of the wavelength of the incident light (λ) to the dimensions of the scattering particle. Rayleigh scattering occurs when λ is much larger than the dimensions of the scattering particle and Mie scattering when the dimensions are comparable. Both Rayleigh and Mie scattering are elastic and cause a change in the trajectory of the scattered photon only. Raman scattering describes a phenomenon in which the trajectory of the scattered photon is altered, but in addition, the interaction causes the emission of light, usually with longer wavelength, from the scattering particle (Splinter and Hooper, 2007).

4.2.2.1 Rayleigh Limit

Scattering of light by tissue components that are much smaller than the photon wavelength involves the Rayleigh limit. The tissue structure includes cellular components such as membranes, cell sub-compartments and extracellular components such as the banded ultrastructure of collagen fibrils. The most important implication of the small size-to-wavelength ratio is that, at any moment in time, the scatter sees only a spatially uniform electric field in the surrounding host. In the classical description, where light is seen as waves, this condition gives rise to a dipole moment in the scatterer, a slight and spatially simple redistribution of the charges in the scatterer. This dipole moment oscillates in time with the frequency of the incident field and as a consequence gives off dipole radiation. For a spherical particle of radius, (a), the differential cross section in the Rayleigh limit is

$$\frac{d\sigma_s}{d\Omega} = 8\pi^4 n_m^4 \left(\frac{n_s^2 - n_m^2}{n_s^2 + 2n_m^2}\right) \frac{a^6}{\lambda^4} (1+\cos^2\theta), \qquad (4.15)$$

Where θ is the angle between the direction of the arriving wave and the leaving direction of interest, and n_m and n_s are the refractive indices of the host medium and the scatterer, respectively.

4.2.2.2 Mie Solution

The Mie regime scattering to objects approximately of the same size as the wavelength of the incident light, which translated to tissue conditions corresponds to cellular structures and collagen fibres. Mie-scattering is dependent on wavelength and highly forward directed. This is predominant in light interaction with biological tissue. The

interaction closely approximates geometrical optics. The cross-section of the scattering particle and the angle of incidence of the photon are used to determine an anisotropy factor g, which is the probability that the photon will be scattered in a solid angle θ. Various cellular structures, such as mitochondria and nuclei, and extracellular components like collagen fibres have sizes on the order of hundreds of nanometers to a few microns and are comparable in dimension to the photon wavelengths generally used in biomedical applications (0.5 to 1 μm).

Even though these structures are not necessarily spherical, their scattering behaviour can be modelled reasonably well by Mie theory applied to spheres of comparable size and refractive index. Because the scatterer is on the order of the wavelength, it experiences a more complex field in the space around it at any moment in time, and thus the motion of charges in the scatterer in response to the field is also complex (Hecht, 2002).

This results in a more complex angular dependence for the scattered light relative to the Rayleigh approximation. There can also be resonances due to the (classical) constructive and destructive interferences of the fields set up in the scatterer. The exact scattering patterns exhibited by the various biologic structures will crucially depend on the detailed shape of the particle.

4.2.2.3 Raman Scattering

In the quantum picture, Rayleigh and Mie scattering is called "elastic" because the energy of the scattered photon is the same as that of the incident photon. A related process is Raman scattering, which, in contrast, is "inelastic." In the Raman process, the frequencies of scattered photons are shifted from the incident frequency by amounts that are characteristic of molecular transitions, usually between vibrational energy states. The term inelastic refers to the fact that the scattered photon either loses energy to (Stokes) or gains energy from (anti-Stokes) the molecule. Raman scattering is extremely weak compared to the elastic Rayleigh scattering. A rough approximation would be that for every 1 Raman-shifted photon there are 106 Rayleigh photons (Vo, 2003). A more precise way of describing the Raman scattering effect is to consider the wave nature of light, rather than a photon in this occasion. Only the electrical component of the electromagnetic wave interacts with molecules in a material to produce Raman Scattering. Both important characteristics are the effect the material has on the properties of the electric field (E) and conversely the effect the electric field has on the material as the light wave passes through the sample (Splinter and Hooper, 2007).

Because of its weak scattering compared to elastic Raleigh scattering, Raman scattering discussion will not be taken further in relation to PPG.

4.2.3 Refraction

Refractive Index N is a measure of the bending of a ray of light when passing from one medium into another. It is determined by the speed of light in the medium. At boundaries, abrupt or continuous, changes in the refractive index increase scattering, refraction and reflection, while refraction usually occurs when light is incident at the boundary between two media with different refractive indices (see **Figure 4-3**) and is governed by **Snell's Law** as below:

$$v_1.sin(\theta_1) = v_2.sin(\theta_2) \qquad (4.16)$$

where θ_1, the angle of incidence, θ_2 is the anlge of refraction, v_1 and v_2 are the speeds of light in the media, and are related to the refractive index of each medium ($n = c_{vaccum}/v$).

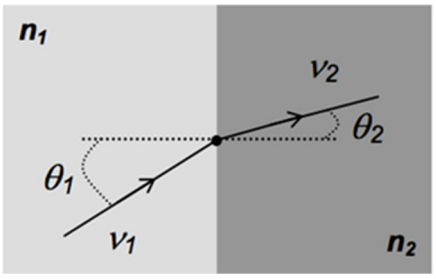

Figure 4-3
Refraction of light at the junction between two media with different refractive indices.

Since skin tissues are heterogeneous in composition, one may need to know the refractive indices for the various tissue constituents or an averaged value for the tissue as a whole. The refractive index is around 1.4 for most tissue types (Delpy et al., 1988). **Table 4-1** presents some of the refractive indices in different cellular elements.

Table 4-1
Refractive indices of cellular level elements (Dunn, 1997; Kumari and Nirala, 2011).

Cellular level elements	Refractive index	Remarks
cytoplasm	1.38	rat liver cell
cytoplasm	1.37	hamster overy cell
cortical cytoplasm	1.35 ~ 1.37	
nucleus	1.39	
cell membrane	1.46	
mitochondria	1.40	rat liver cell
protein	1.5	
deried protein	1.58	
melanin	1.7	
collagen fiber	1.32 to 1.45 (axis) 1.40 to 1.61 (radial)	dry, deminerised tendon

4.3 Optical Properties of Biological Tissues

In Photoplethysmography the light is directed towards the skin, where the structure of the skin layers, blood vessels and blood flow and a number of chromophores react to the light in different ways.

4.3.1 Optical Pathways in Skin

In this section, the optical properties of the biological tissues related to PPG are discussed. The skin has a very complex structure that consists of a variety of cells, fibres, and other components make up several different layers that give skin a multi-layered structure. Veins, capillaries, and nerves form vast networks inside this structure.

Light incident on skin traverses various pathways in each layer of the skin. **Figure 4-4** shows a schematic of the optical pathways in the skin layers. By assuming that the optical properties to be homogeneous on a cellular level, we can estimate the optical properties of each skin layer. Previous work on the optical properties of skin layers or cutaneous optics has employed this approximation of homogeneousity (Aravind Krishnaswamy and Baranoski, 2004).

In this discussion, we consider absorption and scattering to be uniformly distributed across skin layers (Anderson and Parrish, 1981; Nielsen et al., 2008).

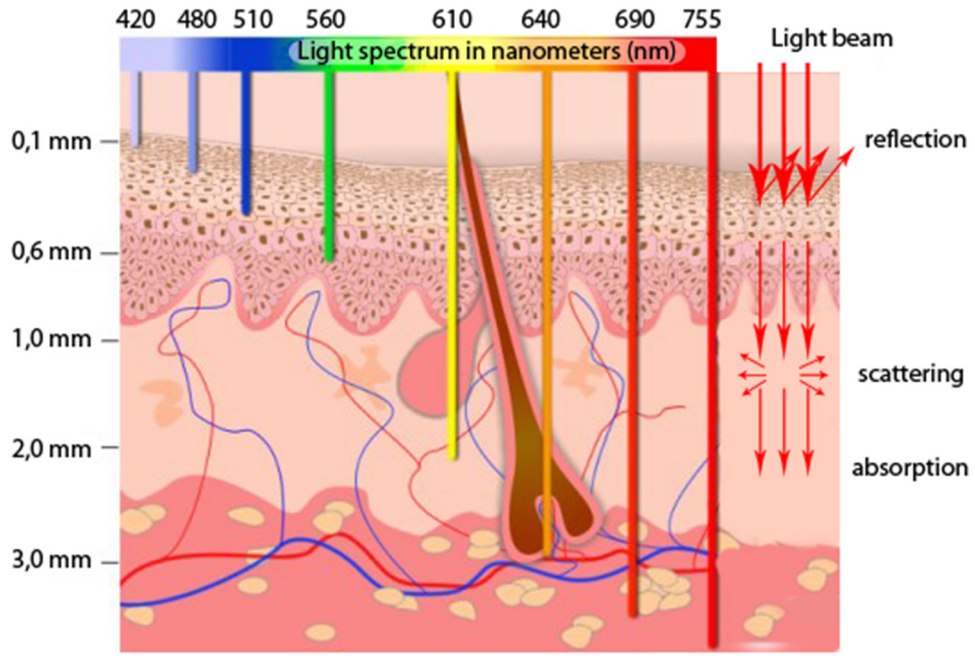

Figure 4-4
A schematic of the optical pathways in skin relating light wavelength and depth of penetration in skin in millimeters (GBS, 2015).

A part of the incident light is first reflected at the surface of the skin, due to the difference in the refractive indices of the outermost layer of the skin; the stratum corneum. The epidermis propagates and absorbs light. The absorption property comes mostly from the natural chromophore, melanin.

The melanin absorption level depends on how many melanosomes per unit volume are in the epidermis, which varies from one individual to another from 1.3% volume of the epidermis in lightly pigmented specimens to 43% fraction in darkly pigmented specimens (Aravind Krishnaswamy and Baranoski, 2004).

It has been proved that transmission of the light varies according to the skin type. The low-melanin dermis transmits from about 50% at 400 nm to 90% at 1,200 nm, while the high-melanin epidermis transmits less than 40% at 400 nm and 90% at 1,200 nm. In general, there is a gradual increase in skin penetration at longer wavelengths. This phenomenon is responsible for the desired effects on the tissue. The structures of the tissue that absorb the photons are known as chromophores and will be discussed in more detail.

Light also propagates in the dermis layer, a layer primarily composed of dense, irregular connective tissue with nerves and blood vessels that vary in size. Where light interacts mainly with the chromophores. Moreover, the dermis is optically thick, and can be viewed as a turbid medium, where a significant amount of scattering takes place. Multiple scattering takes place in the vast network of collagen fibres. As a result, scattering by the dermis can be described as multiple scattering, and it appears to be isotropic throughout the layer, although scattering due to a single collagen fibre is strong in the forward direction (Sandell and Zhu, 2011).

It is important to note that optical interaction with skin layers will majorly contribute to the non-pulsatile component of the PPG signal.

4.3.2 Optical Properties of Erythrocytes

Erythrocytes or Red Blood Cells (RBCs) occupy the vast majority of blood volume and hence, they are of major interest to studying the PPG signal. Erythrocytes contain the strongest absorbers of visible light in the human body, haemoglobin (Hb), and the cells can be easily isolated and studied experimentally. Moreover, the erythrocytes do no show internal structure which allows the opportunity to apply theoretical models of scattering to these cells. The PPG signal is concerned with the pulsatile flow which originates from blood volume changes in the vascular bed and hence, the main focus of this project will be directed towards the role of erythrocytes and their effect on the PPG signal. This section will discuss the main studies that addressed the optical properties of erythrocytes.

The optical properties of erythrocytes have been widely studied in many investigations Some of these investigations are theoretical where, Reynolds et al assumed that the erythrocyte obeys Mie scattering (Reynolds et al., 1976). The absorption and the scattering cross sections obtained from Mie theory were also used by Schmitt et al and Steinke and Shepherd, who described light transport in whole blood by applying the diffusion approximation (Schmitt et al., 1986) and who also did experimental work on the oxygen content of erythrocytes in a flow cell (Steinke and Shepherd, 1988). Moreover, Roggan at al also investigated the optical properties of circulating human blood in a flow cuvette (Roggan et al., 1999). The study investigates such properties in the visible and near infrared range using diffuse backscattering, total transmission and the non-scattered transmission of thin samples. Blood samples were gently stirred and kept flowing through a turbulence-free cuvette with a linear flow and an optical path of 97 μm.

4.3.2.1 Effect of Haematocrit

Erythrocytes obtain absorption and scattering properties dependant on the haematocrit value. This is evident due to the effect of Hct on the absorption and scattering coefficients as seen in **Figure 4-5**. In the study performed by Roggan et al, an increase in Hct up to 50% led to a linear increase in absorption coefficient and a scattering coefficient also increased proportionally but only for values <10% (Roggan et al., 1999). The anisotropy factor was almost constant with 0.002 variations. The scattering coefficient appeared to be independent of blood concentration at Hct>10, and the g factor decreased continuously at Hct 70%, The reduced scattering coefficient $\mu_s' = \mu_s(1-g)$, showed a linear increase up to Hct of 45%, where saturation was observed at high Hct.

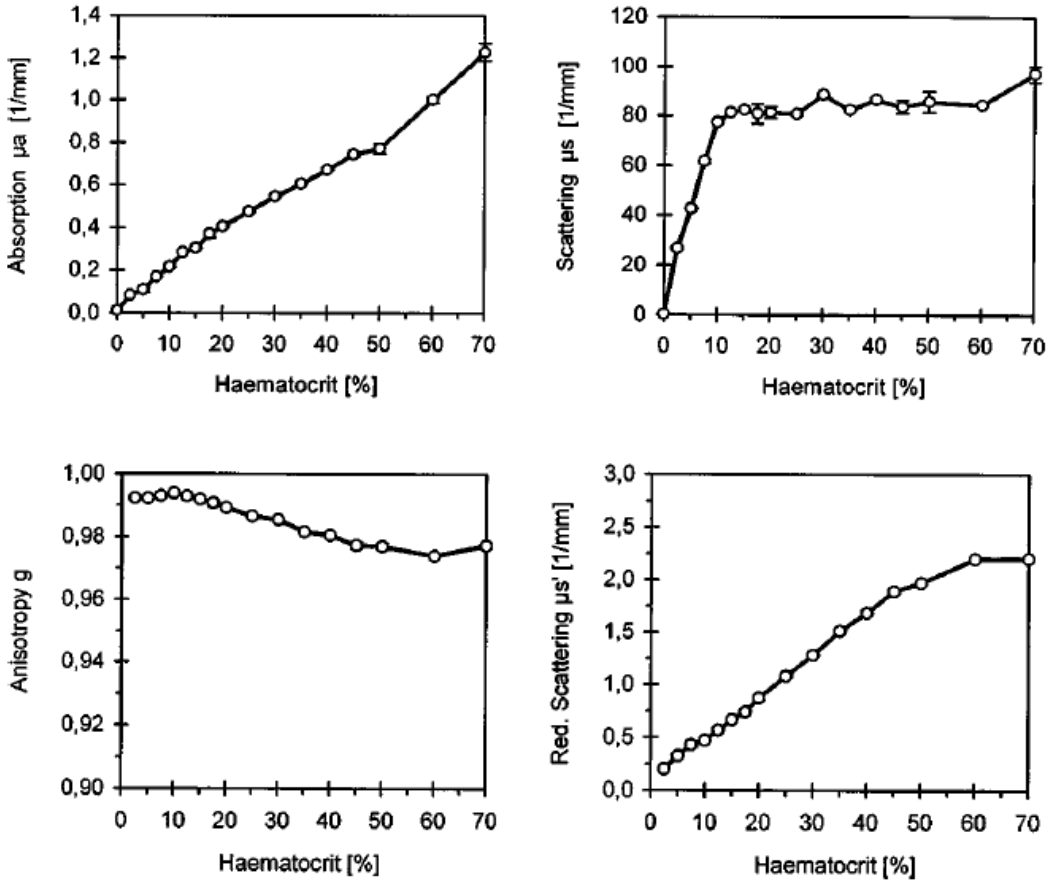

Figure 4-5
Mean values of the absorption coefficient , scattering coefficient, g the anisotropy factor ,reduced scattering coefficient versus haematocrit values at a wavelength of 633 nm.(Roggan et al., 1999).

4.3.2.2 Effect of flow velocity

Roggan et al investigated the effect of flow velocity on the optical properties. The study concluded that low velocities have a significant impact on the optical properties of blood as seen in **Figure 4-6**.

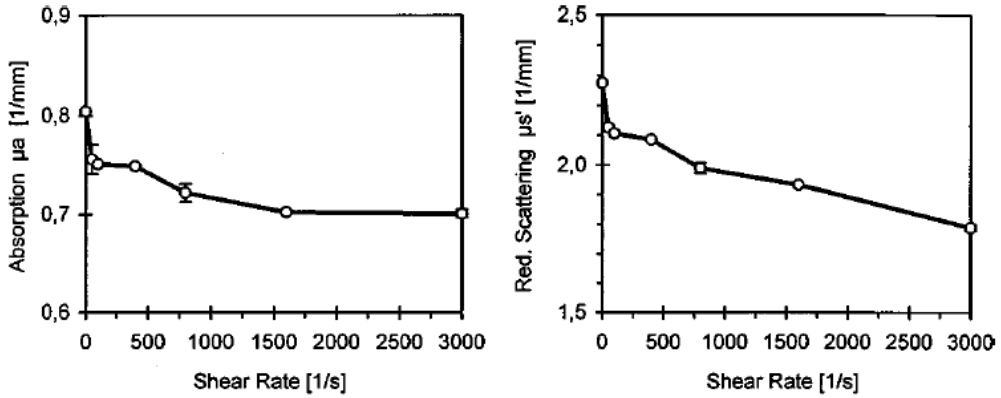

Figure 4-6
Mean values of the absorption coefficient and reduced scattering coefficient versus shear rates at a haematocrit of 41% and using a wavelength of 633 nm (Roggan et al., 1999).

4.3.2.3 Effect of haemolysis

The same study by Roggan et al also observed optical properties obtained from completely haemolysed blood samples without removing the membrane residuals as shown in **Figure 4-7**. The absorption coefficient significantly decreased with increase haemolysis. Scattering coefficient showed a distinct decrease with increasing haemolysis. At complete haemolysis, μ_s amounted to 18% of the value measured for intact blood. The anisotropy factor (g) was constant up to 50% haemolysis and slightly decreased at higher rates. Reduced scattering coefficient decreased continuously reaching values 16% compared to intact blood (Roggan et al., 1999).

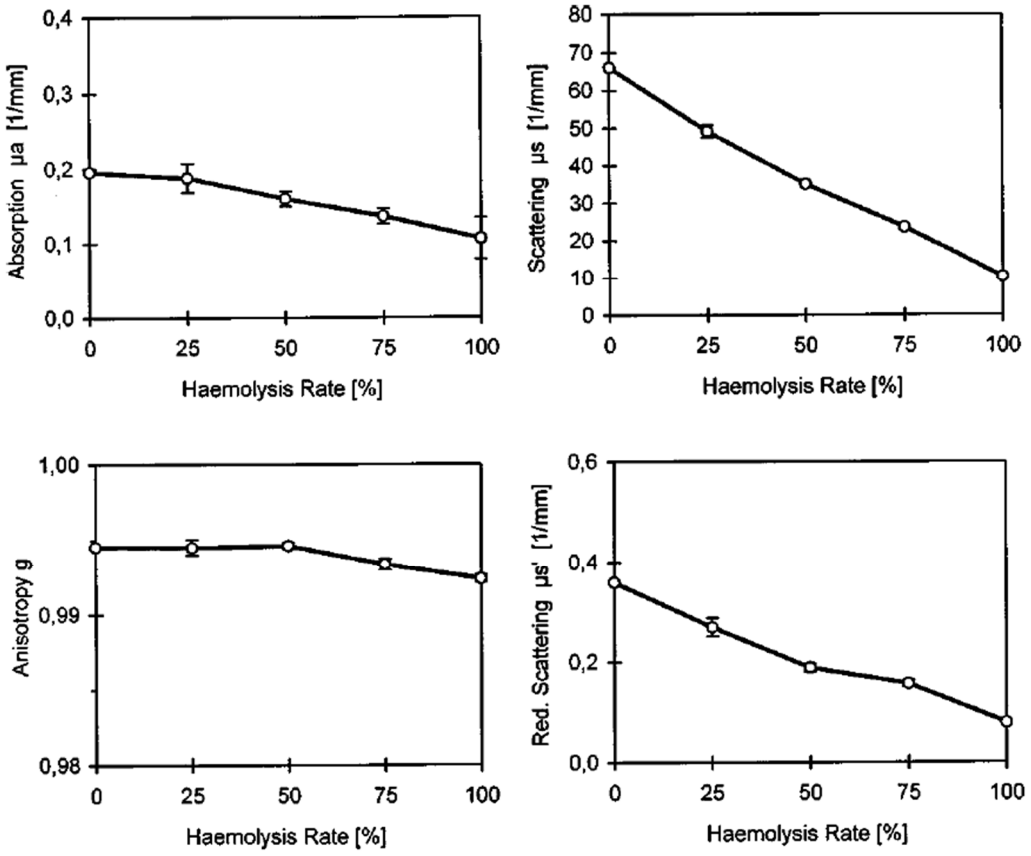

Figure 4-7
Mean values of the absorption coefficient, anisotropy g, scattering coefficient and reduced scattered coefficient versus extent of haemolysis (Roggan et al., 1999).

The effect of haemolysis highlights that when the erythrocytes are destroyed, their haemoglobin is distributed into the whole solution, resulting in a refractive index match and hence the erythrocytes lose their scattering properties. Moreover, the residual membranes have only a minor impact on the scattering properties due to their negligible thickness which is estimated at 4 nm.

4.3.3 Chromophores

The total number of endogenous chromophores that can be found in human tissue is vast. However, most chromophores are only present in smaller concentrations, making them less prominent. Others are active in wavelength regions outside of the interest of this study. Some chromophores even emit light after absorption and are hence named fluorophores, which will not be discussed in this study for their relatively very minor contributions to PPG signals (Kamal et al., 1989).

4.3.3.1 Haemoglobin

A large group of haemoproteins are responsible for the oxygen-carrying function in the body. Once such haemoprotein is haemoglobin (Hb), the actual absorption spectrum of

Hb depends primarily on oxygen-rich blood or oxygen-poor blood. Hb derivatives also exist, however, they do not contribute to the transport of oxygen.

The derivatives include methaemoglobin and carboxyhaemoglobin, which are reversible but the formation of sulfhaemoglobin is irreversible. The dysfunctional derivatives differ in absorption, more or less drastically, compared to the functional haemoglobin (Zijlstra et al., 2000). Also, the concentrations of oxygenated and deoxygenated Hb change according to the function and metabolism of the tissue. Thus, the corresponding changes in absorption can provide clinically useful physiological information. The absorption spectra as obtained by Zijlstra for Hb and some of its derivatives are shown in **Figure 4-8**.

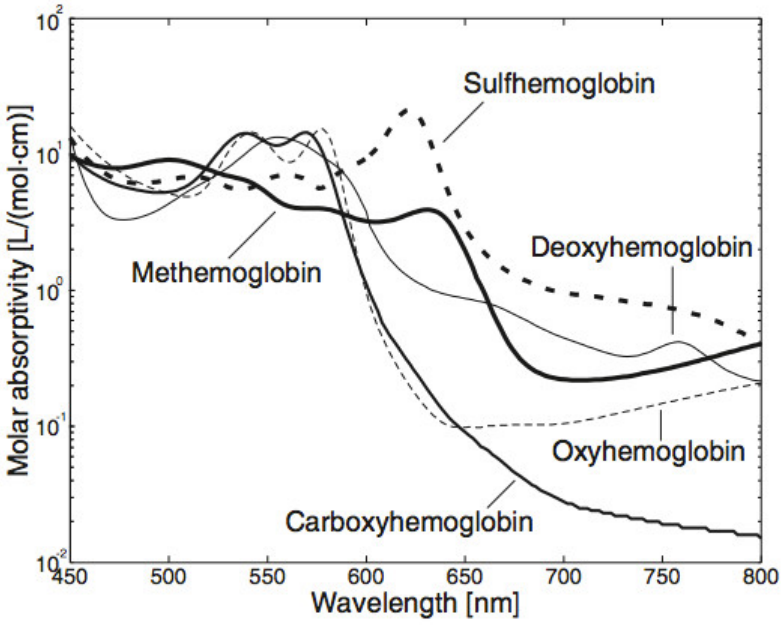

Figure 4-8
Haemoglobin and its derivatives optical absorption spectra (Zijlstra et al., 2000).

4.3.3.2 Melanin

Melanins are the biological pigments ranging in colour from the yellow and red-brown pheomelanin to the brown and black eumelanin. They are found in skin, hair, eyes and retina. The melanin is produced in the melanocytes in the stratum basal of the epidermis. From this layer, the melanin granules, diffuse out into the keratinocytes of the stratum spinosum via the melanocytic dendrites (Aravind Krishnaswamy and Baranoski, 2004).

There are two types of melanin with slightly different absorption spectra as shown in **Figure 4-9**, eumelanin, and pheomelanin. The Melanin Absorption level depends on how many melanosomes per unit volume are in the epidermis, which varies from one individual to another from 1.3% volume of the epidermis in lightly pigmented specimens

to 43% fraction in darkly pigmented specimens (Aravind Krishnaswamy and Baranoski, 2004). Those variations can affect Photoplethysmography signals, which will be discussed later.

It is not the amount of melanin producing units, melanocytes, per square millimetre that determines the colour of the skin, but it is rather the size, amount and distribution of the melanosomes in the keratinocytes that differ. Darker individuals have a higher melanin production and wider distribution of the melanin granules even in the stratum corneum. Fair-skinned individuals, in contrast, have less melanin and the melanin is present as aggregated small melanin granules spread in the epidermis but not present in the stratum corneum. It has also been proposed that melanin extinction is largely due to scattering in the melanin granules. Melanin shows a Rayleigh scattering behaviour and the melanin granules can be regarded as scattering particles. The scattering process has been proposed as originating from the structural formation of melanosomes which, to some extent, act as a polarizer in the skin (Joely Kaufman et al., 2012; Wolbarsht et al., 1981).

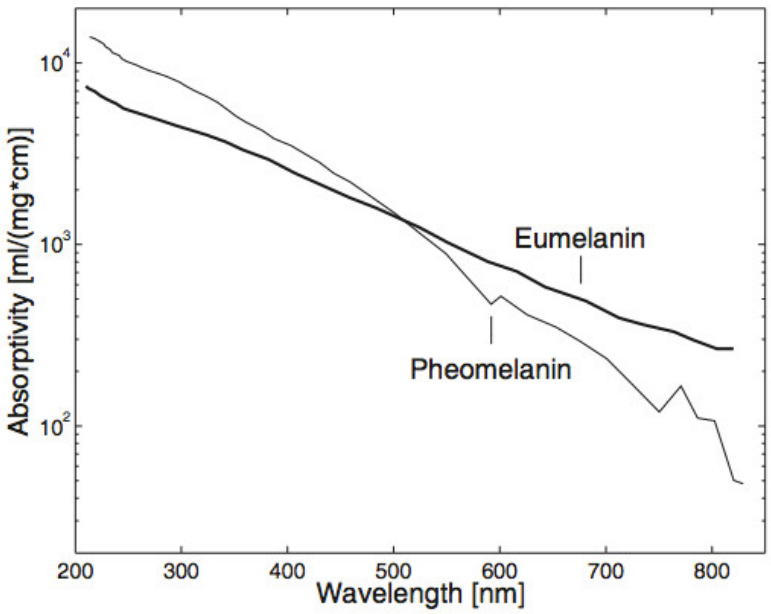

Figure 4-9
Eumelanin and Pheomelanin Absorption Spectra (Joely Kaufman et al., 2012).

4.3.3.3 Lipids

Different lipids, or body fat, can be found throughout the body, e.g. the subcutaneous fat layer and epicardial fat. Adipose tissue containing most of the lipids in different constellations is considered as scattering tissue. However, it can also act as an absorbing substance with its own characteristic absorption (van Veen et al., 2005).

4.3.3.4 Water

Water is a weak absorbing chromophore in the visible wavelength range, but shows increased absorption both in the UV but also in the NIR region as shown in **Figure 4-10**. Water is one of few molecules that colour light due to pure vibrational states of the molecule, and it is found throughout the whole body in the intracellular as well as extracellular fluid, e.g. in the plasma of the blood. The concentration of water ranges from 11% in adipose tissue to 92% in the plasma in humans (Tortora and Derrickson, 2008).

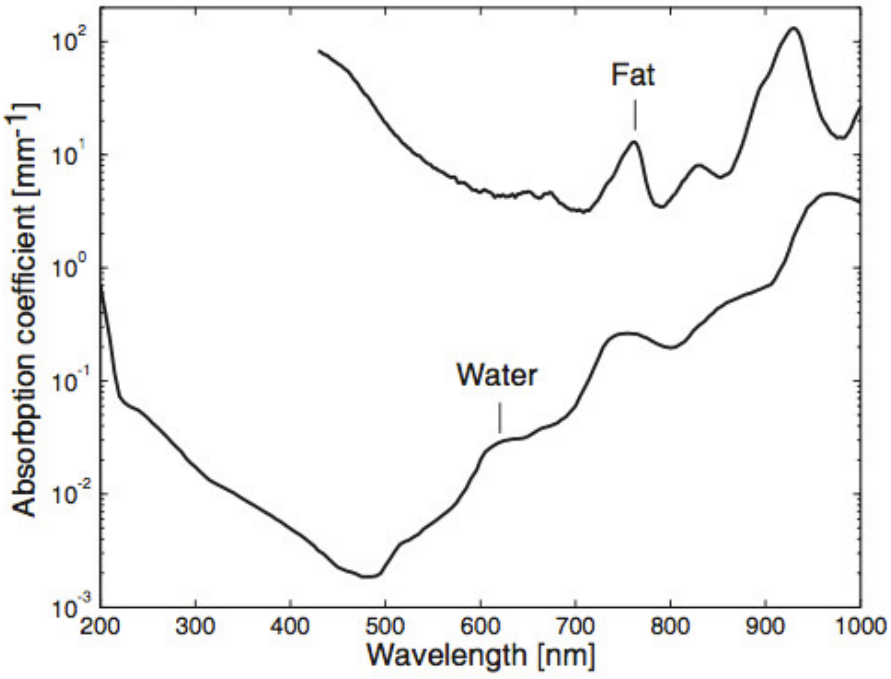

Figure 4-10
Comparison of absorption coefficients for fat and water (Ziljstra et al, 2000).

SUMMARY

This chapter discussed the principles of optics and the optical interaction with biological tissues that are relative to the PPG technique. We highlighted some studies that addressed the role of skin layers, erythrocytes and chromophores in light absorption and scattering. This finally leads us to discuss Photoplethysmography, its principles, history, and applications in the next chapter.

Chapter 5
PHOTOPLETHYSMOGRAPHY

5.1 Introduction

In the previous chapters, we have covered basic concepts of the cardiovascular system, the current state of the art in cardiovascular assessment and basic physical concepts of light interaction with biological tissues. This project is primarily focused on the investigation of the fundamentals of Photoplethysmography (PPG) and the potential of the technique to assess "markers" contributing to cardiovascular disease. PPG describes the study of illumination alterations due to changes in a physical parameter, such as volume, in a localised region of tissues. The basic form of PPG consists of: A light source to illuminate the skin, and a photodetector (PD) to measure the small variations in the light intensity, associated with changes in volume changes. It is a non-invasive technique and usually utilises Red (R) and Infrared (IR) wavelengths.

It is essential to highlight that the true origin of PPG signal is still a subject of debate across all published literature. However, is broadly accepted that Photoplethysmography provides a recording of the pulsatile changes in the microvascular bed of tissue.

This chapter presents a review of the principles of the waveform and operation modes, early and recent history of Photoplethysmography, approaches to investigate the origin

of the signal, the relevant aspects of the practical use of the signal and the limitations associated with the technique and its applications.

5.2 Principles of the PPG waveform

The PPG waveform is divided into two main components:

1. The non-pulsating DC component, a relatively constant voltage offset of which the magnitude is determined by the nature of the non-pulsating material through which the tissue passes. The slowly changing DC component may be extracted using a low pass filter. It includes low-frequency components, under 0.5 Hz, attributed to respiration, sympathetic nervous system activity and thermoregulation (Webster, 1997).
2. The pulsatile AC component. Two important characteristics of the PPG AC pulse waveform were described by Hertzman and Spealman (Hertzman and Spealman, 1937). The appearance of the pulse was defined as two phases: The anacrotic phase being the rising edge of the pulse, and the catacrotic phase being the falling edge of the pulse. The first phase is primarily concerned with systole, and the second phase with diastole and wave reflections from the periphery. A dicrotic notch is usually seen in the catacrotic phase of subjects with healthy compliant arteries. The AC-component is synchronised with the heart rate (Webster, 1997).

A typical PPG signal is shown in **Figure 5-1**.

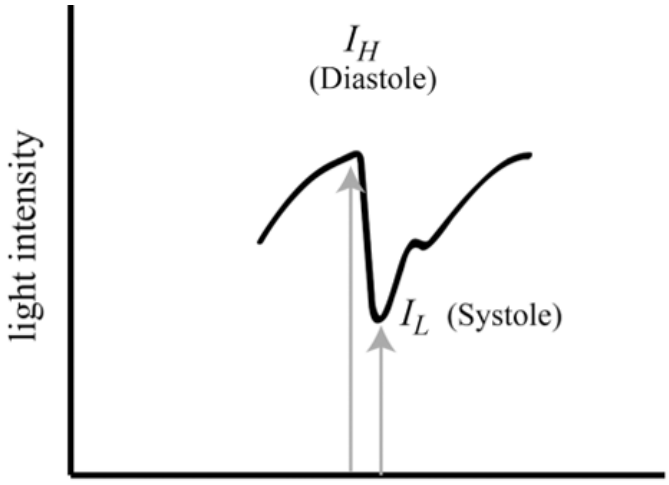

Figure 5-1
A typical Photoplethysmographic signal (Lee et al., 2011). Where, I_L is the small value of reflected amount of light and the peak point of PPG. I_H is the large value of the reflected amount of light and the onset point of photoplethysmography.

5.3 Modes of Operation

The PPG can operate in either transmission or reflection mode (Mannheimer, 2007; Nijboer et al., 1981). In the transmission mode, the light transmitted through the medium is detected by a PD opposite the LED source, while in reflectance mode, the PD detects light that is back-scattered or reflected from tissue, bone and/or blood vessels as illustrated in **Figure 5-2**.

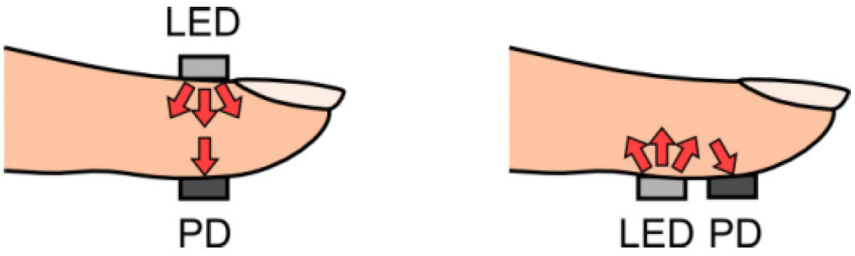

Figure 5-2
Light-emitting diode (LED) and photodetector (PD) placement for transmission- and reflectance-mode Photoplethysmography (PPG) (Tamura et al., 2014).

The transmission mode is capable of obtaining a relatively good signal, but the measurement site may be limited. The sensor must be located on the body at a site where transmitted light can be readily detected, such as the fingertip, nasal septum, cheek, tongue, or earlobe. The fingertip and earlobe are the preferred monitoring positions.

Reflectance mode eliminates the problems associated with sensor placement, and a variety of measurement sites can be used. However, reflection-mode PPG is affected more

by motion artefacts and pressure disturbances. Any movement, such as physical activity, may lead to motion artefacts that corrupt the PPG signal and limit the measurement accuracy of physiological parameters. Pressure disturbances acting on the probe, such as the contact force between the PPG sensor and measurement site, can also deform the arterial geometry by compression. Thus, in the reflected PPG signal, the AC amplitude may be influenced by the pressure exerted on the skin (Challoner and Ramsay, 1974; Hertzman and Roth, 1942; Jespersen and Pedersen, 1986; Nijboer et al., 1981).

5.4 Early and Recent History on the Origin of the PPG

The first report of using a similar technique was used for continuous recording of peripheral circulatory changes in the rabbit ear following venous occlusion. It also described the recordings obtained from the skin of the human fingers using a reflection mode PPG system (Molitor and Knalzuk, 1936).

Hertzman's early work describes the use of reflection mode to establish a valid method for measuring blood flow and blood volume changes. Later, the AC and DC components of the signals were separated using electronic amplifiers in order to monitor vasomotor activity. There were also attempts to use the signal for assessing the completeness of sympathectomy. However, the early researchers in this field were limited by the size, sensitivity, and reproducibility of the available technology (Hertzman, 1938; Hertzman and Roth, 1942, 1942).

In the 1960's, accompanying the evolution of semiconductor technology, further investigations took place. There were attempts to detect the onset of cutaneous vasodilation using PPG (Challoner and Ramsay, 1974; D'Agrosa and Hertzman, 1967) More recently PPG has been widely used with the introduction of pulse oximetry as a non-invasive method for monitoring patient's blood oxygen saturation (Aoyagi, 2003; Sinex, 1999).

Several researchers have investigated the optical processes in relation to PPG signal. They have highlighted the key factors that can affect the amount of light received by the photodetector; these factors include the sensor configuration, blood volume changes, blood vessel wall movement and the orientation of red blood cells (RBC).

For almost a century, quantification of haemodynamic measurements with the PPG has rested upon the assumption that the PD output could be considered a linear function of intravascular volume, and this assumption might be acceptable for the minute volume changes detected as a consequence of normal arterial pulsation in the microcirculation.

However, previously obtained results indicated that PPG output depends logarithmically on the behaviour of the erythrocytes during blood circulation, and thus compliance studies which imply much larger alterations of vascular volume will be invalidated if this relationship is not taken into account. Hence, this confirms once again the challenges of quantitative PPG measurements (Björn, 2007; de Trafford and Lafferty, 1984; Jespersen and Pedersen, 1986; Shelley, 2007).

Some of the experimental set-ups suggested that the alternating PPG signal was reacting to the orientation of the RBC during the cardiac cycle, instead of volumetric changes (D'Agrosa and Hertzman, 1967), also, it has been pointed out that changes in the blood distribution between the vascular areas can play a role in signal generation (Hocherman and Palti, 1967). Literature reports can be reconciled with the view that scattering and absorption of light by blood-filled vessels have major effects on the PPG signal (Nijboer et al., 1981).

The PPG signal still leaves an open question of what does it actually measure. Attempts to quantify the pulse amplitude have been unsuccessful. The orientation effect of erythrocytes has been demonstrated by recording pulsatile waveforms in a glass tube where volumetric changes should not be possible (Jespersen and Pedersen, 1986). However, the role of erythrocyte orientation and the mechanism it contributes to the generation of the PPG waveform is not fully understood (Anderson and Parrish, 1981; Nielsen et al., 2008; Nijboer et al., 1981; Ochoa and Ohara, 1980; Rolfe, 1979).

The difference in PPG pulse amplitude between two locations (forehead and finger) noted in Mannheimer's experiment (Mannheimer, 2007), highlights an interesting and poorly understood aspect of Photoplethysmography, imposing a simple but rather a difficult question to answer; where does the optical "pulse" actually come from? A pragmatic answer is that the magnitude of the light intensity comes directly from the modulating change in tissue opacity and hence, optical density. However, the question of what are the major factors that alter tissue opacity is not fully understood.

More recently, a technique termed Blood Pulsation Imaging (BPI) became visible in the literature, as a non-invasive optical method based on PPG used for the visualisation of changes in the spatial distribution of blood in the microvascular bed. The method is based on the detection of time-varying modulation of each pixel in the recorded video frames synchronously with the heartbeats. One of the BPI studies highlighted an observation of the presence of two inverted signals in adjacent locations (Teplov et al.,

2014). Another recent study highlighted the importance of arterial stiffness in the origination of the PPG signal using BPI (Kamshilin et al., 2015). The study suggests that elastic deformation of the dermis caused by transmural arterial pressure changes plays a key role in the formation of the PPG waveform when subject's skin is illuminated by light with small penetration length (510-560 nm). At deeper penetrating depths or longer wavelengths, the influence of the dermis compression is diminished because of the efficient interaction of the light with varying blood volume inside pulsating arteries (Kamshilin et al., 2015).

Finally, we conclude some of the factors that have been noted to affect the PPG waveform which can be summarised as:

1. The periodic increase and decrease in the tissue blood fraction.
2. The degree of cutaneous vessel distensibility.
3. The spacing between the emitter and detector (wider separations associated with larger measured pulse amplitudes) and the depth of the pulsing vasculature.
4. The extinction coefficient of the modulating blood volume at the measurement wavelength.
5. The volumetric and flow-dependent blood-scattering contributions from the erythrocytes in the blood
6. Venous pulsations, direct from the right heart or indirectly from adjacent arteries.
7. The autonomic function and the role of vasoconstriction and vasodilation and the concentrations of the chemical release associated with both mechanisms.

5.5 PPG Applications

PPG has been applied in many different clinical settings, including clinical physiological monitoring, vascular assessment, and autonomic function. Some of these applications are discussed briefly in this section.

5.5.1 Blood Oxygen Saturation

Pulse Oximetry has been one of the most significant technological advances in clinical patient monitoring over the last few decades (Webster, 1997). It utilises PPG measurements to obtain information about the arterial blood oxygen saturation (SpO_2). Some of the main areas in which pulse oximeters are used include anaesthesia, fetal monitoring, neonatal and paediatric care, dentistry and oral surgery, and sleep studies (Kyriacou, 2013, 2006; May et al., 2014; Zaman et al., 2013). In the early 1990's, pulse

oximetry became a mandated international standard for monitoring during anaesthesia following the publication of the Harvard minimum standards for monitoring in 1986. It is considered as a necessary monitoring technique for the continuous monitoring of blood oxygen saturation in patients under anaesthesia and the determination of desaturation events (Chan et al., 2007).

The technique utilises red and infrared PPG signals to indicate oxyhaemoglobin and deoxyhaemoglobin in the blood. The AC and DC components are derived at each wavelength and a ratio of AC over DC is obtained which compensates for changes in incident light intensity, removing a complicated variable from the equation. Performing this operation at each wavelength is capable of isolating the relative absorbance of reduced and oxygenated Hb. The ratio of the red signal (AC_{660nm}/DC_{660nm}) to the infrared signal (AC_{940nm}/DC_{940nm}) reflects a similar ratio of reduced to oxygenated Hb, which can be then converted to oxygen saturation using calibration curves.

5.5.2 Blood Pressure

Arterial blood pressure is a very important clinical variable to measure. The measurement of the arterial pressure waveform at the finger with a continuous beat-by-beat basis was introduced in the early 1980s. The method is based on the dynamic (pulsatile) vascular unloading of the finger arterial walls using an inflatable finger cuff with built-in PPG sensor. Blood pressure was also estimated using an algorithm based on the pulse arrival time and was compared with conventional arm blood pressure measurements. Their approach showed promise as a method for home monitoring of blood pressure. Using empirically determined transfer functions, it is possible to derive the arterial blood pressure pulse from PPG measurements (Asif-Ul-Hoque et al., 2011). The various methods and limitations of these methods were further discussed previously in **Chapter 3**.

5.5.3 Arterial Stiffness

Arterial stiffness is recognised as a vital indicator of cardiovascular health at an early stage of atherosclerosis. PPG was used to derive a host of indices for empirical estimation of arterial stiffness. The stiffness index, the augmentation index, Pulse wave velocity using the AC component of the PPG signal or its second derivative. These methods and their applicability and limitations for estimation of arterial stiffness using PPG were further discussed previously in **Chapter 3**.

5.5.4 Respiration

Respiration causes variation in the peripheral circulation, making it possible to monitor breathing using a PPG sensor attached to the skin. The low frequency respiratory induced intensity variations in the PPG signal are well documented (Johansson and Öberg, 1999; Nakajima et al., 1996) These variations are not fully understood but is believed to be caused by skin blood volume fluctuations induced by the respiratory variations in intrathoracic pressure transmitted to the measurement site by the venous system (Meredith et al., 2012).

5.5.5 Vascular Assessment

Disease detection with PPG is possible because the peripheral pulse usually becomes damped, delayed and diminished with increasing severity of some vascular diseases, particularly peripheral arterial disease (Bortolotto et al., 2000). Multi-body site PPG measurements have been proposed for peripheral vascular disease detection. It was also documented that PPG technique can be used to detect endothelial dysfunction in diabetic patients using the PPG-derived reflection index (Chowienczyk et al., 1999).

PPG pulse shape was also used to characterise healthy subjects and Raynaud's patients and found that both the pulse amplitude and the slope of the rising edge were good markers for the condition. The DC component of the PPG waveform was also used for the noninvasive assessment of lower limb chronic venous insufficiency (Cooke et al., 1985).

5.5.6 Autonomic Function

The PPG signal is composite in nature and has low-frequency components relating to respiration, blood pressure control, and thermoregulation, as well as the high-frequency components relating to the heart synchronous pulse waveform. Meanwhile, PPG shows considerable potential for neurological assessment, with the capability to give new insights into the physiology and pathophysiology of the central and peripheral nervous systems. The PPG signal could provide basic information about heart rate (HR) and its variability, and highly suggests a good alternative to understanding dynamics pertaining to the autonomic nervous system (ANS) without the use of electrocardiogram (ECG) device (K. Hamunen et al., 2012).

5.5.7 Other Clinical Parameters

The stroke volume (the amount of blood pumped out of a ventricle during one ventricular contraction) can be estimated from PPG-derived pulse contour analysis on a beat-by-beat

basis. However, there is an ongoing discussion in the literature regarding the accuracy of PPG-based cardiac output assessments (Azabji Kenfack et al., 2004).

In a recent study, which aimed at verifying the usability of PPG technique for haemodynamics measurements by measuring multiple pulse wave parameters, which refer to local and regional arterial stiffness. This study used PPG sensors -only IR- attached on multiple sites of the leg arteries and verified that it is a reliable method for measuring haemodynamics parameters (Grabovskis et al., 2011).

5.6 PPG Limitations

The PPG signals have been widely applied in clinical assessments and furthermore in investigational studies as discussed above. However, the technique incurs some limitations for a variety of reasons.

5.6.1 Abnormal Haemoglobin Oxygen Content

It has been noted that pulse oximetry's ability to monitor oxygen delivery deteriorates when the oxygen concentration is too much or too little. Lack of oxygen at a cellular level is termed *hypoxia*. Hypoxia can be further categorized into four groups: hypoxic hypoxia (arterial Hb oxygen saturation is low), anaemic hypoxia (Hb concentration is low—but may be well saturated), stagnant hypoxia (low cardiac output or vessel occlusion), and histotoxic or cytotoxic hypoxia (oxygen is delivered, but cells are unable to utilise it) (Roach et al., 2002). Of these categories, pulse oximetry can measure and indicate only one—hypoxic hypoxia— though a device may produce readings during instances of other types of hypoxia. Thus, a patient may be globally or locally hypoxic despite *Sp*O2 readings to the contrary. Pulse oximetry is insensitive to the delivery of too much oxygen—*hyperoxia*. This limitation of pulse oximetry is important in monitoring patients receiving supplementary oxygen, particularly premature babies, and neonates, who can suffer retinopathy, resulting in blindness, if their arterial oxygen saturation is allowed to go too high. The second limitation of pulse oximetry is that it requires a pulse. Though it is desirable to monitor the oxygen saturation of a patient experiencing cardiac arrest, or, exhibiting an irregular pulse, low perfusion, or low blood volume (Roach et al., 2002).

5.6.2 Motion Artefacts

Motion artefact can influence the measurement signal and lead to a disrupted readout (Alzahrani et al., 2015). It is indicated that the greatest and worst cause of artefact noise that contaminates the PPG signals is Motion Artifact (MA) produced from physical

activity, shivering or seizure activity. Thus, various signal processing techniques have been proposed to remove MA and recover the PPG signals (Nemati et al., 2014).

5.6.3 Blood Pathologies

Blood pathologies such as anaemia, sickle cells, and sepsis have been shown to affect the precision of pulse oximetry measurements.

Anaemia appears to adversely affect the accuracy of pulse oximetry, although the mechanism is unclear, and it may do so only in the presence of hypoxia. In theory, anaemia should not affect pulse oximetry, as the ratio of relative absorbance should be preserved and unchanged by changes in total haemoglobin concentration within the sample. However, a retrospective study found an underestimation of oxygen saturation by pulse oximetry in anaemic subjects, inversely proportional to Hb concentration and most pronounced at a SpO2 less than roughly 80% (Severinghaus and Koh, 1990). A study of non-hypoxic human patients with acute anaemia from haemorrhage down to a Hb value as low as 2.3 g/dl (normal range 12 to 14 g/dl) showed good agreement with pulse oximetry (Jay et al., 1994).

Sickle cell anaemic patients are known to have rigid and sticky blood cells that are deformed into a shape of crescent moons. Complications of sickle cell disease, such as vasoocclusive crisis and acute chest syndrome, are often precipitated or exacerbated by hypoxemia and can result in a vicious cycle of additional sickling and vasoocclusive crises. Accurate detection of hypoxemia in patients with anaemic sickle cells plays an important role in mitigating further red blood cell sickling. The accuracy of pulse oximetry in monitoring oxygenation in sickle cell disease has been debated. A study of 24 patients with sickle cell disease determined that blood oxygen saturation measured by a pulse oximeter (SpO_2) underestimated blood oxygen saturation measured using arterial blood gas sampling (SaO_2) readings. This difference was clinically insignificant. While some investigators conclude that as long the PPG waveform is present, pulse oximeter can be used in patients with sickle cell disease reliably without misdiagnosing either hypoxemia or normoxeamia (Ortiz et al., 1999), others conclude that the technique should be used with caution in this patient group and it might produce variable results (Pianosi et al., 1993).

Sepsis is the infection of the blood. There are conflicting studies on how SpO_2 is biased in the setting of sepsis and septic shock. Secker and Spiers compared 80 paired SpO_2 and SaO_2 readings in patients with septic shock and showed that only in those with low

systemic vascular resistance, the SpO_2 underestimated the SaO_2 by a mean of 1.4%, a level that was statistically significant but unlikely to be clinically important (Secker and Spiers, 1997). These results are supported by a human study where induction of hyperemia in one arm of volunteers resulted in lower SpO_2 than the control arm (Broome et al., 1993) A hypothesis to explain this phenomenon is that vasodilation from the sepsis resulted in creation of arteriovenous shunts that culminated in venous pulsations and spurious detection by the pulse oximeter of some venous blood as arterial (Broome et al., 1993).By contrast, a review of 88 patients with severe sepsis and septic shock found that in those with hypoxemia (defined as $SaO_2 < 90\%$), SpO_2 significantly overestimated SaO_2 by nearly 5% (Wilson et al., 2010). In several studies examining critically ill patients with various acute illnesses, some found SpO_2 underestimated SaO_2 while others found the opposite. Even in those studies that examined only septic patients, factors that may account for a difference in the direction in which SpO_2 is biased include differences in: (i) the extent of fluid resuscitation and tissue perfusion, (ii) sepsis-induced cardiac dysfunction, (iii) sites interrogated by the pulse oximeter probe, (iv) types of pulse oximeters and probes used, (v) vasoconstrictor use, and (vi) the presence of other co-morbid conditions that may spuriously affect SpO_2 values unpredictably. Thus, a number of variables that occur in patients with severe sepsis and septic shock make it difficult to predict which direction SpO_2 may be biased

5.6.4 Skin Pigmentation and Nail Polish

Skin pigmentation has shown variable effects on pulse oximetry (Volgyesi and Spahr-Schopfer, 1991). Primarily, dark pigmentation is linked with significantly more signal detection failures. It has been suggested that the less pigmented nail beds may offer particularly good probe sided in these patients (Severinghaus and Kelleher, 1992). More concerning, are some studies of pigmentation effects which have shown an overestimation of oxygen saturation The mechanism of such an artefact if present, is unclear, and probably arise from the scattering properties of melanin cells, where the light is diffused before it reaches the pulsatile vessels. Moreover, it could be a reflection of the relative lack of darkly pigmented subjects. In contrast, SpO2 data obtained from a study recruiting 284 patients divided into 3 groups of skin colour (light, intermediate and dark) found that skin pigmentation does not affect the bias or precision of pulse oximetry or any clinically significant effect on the PPG signal quality (Adler et al., 1998).

There is also evidence for the effects of nail polish on pulse oximetry (Hinkelbein et al., 2007) When demonstrated, most interference appears to arise from blue or black polish.

It is probably advisable to avoid possible interference by using other probe sites, removing the nail polish, or even simply placing the probe sideways on the digit to remove the nail from the transmission path.

SUMMARY

This chapter provided an introduction to the PPG technique, its history, and schools of thought on the origin of the signal, applications, and limitations of the technique. Some of the discussed limitations are yet poorly understood (e.g. blood pathologies) and hence they present obstacles in using the PPG as a reliable tool for clinical assessment, especially in the case where PPG techniques will be desirable for personal home use.

CHAPTER 6
DEVELOPMENT OF PPG PROBES AND TEMPERATURE MEASUREMENT SYSTEM

6.1 Introduction

The design and development of the PPG finger and tube probes are presented in this chapter. Finger probes were used to investigate PPG signals in healthy volunteers under varied flow conditions by stimulating the sympathetic nervous system. Tube probes were used to investigate the PPG signal generated from pulsatile flow under controlled flow scenarios in an arterial model that simulates the human circulation.

The details of the design, mechanical fabrication of the finger and tube probes, as well as the performance evaluation tests, are the subject of this chapter.

6.2 Finger probes

Two identical prototype reflectance finger probes were constructed utilising two surface-mount InfraRed (IR) emitting diodes (IREDs), two Red (R) emitting diodes (REDs) and a surface-mount silicon photodetector (see **Figure 6-1)**. The photodetector positioned in the reflectance mode detected radiation backscattered by the blood flow and surrounding tissues from all IREDs and REDs and gave an output current proportional to the detected radiation level. A multicore cable transported the power to the emitters via from the main PPG processing system and also carried the photodetector signals to the trans-impedance amplifier in the PPG system.

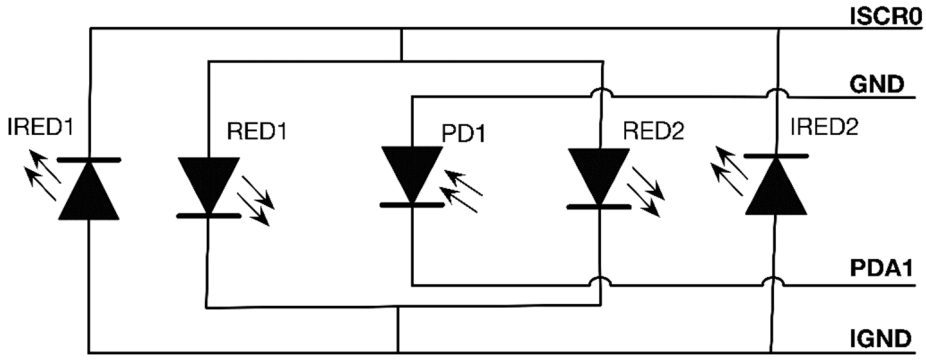

Figure 6-1
Schematic Diagram of the reflectance finger probe configuration.

6.2.1 Choice of LEDs and Photodiodes

The LEDs were chosen for their appropriate wavelength, low power consumption, and wide viewing angle. The Red LEDs have a peak wavelength of 660 nm and the Infrared LEDs 880 nm. A number of design configurations were initially produced to test the optimum separation distance. A five mm separation between LEDs' centre and the centre of the photodetector provided the best signal quality without photodetector saturation. chosen photodiodes were TEMD5020X01 (Vishay, US) with high photo and high radiant sensitivity that allow detection of the full range of wavelengths of interest. **Table 6-1** lists the characteristics of the chosen LEDs and those for the photodetector are listed in **Table 6-2.**

Table 6-1
Optoelectronic characteristics of the chosen Light Emitting Diodes (LEDs)

	R660	IR880
Model	KP-2012SRC-PRV	170 0805 Standard
Reverse Voltage	5V	5 V
Max Reverse Current	75 μA	100 μA
Continuous forward Current	30 mA	50 mA
Power Dissipation	75mW	80 mW
Capacitance	50 pF	45 pF
Wavelength spectrum	640-660 nm	840-880 nm
Operating temperature range	40 to + 85 °°C	-40 to + 85 °C
Soldering temperature	270°C	300°C
Length x Height x Thickness	2.0 x 1.25 x 1.1 mm	2 x 1.25 x 1.2 mm

Dimensions of the top, side and back views in mm (inch).

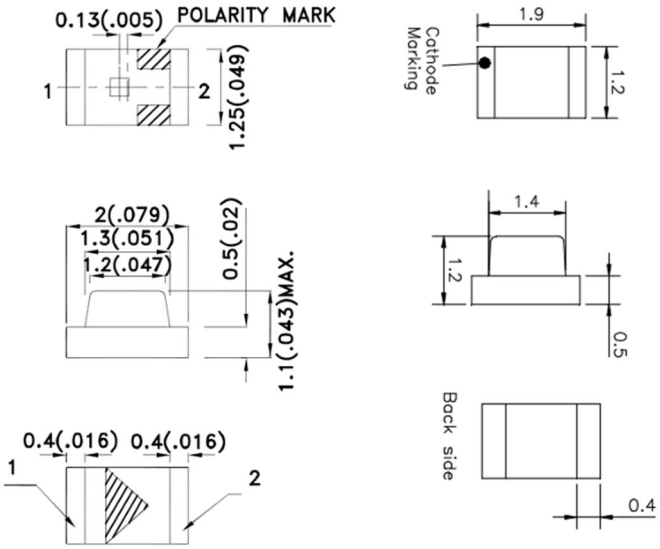

Table 6-2
Optoelectronic characteristics of the chosen Photodetector

Model	TEMD5020X01
Reverse Voltage	60 V
Max Reverse Current	30 nA
Continuous forward Current	50 mA
Power Dissipation	215 mW
Capacitance	17-48 pF
Wavelength spectrum	430 to 1100 nm
Operating temperature range	-40 to + 100 °C
Soldering temperature	260°C
Length x Height x Thickness	5 x 4.24 x 1.12 mm

Dimensions of the top, side and back views in mm.

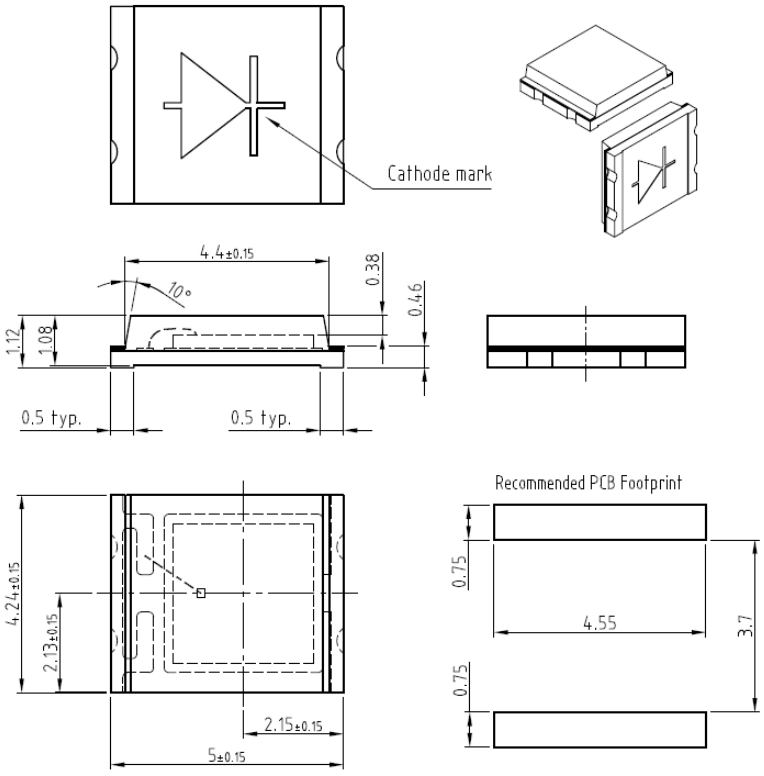

6.2.2 Connectors and Cables

The connectors of choice were the 9-way D-sub connector (**Figure 6-2b** and **Figure 6-2c**). Female connectors were mounted on the probe board in the PPG processing system (**Figure 6-2b**) and 1 m screened flexible PVC cable was used to join the probe

circuit with a male 9D connector (**Figure 6-2c**). The choice of the cable is of importance in the design of PPG sensors due to its capabilities of reducing interference.

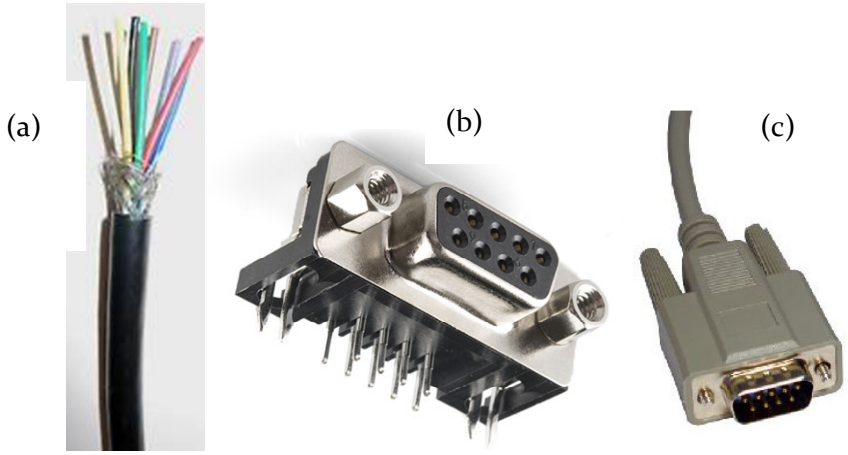

Figure 6-2
Cable and connectors. (a) cable used for probe connections. (b) D-sub connector fixed in processing system. (c) Probe D-sub connector.

The cable comprised tinned copper stranded conductors covered by 0.2 mm PVC, overall tinned copper braided screen with an outer black PVC sheath. The cable features a maximum working voltage of 250 V, a maximum current per core of 0.25 A and a core/Screen capacitance (nominal) of 85 pF/m and a resistance of 384 Ω/km per core.

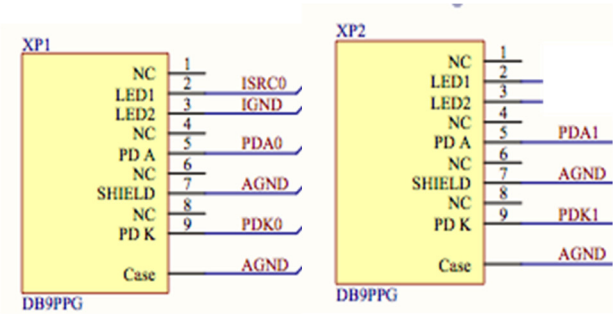

Figure 6-3
The probe input connectors mounted on the PPG processing System.

6.2.3 Mechanical Construction

The probe circuits were designed in Altium Designer Package (Altium, US) as seen in **Figure 6-4**. The distance between the centre of both LEDs and the Photodetector was maintained at 5 mm in order to provide a more uniform distribution of light (Webster, 1997).

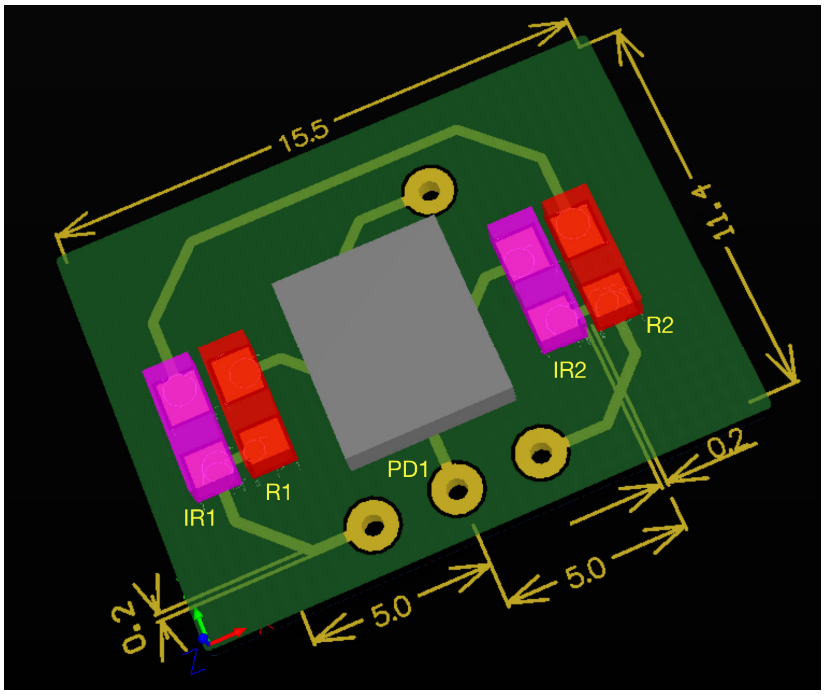

Figure 6-4
3D -view of the designed PCB of the reflectance finger probe showing both Infrared LEDs (IR1 and IR2) , both red LEDs (R1 and R2) and the PhotoDiode (PD1). The dimensions are stated in millimeters.

The Polychlorierte Biphenyle (PCB) circuit of two identical finger probes was etched by photoengraving, by using a photomask in order to remove the photoresist coating selectively. The chemical etching is done in an acid bath of ferric chloride at 40 °C. And the copper tracks are tin plated in a tin sulphate saturated solution for few minutes. The boards were cut, and the holes were drilled. The chosen components were soldered in the oven at two stages (100°C for 1min, and 120 for the 30s). The boards (10 mm x 6 mm) and were then coated with medical grade epoxy resin (Dymax 141-M, Dyamx, US) and cured in UV light, in order to produce a smooth surface and protect the optical components of the probes when getting into direct contact with tissue. Also, epoxying the probes made them water resistant. The probe PCBs were soldered to the 9D-connectors via the 9-core cable as described in the previous section. Faulty commercial pulse oximetry clips (Masimo, US) were obtained from a hospital and reused to host the probe PCBs, where the probes can fit the finger comfortably and without causing significant pressure.

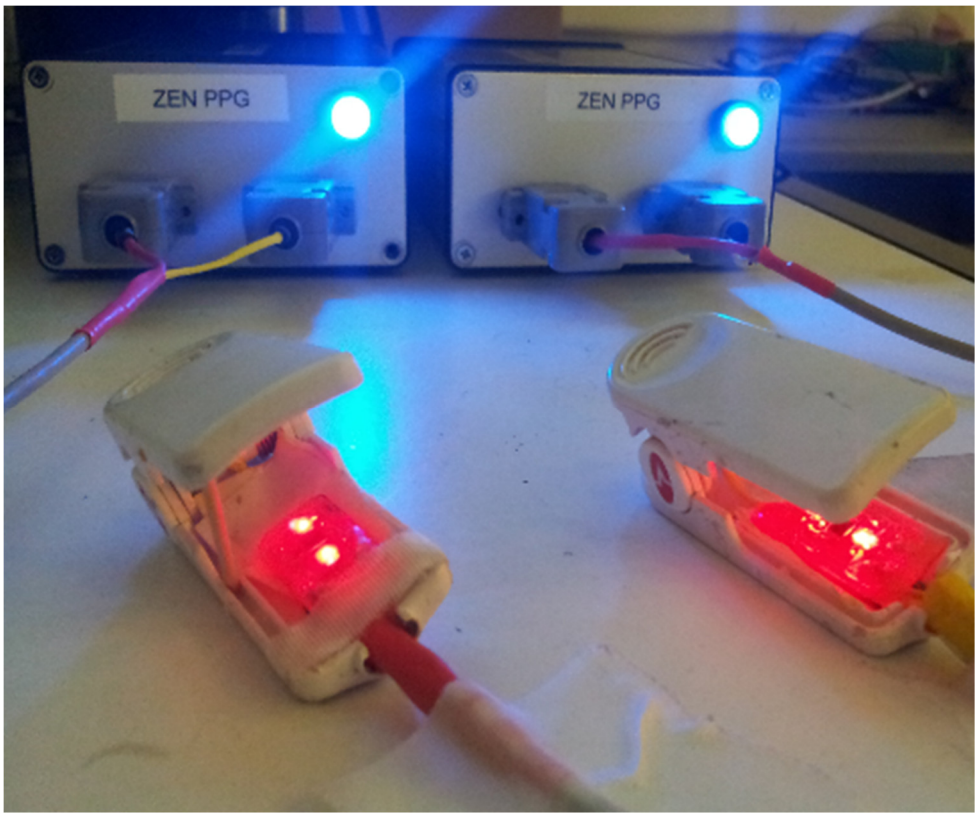

Figure 6-5
A picture of the assembled finger reflectance PPG probes operating while each is connected to a PPG processing System.

6.2.4 Performance Evaluation

The functionality of the finger probes was tested in the laboratory. The PPG finger probes were connected to the PPG processing system (which will be described in detail in the next chapter) via the 9-way D-sub connector. The processing system allowed control of the current source used to drive the red and infrared emitters. The optimum current source was found to be at 25 Ma, which provides sufficient illumination for a good-qaulity signal and does not result in the saturation of the photodetector. A trans-impedance amplifier is used to convert the output current of the photodetector into a signal voltage and a PPG pre-amplification and low-pass filtering stage with a cut-off frequency of 40 Hz. The output of the PPG processing system was connected to a virtual Instrument on a personal computer, implemented in LabVIEW (National Instruments, US) which will also be described in more detail in the next chapter. Red and infrared PPG signals were obtained, displayed and recorded on the computer screen by clipping the PPG probe on the index finger. The PPG signals (**Figure 6.6**) were of good quality, with amplitudes ranging between 2 mV and 20mV and high signal-to-noise ratio (SNR).

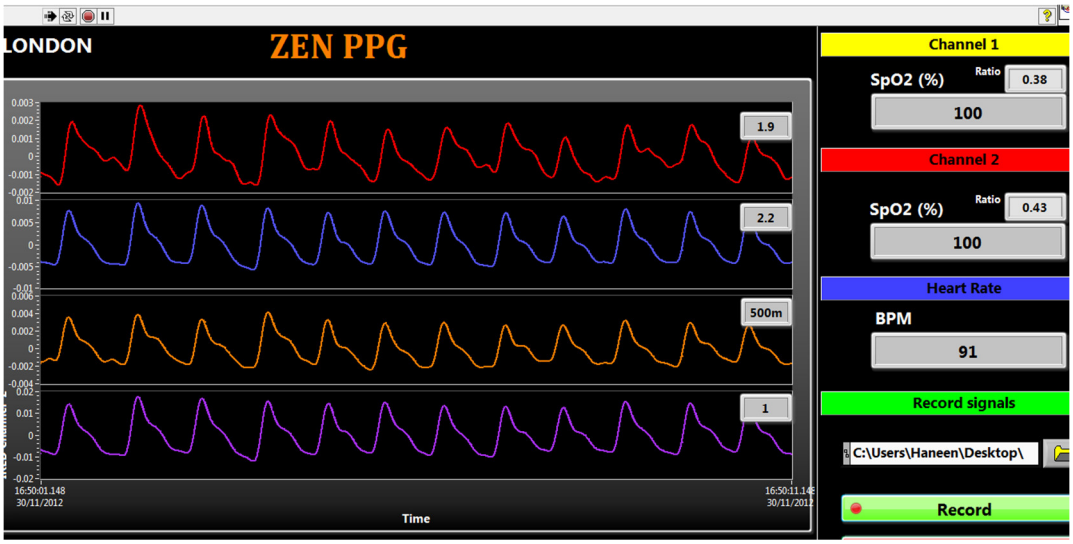

Figure 6-6
Evaluation of the finger probes, stacked charts for reflectance red and infrared PPG signals are shown. Inverted PPG_{AC} for one finger probe on the top two charts. PPG_{DC} levels are shown, on the upper right of each chart, as an average and is updated every five cycles. Blood oxygen saturation (SpO_2) and heart rates (Beat per Minute) are shown on the right side of the screen.

6.2.5 Temperature Tests on Finger Probes

The finger probes were designed for use in a cold pressor test. This requires the volunteer to clip the finger probes on the index fingers on each hand and undergo an immersion of one hand in an ice bath. The probes were designed to maintain their functionality in water and at low temperatures. Temperature tests were conducted to investigate the performance of the finger probe during an ice immersion.

6.2.5.1 Design and Development of the Temperature Measurement System

Two identical TSD202A (BIOPAC Systems, Germany) sensors were connected in a temperature linearization circuit.

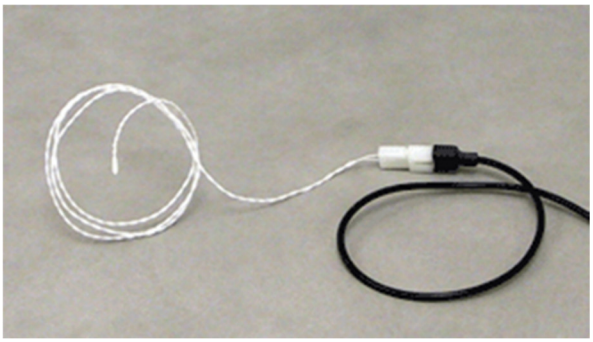

Figure 6-7
Picture of the TSD202A Thermistors implmented to use in the volunteer expirements .

The TSD202A seen in **Figure 6-7** employs a fast response thermistor with a response time of 0.6 seconds and is appropriate for use in locations where temperature changes rapidly. The thermistor can be useful for measuring skin temperature and be attached using medical tape on the surface of the skin. However, the thermistors need to be calibrated as will be described in the next subsection. The choice of the resistors used included an experimental part by multiple calibration processes in determining the minimum and maximum output voltages corresponding to the change in temperature.

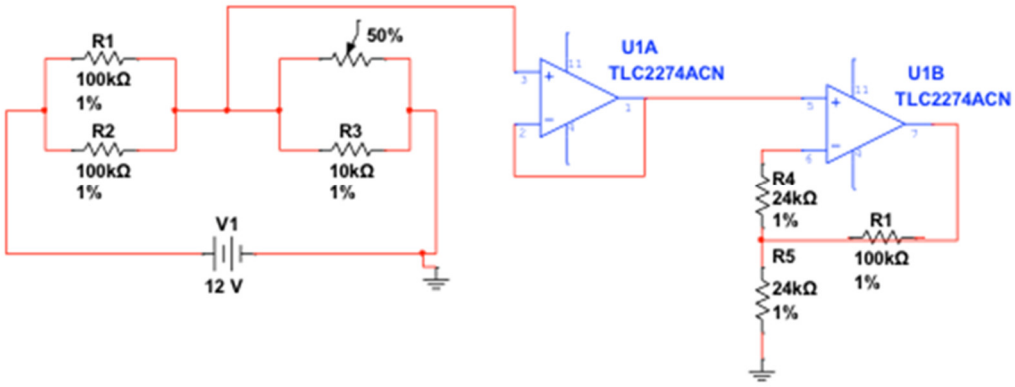

Figure 6-8
Schematic of the temperature System, connected to the thermistor (variable resistor) and fed into the linearization circuit.

6.2.5.2 Thermistors Calibration

Thermistors were preferred for their advantage of a very high sensitivity to temperature changes over thermocouples, but the disadvantage of a nonlinear characteristic can be a limitation. This limitation was resolved by calibrating both thermistors using a constant climate chamber.

In the constant climate chamber (BINDER GmbH, Germany), the environmental parameters can be controlled. In this case, the chamber was set to warm up, starting from 4 °C to 39 °C with constant temperatures for five minutes for each one degree. The data was sampled at a 10 Hz rate and saved to a tabular text file using a virtual instrument implemented in LabVIEW.

A Matlab code was developed to import the saved sampled data and filter the obtained data with a Butterworth 2nd order lowpass filter at a cut-off frequency of 5 Hz. At each step (5 minutes at each degree), the average of the middle 3 mins is extracted to provide a linear equation for each thermistor.

The temperature-voltage conversion linear fit can be seen in **Figure 6-9** for both thermistors.

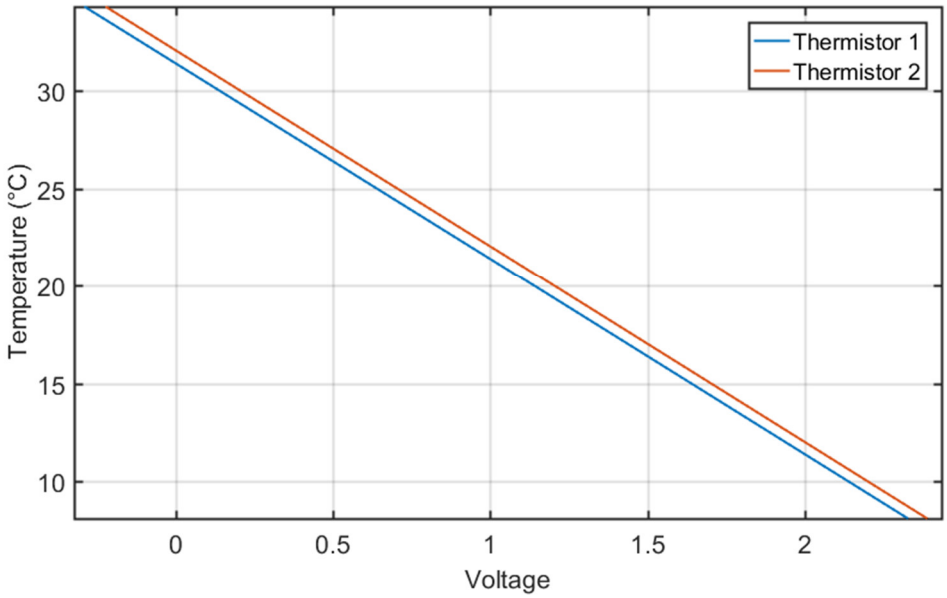

Figure 6-9
Plot of measured temperatures versus measured voltages as obtained from the temperature control chamber for both thermistors.

The resulted linear and non-linear equations for the temperature in Celsius degrees in relation with the delivered voltage was generated: The measurement system is capable of detecting temperature values with an accuracy of 1 °C in the desired range of 4 to 39°C, corresponding to a range of voltages between 0.20-2.5 V.

6.2.5.3 In vivo measurements

In vivo measurements were also made in a normal healthy volunteer. The finger probes were placed on the index finger. The thermistors were attached to the inside corner of the PPG probes. A baseline reading was established for 2 mins and then the volunteer underwent an ice immersion of the right hand. After the immersion, the recording continues for 10 minutes. Each PPG probe was connected to a PPG processing system and then connected to a virtual instrument designed in LabVIEW to display the PPG and the temperature signals obtained. The signals were recorded for further analysis. A typical set of the data obtained is shown in **Figure 6-10**.

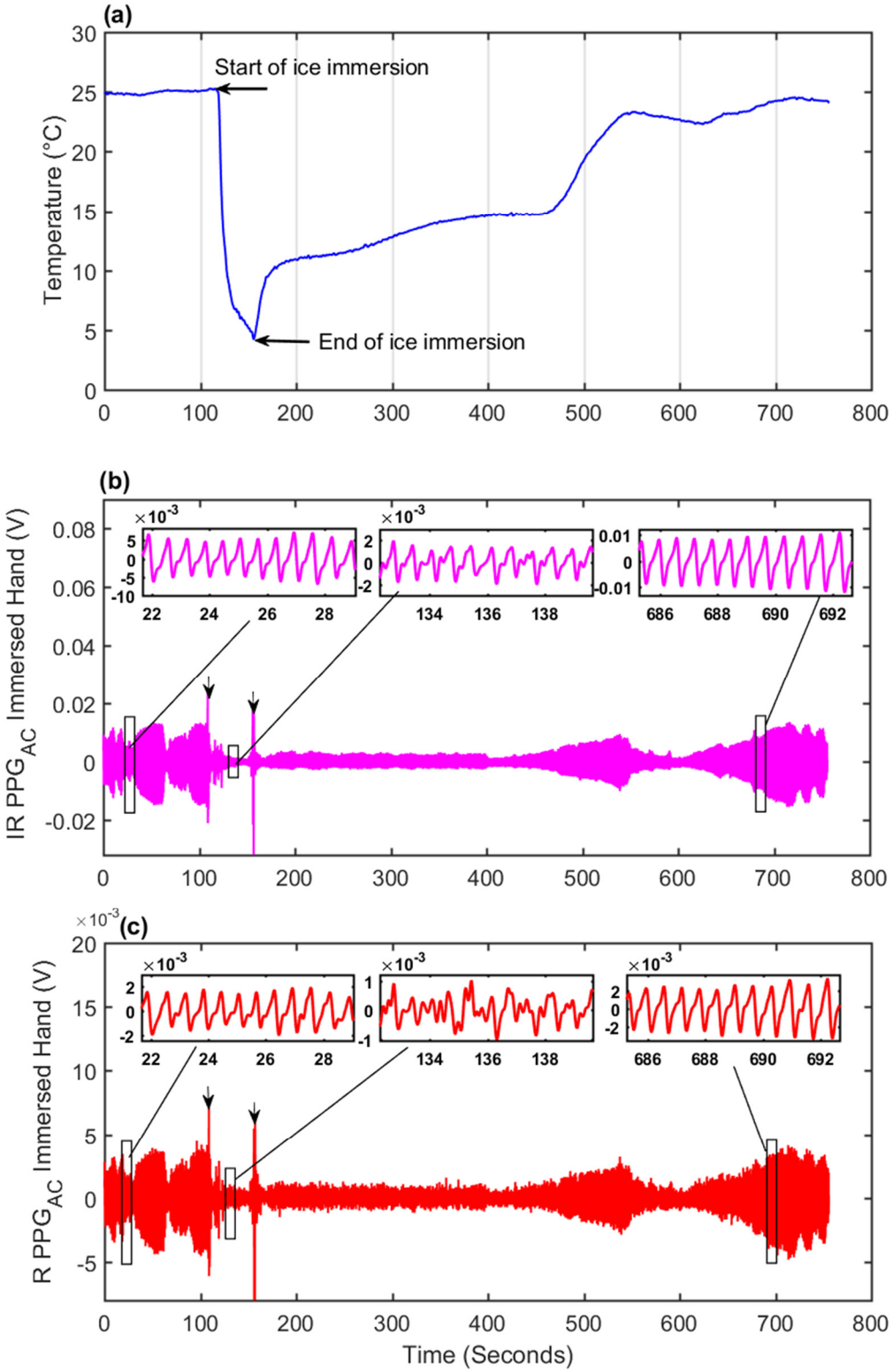

Figure 6-10
Typical set of data obtained from an in vivo investigation during the immersion of the right hand in ice for 30 seconds indicated with black arrows. Magnifying figures show a close-up during the three stages, before, during and after ice immersion. (a) Temperature signals. (b) Infrared AC PPG signals and (c) Red AC PPG signals.

This experiment has established that the PPG probes perform properly during the ice immersion. After the immersion, the PPG signals have returned to normal amplitude and

morphology emphasising that any changes during the immersion are due to physiological changes and are not in any way related to the altered performance of the probes.

6.3 Tube Probes

Two identical reflectance tube probes were designed in Altium Designer Package as seen in **Figure 6-11**. The two tube probes comprised of the surface mount optical components as follows: one RED and one IRED as described in more detail in Table 6-1, and one photodetector as previously described in **Table 6-2**. The distance between the emitters and the photodetector was also maintained at 5 mm (Webster, 1997) as can be seen in **Figure 6-12.**

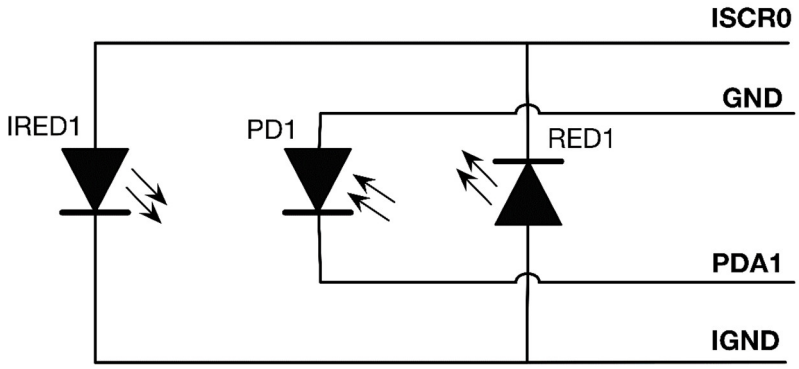

Figure 6-11
Circuit diagram of the optical components for the tube PPG probe.

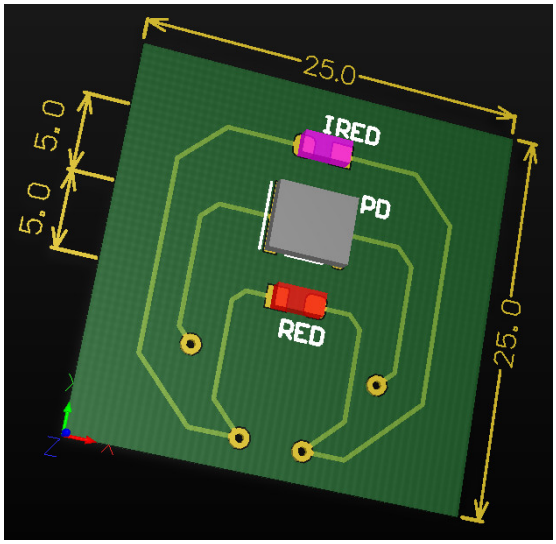

Figure 6-12
3D View of the PCB circuit design of the tube probe showing the configuration of the optical components. Infrared Emitting Diode (IRED), Red Emitting Diode (RED) and the PhotoDiode (PD). All dimensions are in mm.

6.3.1 Mechanical Construction

The circuits of the tube probes were printed using CNC engraving machine (LPKF). The PCBs were then coated in medical grade epoxy resin (Dymax 141-M, Dynmax, US) and cured in UV light, for water-resistance tube probes. The MakerBot Replicator (MakerBot, US) allowed the manufacturing of the designed encasing using Acrylonitrile Butadiene Styrene (ABS) black filament. **Figure 6-13** shows the final 3D design including the PCB and the plastic encasing using SolidWorks (SolidWorks, US). **Figure 6-14** shows a close-up photograph of the complete design of the two identical reflectance tube probes.

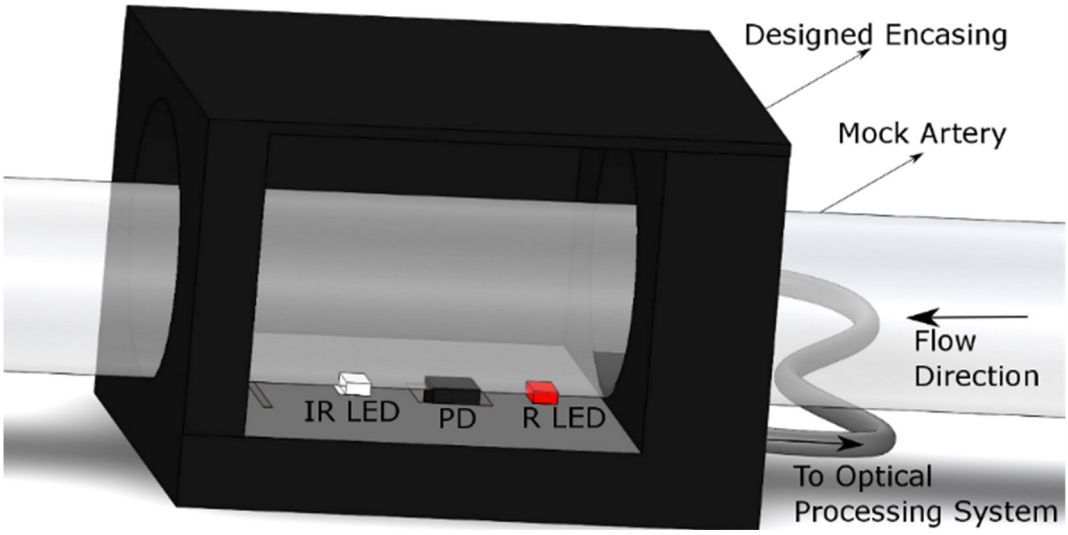

Figure 6-13
3D design of the tube probe PCB and the 3D designed encasing. Showing Infrared LED (IRLED), Red LED (R LED) and a photodetector (PD).

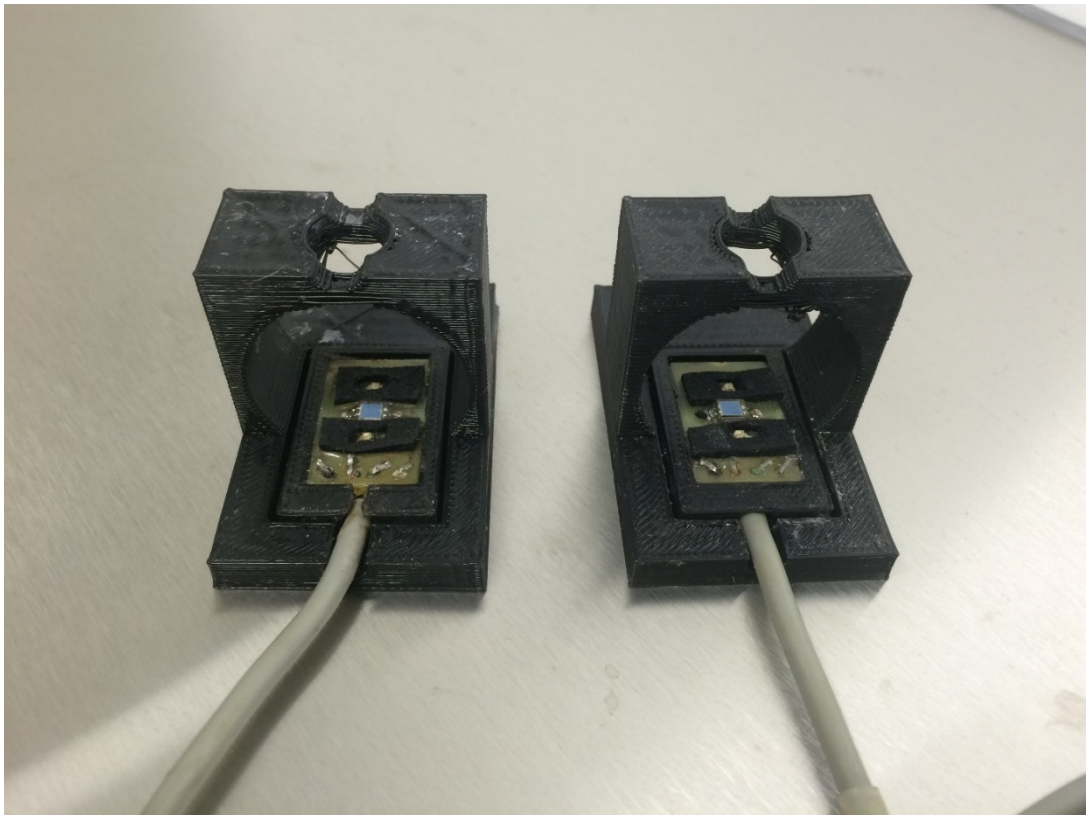

Figure 6-14
Picture of final two identical tube probes manufactured and assembled.

6.3.2 Tube Probes Evaluation

In vitro simulations were made to evaluate the performance of the tube probes. The *in vitro* setup comprised of a pulsatile pump (Harvard apparatus, US), a custom-made reservoir and a model of the artery using a flexible PVC tube with an 8 mm diameter. A more detailed description of the full *in vitro* setup can be found in **Chapter 9**. The tube probes were fitted on the arterial model and allowed minimal contact during the expansion of the tube. Each PPG probe was connected to a PPG processing system and then connected to a virtual instrument designed in LabVIEW to display red and infrared reflectance PPG signals. The infrared and red PPG signals were recorded for further analysis. The data were filtered to extract the AC and the DC components. Pressure signals were also recorded as a reference to the signal frequency and morphology. A typical set of the data obtained is shown in **Figure 6-15**.

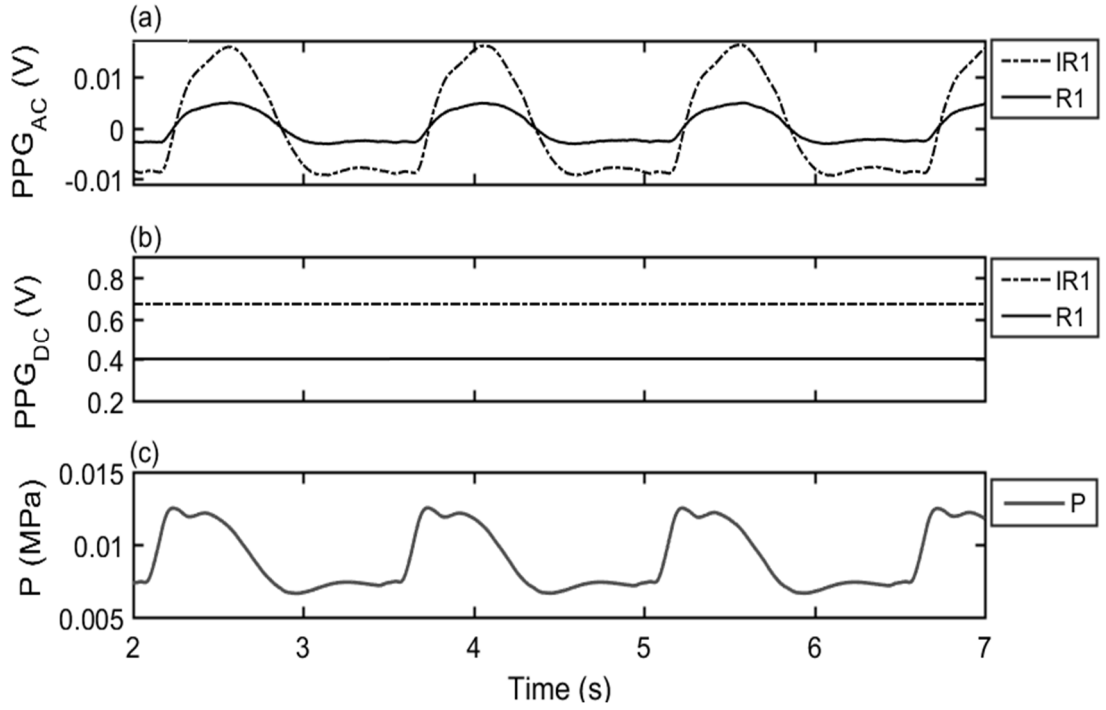

Figure 6-15
A 5-second capture of the collected signals at a stroke volume of 30 ml and a frequency of 0.67 Hz. Panel (a) presents PPG_{AC} components for Red (R) and InfraRed (IR) signals. Panel (b) presents PPG_{DC} levels for R and IR signals, and panel (c) shows pressure signals (P).

This brief experiment confirmed that the tube PPG probes provide high-quality red and infrared PPG signals and are synchronised with the pressure signals. Despite this synchronisation, PPG and pressure signals differ in the morphology due to the fact that that one is optical and the other is mechanical. Different factors affect each of these signals and hence, though are synchronised and have similar patterns, they obtain different morphologies.

SUMMARY

This chapter presented the design, development and evaluation of the finger and tube reflectance PPG probes. The former will be used in an *in vivo* investigation further discussed in Chapter 8, and the later will be used in the *in vitro* investigations (Chapter 10-13). All developed probes operate successfully within expected parameters producing good quality PPGs at both wavelengths.

The next chapter will discuss the design and development of the PPG and ECG processing systems, the data acquisition system, and the offline analysis Matlab script.

Chapter 7
DEVELOPMENT OF THE PPG PROCESSING SYSTEM

7.1 Introduction

The previous chapter has focused on the design and the development of the PPG finger and tube probes that will be used in the *in vivo* and *in vitro* experiments. This chapter will target the technical design and development of the PPG processing system, the data acquisition system designed to collect, display and record the data, and the offline data analysis script prepared for data and statistical analysis.

The designed PPG processing system was simulated and routed using Altium Designer Package (Altium, US). The system is constructed to pre-process, record and display raw PPG signals from two channels, for two wavelengths on a personal computer. The development process will be described in the mechanical design section, and the functionality of the system will be discussed in the hardware section. The system offers many advantages as a dual channel, two-wavelength system. It is convenient to customise the system for specific functions. The system is split into separate boards, containing surface mount components, a programmable microcontroller, adjustable capacitors and resistors on the trans-impedance board that allow gain control, and control of the driving currents in both channels. It also has the capability to continuously monitor some of the major parameters (e.g. Battery Voltages, LED driving current). Moreover, it is compatible with the commercial and custom-made probes, which makes it ideal for experimental set-ups. A block diagram of the system is presented in **Figure 7-1**.

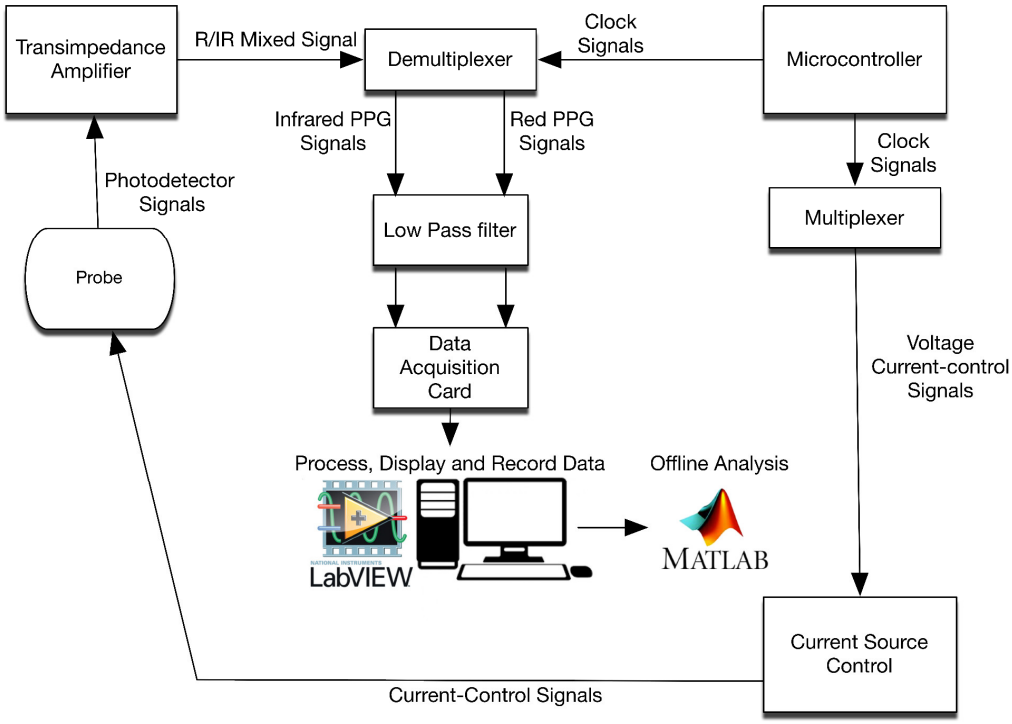

Figure 7-1
Block diagram for the PPG processing system showing connections for one channel/probe.

7.2 Mechanical Description

The circuit of the PPG processing system is divided into 6 Printed Circuit Boards (PCBs). The 2-sided boards included the power board, the core board, the current source board and the trans-impedance board. Each of the mentioned boards had a through-hole right

angle 50-way male header (TSW-125-08-X-D-RA, Sametc Inc.) that allowed them to be assembled on the assembly board. The assembly board or the bus board consists of six 50-way SAMTEC surface mount female connectors (SSM-125-X-DV, Sametc Inc.). The core board included the (68 pin NI 6035E-6036E) as a port for the data acquisition card connection. The final device picture and 3D design are presented in **Figure 7-2** .

The development process of the system can be divided to printing the boards and fixing the components as following:

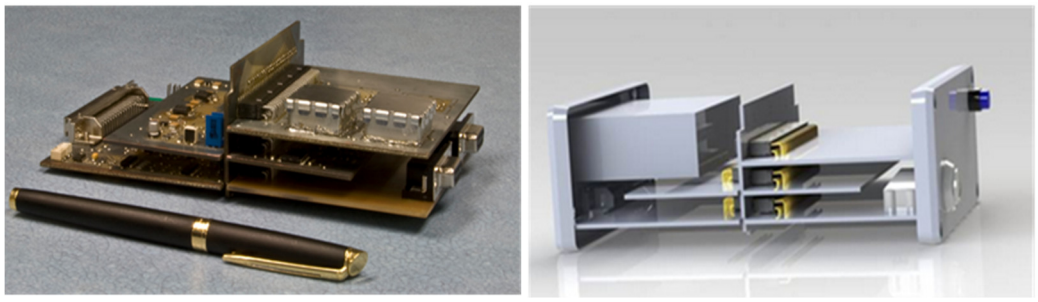

Figure 7-2
Mechanical Description of the ZEN PPG System. (a) Picture of the final designed PPG processing device and (b) 3D design of the PPG processing system using SolidWorks.

7.2.1 Boards Printing

Using the CCD/2 CNC machine, each of the boards was routed and the holes were drilled, and finally the board was cut. Each board was scrubbed and plated using dissolved Seno immerse tin powder. The drilled holes were filled manually using a metal wire to connect the bottom and the top layer of the two-sided boards (known as vias).

7.2.2 Component Fixing

The stencils were designed using CAD software, which was printed on plastic 2 mm thick paper, using the CCD/2 CNC machine. Each board was fixed into a wooden window, to make it accessible on both sides, the stencil sheets were also aligned on the top and if needed the bottom layer of each board. Solder paste (RA10, Multicore, US) with melting temperature of 179°C was brushed on the stencil sheets, covering the pads of the components and the tips of the vias on both sides. The wooden window and the stencils were removed. Most of the electrical components were aligned on the boards, and each board was baked in the oven for two stages (80 °C for 1:00 min, and 180°C for 1:30 mins) which matched the threshold for all the used components. The remained components, mostly with lower temperature threshold (e.g. connectors, the switch, and the battery casing) were soldered manually. The PPG processing system was assembled and evaluated.

7.2.3 Device Assembly

The bus board, used as a double assembly layer, can handle up to 300 pins, 50 for each board (SSM-125-X-DV, Sametc Inc.) which can be seen in **Figure 7-3(a)**, accompanied by the core board 50 through-hole gold plated header (TSW-125-08-X-D-RA, Sametc Inc) seen in **Figure 7-3(b)**) and the (NI 64-pin, seen in **Figure 7-3(c)**) connector connecting the core board to the computer using a suitable NI DAQ-card.

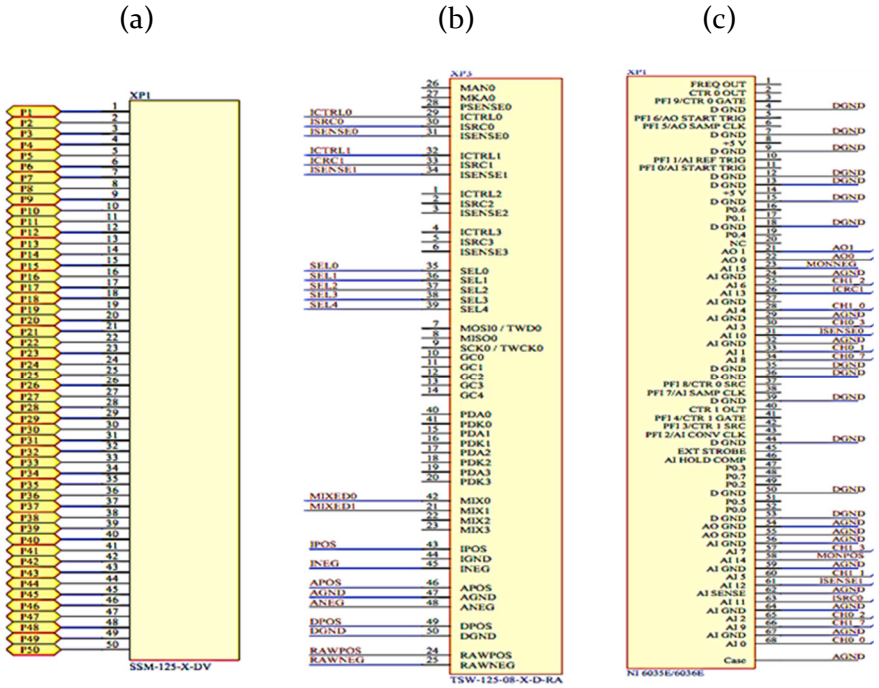

Figure 7-3
Connectors used in the PPG processing system. (a) bus board female connector SSM-125-X-DV (b) the male through-hole gold plated header (TSW-125-08-X-D-RA) used for all other boards (c) single 68-pin connector for the data acquisition card terminal. The connectors show net label names and locations.

7.3 Hardware Description

7.4 The Power Supply

The system is powered by dual 9 V batteries, connected to the power board with a 3 header connector (281695-3). Using +5 V, -5 V, +3.3 V, -1.4 V voltage regulators (MC78M05CDTG, MC79M05CDTG, On Semiconductor, US), (MCP1703T-3302E/CB, Microchip Technology, US) and (LT1964ES5, Linear Technolgoy, US) respectively. The former two voltages (net labels: IPOS, INEG) were generated to be used for multiplexing and driving the LED currents. The latter two output voltages (net labels: APOS, ANEG)

were used to power all the analogue chips on the trans-impedance and core boards. An extra +3.3 V voltage regulator was used to generate the voltage supply (net label: DPOS) to operate the microcontroller (Atiny313, Atmel, US) on the core board. The circuit design for the power supply is shown in **Figure 7-4**.

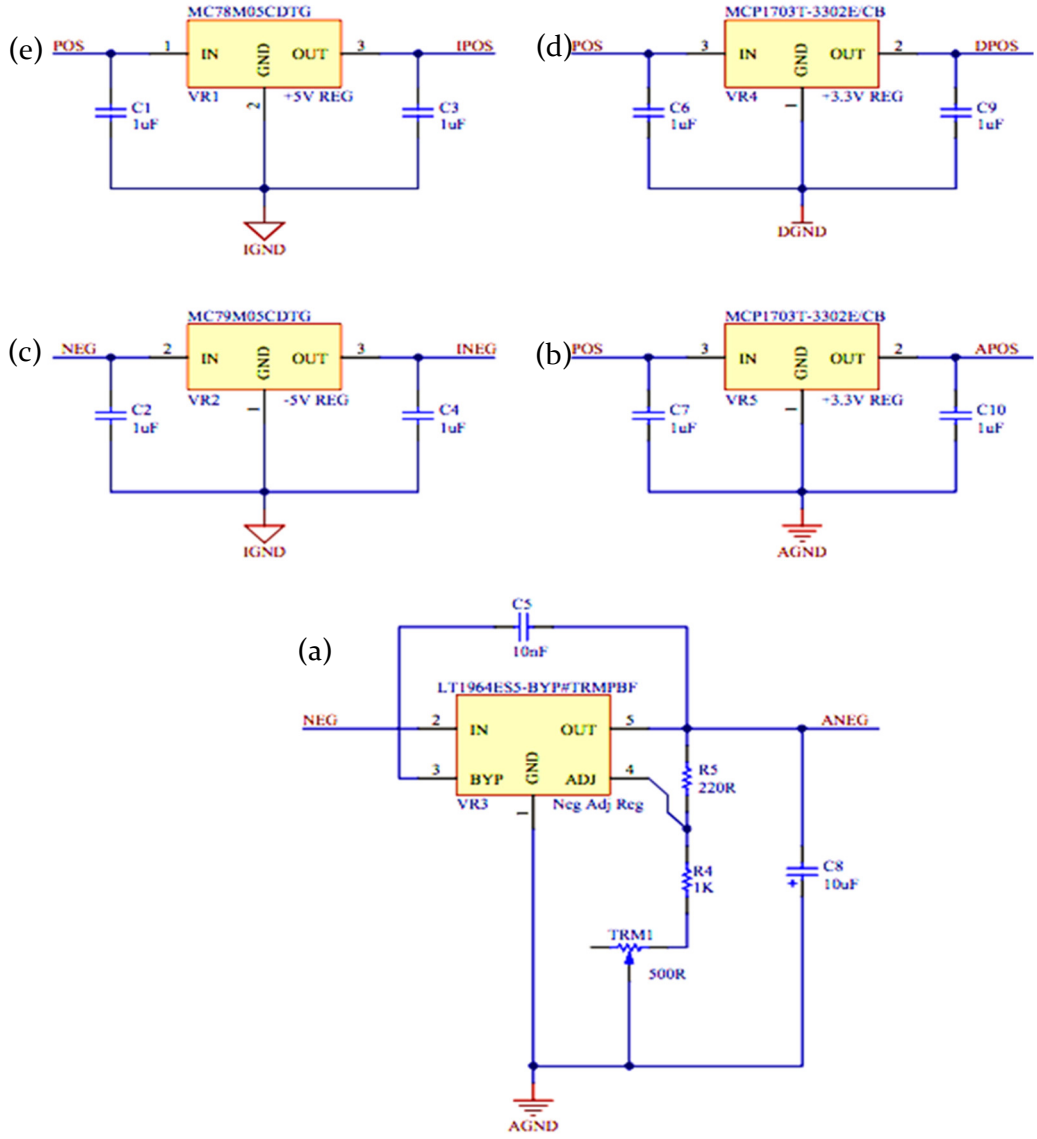

Figure 7-4
The circuit design of the power board showing voltage regulators, passive components, and net labels.(a) circuit outputing net label IPOS, a voltage of 5 V, (b) circuit outputing net label INEG, avoltage of -5 V, (c) circuit outputing DPOS, a voltage of 3.3 V, (d) Outputing APOS , 3.3 V and (e) an adjustable circuit designed to output ANEG, 1 V

7.4.1 The Input Channels

The probe board, provides two input channels via a standard D-9 connector, using the same commercial pin configuration for LEDs and photodiodes. The input photocurrents from each photodiode (2 channels for each box) are converted using a trans-impedance

amplifier (OPA380, Texas Instruments, US) for each channel. The outputs are two mixed voltage signals for both Red and Infrared photocurrents, obtained from the photodiodes.

First, those voltage signals are converted to current signals (net labels: MIXED00, MIXED01). In order to create an ideal current source, the voltage across the load is to be adjusted to zero. This is achieved using the trans-impedance amplifier, outputting the mixed signals for each channel (connected to the photodiode) from each trans-impedance amplifier. This output is passed (again through the bus board) to the demultiplexing operation using the multiplexer/demultiplexer MCT4051BDG (ON Seminconductor, US) to split the Red and Infrared signals, and as synchronised with the master clock operated by the microcontroller.

7.4.2 The Transimpedance Amplifier

Transimpedance amplifiers are usually operated at very high gain. This produces a strong tendency for the amplifier to go into oscillation at some high frequency above the gain bandwidth cutoff. This problem can be eliminated by adding a small capacitor in the feedback loop, which lowers the gain at very high frequencies. The trans-impedance amplifier circuit design can be seen in **Figure 7-5**.

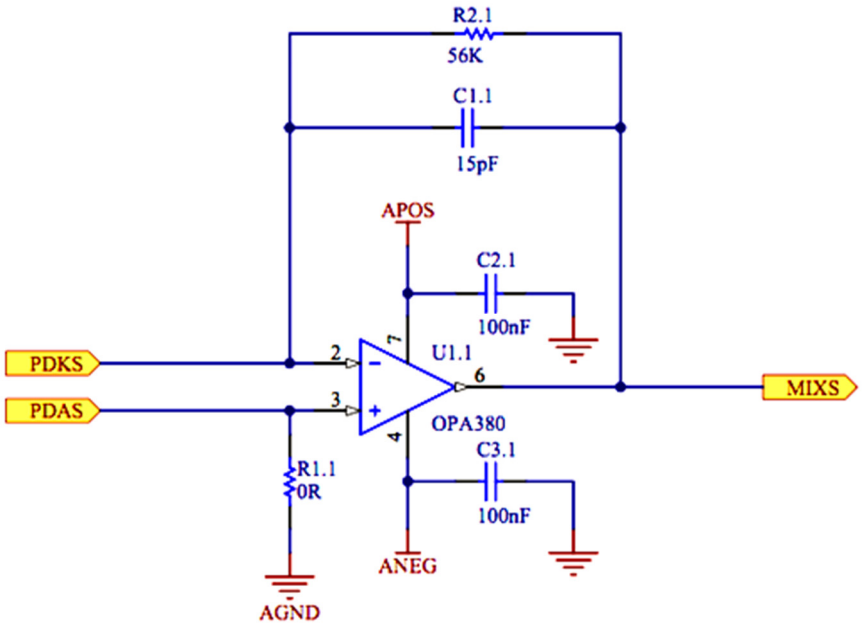

Figure 7-5
The Transimpedance Amplifier design for one channel, located on the Transimpedance board. Showing net labels, Photodetector cathode (PDKS) and photodetector anode (PDAS). The output signals is the mixed red and infrared PPG signals (MIXS).

The gain of the trans-impedance amplifier is proportional to the feedback resistor, which can be adjusted by replacing R2 and C1 (pinned components) to avoid saturation.

The negative feedback amplifier will provide gain stability, linearity, frequency response, step response and reduces sensitivity to parameter variations due to manufacturing or environment. Because of these advantages, negative feedback is used in this way in most of the gain configurations.

The PPG processing system provides the flexibility of controlling the LEDs driving current. However, the determination of the current for both channels can be controlled separately, digitally-configured for *Channel 1* and manually-configured for *Channel 2*. The difference in both channels is due to the limitation of the data acquisition card that is limited to two analogue outputs.

7.4.3 The Driving Current in Channel 1

In *Channel.1*, analogue voltages are generated in a virtual instrument implemented in LabVIEW of a maximum of ±5V which is passed into the core board (using the DAQ-card port 64 NI connector). At the core board, the analogue voltages are fed into the attenuator (See **Figure 7-6**), to provide an output of +1 V (net label: ICPOS0) and -1 V (netlabel: ICNEG0).

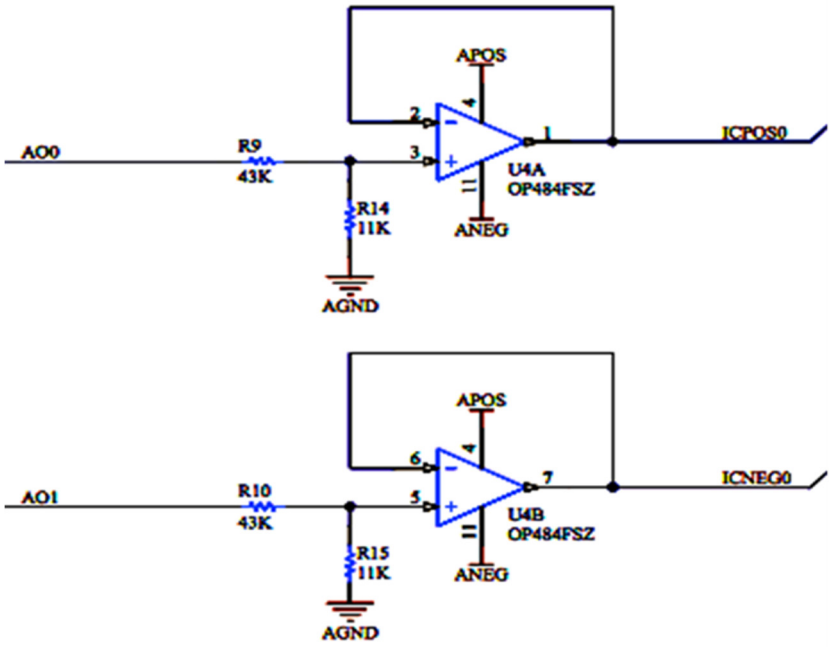

Figure 7-6
Circuit diagram of the Attenuator using the operational amplifier OP484FSZ, located on the core board. The circuit recieves an analogue signal outputed from labview tp generate current-signals (ICPOS and ICNEG).

7.4.4 The Driving Current in *Channel 2*

In *Channel 2*, the driving current is controlled manually using trimmers (component labels: R20, R18) on the core board. The V_{ref} is generated using the high precision, low noise, low dropout voltage reference, packaged in the LM4140 (Texas Instrument, US). The LM4140 is designed to combine high accuracy, low drift and noise with low power dissipation in this small package. Providing a choice of output voltages 1.024 V and 1.250 V. Where V_{ref} is set to 1.024 V in this application as seen in **Figure 7-7**. V_{ref} is then fed into the Op-amp (OP484FSZ, Analog Devices, US) , which is used as a comparator (comparing V_{in} with V_{ref}) as seen in **Figure 7-8**. The trimming attenuator outputs +1 V (net label: ICPOS1) and the trimming inverting attenuator outputs -1 V (net label: ICNEG1).

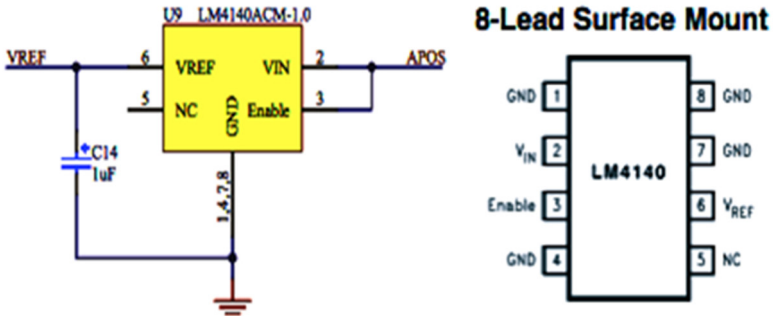

Figure 7-7
Schematics of the voltage-controlled current-generator circuit on the current source board.

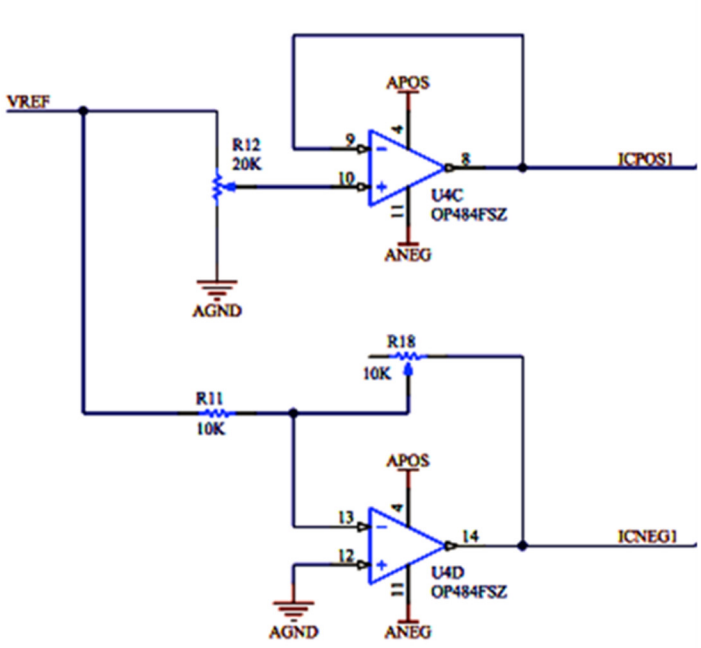

Figure 7-8
Circuit diagram of the manually configured trimmers used with the OP484FSZ with ±1 V Attenuator to output the current signals (ICPOS1 and ICNEG1).

7.4.5 The Current Limiters

The outputs of all attenuators are current signals ,positive (POS)_and negative (NEG) (net labels: ICPOS0, ICPOS1, ICNEG0, ICNEG1) are passed through the multiplexer (MC14052BD, ON Semiconductor, US), located on the core board. The multiplexer outputs the two identical current signals that drive the REDs and IREDs. This is essential to distinguish between the different wavelengths of light in the photodetector signal, as the two LEDs are alternately switched on and off as will be described in more detail in section 7.4.7. The two identical current signals (net labels: ICRTL0 and ICTRL1) are then fed to the current source board.

In the current source board, an operational amplifier is used as a voltage-controlled current generator circuit the so-called Howland current source, which is modified with an NPN-PNP transistor (PMD3001D, NXP Semiconductors, US) component label: Q1 as seen in **Figure 7-9**, in order to limit the voltage. The current source inputs have two stable states, ON or OFF for each channel. In the ON (positive) case, the NPN transistor is active and switches one LED ON, and in the OFF (negative) case, the PNP transistor is active switching the other LED ON.

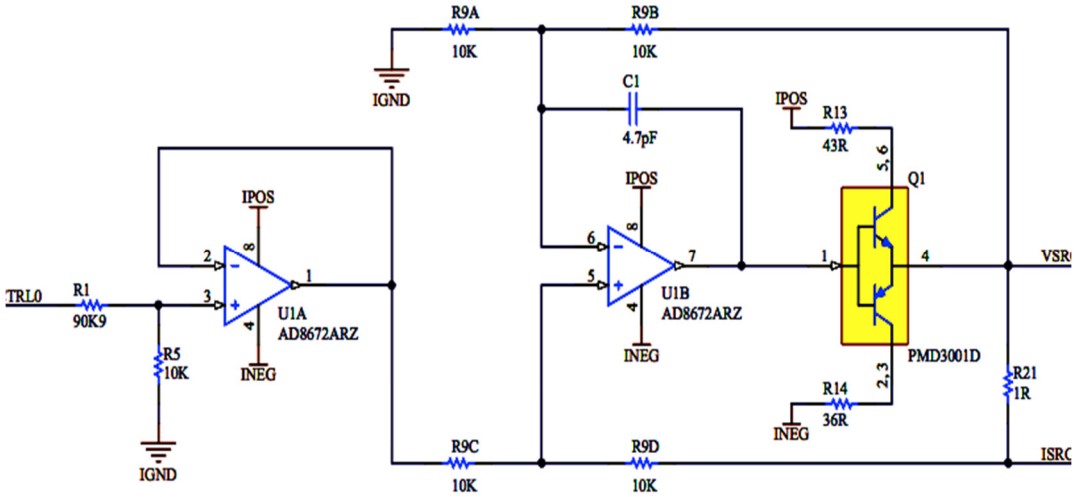

Figure 7-9
Circuit diagram of the Howland circuit (voltage controlled current generator) designed to alternate two LEDs on and off and never both on at the same time.

The transconductance coefficient (op-amp AD8672ARZ Analog Devices, US) is labelled as U1 and reduces the multiplexed ±1 V signals received from the core board to ±100 mV (See **Figure 7-9**), where the gain (G_m) can be calculated as $G_m = R_5/R_1+R_5 = 0.11$.

Those signals are then passed to the transconductance amplifier labelled as U1B, and U2B convert the voltage values to current. Feeding them into the instrumentation amplifier packaged in the INA2128 chip (Texas Instrument, US) and is labelled as U5A and U5B in **Figure 7-9**. The INA2128 is a dual, low power instrumentation amplifier that offers excellent accuracy (**Figure 7-10**).

The amplifier output voltage is the product of its output current and its load resistance. $R_{(G)}$ is allocated the value of 5k6Ω, as advised in the data sheet. Hence, the calculated (G) gain of the Instrumentation amplifier (G),

$$G = 1 + \frac{50k\Omega}{R_G}, \quad G = 10 \qquad (7.1)$$

The voltage gain is the output voltage (net labels: VSRCo or VSRC1) divided by the differential input voltages (net labels: ISRCo or ISRC1).

The output current is a linear function of the differential input voltage calculated as follows:

$$I_{out} = (V_{in+} - V_{in-}).G \qquad (7.2)$$

Where V_{in+} and V_{in-} are the voltages at the non-inverting and inverting input respectively, and G is the transconductance coefficient of the amplifier.

In the case of virtual inputs of 1 V at AC_0 and -1 V at AC_1, the attenuated and multiplexed current signal outputted (I_{out} , net label: ISENSE) would be I_{out} = 1 x 0.2 x 0.1 = ±20mA. I_{out} maximum value is 100 mA, on the occasion that V_{in} is +5 Volts.

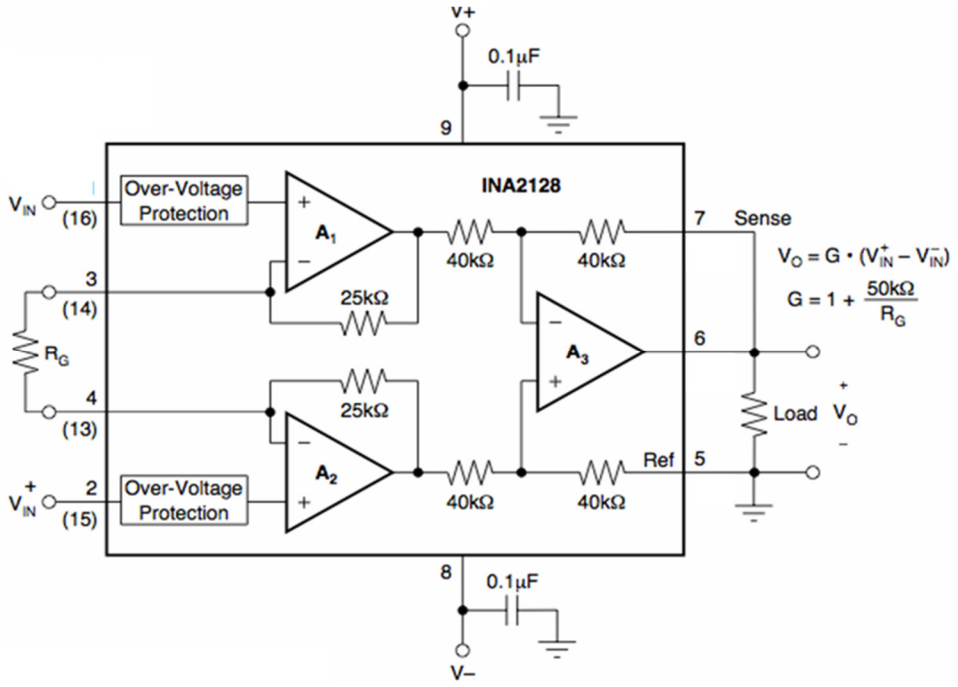

Figure 7-10
The Low-Power Instrumentation Amplifier (INA2128).

7.4.6 The Microcontroller

The chosen component was packaged in the Atmel ATtiny2313-20SU (Atmel, US), with a schematic seen in **Figure 7-11a**. The component uses the high performance and low power RISC architecture. The AVR microcontroller provides 2 Kbyte of in-system self-programmable flash, 128 Bytes of in-system programmable EEPROM, 128 Bytes Internal SRAM. The chip is located on the core board, supplied with ±3 V (net label: DOPS).

The microcontroller functions as a timing generator and the STK500 (Atmel, US) was connected to the microcontroller by the 6-pin ISP header located on the core board as seen in **Figure 7-11b**.

Using the AVR microcontroller interface (Atmel, US), the ATiny23313-202su is programmed to generate the digital signal at a frequency of 1000 Hz.

(a)

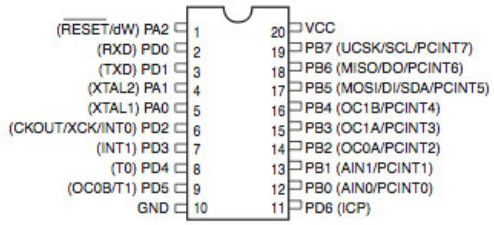

(b)

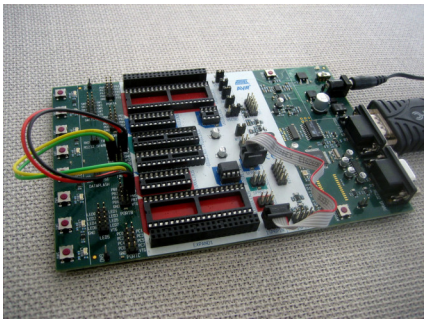

Figure 7-11
(a) Schematic of the Atmel ATtiny2313-20SU. (b) The STK500 connection PC-microcontroller.

7.4.7 Multiplexing

A multiplexer can be viewed as a multiple-input single-input device that allows many signals to share one device. The multiplexer of choice in the PPG processing system is the MC14052BD (On Semiconductor, US). The MC14052BD is a dual 4-channel analogue multiplexer with digitally-controlled analogue switches. The device features low ON impedance and very low OFF leakage current. The supply voltage range is 3 to 18 V. It features linearized transfer characteristics and low noise estimated at $12nV/\sqrt{Cycle}$.

The multiplexer was aimed to output a voltage control signal that will be fed into the current source to be converted to a current signal. The signals are synchronised with the microcontroller to allow driving the REDs and IREDs separately as each LED is alternately switched on and off. The signals determined digitally in Channel 1 (net labels: ICPOS0 and ICNEG0) and manually in Channel 2 (net labels: ICPOS1 and ICNEG1) are fed into the attenuator as previously described and then to the multiplexer. The signals are then synchronised with the programmable microcontroller. The clock signals in the microcontroller seen on the oscilloscope as labelled on the core board routeing map CMUX0 and CMUX1 are seen in **Figure 7-12**. The signals alternate at a frequency of 1000 Hz, with a 2.8 V maximum voltage.

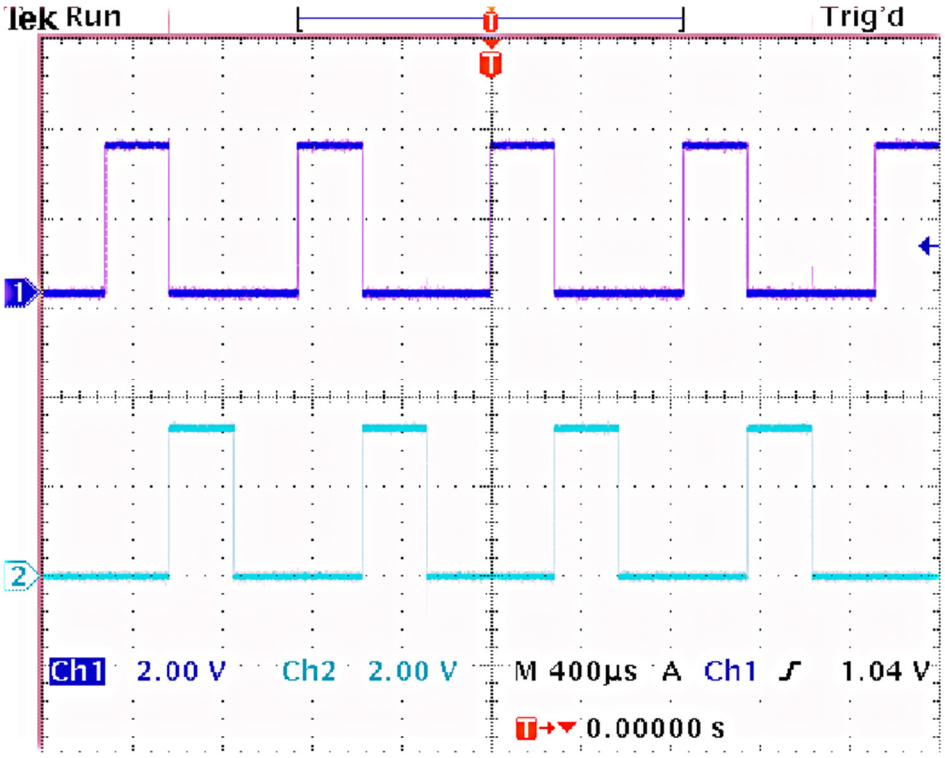

Figure 7-12
Clocks generated from the microcontroller as displayed on the oscilloscope CMUX0(top) and CMUX1(bottom).

The outputs of the multiplexer (net labels: ICTRL0 for channel 1 and ICTRL1 for channel 2) are seen in **Figure 7-13**. Each of those signals operates to alternate between red and infrared LEDs as the follows Red ON, both OFF, Infrared ON.

Both current control voltage signals will be fed into the transconductance coefficient in the current source board and finally converted to current. The current signals will also

be fed into the NI DAQ-connector to display the driving current values on the computer screen, using the virtual instrument (VI).

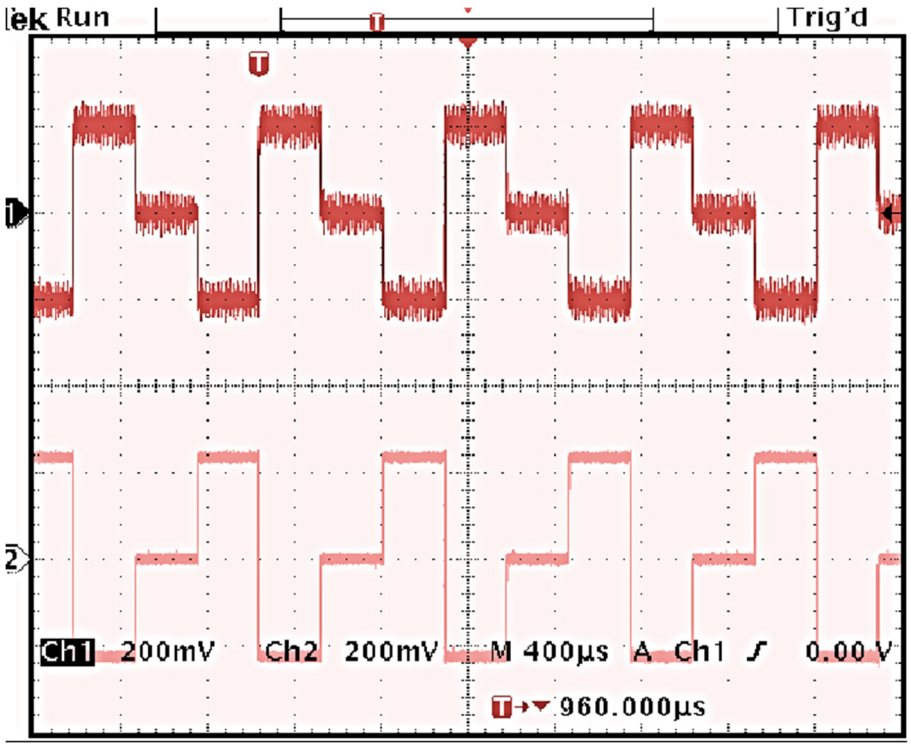

Figure 7-13
The outputted current control voltage signals form the multiplexer. ICTRL0 for *channel 1* and ICTRL1 for *channel 2*. 1/3 cycle Red ON, both OFF, Infrared ON.

7.4.8 Demultiplexing

The two identical demultiplexers (MC14051BDG) located on the core board, receive the input clock MUX0, MUX1, MUX2 from the master clock programmed in the microcontroller. The MC14051BDG bring the same features as the MC14052B but come packaged in a single channel and implements an SP8T solid-state switch. The function of the demultiplexer is to split the mixed input R/IR signal by simple-hold function.

The master clock programmed within the microcontroller controls the demultiplexer clocks for splitting the mixed PPG signal. The clock signals displayed on the oscilloscope screen can be seen as below. Each channel is assigned a demultiplexer. The demultiplexer outputs separated Red and Infrared signals. Those raw signals are then fed into the filters.

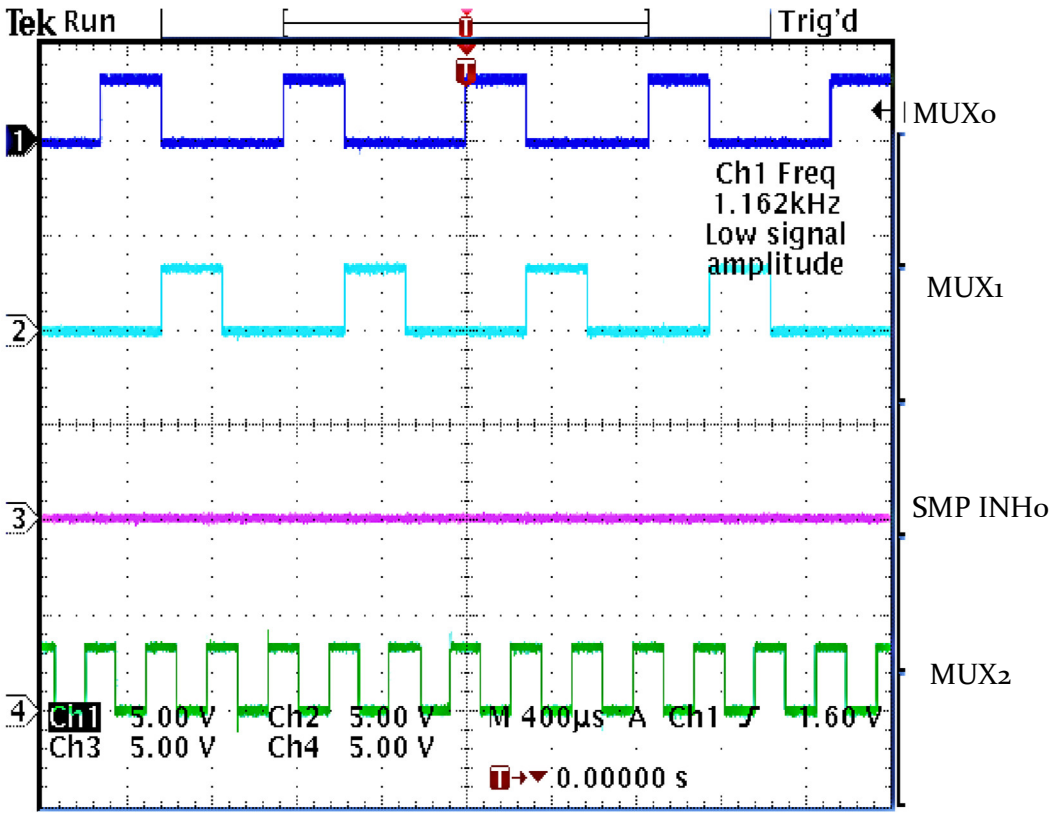

Figure 7-14
The clock signals generated by the programmed microcontroller that allows the performance of the sample-hold effect in the demultiplexer in order to split the mixed signal into raw red and infrared signals.

7.4.9 Low Pass Filter

A low pass filter (**Figure 7-15**) was then used to remove the high-frequency switching noise from the demultiplexed raw signals. The cutoff frequency was - $f_c = \frac{1}{2\pi RC}$ = 40Hz.

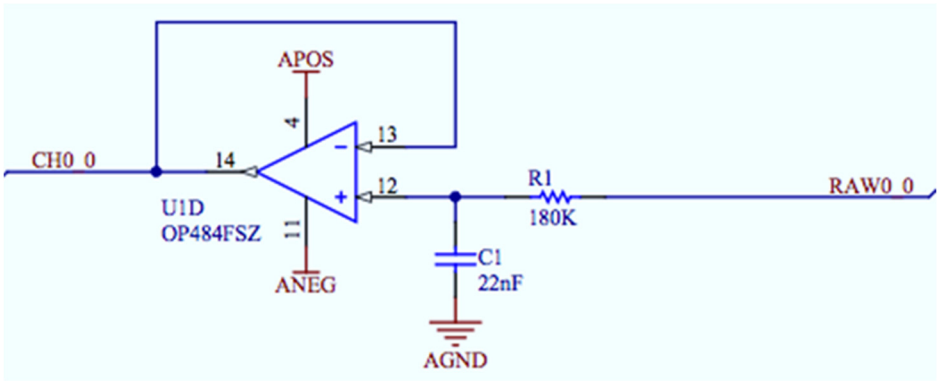

Figure 7-15
The schematic of the circuit design of the low-Pass filter with a cut-off frequency of 40 Hz used to filter the raw red and infrared signals.

7.5 Evaluation of the PPG Processing System

The PPG processing system has been evaluated first by monitoring signals from commercial probes. The in-house built probes were then evaluated using the PPG

processing system. The PPG signals have been continuously monitored and produce good quality signals.

The values of R2 and C1 on each channel of the trans-impedance amplifier on the core board were chosen by mathematical calculation and experimental tests in configuration with the in-house built finger probes and their saturation levels for optimum light distributions. The same gain values were maintained to use in the tube probes.

7.6 Design and Development of the ECG system

The design and development of this system were necessary for the first *in vivo* experiments. The need for an ECG signal to analyse PPG signals is vital due to the fact that the PPG signal provides heart rate pulsations from skin surfaces and the availability of the ECG signal might aid in the further understanding of the PPG behaviour. Recent studies are still investigating the possibility of PPG signals to be used for heart variability that provides information about the autonomic nervous system in an effort to perhaps replace the ECG signals as PPG signals are more easy and practical to be acquired (K Hamunen et al., 2012; Lu et al., 2008).

7.6.1 ECG System

The electric signal generated from the heart can be approximately represented as an electric dipole in the conducting medium of the thorax which is seen in the electrocardiograph signal. The common mode voltage on the body is sensed by the two averaging resistors, inverted amplified and fed back to the right leg. The precision instrumentational amplifier INA114 (Bur-Brown/Texas Instruments, US) provides, high CMRR (115 dB) and a very high input impedance ($10^{10}\ \Omega$). The R_G resistor was assigned to be 560 Ω, providing a gain of 90 to the instrumentation amplifier.

The resistor values for R_f and R_{in} were chosen to be 100 kΩ and 10 kΩ, respectively. By equation, this provides a gain of 10 to the output signal of the instrumentational amplifier. A bandpass filter was used to remove DC level and environmental artefacts. The high and low pass Sallen and Key filters were used.

The cutoff frequency for this filter configuration is given by

$$fc = \frac{1}{2\pi\sqrt{R_1 R_2 C_1 C_2}} \qquad (7.3)$$

For the high pass filter, the values of the resistors and capacitors were chosen as 1 MΩ and 1 µF for a cut-off frequency of 0.16 Hz. The low pass filter was chosen to have a cut-

off frequency of 40.83 Hz, with resistors and capacitors values of 3.9 kΩ and 1 µF.The bandpass filter is of unity gain with both resistors and capacitors of the same value, giving it a quality factor of 0.5.

The power supply for the circuit was provided by two heavy duty 12 V sealed lead-acid batteries connected in a parallel configuration. This configuration gives an improved capacity rating to the circuit, and consequently a longer battery time before discharge.

7.6.2 Mechanical construction

The circuit board, power supply, and data acquisition card were enclosed in an aluminium instrument case. The case will enclose the ECG leads mounted on the front panel and the thermistors connections described in the previous chapter. The system is connected to DAQ-card the processing system to process, display and record the signals.

The ECG was evaluated by using an ECG simulator, connected to the circuit with a Default of 60 Heart Rate. A volunteer investigation was also performed using ECG electrodes connected via the lead I configuration (left hand, left leg, right hand). The results are illustrated as in **Figure 7-16.**

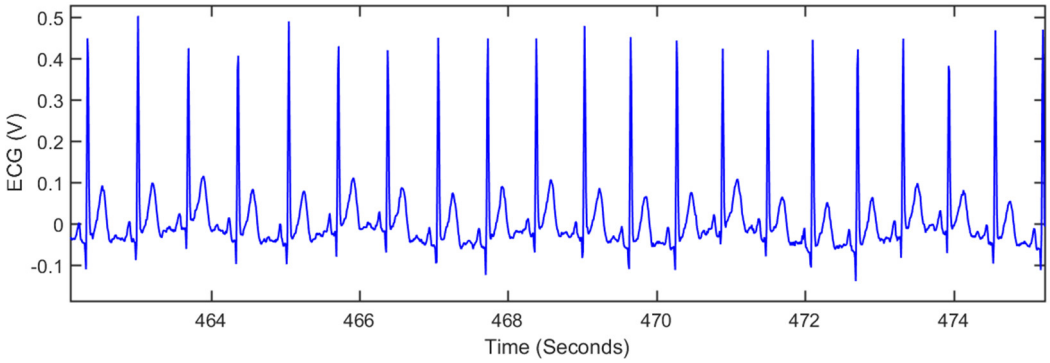

Figure 7-16
A sample of the collected ECG signal (healthy male volunteer, 28 years).

7.7 Data Acquisition System

The acquisition system was developed using LabVIEW. LabVIEW is a graphical programming environment in which program applications known as virtual instruments (VIs) are created and executed. A VI can perform a wide variety of operations including sampling analogue signals, performing calculations and signal processing, plotting real-time graphs and recording data arrays as text files. Analogue outputs can also be controlled as well as digital input and output via an interface card. VIs are created using a graphical user interface (GUI) called the *block diagram*, which resembles a flowchart. The block diagram shows connections between all the component controls, functions

and indicators, and other functions such as calculation nodes or loops. The VI is executed using another GUI called the *front panel*, which shows all controls as well as graphical and numerical indicators. Objects on the block diagram are wired together, and wires represent the transfer of data from one function to another. Complex functions can be created and saved as *sub-VIs* and several sub-VIs can be called by one VI, greatly simplifying the final program.

7.7.1 Data Acquisition Cards

The PPG processing system described above provide outputs via a single 68-pin VHDCI female connector, which is connected to a 16-bit data acquisition unit (NI USB-6212 Mass terminal) (National Instrument, US). This device is connected via a USB terminal to a personal computer running Microsoft Windows 7. The data acquisition unit has 16 analogue input channels with a maximum sampling rate of 400 KSample/s for one channel. The unit also provides two analogue outputs which were used for controlling the current delivered to the LEDs in one channel. The unit also provides 24 digital I/O lines. The temperature and ECG processing systems described above provide outputs which were connected to (NI USB-6212 screw terminal). This device is identical to NI USB-6212 Mass terminal except for connection method which allows wire connections.

7.7.2 Virtual Instrument Developed for *in vivo* Experiments

A virtual instrument (VI) was created to continuously sample the channels and record the output voltages in an easily accessible file format. **Figure 7-17** shows the VI front panel for 'Acquisition VI.vi'.

When the VI is run, the PPG waveform is displayed in real time along with a numerical display of the DC output voltage. When the STOP button is pressed the entire set of acquired data is saved in a tab-delimited spreadsheet file for later analysis. **Figure 7-18** shows the VI block diagram. The VI initially configures the data acquisition hardware (PCMCIA card) for analogue input The DAQ Assistant Express Vi launches to create a new task to input the data, where it is acquired continuously by placing a while loop. On each cycle of the loop, each input channel is sampled and the values displayed on the relevant graph or numeric display. Each scan produces a 1-dimensional array.

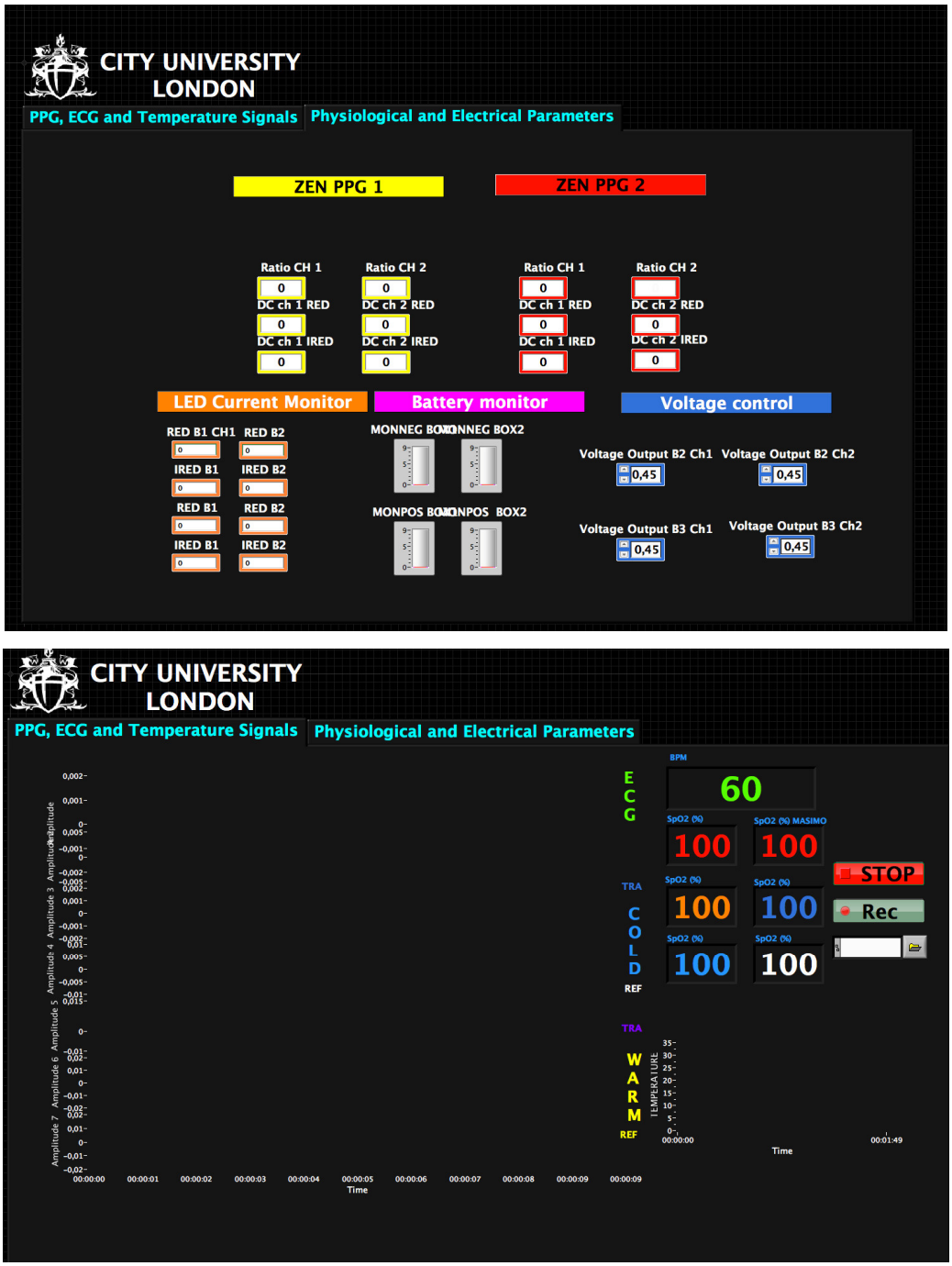

Figure 7-17
LabVIEW Virtual Instrument front diagram used for in vivo experiments.

This VI provides the possibility of editing the physical channels of the DAQ Device from where the signals are being acquired. For both used DAQ-cards, the input terminal configuration was chosen to be RSE (referenced single-ended) where the voltage is measured with respect to ground, also connected to the DAQ Device. Maximum and minimum values were configured to +5 and -5V.

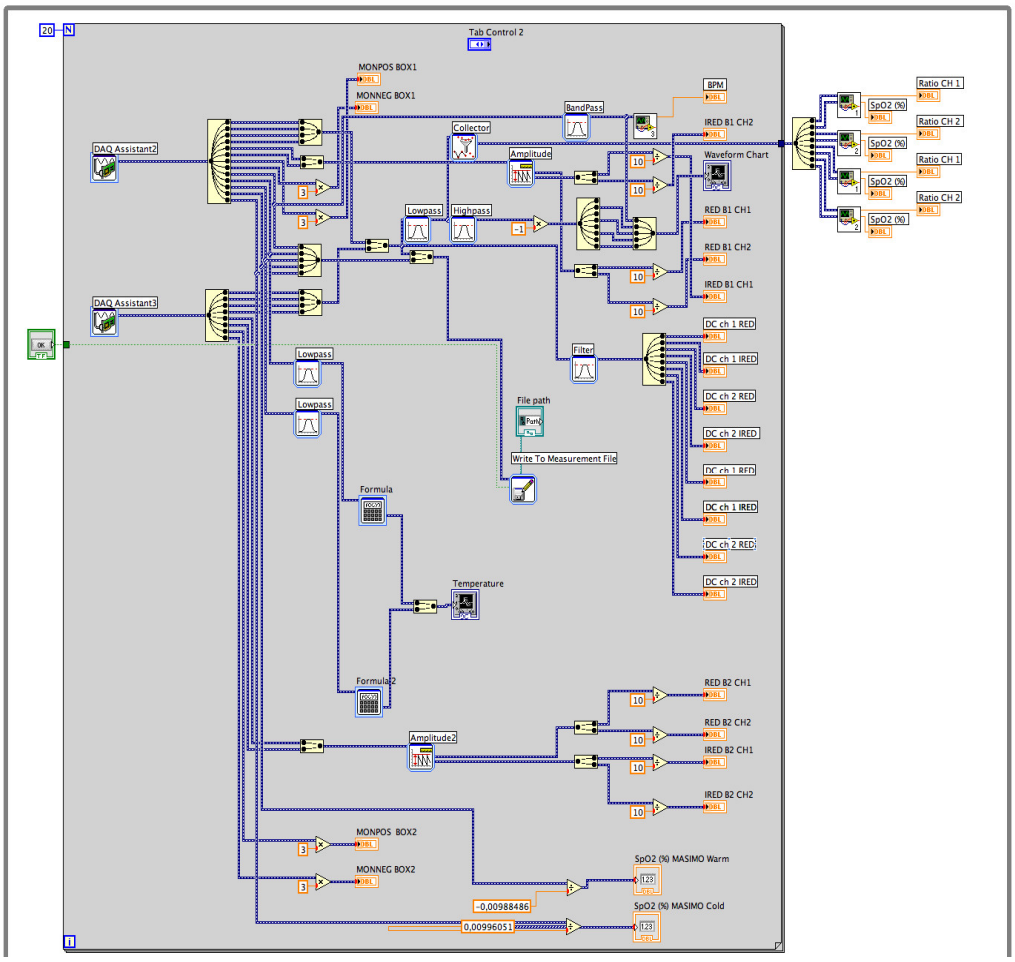

Figure 7-18
LabVIEW Virtual Instrument block diagram used for *in vivo* experiments.

The following set of data was collected at a rate of 1000 samples/ second and displayed on the front panel:

- ECG signals, which are filtered with a bandpass 2nd order Butterworth filter with a cut-off frequency range 0.5-20 Hz.

- The temperature measurements are also filtered with a converted to degree Celsius using the obtained calibrated equations.

- Driving currents and battery monitor values.

- PPG Red and Infrared signals

Eight mixed AC/DC raw PPG signals (2 x transmittance R and IR, 2 x reflectance R and IR) were acquired which were processed with:

- A low pass filter with 0.05 Hz cut-off frequency to extract DC values for all transmission and reflectance R and IR mixed signals, and will be displayed on the front panel for monitoring DC values.
- A band pass filter with a cut-off frequency range between 0.15- 20 Hz was used to extract the AC component of the PPG signals to be displayed on the front panel. The Butterworth filter is used for its smooth bandpass response, thus, no valuable information is lost.

The following set of data was collected at a rate of 1000 samples/ second and recorded for offline analysis:

- Raw reflectance red and infrared mixed AC/DC signals.
- Raw transmittance red and infrared mixed AC/DC signals.
- Raw ECG signals.
- Raw temperature signals from both thermistors.

All raw unprocessed and unfiltered signals were saved in a text tabular format file using the write to the measurement file VI

7.7.3 Virtual Instrument developed for the *in vitro* Experiment

The PPG processing system described above provide outputs via a single 68-pin VHDCI female connector, which is connected to a 16-bit data acquisition unit (National Instruments DAQCard PCIe-6321). This device takes the form of a Personal Computer Memory Card International Association (PCMCIA) and was installed in a personal computer running Microsoft Windows 7. The data acquisition unit has 16 analogue input channels with a maximum sampling rate of 250 KSample/s for one channel. The unit also provides two analogue outputs which were used for controlling the current delivered to the LEDs in one channel. The unit also provides 24 digital I/O lines. Pressure and flow signals were digitised using the NI 9172-c data acquisition card (National Instruments, US). **Figure 7-19** shows the VI front panel for 'InVitro Acquisition VI.vi'.

Figure 7-19
LabVIEW Virtual Instrument front diagram used for *in vitro* experiments.

When the VI is run, the PPG waveform is displayed in real time along with a numerical display of the DC output voltage. When the STOP button is pressed the entire set of acquired data is saved in a tab-delimited spreadsheet file for later analysis. **Figure 7-20** shows the VI block diagram. The VI initially configures the data acquisition hardware (PCMCIA) for analogue input The DAQ Assistant Express VI launches to create a new task to input the data, where it is acquired continuously by placing a while loop. On each cycle of the loop, each input channel is sampled and the values displayed on the relevant graph or numeric display.

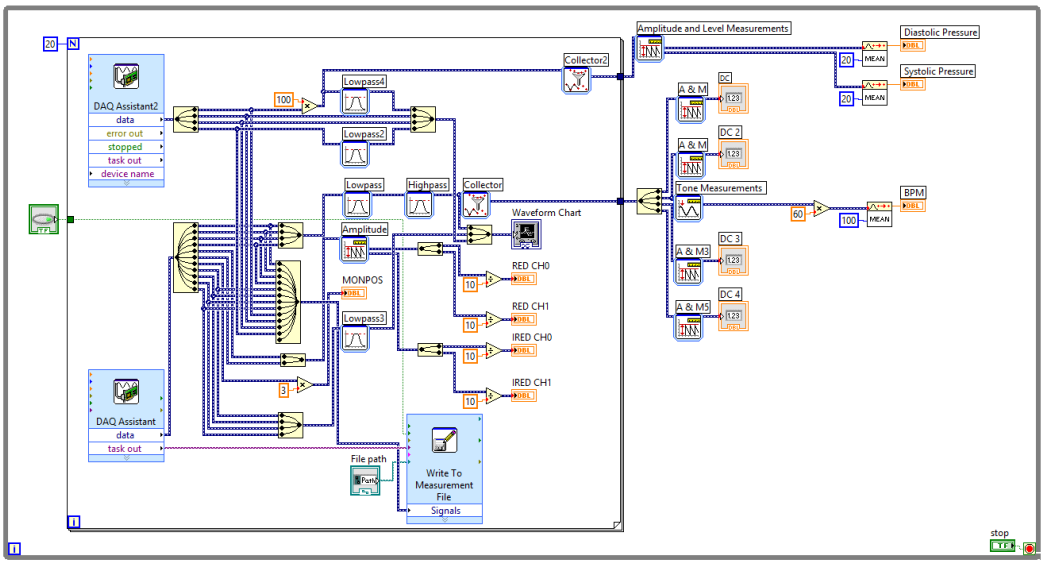

Figure 7-20
LabVIEW Virtual Instrument block diagram used for *in vitro* experiments.

For both used DAQ-cards, the input terminal configuration was chosen to be RSE (referenced single-ended) where the voltage is measured with respect to ground, also connected to the DAQ Device. Maximum and minimum values were configured to +5 and -5V.

The data corresponding to each signal acquired from the instrumentation system is passed into a for-loop of 20 iterations which is positioned inside a while loop and hence performs continuously. However, the for loop allows smoother display of a large amount of data being recorded and avoids buffering effect in the DAQ card.

The following set of data was collected at a rate of 1000 samples/ second:

- Red and Infrared PPG signals.
- Pressure signals obtained from the pressure transducer.
- Forward and backward flow signals obtained from the ultrasound Doppler.
- Driving currents and battery monitor values

7.8 Development of the Signal Offline Analyses Software

A script was developed in Matlab 2014 (Mathworks, US) to resample, process and analyse the collected signals.

7.8.1 Filter Design

In order to determine the appropriate filtering requirements, the power density spectra were generated using a Hamming window from a raw Infrared PPG signal from a volunteer as seen in **Figure 7-21**.

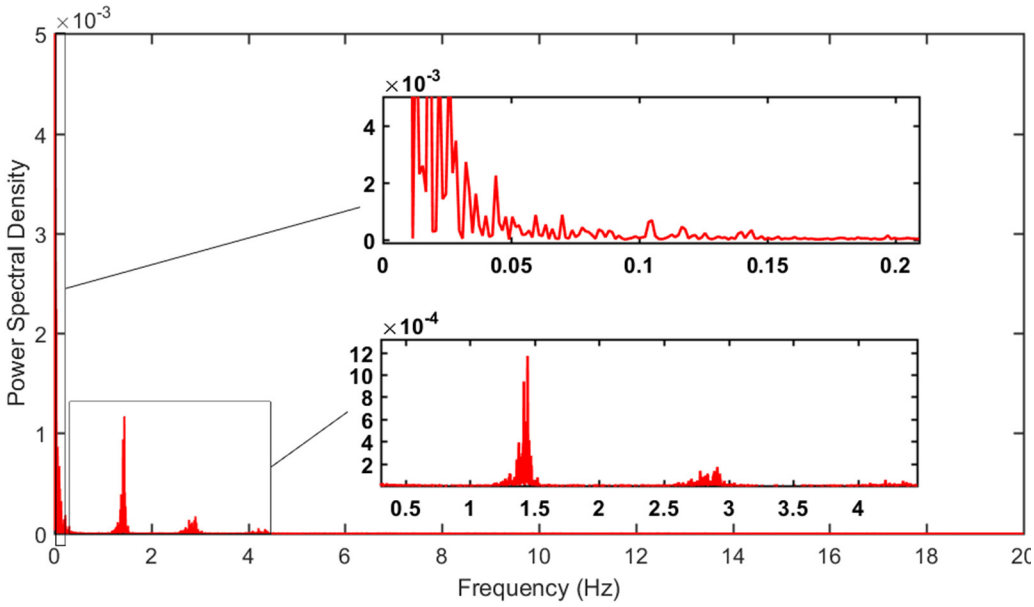

Figure 7-21
Power Spectral Density estimated from Infrared PPG signal form a volunteer (Male, 28 years old). A close-up of the low and high frequency ranges is shown.

A Butterworth bandpass filter was designed to extract the AC component of the raw PPG signal with cutoff frequencies within the appropriate range of 0.15 and 20 Hz. The response of the designed filter is simulated and seen in **Figure 7-22**.

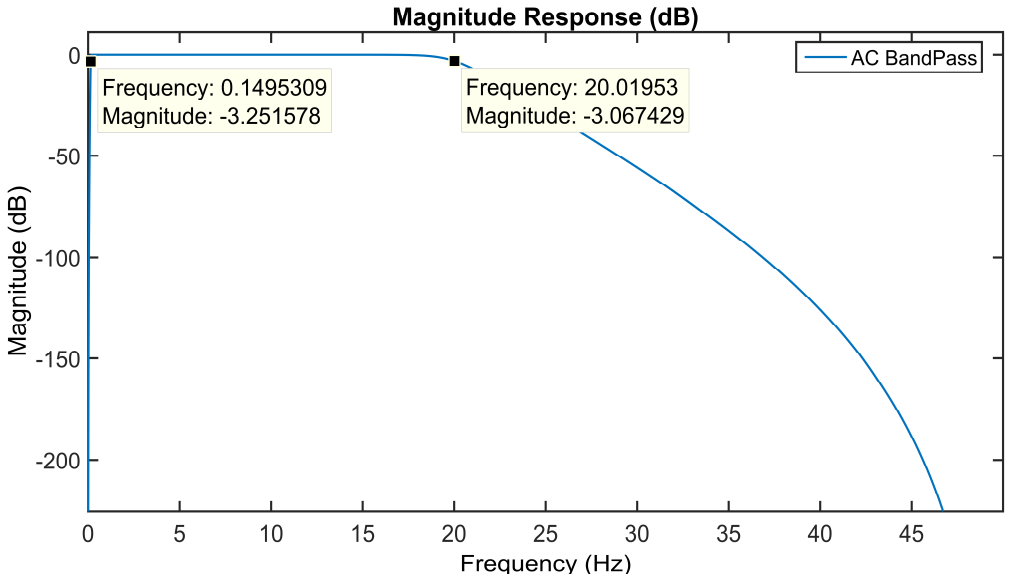

Figure 7-22
Magnitude response of the bandpass filter designed to extract the PPG AC component.

The DC component, however, is seen to be in the region less than 0.05 Hz, with maximum values at zero Hz. Hence, a low pass filter was designed with a cut-off frequency of 0.05. A magnitude plot of the designed filter is seen in **Figure 7-23**.

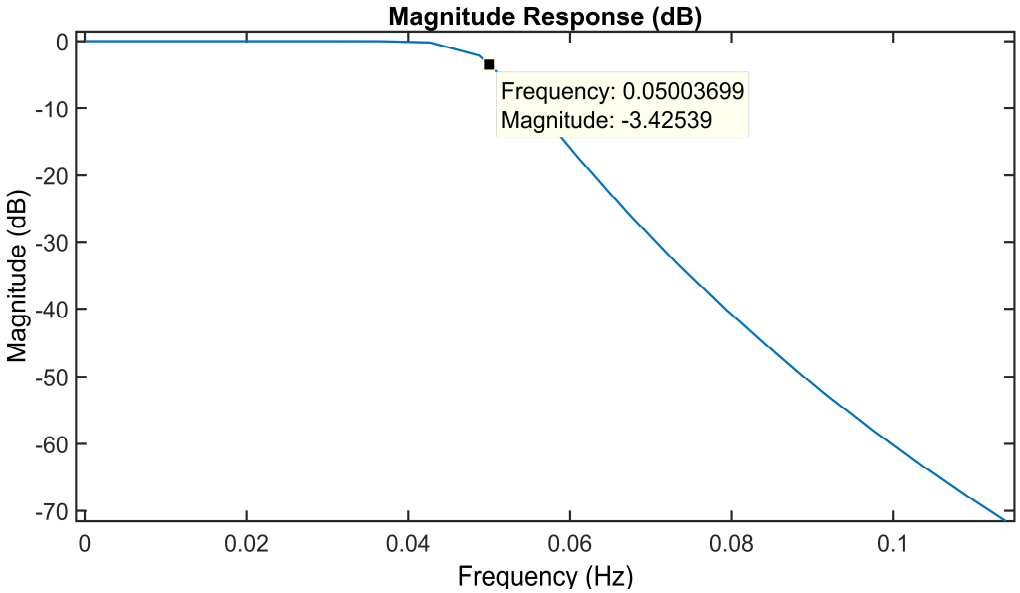

Figure 7-23
Magnitude response of the low pass filter designed to extract the PPG DC component.

7.8.2 Filtering and Peak Detection

A Matlab script was written as in the flow chart seen in **Figure 7-24**. The script extracts the AC and DC components of the PPG signal using the previously described filters. Then, the peaks and valleys of the AC signal are detected using a custom made algorithm using the first and second derivatives, input locations and values of the peaks and valleys in an array and save it for later statistical analysis.

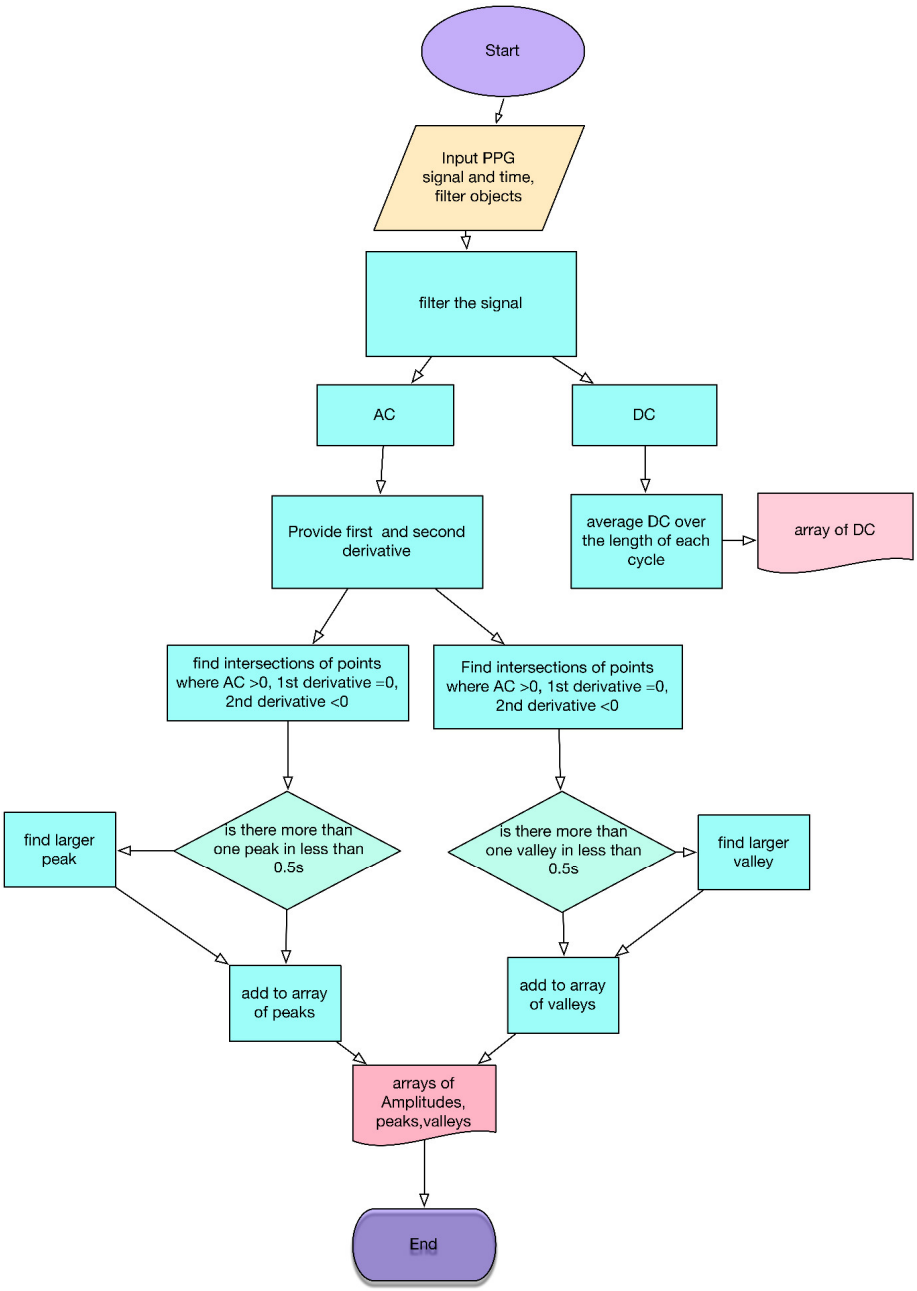

Figure 7-24
Flow chart of the program applied as a Matlab script for PPG filtration and peak detection.

A sample of the results obtained from filtering the Infrared raw PPG data from a volunteer is seen in **Figure 7-25**. Infrared AC and DC components were extracted efficiently and are of high quality.

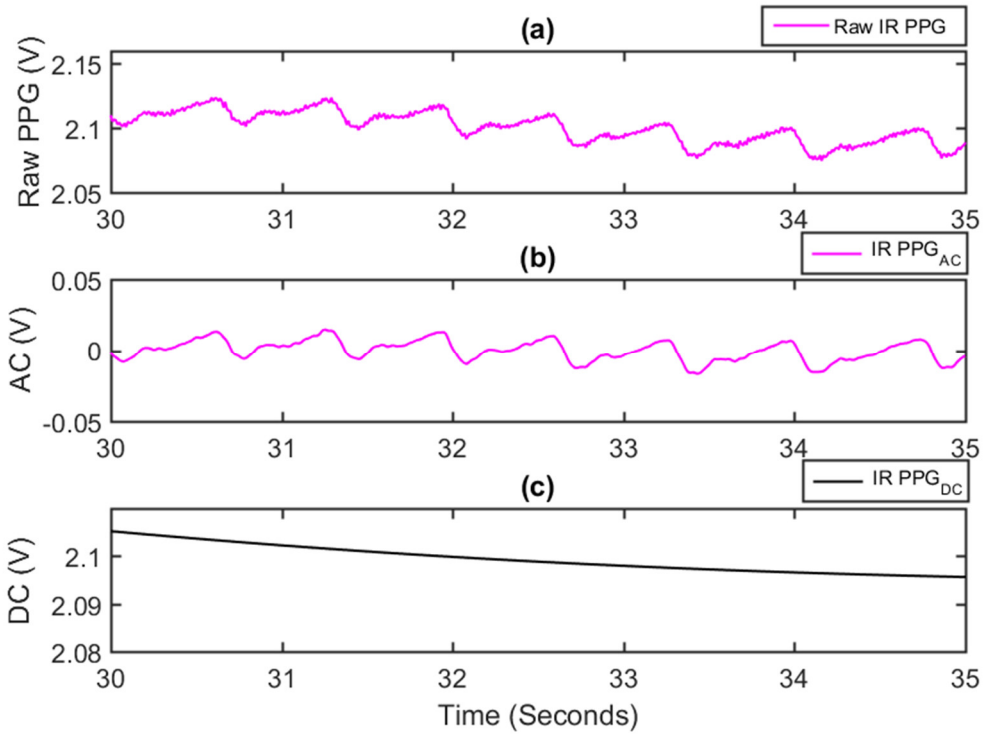

Figure 7-25
PPG data obtained from a volunteer (male 28 years old). (a) Raw PPG signal, (b) AC component, and (c) Infrared DC component.

The used method for the peak detection algorithm is shown in **Figure 7-26**, which displays a sample of the Infrared AC PPG signal and its first and second derivative amplified. It can be seen that peaks and valleys can be detected successfully.

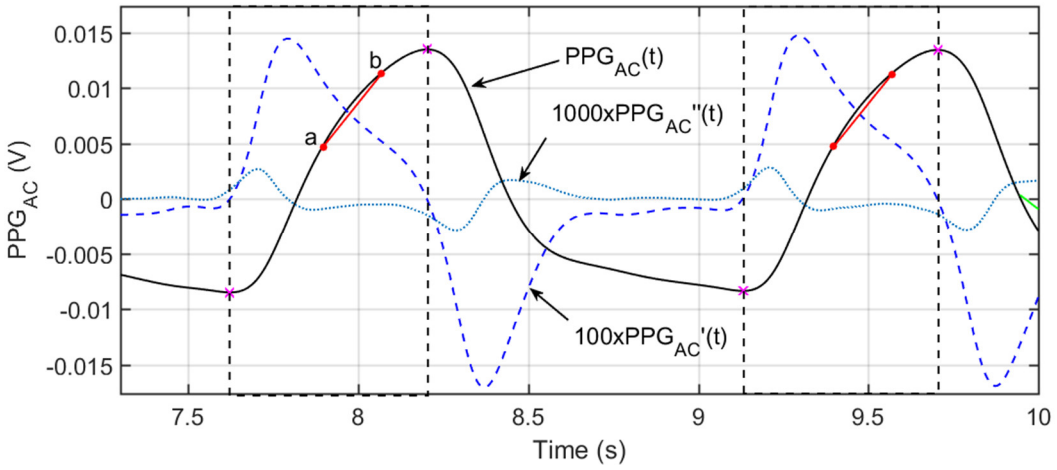

Figure 7-26
Sample of PPG signal showing Peak detection method, PPGAC'(t) is first derivative and PPGAC''(t) is second derivative. Sample was obtained from the pulsatile pump at 0.67 Hz and 70 ml stroke.

The method was effective in detecting peaks and valleys in all PPG signals obtained from the *in vivo* and *in vitro* investigations. The same method was also used for pressure and flow signals in the *in vitro* setup. A 24-second sample of Infrared red PPG_{AC} data obtained from the *in vitro* investigation is shown in **Figure 7-27**.

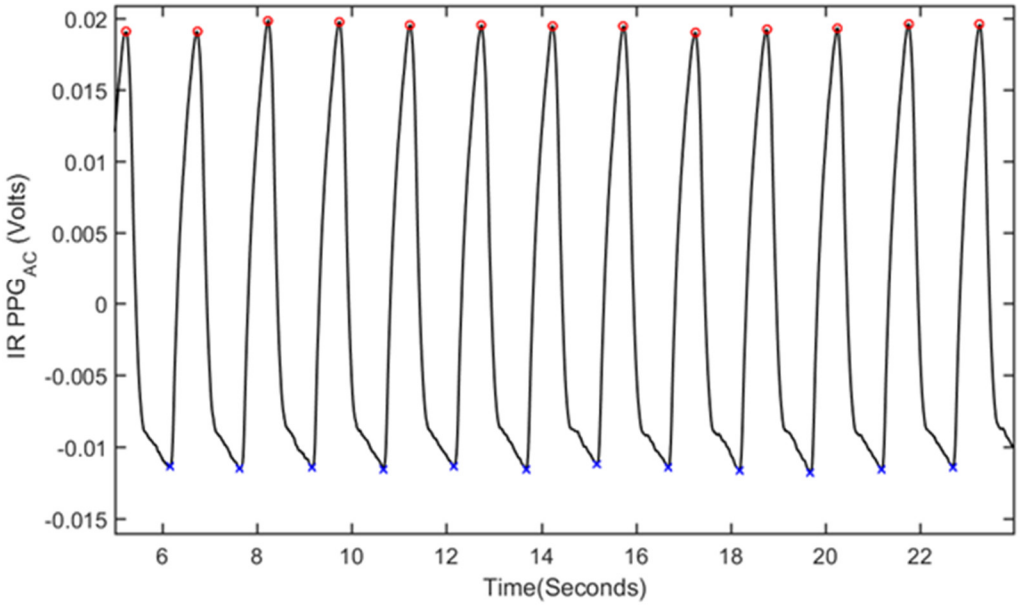

Figure 7-27
24-seconds sample showing peak and valley detection of a PPG obtained from the *in vitro* pulsatile pump at 0.67 Hz and 70 ml stroke volume.

7.8.3 Data Analyses

A Matlab function was also written to analyse the morphology of the signals by calculating the time rise, time fall and rising slopes for each cycle of the PPG and pressure signals.

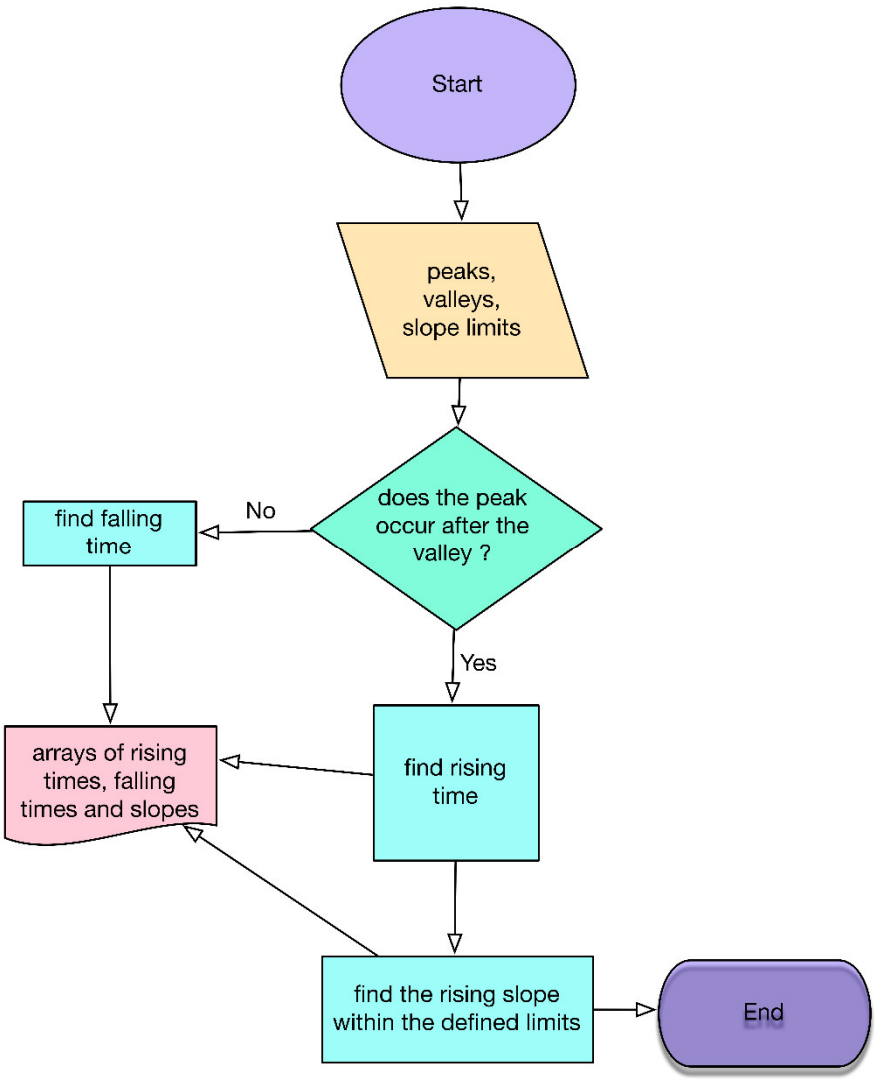

Figure 7-28
Flow chart applied in Matlab for signal analysis.

The defined limits are aimed to avoid the peak region and were limited between the 60% and 90% after the peak for the falling slopes and between the 60% and 90% after the valley for the rising slopes. A sample of an analysed signal is shown in **Figure 7-29.**

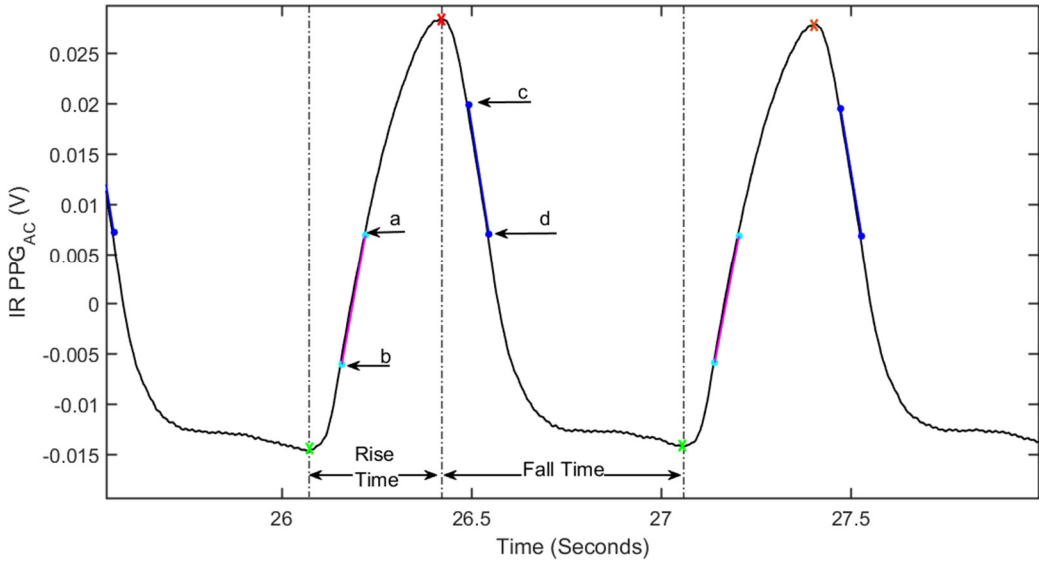

Figure 7-29
A sample of an analysed Infrared AC PPG signal showing time limits and the rising and falling slopes.

7.8.4 Statistical Analyses

Statistical analyses were performed using the statistical analysis package in Matlab (Mathworks, Inc. Natick, MA).

- The goodness of model fitting was evaluated with the Sum Square Error (SSE), R-square and the Root Mean Square Error (RMSE). Where SSE shows variation from the mean. R-square is the percentage of the response variable variation, and RMSE is the square root of the variance of the residuals and indicates the absolute fit of the model to the data.

- Correlation significance is stated with a p-value and t-value.

- A statistical two-way t-test was also performed with values of $p \leq 0.05$ considered to be significant and those where $p<0.001$ are highly significant.

- Multiple Comparison tests were performed with Dunn-Sidák approach. It uses critical values from the *t*-distribution, after an adjustment for multiple comparisons that was proposed by Dunn and proved accurate by Sidák (Seidler et al., 2000).

SUMMARY

This chapter discussed the design, development and evaluation of the PPG processing system including the mechanical and electrical description. The chapter also presented details of the data acquisition system including the virtual instrument developed in

LabVIEW which will be used during the *in vivo* and *in vitro* investigations. The design of the custom-made Matlab script was also presented. The script will be used for offline data analysis of PPG signals to extract AC and DC components, detect peaks and valleys of AC signals, and further analytics of the signals. The filters used and the performance of the written script was evaluated and showed acceptable results.

Chapter 8
IN VIVO PPG INVESTIGATION DURING A HAND COLD PRESSOR TEST

8.1 Introduction

This chapter will present the first investigation of the project. PPG signals are obtained from volunteers who are exposed to cold temperatures in one hand or as commonly known as the cold pressor test. The cold pressor test is a standard autonomic function test commonly used in cardiovascular research to assess sympathetic activity. The test is postulated to induce a largely alpha-adregnic challenge which has a marked effect on evoking cutaneous vessel vasoconstriction, shunting blood from the superficial to the deep venous system, transferring heat from the arteries to the veins, and effectively reducing skin temperature to maintain core temperatures (Isii et al., 2007). Moreover, the cold pressor test was long related to an increase in blood pressure and heart rate. Heart rate increases are also associated with changes in stroke volumes and arterial stiffness (Kalfon et al., 2015; Mourot et al., 2009). All of which can affect blood rheological properties. The aim of this study is to investigate the PPG signals (AC and DC components) during baseline periods, and under the induced changes of the cold pressor test that can simulate a scenario of cardiovascular stress.

Previous studies investigated the effect of the cold pressor test on the PPG signal in different locations (e.g. outer ear, finger, leg) (Awad et al., 2001; Korhonen, 2006; Mourot et al., 2009; Selvaraj et al., 2008). However, these studies were limited to analysing the AC component only where the DC components were overlooked. Most of the studies also

did not observe the changes throughout the rewarming period where the parasympathetic stimulation is overtaking the sympathetic. Moreover, we were unable to identify a study that investigated the PPG signals in both hands while one undergoes cold exposure. This approach will allow the study of the generic factors of sympathetic and parasympathetic stimulation throughout the circulation in the upper limbs and not only local factors in the exposed hand.

The designed study observes the changes in the AC and DC components of the PPG signals recorded from both hands of volunteers during a 30-second ice immersion of the volunteers' right hand. The immersion takes place in an ice bath tub (ice and water until the wrist, temperature 0-4 °C). This period is sufficient to cause a temperature shock in the human body, stimulating the autonomic nervous system, where local vasoconstriction takes place. The study protocol and results of 22 volunteers will be presented in this chapter.

8.2 Subjects

Twenty-two healthy volunteers (age 25.5 ± 4.4, male 12 and female 10) with no history of cardiovascular disease, hypertension or other diseases were recruited in this study. The City University Senate Research Ethics Committee granted ethics approval for this study. All subjects gave informed written consent for their participation.

8.3 Testing Protocol and Materials

A block diagram of the volunteer study is shown in **Figure 8-1.** All testing has completed in the Biomedical Engineering Research Laboratory at City University London, UK.

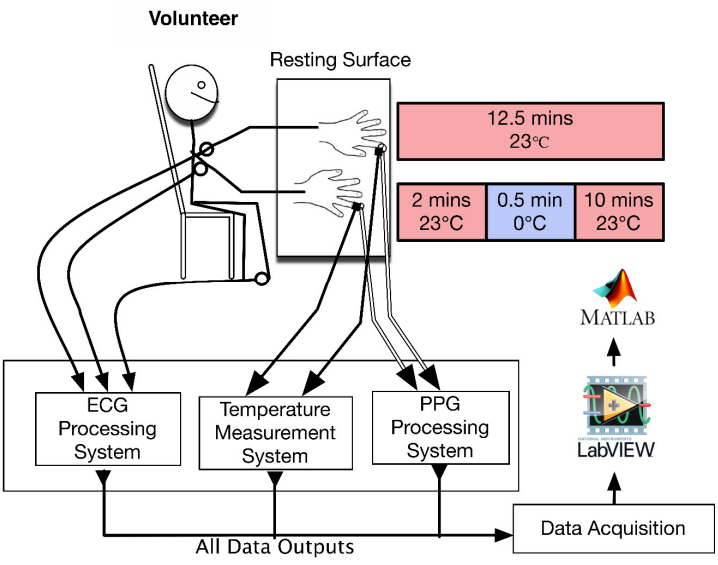

Figure 8-1
Block diagram of the setup of the volunteer study.

During this study, the room temperature was maintained at 21 ± 2 °C. Subjects were required to acclimatise to the testing room temperature upon arrival for a few minutes. During this time, subjects completed the consent form, and the following sensors were placed: -

1. ECG electrodes for LEAD I configuration.
2. Two identical custom made Reflectance PPG sensors (previously described in Chapter 6) were attached to each index finger.
3. The skin temperature sensors (previously described in Chapter 6) were attached to each index finger on each hand.

Each subject was directed to sit comfortably and rest their hands on a bench top approximately at the level of the subject's heart. The subject was instructed to maintain a stable upper-body position and maintain their movement to the minimum. A baseline reading was obtained for two minutes. The subject subsequently fully immersed their hand (until the wrist) into the ice-water bath (maintained at 0-4 °C) for 30 seconds as requested (the immersion occurs with the water probes attached sensors). After the 30-second immersion, the volunteer is advised to slowly move their hand and place it on a dry towel. The rewarming period is observed for an average of 10 minutes for each volunteer until the skin starts to recover its previous temperature and the ice immersion effects are diminishing.

The PPG processing system, the ECG and temperature processing system as described in **Chapter 6** and **Chapter 7** were used in this study. The recorded IR and R PPG signals were connected via the USB-6212 data acquisition card (National Instrument, US). ECG and temperature signals were connected via USB-6212 Mass terminal data acquisition card (National Instrument, US). All signals are then fed into a virtual instrument via LabVIEW for online display, processing and recording of raw signals for further offline data and statistical analysis.

A picture of the implemented setup can be seen in **Figure 8-2(a).** A picture showing a volunteer during the experiment can be seen in **Figure 8-2(b)**.

(a)

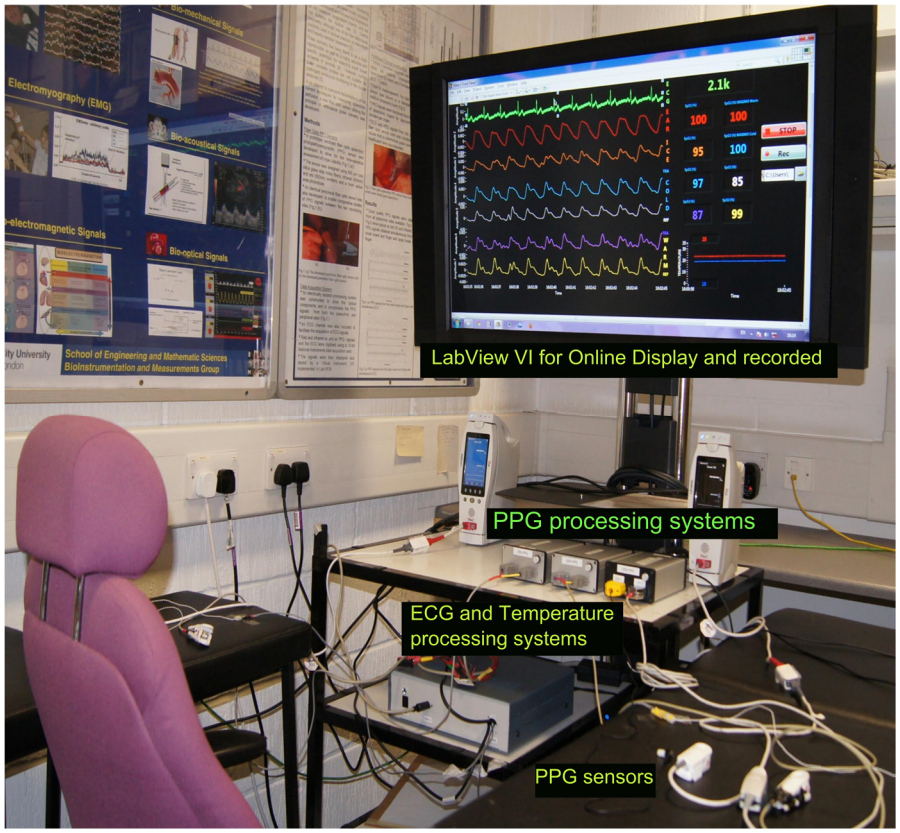

(b)

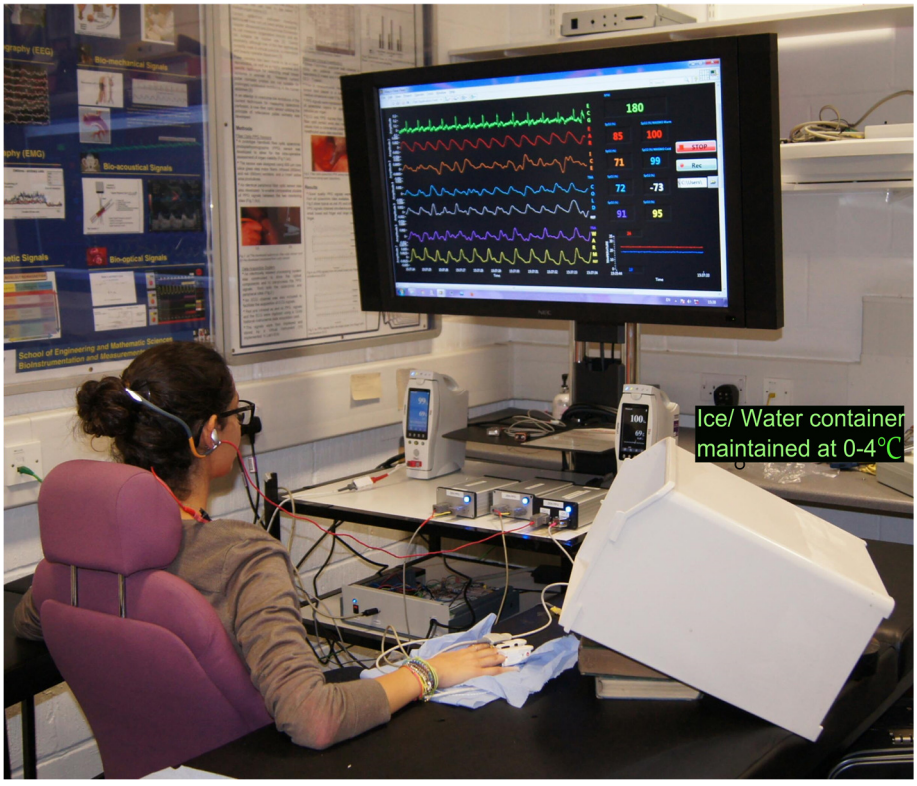

Figure 8-2
Shows the implemented volunteer setup. (a) Sensors, processing system and display screen. (b) a snapshot taken during an experiment where the sensors are attached to the participant and the signals are being displayed and recorded.

8.4 Data Analyses

Data were successfully obtained from all volunteers. The suggested analysis method will be to extract the AC amplitudes, DC levels and other analytics for each volunteer, before, during and after the ice immersion event. The three segments will be referred to as baseline (s1), immersion (s2) and rewarming (s3) periods. The offline data analysis protocol followed for PPG, included the peak/valleys extraction as described in **Chapter 7.** A sample of the analysed PPG signal from a male volunteer aged, 26 years old is shown in **Figure 8-3**, which shows analysed IR PPG signals from the right hand (immersed) throughout the baseline period (**Figure 8-3(a)**), the immersion period (**Figure 8-3(b)**) and the rewarming period (**Figure 8-3(c)**).

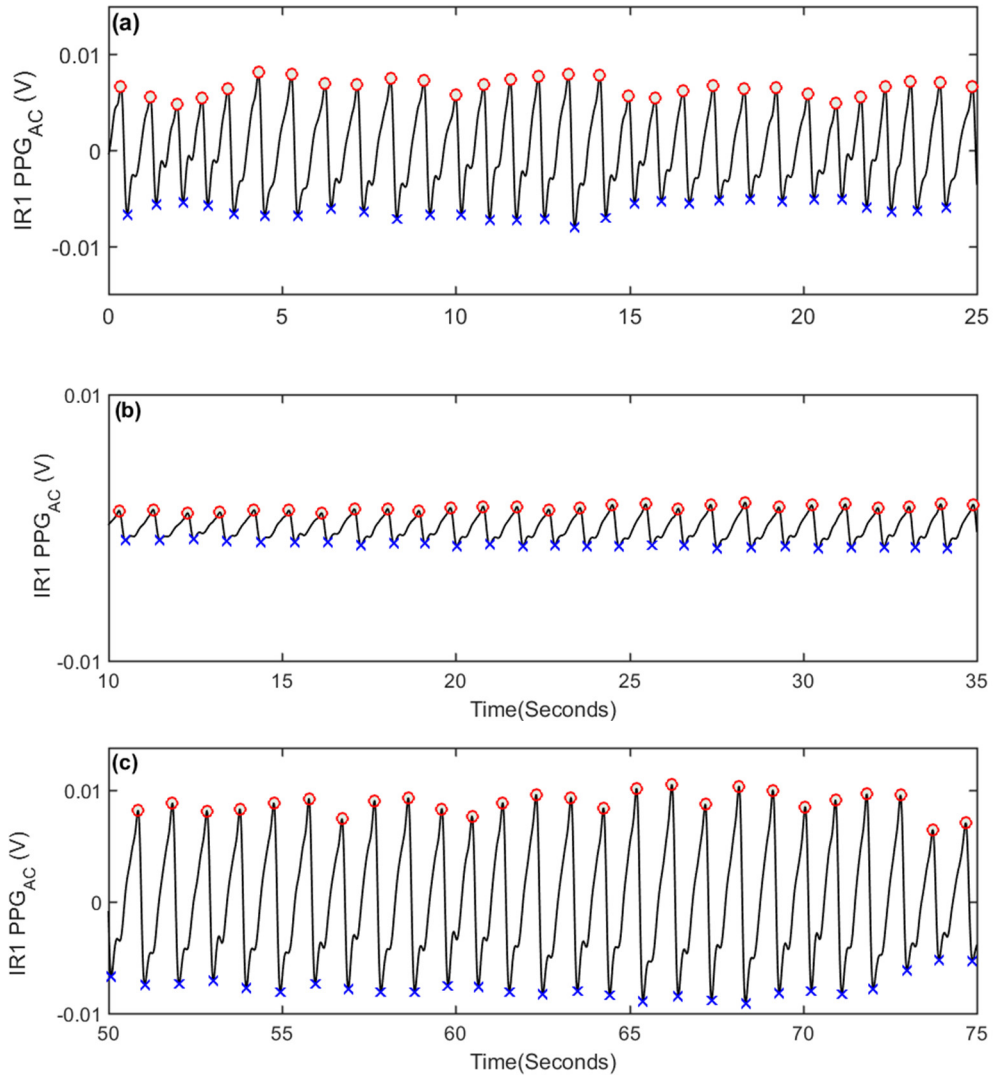

Figure 8-3
A sample of the PPG data showing peaks and valleys detected on IR PPG$_{AC}$ signals from the right hand. (a) A sample obtained during the baseline period.(b) a sample obtained during the immersion period. (c) a sample obtained during the rewarming period.

In regards to ECG signals, the QRS peak for the collected ECG signals was also obtained to detect heart rates using a custom-made Matlab script as described in **Chapter 7**. A sample of the analysed signal is shown in **Figure 8-4**.

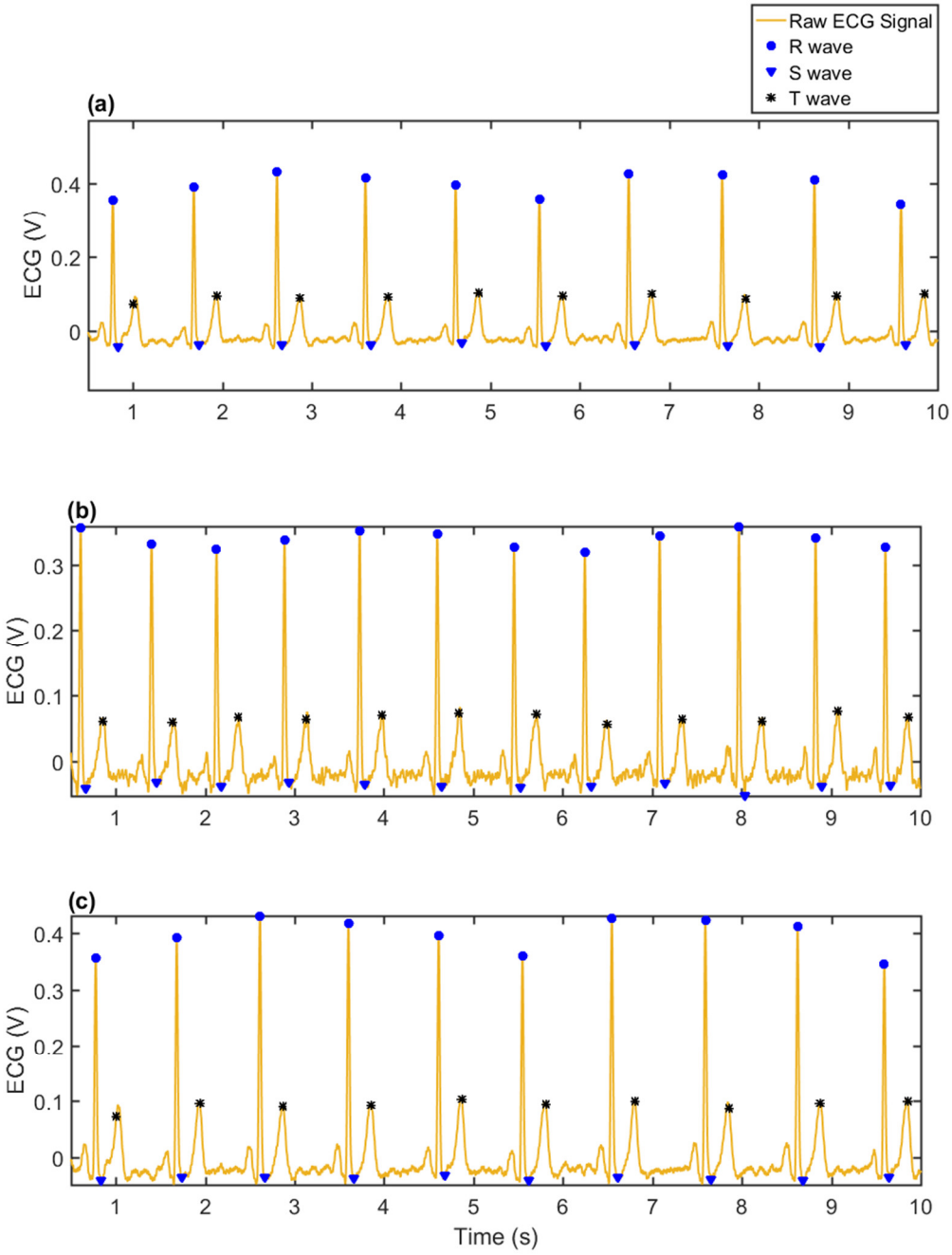

Figure 8-4
ECG waveform, showing filtered, smoothed and processed signal highlighting R-waves, S-waves and T waves with the adaptive thresholds. The signals are chosen from a random volunteer. The volunteer is a healthy female aged 32 years old. (a) ECG obtained during the baseline period. (b) ECG obtained during ice immersion period. (c) ECG obtained during the rewarming period.

Statistical analysis was performed on the three segments (baseline, immersion and rewarming). The analysis included finding the average ± SD values for DC levels and AC

amplitudes in all volunteers. One-way ANOVA statistical test was performed on the baseline-immersion-rewarming data and a multi comparison was performed using the sidak adjustement. P values less than 0.05 are considered significant and those less than 0.01 and 0.001 are considered highly significant. The star system was used to represent significance on the graphs in accordance with the following criteria; * represents p<=0.05, ** represents p<=0.01 and *** represents p<=0.001.

8.5 Results

The recorded signals were of high quality. This section will overview the change in Red and Infrared PPG_{AC} amplitudes and R and IR PPG_{DC} signals levels in both hands. Heart rates obtained from the ECG signals are also shown. All signals are studied along with the change in temperatures in both hands.

8.5.1 Temperature Signals

A sample of the temperature signal measured at the right hand is shown in **Figure 8-7(c)**, and those obtained from the left hand are shown in **Figure 8-6(c)**. The average ± SD values for temperature signals averaged of all volunteers calculated at the three segments (before, during and after the ice immersion) are shown in **Figure 8-5(a)** for the right hand and in **Figure 8-5(b)** for the left hand. It is clear that the cold pressor test succeeded in lowering surface temperatures in the right hand (the only hand undergoing the immersion) with average values dropping in a highly significant manner from 21.10 ± 1.79 °C at baseline to 4.02 ± 1.75 °C. This is an average of 81 % of the relative drop in all volunteers. During the 10 minutes of rewarming, skin temperatures approached 12.50 ± 1.79 °C with an average relative increase of 223.06% compared to the immersion period, which with no doubt is a highly significant change. Nonetheless, this change is still 38.48% less than the values observed at baseline. The left hand, however, experienced a completely different temperature change patterns. During the immersion, left-hand temperatures increased significantly with a relative change of 0.43%. While during the rewarming period, temperature values continued to increase in a highly significant manner to hit a relative change of 5%, when compared to baseline values.

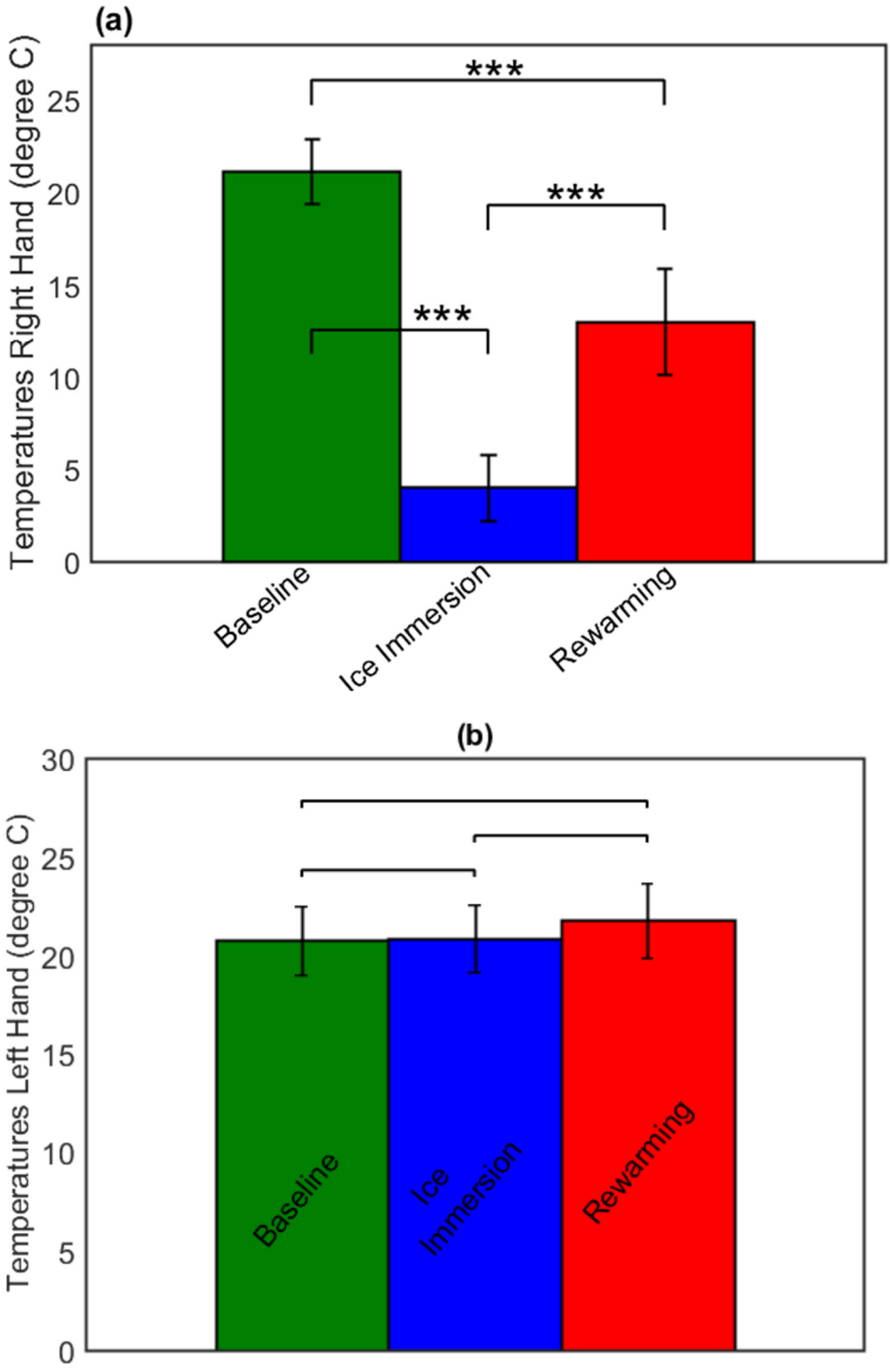

Figure 8-5
The average ± SD values for temperature signals averaged of all volunteers calculated at the three segments (before, during and after the ice immersion). (a) showing temperature values in degree Celsius obtained from the right hand (undergoing the immersion).(b) Showing temperature values obtained from the left hand.

8.5.2 PPG AC Signals

A sample of the processed Red and Infrared PPG_{AC} signals along with the hand temperatures during an experiment are presented for the left hand in **Figure 8-6**. Those obtained from the right hand are shown in **Figure 8-7**.

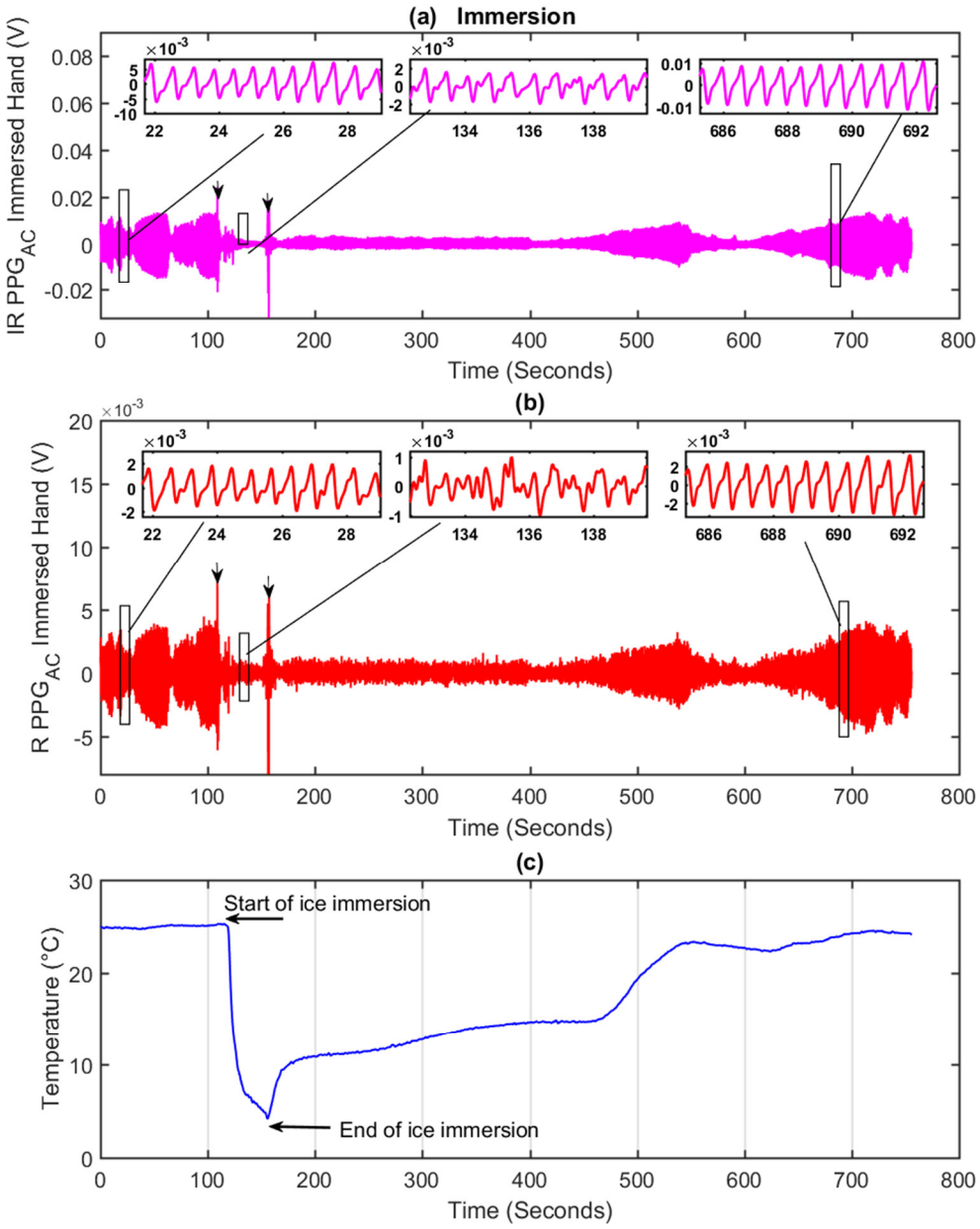

Figure 8-6
Typical set data obtained from the right hand during the in vivo investigation.

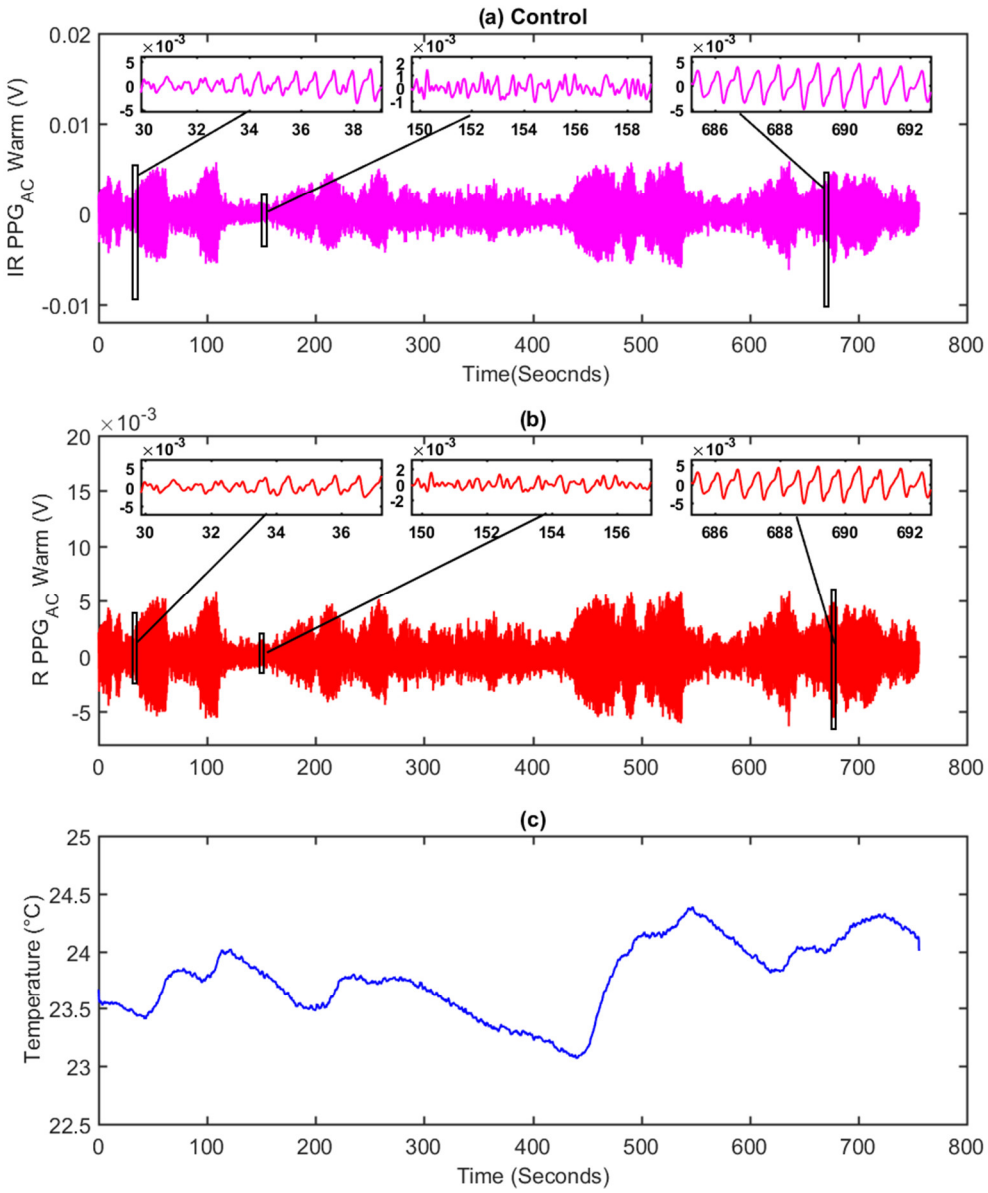

Figure 8-7
Typical set data obtained from the left hand during the in vivo investigation.

AC Amplitudes of R and IR PPG signals were measured for each volunteer before, during and after the ice immersion. The average ± SD of the values obtained from all volunteers are displayed in f**igure 8-8**. The figure shows magnitudes for R and IR PPG_{AC} signals from both hands. **Figure 8-8(a)** and **Figure 8-8(b)** showing R and IR AC amplitudes, respectively as obtained from the left hand, and **Figure 8-8(c)** and **Figure 8-8(d)** showing R and IR AC amplitudes, respectively as obtained from the right hand**.** The statistical significance of each combination is presented using the three-star system. Clearly, AC amplitudes dropped significantly during the immersion in both hands. During the rewarming period, AC amplitudes returned to baseline values showing a full recovery in the left hand. However, **Figure 8-8(c)** and **Figure 8-8(d)** show that the right hand did not recover fully during the rewarming period, nevertheless showed a significant increase in AC amplitudes.

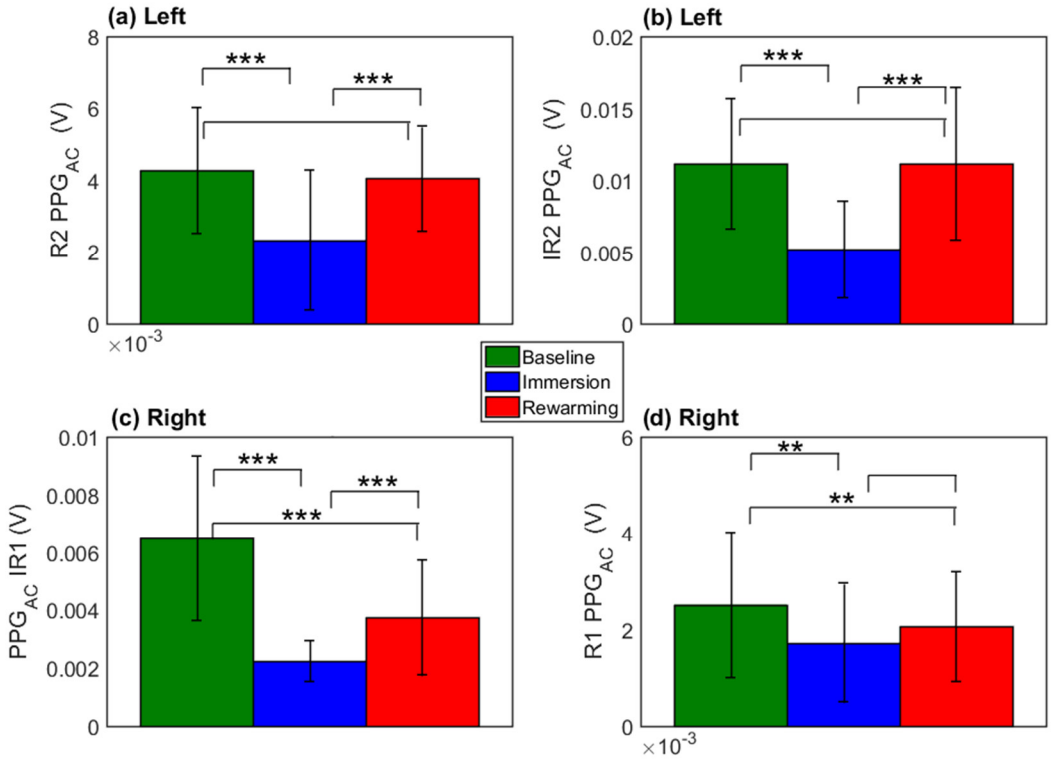

Figure 8-8
Average ± SD of AC amplitudes obtained from all volunteers of PPG signals stating the statistical significance between each pair of the experimental stages.Values are obtained from (a) Red (R2) PPGAC at left hand (b) Infrared (IR2) PPGAC at left hand. (c) Red (R1) PPGAC at right hand (immersed). (d) Infrared (IR1) PPG_{AC} at the right hand.

Table 8-1
Mean Percent Change in Red(R) and Infrared (IR) AC amplitudes in the left hand (R2 and IR2) and in the right hand (R1 and IR1) showing p-values.

Period combination		Left Hand		Right Hand	
		R2	IR2	R1	IR1
Baseline, Immersion	Difference	-45.33 %	-53.42%	-31.62%	-65.39%
	P_value	<0.001	<0.001	<0.01	<0.001
Immersion, Rewarming	Difference	73.25%	114.73%	19.42%	66.60%
	P_value	<0.001	<0.001	<0.001	>0.05
Baseline, Rewarming	Difference	-5.28%	0.01%	-18.33%	-42.33%
	P_value	>0.05	>0.05	<0.001	<0.01

8.5.3 PPG DC Signals

A sample of the processed Red and Infrared PPG_{DC} signals along with the hand temperatures during an experiment are presented for both hands in **Figure 8-9**. Average $\pm$ SD of DC levels of R and IR PPG signals obtained from all volunteers from both hands are shown in **Figure 8-10**. **Figure 8-10(a)** and **Figure 8-10 (b)** showing R and IR DC levels, respectively as obtained from the left hand, and **Figure 8-10 (c)** and **Figure 8-10(d)** showing R and IR DC levels, respectively as obtained from the right hand**.** The statistical significance of each combination is presented using the three-star system.

A significant increase in DC levels was evident in both hands during the immersion. In fact, average DC levels continued to increase even during the rewarming period when the parasympathetic stimulation was more dominant. In the right hand, DC levels increased by 10% during the immersion, and another 5-6% during the rewarming period. However, in the left hand, R DC levels increased by 1% during the immersion and continued to increase for another 3% during the rewarming period. IR DC levels increased by 3% during the immersion and continued to increase for another 2% during the rewarming period. All changes were highly significant.

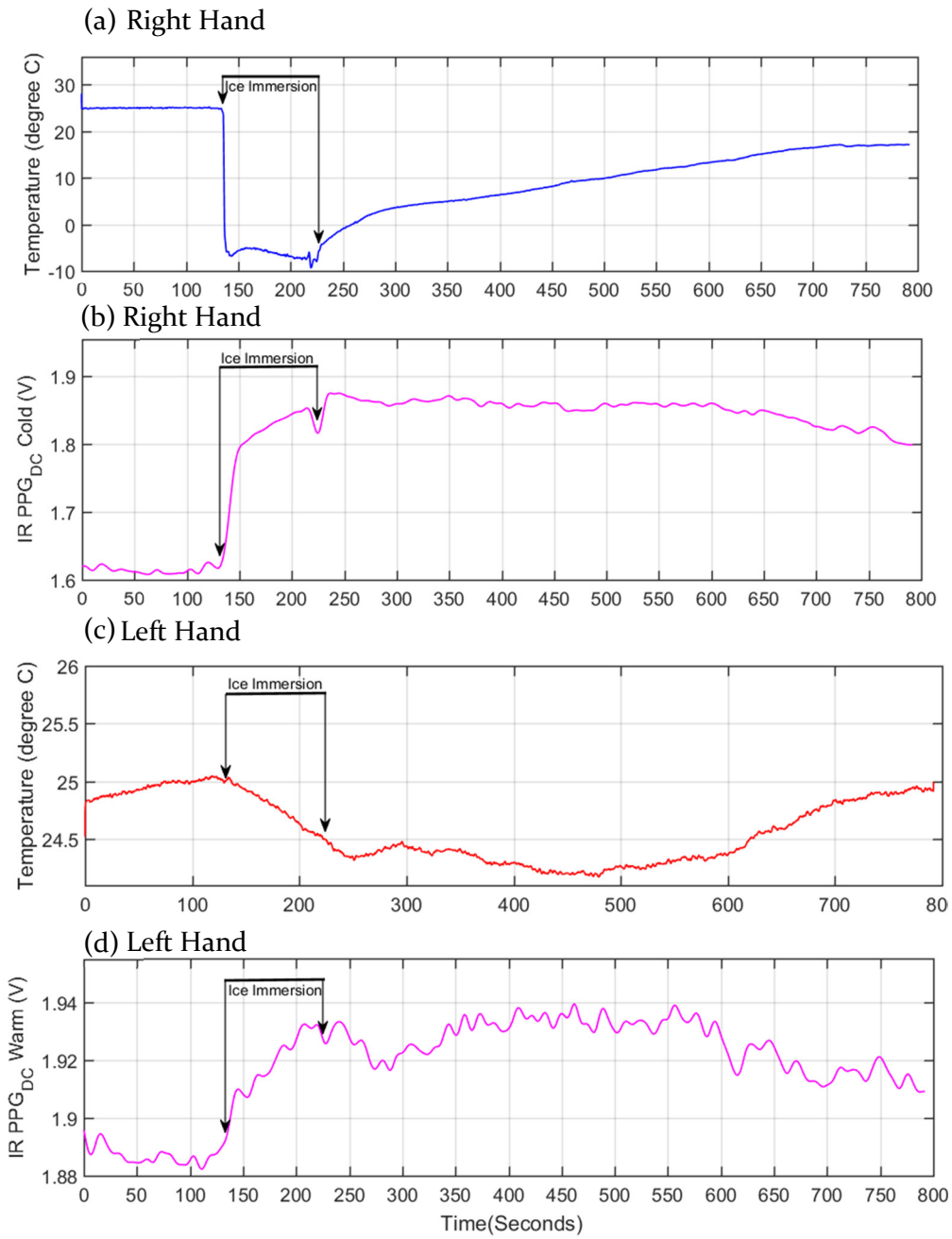

Figure 8-9
A sample of a volunteer (Male, 28 years old) data during the ice immersion experiment. Showing DC levels from Infrared (IR) PPG signals along with skin temperatures in both hands. (a) Skin temperatures measured at the right hand (immersed). (b) DC levels from IR PPG signals obtained from the right hand. (c) Skin temperatures measured at the left hand. (d) DC levels from IR PPG signals obtained from the left hand.

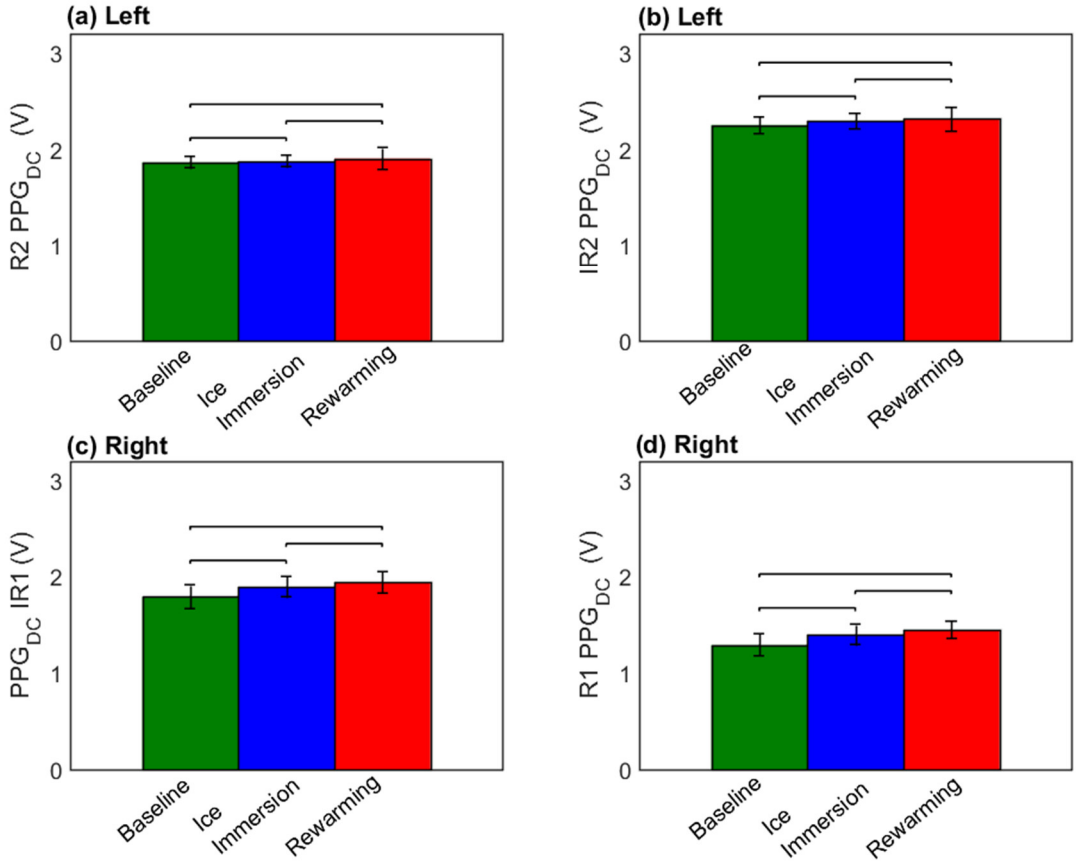

Figure 8-10
Average ± SD of DC levels of PPG signals obtained from all volunteers stating the statistical significance between each pair of the experimental stages.Values are obtained from (a) Red (R2) PPGAC at left hand (b) Infrared (IR2) PPG_{AC} at left hand. (c) Red (R1) PPG_{AC} at right hand (immersed). (d) Infrared (IR1) PPGAC at the right hand.

Table 8-2
Increase in Red(R) and Infrared (IR) DC levels in the left hand (R2 and IR2) and in the right hand (R1 and IR1) showing p-values.

Period combination		Left Hand		Right Hand	
		R2	IR2	R1	IR1
Baseline, Immersion	Difference	1.20 %	4.58%	10.38%	10.34%
	P_value	<0.001	<0.001	<0.001	<0.001
Immersion, Rewarming	Difference	2.67%	1.95%	5.56%	4.71%
	P_value	<0.001	<0.001	<0.001	<0.001
Baseline, Rewarming	Difference	3.88%	6.53%	15.94%	15.05%
	P_value	<0.001	<0.001	<0.001	<0.001

8.5.4 ECG Signals

A sample of the ECG signals for a male volunteer during the *in vivo* experiment is presented in **Figure 8-11**. The R wave which is detected accurately using the Matlab script as shown earlier in **Figure 8-4** was used to provide the gold standard heart rate measurement.

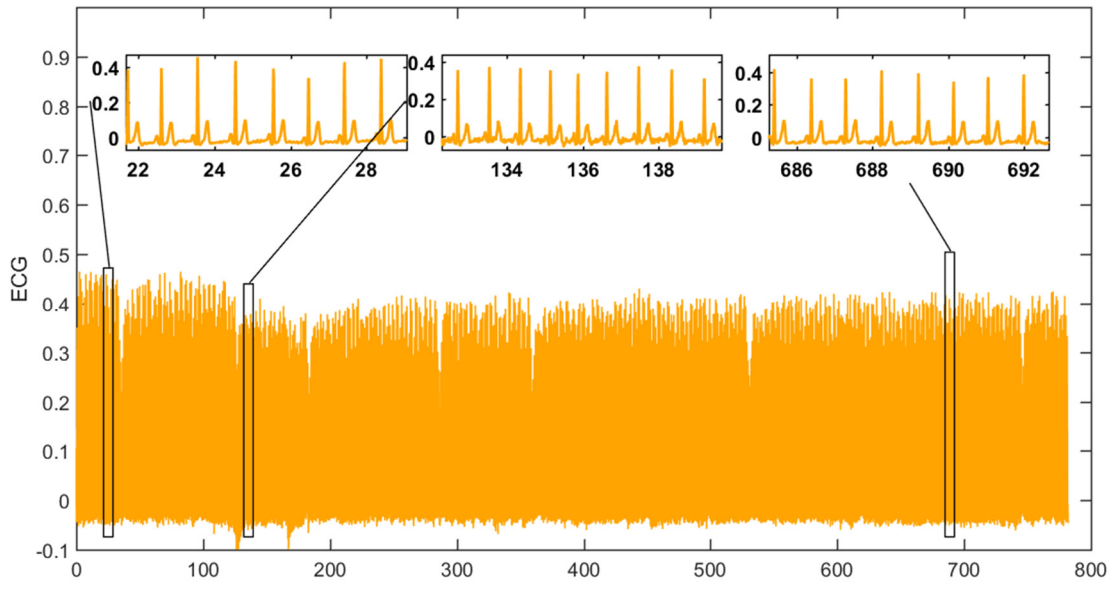

Figure 8-11
ECG signals recorded throughout the cold pressor test. Ice immersion occurs on the mark of 120 seconds and continues for 30 s. The signal is filtered with a low-pass filter of the cut-off frequency of 30 Hz.

The average ± SD of Heart Rates as obtained from all 22 volunteers are presented in the histogram in **Figure 8-12** for the baseline, ice immersion and rewarming periods. During the immersion, a significant increase in heart rates was observed. During the rewarming period, a full recovery back to baseline values was observed.

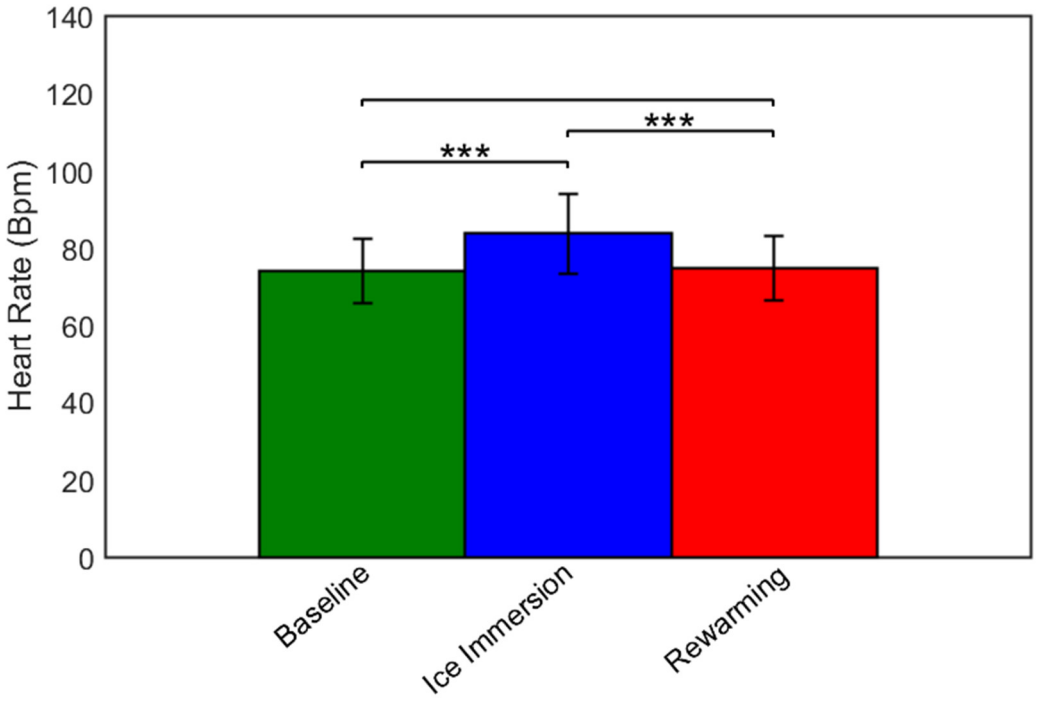

Figure 8-12
Average ± SD of Heart Rates as calculated from the ECG signals obtained from all volunteers stating the statistical significance between each pair of the experimental stages.

SUMMARY

This chapter presented an overview of the volunteer study where 22 healthy volunteers undertook a 30-second ice pressor test in the right hand while ECG signals, temperature, R and IR PPG signals are being recorded in both hands. R and IR AC amplitudes and DC levels were analysed for baseline, immersion and rewarming stages. The results showed a significant increase in heart rates during the immersion with a full recovery back to baseline values during the rewarming stage. AC amplitudes dropped significantly during the immersion in both hands. A full recovery of AC amplitudes was observed in the left hand during the rewarming period. In the right hand, AC amplitudes increased significantly in the rewarming period when compared to the immersion stage, however, a full recovery was not observed. DC levels increased in both hands during the immersion and continued to increase during the rewarming period.

The morphology of the PPG signal during the immersion underwent significant changes, this included the appearance of a prominent dicrotic notch that was not visible during the baseline period and was eliminated during the rewarming period. In some cases, the morphology of the PPG signal was completely disturbed, not only in the hand exposed to cold but also in the left hand as seen in **Figure 8-7**.

This study is in agreement with previous research that the PPG signal is a valid method for detection of vasoconstriction during a sympathetic stimulation. However, the study highlights further aspects of understanding the PPG signal. The sympathetic stimulation, in this case, is of a localised nature. Still, the PPG signal was altered in both hands. The fact that both hands recovered in different patterns during the rewarming period emphasises that there are generic factors that alter the whole blood circulation during the cold pressor test.

The cold pressor test was long related to changes in blood pressure. Heart rate increases are also associated with changes in stroke volumes, arterial stiffness, and pressure values. All of which might affect blood rheological properties. This study highlights that factors such as blood pressure, stroke volume, blood rheology and arterial stiffness may play a major role in changes in the AC amplitudes and DC levels of the PPG signal.

The next chapter features a controlled *in vitro* pump-arterial model which is designed to investigate the behaviour of PPGs during changes in blood/fluid pressure, wall stiffness and blood/fluid viscosity. This approach allows the possibility to study these factors separately and further eliminate the chemical control of vassal tone. We believe that an *in vitro* approach can provide an in–depth fundamental investigation of the mechanics of the circulation and the way in contributes to the generation of the PPG signal.

Chapter 9
DESIGN AND DEVELOPMENT OF THE *IN VITRO* EXPERIMENTAL SETUP

9.1 Introduction

The previous *in vivo* study have led us to question the effect of the mechanical factors in the circulation on the PPG signal. Such factors include; the pumping power of the heart due to an increase in heart rate, the expected change in blood pressure, arterial stiffness and a possible change in stroke volume and haemorheological properties. We have established that the ultimate way to investigate such factors is by targeting the fundamentals of PPG interaction with the pulsatile flow in a controlled experimental setup. This approach can be achieved using an *in vitro* setup. The setup will be designed to allow control of the pumping action by adjusting pumping rates and stroke volumes, the mechanical properties of the arterial models and the characteristics of the circulating fluid. For a more in-depth exploration of the effect of such factors on the PPG signal and its AC and DC components, pressure and flow signals will also be recorded during the investigations.

This chapter aims to describe the design and implementation of the *in vitro* setup and the allocation of the optical, flow and pressure sensors. A summary of the proposed protocol will be presented and an evaluation of the setup performance will be discussed.

9.2 Setup

The *in vitro* model consists of three main components: the pulsatile pump, the arterial network model, and the reservoir. A block diagram of the designed *in vitro* model is seen in **Figure 9-1.**

The pump: A pulsatile pump (*Model 1423* PBP, Harvard Apparatus, US) was used to generate the pulsatile flow. The pump allows control of stroke volume, and diastolic/systolic time ratio, and pumping rates. It is designed to maintain a laminar flow and minimal haemolysis of blood cells and was maintained to pump continuously during the investigations at a time ratio of 25% for systolic and 75% diastolic phases.

The reservoir: A custom made Plexiglas fluid reservoir (Volume: 5 L) containing the fluid for the circulation was also constructed.

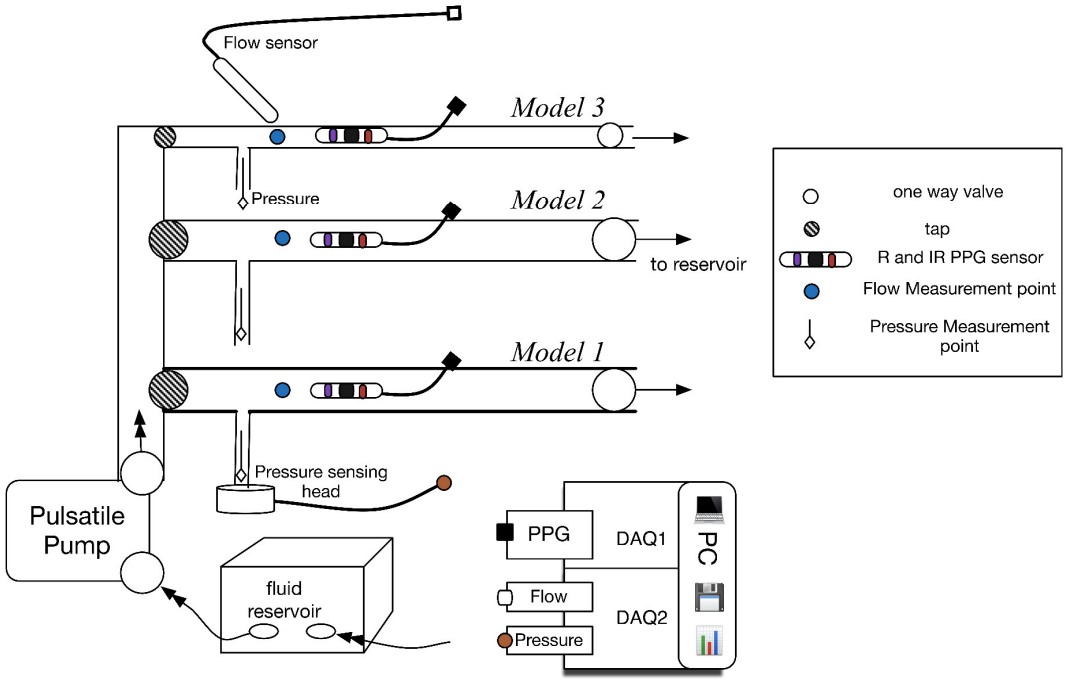

Figure 9-1
Block diagram of the designed pulsatile pump/arterial network model and reservoir.

The arterial network model: An arterial network model was designed to contain the tube models and produce a range of patterns of mechanical forces at the inner surface of the elastic tubing. A flexible PVC tubing (length 20 cm, OD: 22 mm, and ID: 16 mm) was connected to the input of the system to enable the flow to be fully developed before entering the model.

The model consisted of different transparent tubes (Length: 30 cm) with different elasticities. The purpose of the different elastic tubes is to mimic the change from healthy arteries to an advanced stage of ATH with reduced elasticity and increased wall thickness. Three different models of tubes are documented in **Table 9-1** as follows:

-*Model 1*: *Model 1* consisted of a PVC tube (*E*:24 MPa, ID: 16 mm, OD: 1.8) which simulates a large artery affected with ATH, with increased IMT and AS.

-*Model 2*: a silicone rubber tube (E: 6.5 MPa, ID: 16 mm, OD: 0.9 mm) which simulates a healthy artery.

- *Model 3*: a Tygon tube (*E*: 17 MPa, ID: 6 mm, OD: 1) which simulates a small artery.

Table 9-1
Dimensions of the arterial models

	Model 1	*Model 2*	*Model 3*
Inner diameter (mm)	16	16	6
Wall thickness (mm)	1.8	0.9	1
Elastic Modulus (MPa)*	24	6.5	17

*Elastic Modulus was measured using the Instron mechanical testing device

The model was mounted onto a specially designed support system which incorporated rubber clamps to hold the tubes straight at a constant length without interfering with their movement. The support system was resting on the bench top. An initial axial stretch of 1-2% was used to ensure that the flexible tubes remained in a straight position during the pumping phase. One-way check valves (Smart Products, US) with pre-set opening pressure (50 mmHg) were introduced at both ends of each tube which provided the control over the resistance and backwards flow. Valves were also introduced at the entrance of each tube to allow control of flow paths and switch to bypass tube in order to eliminate any bubbles in the system. The room temperature during all *in vitro* experiments was maintained at 23 $\pm$ 0.5 ℃. A picture of the designed setup can be seen in **Figure 9-2**.

9.2.1 Sensors

The sensors fixed on the arterial network included the PPG sensor, the pressure sensor, and the flow sensor. Sensor allocation can be seen in **Figure 9-2**. The tube PPG sensor was previously described in **Chapter 6** and was fixed at the centre of each model. The PPG sensors were located in a position that allows the tubes to expand without imposing significant pressure. The pressure was measured at the entrance of each tube using a

catheter tip research grade transducer (Harvard Apparatus, U.S.) inserted through the lumen of the model.

Flow rates were measured at the centre of each tube using an ultrasound Doppler (MD2, Huntleigh Healthcare, UK) with an 8 MHz probe. A 3D printed holder was also designed to hold the probe at a 60 ° angle with the tube without interfering with the tube's wall motion. The sensor allows the output of two signals, forward and backward flow signals. They will be presented as flow1 and flow2, respectively, due to the interest in velocity profiles, rather than mean flow velocities. The device was then calibrated using the manufacturer instructions, where a voltage signal is generated to correspond to specific Doppler frequencies. Flow velocity was then calculated using the Doppler effect equation.

9.2.2 Instrumentation

PPG processing system: The used PPG processing system was fully described in **Chapter 7**. The recorded R and IR PPG signals were then fed into the PCIe-6321 data acquisition card (National Instruments, UK). The data acquisition was achieved using the LabVIEW VI which was described in **Section 7.7.3.** The signals were recorded for further processing and analysis using the Matlab script described in **Section 7.8.**

Pressure and Flow: The research grade pressure transducer and the ultrasound flow Doppler are both commercially available devices. The outputs of the processing systems were fed into a the 9172-c data acquisition card (National Instruments, UK) and via a LabVIEW, Virtual Instrument to display and record the collected signals for further offline analysis.

9.3 Protocol

The *in vitro* experiments were divided into four stages to investigate different factors and their effect on the AC and DC components of the PPG signal:

1- The role of pumping power, pumping frequency and stroke volume on the generation of the signal in models with different cross-sectional areas. (Highlighting the role of transmural pressure signals and fluid volume).
2- The role of the fluid viscosity on both components of the PPG signal.
3- The role of circulating equine blood highlighting the role of erythrocytes presence and thromboplastin activation on the PPG signal.
4- The role of wall stiffness on the PPG signal.

A more detailed description of the protocol and the used parameters in each stage are summarised in **Table 9-2.**

9.3.1 Fluid Handling

Different fluid mixtures were used during different stages. During the first and fourth experimental stages, Cobalt (II) Nitrate in saline solution (0.9%) was used. Saline solution was used to replicate blood chemical content without the presence of erythrocytes. The solution was prepared using extra pure hexahydrate Cobalt (II) Nitrate powder $Co(NO_3)_2$ (Fischer Scientific, UK) with saline solution to produce 2 L of a 0.6 mol/L solution. During the second experimental stage, extra pure hexahydrate Cobalt (II) Nitrate powder $Co(NO_3)_2$ (Fischer Scientific, UK) was mixed with PEG of molecular weight 6000 (Fischer Scientific, UK) in saline solution to produce 2 L of a 0.6 mol/L solution. The third experimental stage required equine blood. More details on blood testing will be discussed in **Chapter 12**. All fluids underwent a fluid testing protocol as summarised in **Table 9-3**. Fluid density was measured using one ml sample and high-precision scale. The fluid optical properties were measured in the visible and near infrared region using a spectrophotometer (Lambda 1050, Perkin Elmer). Fluid viscosity was measured at shear rates of 40, 60 and 90 rpm using a cone/plate viscometer LVD3T (Brookfield, US). pH and conductivity measurements were obtained using the pH/conductivity meter (Jenway, UK). pH, conductivity, and fluid viscosity were measured at a constant temperature using the circulating water bath (Grant). A photograph of the *in vitro* experimental setup is shown in **Figure 9-3**.

Table 9-2
Parameters used during each stage of the *in vitro* experiments

Stage and focus	Parameter	Value
Stage 1 Pressure, flow dynamics, and cross-sectional area	Fluid	Cobalt Nitrate solution
	Concentration (mol/L)	0.6
	Fluid density (g/m^3)	1.091
	Stroke volume (ml)	30, 70
	Pulsating frequency (Hz)	0.67, 1, 1.8
	Model	1 and 3
Stage 2 Wall Stiffness	Fluid	Cobalt Nitrate solution
	Concentration (mol/L)	0.6
	Fluid density (g/m^3)	1.091
	Stroke volume (ml)	30, 70
	Pulsating frequency (Hz)	0.67, 1, 1.8
	Model	1 and 2
Stage 3 Fluid viscosity	Fluid	Cobalt Nitrate + Cobalt Nitrate PEG6000 solution
	Concentration	0.6
	Fluid density	1.110
	Stroke Volume(ml)	30, 70
	Pulsating Frequency (Hz)	0.67, 1, 1.8
Stage 4 Blood rheology: RBC's presence and clotting	Fluid	Whole equine blood
	Fluid density	1.025
	Ht concentration	0.45
	Stroke volume (ml)	30, 70
	Pulsating frequency (Hz)	0.6, 1, 1.5,1.9

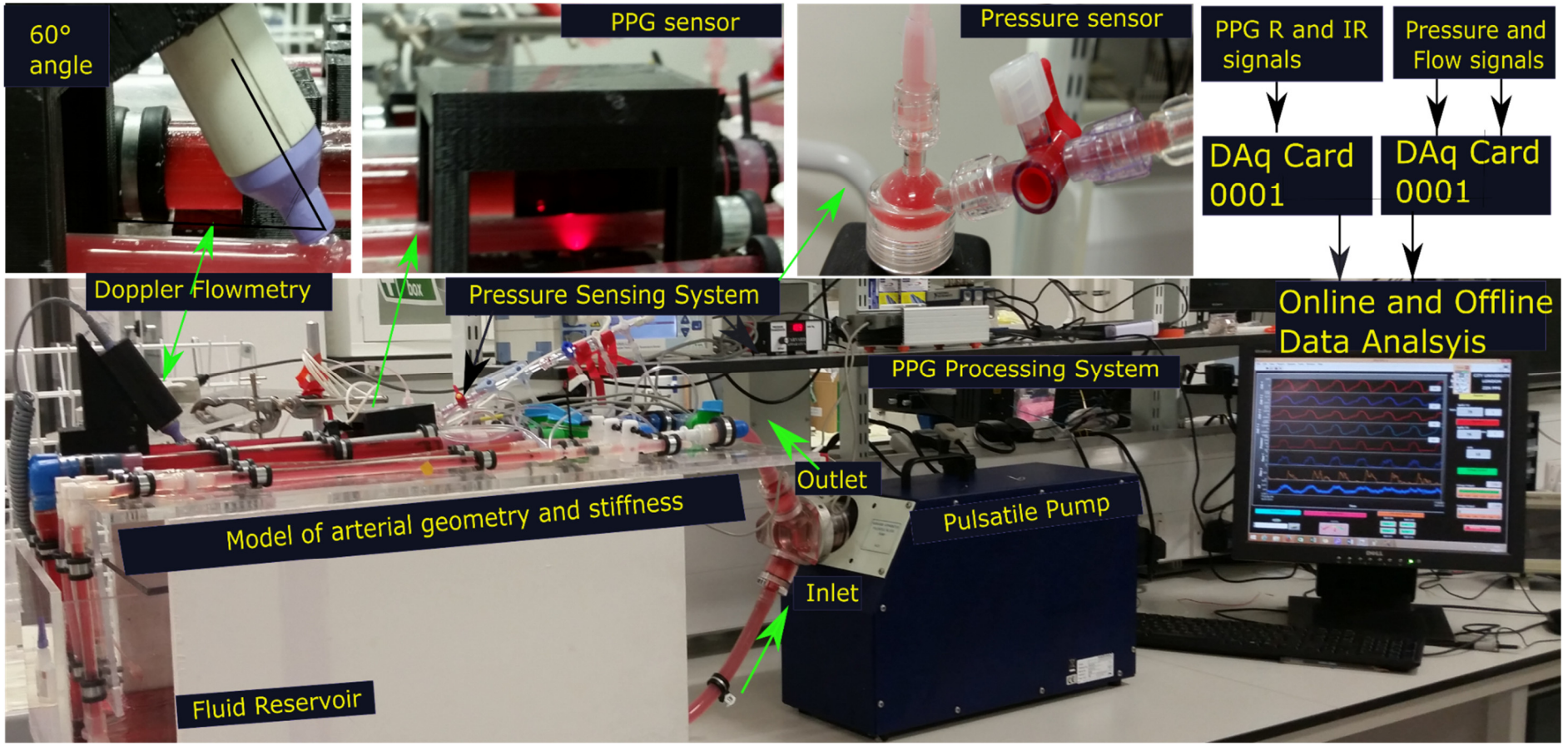

Figure 9-2
The designed and fabricated hydraulic system including the pulsatile pump, the arterial network model, the flow, pressure and PPG sensors, the processing systems and the data acquisition system.

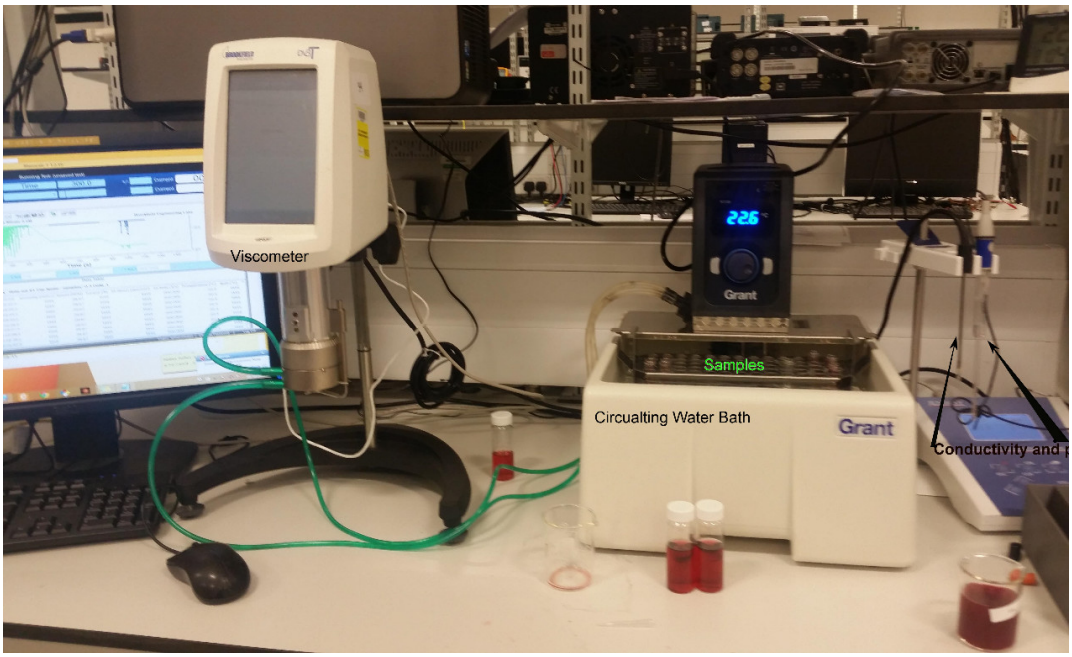

Figure 9-3
Experimental Setup for measurement of mechanical and electrical fluid properties. Showing temperature-controlled water bath containing fluid samples and the conductivity/pH probes. The water bath also circulates to the chamber of the cone/plate viscometer, where viscosity values are measured at varying shear rates.

Table 9-3
Summary of the fluid testing protocol

Test	Device	Comments
Fluid density	Scale, pipette	
Viscosity	Cone/plate viscometer LVD3T, Brookfield, US).	Shear controlled sample 40-100 Rotation per minute
Optical spectra	Lambda 1050, Perkin Elmer, US	Visible and near infrared range
pH levels and Conductivity	pH/conductivity meter, Jenway, UK	

Flow rates were controlled by adjusting the pump to operate for 10 mins at each pumping frequency representing a heartbeat of 40, 60 and 90 bpm. This was followed by a change in flow rates by adjusting the stroke volume from 30 ml to 70 ml. At each stroke volume, the pump was adjusted to pump at the three different pulse frequencies (40, 60, 90 bpm). To avoid any inaccuracies, we assured a bubble-free flow and a steady pulsatile pattern. The designed model allowed bypassing any trapped bubbles and adjustment of pressure

limits by using the one-way check valves installed at each model and stopcocks at the entrance for each model.

9.4 Evaluation

The *in vitro* model was built with an aim to simulate the human pulsatile flow and allow measurements of PPGs, pressure and flow signals in a controlled environment. The controlled parameters are aimed to simulate normal and diseased scenarios of the human circulation and study the effect of the mechanical factors on the generation of the PPG signal. These scenarios include hypotensive, normotensive and hypertensive conditions. An evaluation of the system is presented in this section. This includes observations of flow patterns, the noise generated from the movement of the setup and the quality of the collected PPG, pressure and flow signals.

9.4.1 Flow Patterns

The *in vitro* model was designed to allow fully developed laminar flow in the arterial network model. Following Reynold's observations in 1920, a dye-injection test was used to evaluate the laminar flow in all tubes. The pump was set to operate at 1 Hz, while the reservoir contained 2 L of tap water. One ml of cobalt nitrate solution was injected at the entrance of each tube through the lumen. The pattern of the dye flowing in the tube was observed. As seen in **Figure 9-4**, the injected dye at the entrance of the tube travelled in a clear streakline located at the centre of the tube. There is no evidence of any diffusion occurring within the surrounding layers. This experiment was repeated in all arterial models and it was established that the governing flow is a laminar flow.

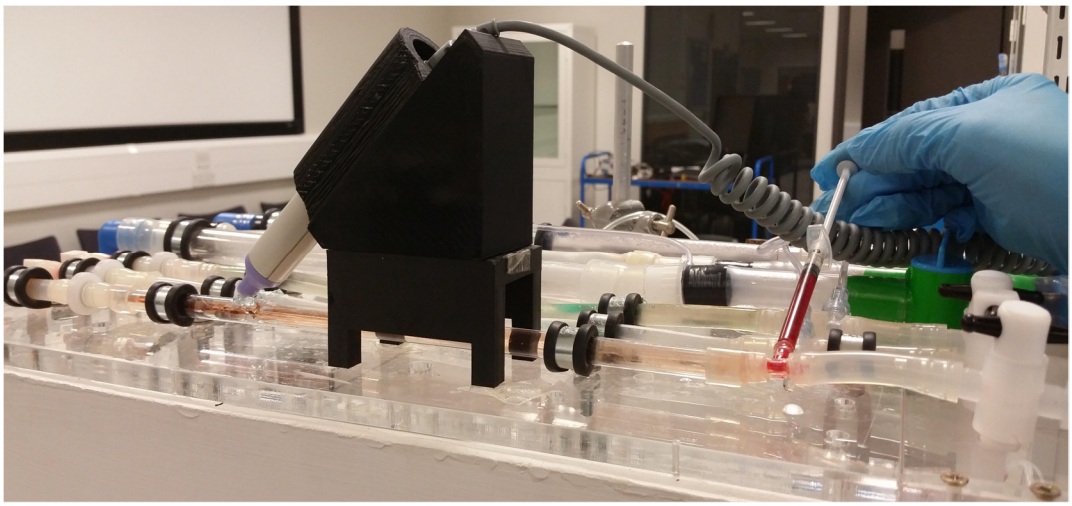

Figure 9-4
Laminar flow evaluation test: One ml dye injection test was used to observe flow pattern in distilled water circulation. The dye can be seen to flow in the middle of the tube with the no-mix layer as expected in laminar patterns.

9.4.2 Noise

The PPG generation from the pulsatile flow is known to be related to volumetric changes. Our understanding is that fluid and wall movement are both important in this process. However, it is important to monitor any noise that is originally generated from the setup due to the shaking or movement of the platform or the arterial models. In order to evaluate such effects, the pump was set to operate without any fluids. The signals were normally recorded and observed. **Figure 9-5** shows a sample of the obtained PPG signals, pressure, and both forward and backward flow signals as obtained from the pulsating empty pump. The pump was set to operate at 70 ml of stroke volume at 1 Hz of pumping frequency.

It is clear that there is no presence of pulsating component in all the signals. For further confirmation, the power spectral density was generated using a custom written script in Matlab. As seen in **Figure 9-6,** it is clear that the pulsating component is not present and that there is a minimal amount of noise specifically at 10 Hz which can be eliminated using a low-pass filter.

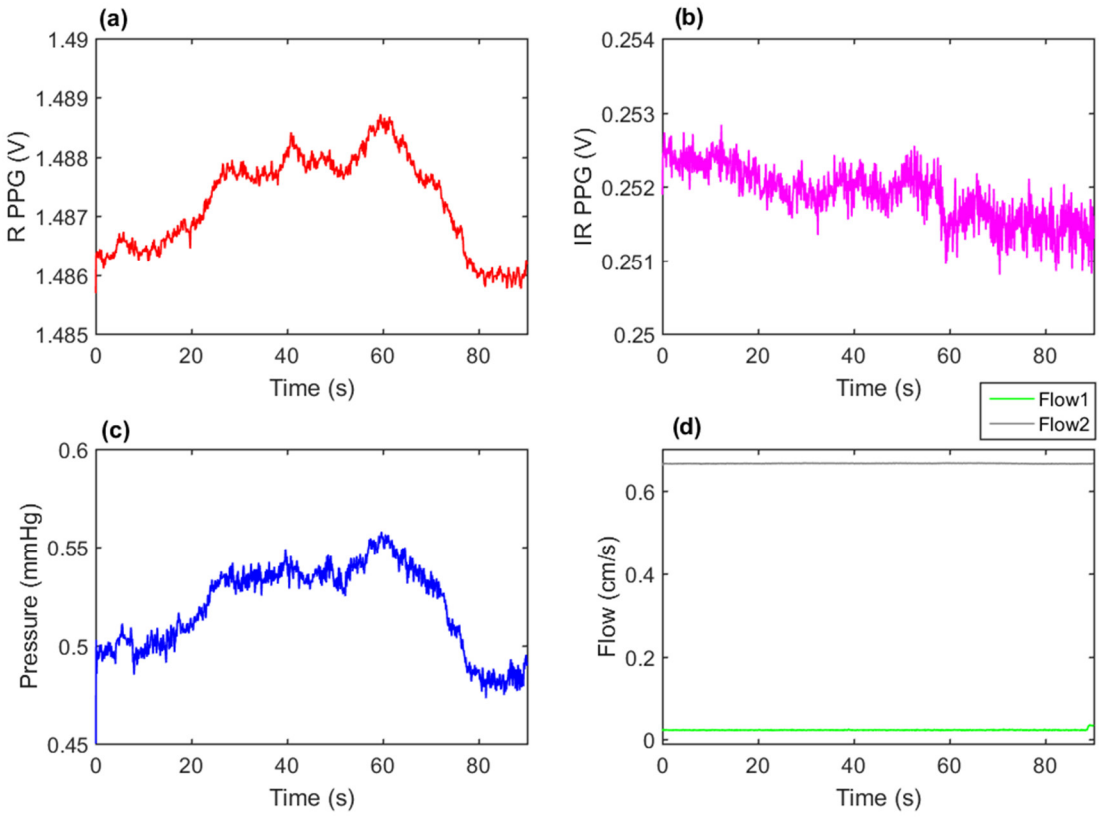

Figure 9-5
Signals collected while the pump is operating without any fluid. (a) Red PPG signals (b) IR PPG signals. (c) Pressure signals. (d)forward (Flow1) and backward (Flow2) flow velocity signals.

SNR is calculated to range from 39 to 55 dB. The lower limit is estimated using the maximum noise observed at 0.4 mV and the minimal noise observed of 0.02 V, 39 dB. The minimum amount of noise observed from an empty pump was estimated at 0.2 mV and considering the maximum PPG signal observed is 0.05 V, and hence the upper limit for the noise-to-signal-ratio is 55dB.

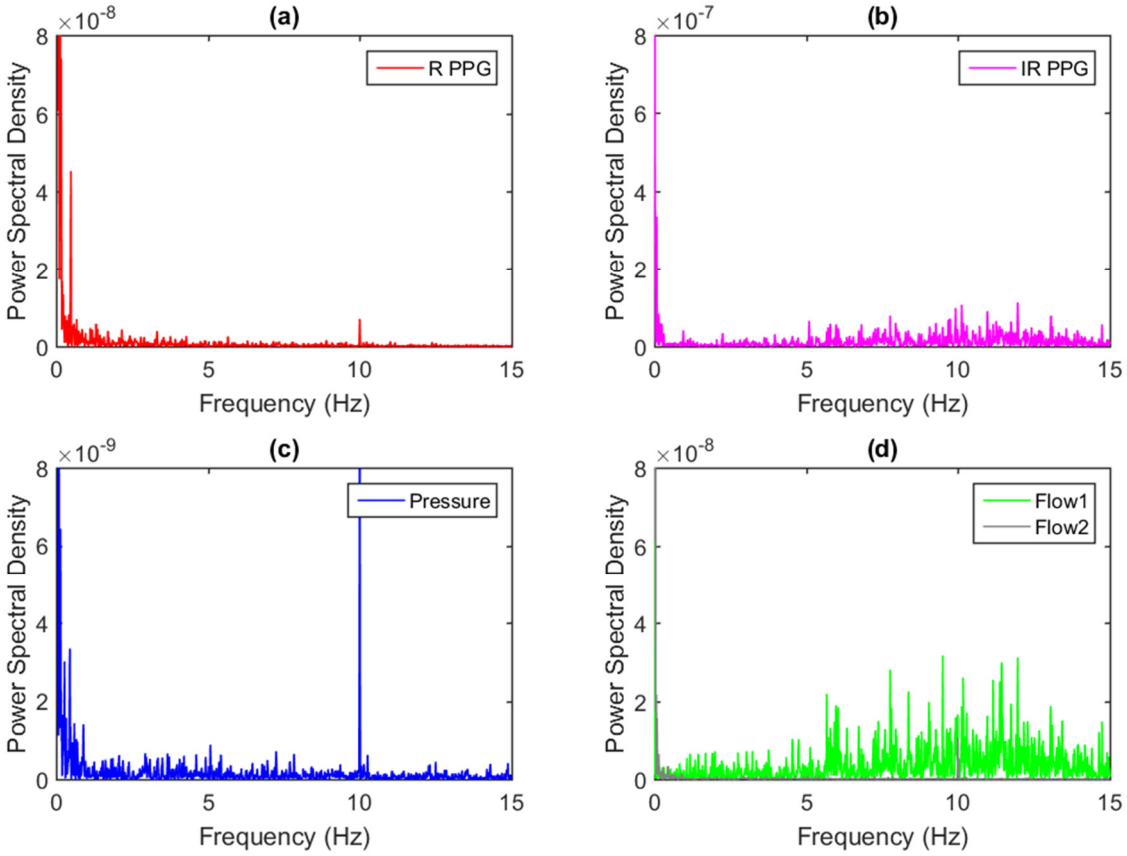

Figure 9-6
Power Spectral Density for the collected signals while the pump is operating without any fluid. (a) Red PPG signals (b) IR PPG signals. (c) Pressure signals. (d)forward and backward flow velocity signals.

9.4.3 Collected Signals

9.4.3.1 Optical signals

The obtained PPG signals were of high quality. In order to evaluate the PPG signals, two sensors were aligned along the arterial model. The two sensors were located at a distance of 10 cm apart. The signals are obtained at low and high resistance to evaluate the quality of the PPG signals even at low flow rates. **Figure 9-7** shows R and IR PPG signals from both sensors (Sensor 2 at the entrance of the model and sensor 1 closer to the end of the model). The signals are obtained from *Model 1* at 70 ml of stroke volume, 1 Hz pulsating

frequency while circulating Cobalt Nitrate-distilled water solution with a concentration of 0.45 M. The signals are combined AC and DC PPGs, low-pass filtered with a cut-off frequency of 40 Hz.

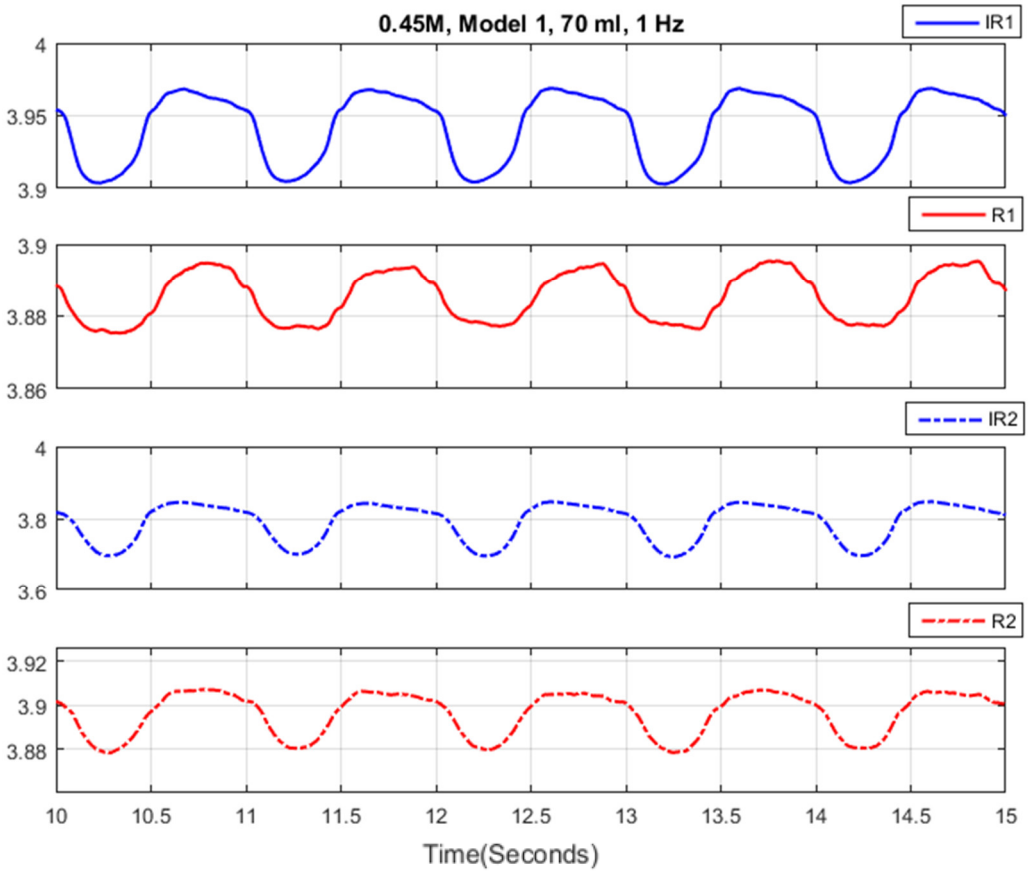

Figure 9-7
R and IR PPG signals obtained from Model 1 from two sensors (R1 and IR1 at the end of the model and R2 and IR2 at the model entrance region). Stroke volume of 70 ml and pumping frequency of 1 Hz. The fluid is circulating only in Model 1 which simulates high resistance circulation.

Figure 9-8 shows R and IR PPG si gnals from both sensors (Sensor 2 at the entrance of the model and sensor 1 closer to the end of the model). The signals are obtained from *Model 1* at 70 ml of stroke volume, 1 Hz pulsating frequency while circulating Cobalt Nitrate-distilled water solution with a concentration of 0.45 M. The signals are combined AC and DC PPGs, low-pass filtered with a cut-off frequency of 40 Hz. The flow was controlled to circulate in *Model 1* and *Model 2* to simulate low resistance flow.

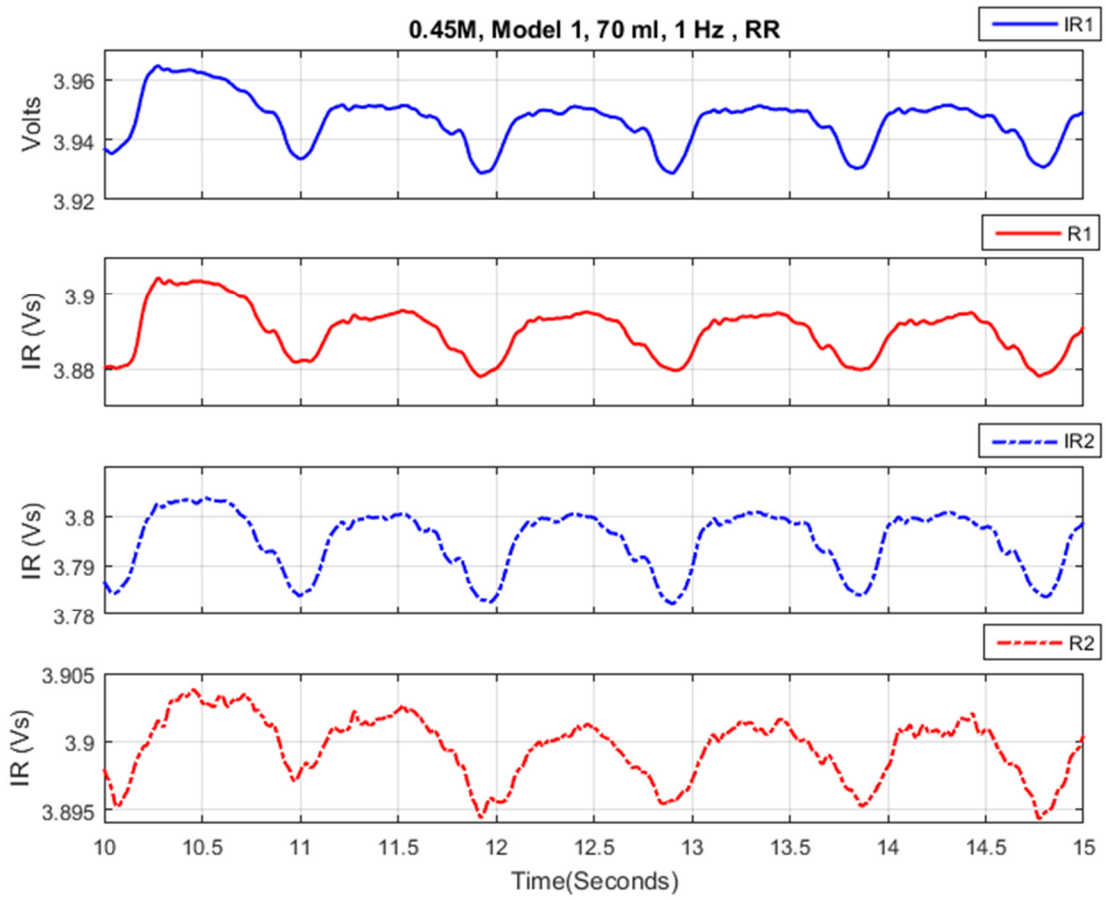

Figure 9-8
R and IR PPG signals obtained from *Model 1* from two sensors (R1 and IR1 at the end of the model and R2 and IR2 at the model entrance region). Stroke volume of 70 ml and pumping frequency of 1 Hz. The fluid is circulating in *Model 1* and *Model 2* which simulates low resistance circulation.

It is evident that the PPG signals are of good quality with both sensors showing similar morphology at both red and IR wavelengths. This observation highlights that the flow is fully developed and there is minimal difference in the PPG signal when obtained from different locations in the same model. As expected, PPG signals presented in **Figure 9-7** show better quality signals with larger amplitude and smoother morphology. While, at a lower resistance, where flow velocity is reduced, PPG signals presented in **Figure 9-8** still show acceptable PPG signals, however, the amplitude is reduced and the morphology is not as smooth. This evaluation test has established that the obtained PPG signals are of good quality even at very low flow resistance. The test also assessed in setting the limits for flow resistance that can provide PPG signals with better quality.

9.4.3.2 Pressure signals

The pressure diastolic and systolic values can be controlled via the pumping power of the pump by altering the stroke volume and the pumping speed. Also, it can be controlled

with the column height of the water in the reservoir and the position of the reservoir. The system was designed to give normal pressure signals (simulating normotensive scenarios) at 30 ml of stroke volume and 1 Hz in *Model 2*. The allocation of the reservoir and the overall resistance of the circulation was adjusted to obtain the normotensive scenario, which seen in **Figure 9-9.** For evaluation purposes, a normotensive and a hypertensive scenario were tested in *Model 2* as can be seen in **Figure 9-10**.

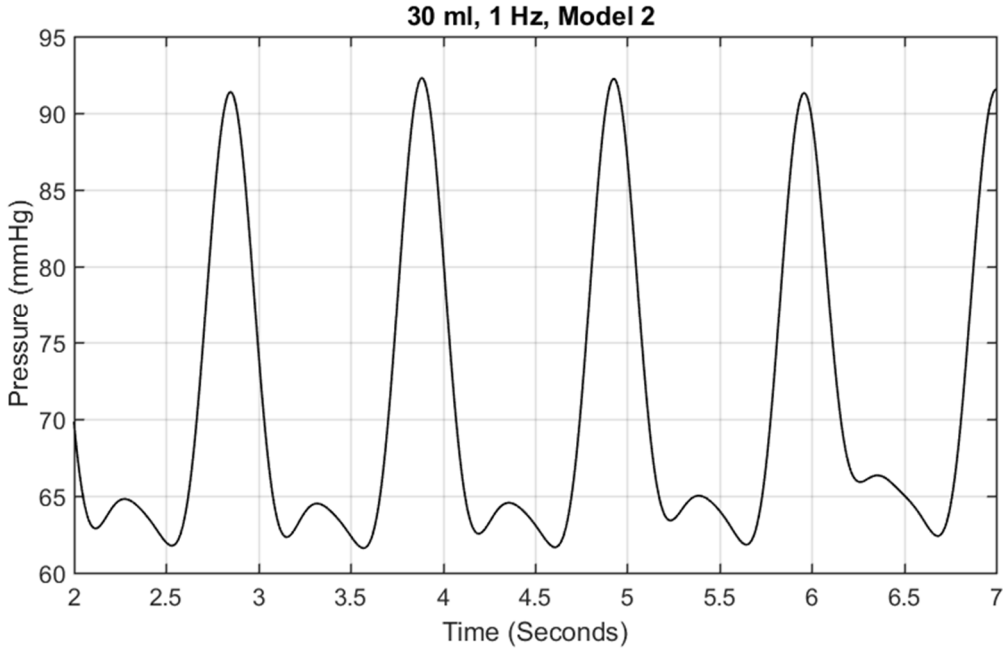

Figure 9-9
Pressure signals obtained from *Model 2* at a stroke volume of 30 ml and pulsating frequency of 1 Hz. The limit of 91/62 is perceived as a simulation of a normotensive scenario.

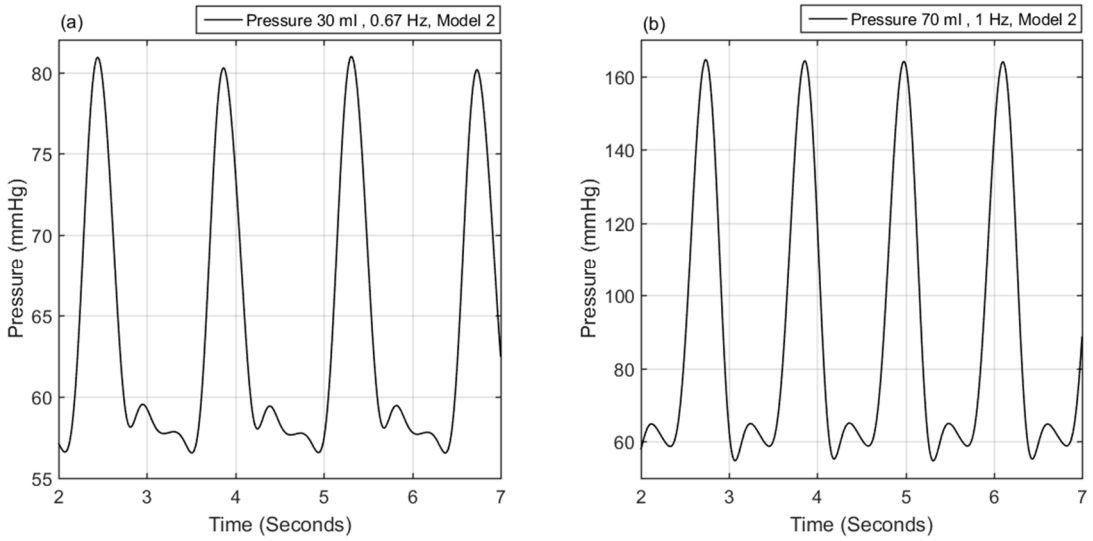

Figure 9-10
Pressure signals obtained from *Model 2*. (a) Hypotensive scenario obtained at a stroke volume of 30 ml and pumping frequency of 0.67 Hz with a systolic/diastolic ratio of 81/57. (b) The hypertensive scenario at a stroke volume of 70 ml and pumping frequency of 1 Hz with a systolic/diastolic ratio of 161/60.

It is clear that the recorded pressure signals are of good quality and in agreement with the limits of normal systolic/diastolic ratio for a normotensive scenario. The hypotensive and hypertensive scenarios are clearly reflected in the systolic pressure values, however, the change in the diastolic value is less visible according to the required limits. The diastolic value is majorly affected by the fluid column height and reservoir location, both of which will not undergo any changes throughout the experiment.

9.4.3.3 Flow signals

The ultrasound Doppler (MD2) was used to detect flow velocities using the Doppler shift method. Placing the probe to target the middle of the tube at a fixed angle is of importance and the pressure exerted at the tube is of relevance. The 3D designed probe holder is seen in this section, and is also pictured in **Figure 9-2** and **Figure 9-4**. A close up of the holder and the ultrasound probe is seen in **Figure 9-11**.

However, it is important to mention, that the probe was fixed with a small gap separating it from the tube, hence, at high pumping speeds and high stroke volumes, the radial displacement of the pulsating model might exert forces on the probe and alter the signal. This might produce weaker signals at low stroke volumes and pumping speeds. However, this measurement was utilised as guidance and was not crucially required for validation of the results. Forward and backward flow signals are obtained for the same limits previously used for pressure signals. **Figure 9-12** shows flow velocity signals obtained from a normotensive simulation.

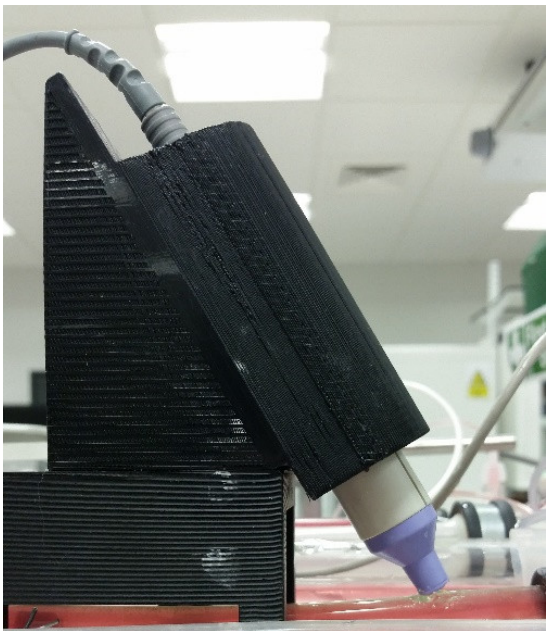

Figure 9-11
8 MHz Ultrasound probe and 3D designed holder.

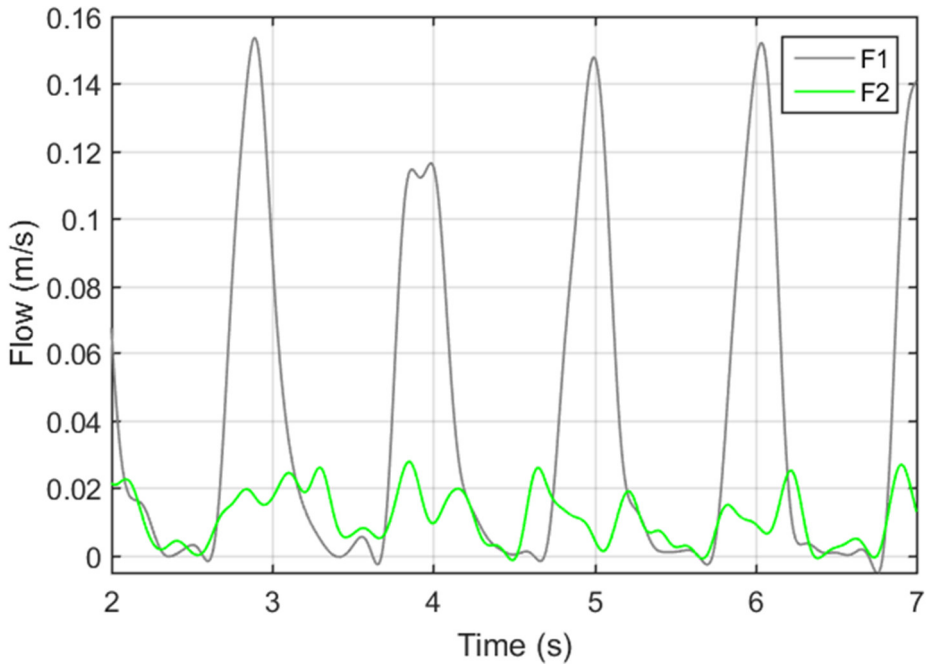

Figure 9-12
Forward and backward flow signals obtained from *Model 2* at a stroke volume of 30 ml and pulsating frequency of 1 Hz. The limit of 91/62 is perceived as a simulation of a normotensive scenario.

Figure 9-13 shows forward and backward flow velocity signals obtained from a hypotensive and hypertensive simulations in *Model 2*.

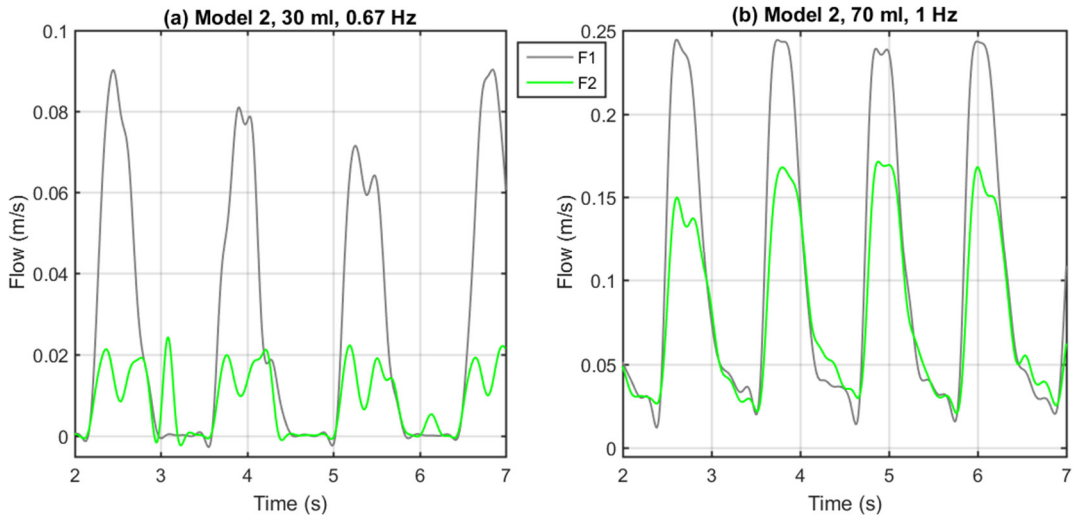

Figure 9-13
Pressure signals obtained from *Model 2*. (a) Hypotensive scenario obtained at a stroke volume of 30 ml and pumping frequency of 0.67 Hz (b) Hypertensive scenario obtained at a stroke volume of 70 ml and pumping frequency of 1 Hz.

It is evident from **Figure 9-12** and **Figure 9-13** that the recorded forward and backward flow signals are of high quality and in agreement with the expected change of flow velocities with the changing pumping speeds and stroke volumes.

SUMMARY

This chapter presented the design and development of the *in vitro* setup and sensor allocation. A summary of the *in vitro* experimental protocols was presented. The preparation and testing methods of the chemical and physical properties of the used fluids were presented. Finally, the PPG, pressure, and flow signals were evaluated under different flow conditions to check the quality of the acquired signals. The signals are of good quality with high signal-to-noise-ratio. The following chapters will describe in detail the first stage of *in vitro* experiments where the focus is directed towards the effect of stroke volumes, pumping frequencies and cross-sectional areas on the components of the PPG signal.

Chapter 10
IN VITRO INVESTIGATIONS OF PPG INTERACTION WITH PULSATILE FLOW

10.1 Introduction

This chapter will present the first stage of experiments using the *in vitro* setup described in the previous chapter. Primarily, by analysis of both components (AC and DC) of R and IR PPG signals, forward and backwards flow velocities and pressure values under distinctive flow conditions. Flow patterns are controlled by a change in stroke volumes and pumping frequencies in two arterial models with different cross-sectional areas.

The focus of this chapter is the utilisation of PPGs in the non-invasive measurement of pressure. As previously discussed in **Chapter 3,** the interest in the PPG technique arises as it might hold the potential for a non-invasive, affordable, practical and continuous monitoring tool for blood pressure.

Previous studies have not provided a sufficient understanding of the behaviour of the PPG signal with the dynamics of the flow. We were unable to identify any studies that thoroughly addressed the effect of flow and pressure changes in the PPG signal. It seems that most investigators have rested on the assumption that the PPG signal is a direct product of volume pulsations, and they have, in our opinion failed to investigate rigorously the relationship of PPG and pulsatile flow in an effort to further understand the origin and the nature of the DC and AC components of the PPG signal.

The question that arises is, even if PPG is a sole product of volume changes, is the signal a measure of volumetric strain? If it is, does it allow a direct and reliable measurement of

pressure values from the Pressure-Volume relationship? And how do stroke volumes, cross-sectional areas, and pumping frequencies affect this relationship?

This chapter aims to address these questions and investigate the role of pumping rates, stroke volumes, and tube cross-sectional area in altering the AC and DC PPG components at both wavelengths. Moreover, we compare raw, normalised and adjusted pulse volume values in providing an accurate tool for pressure measurements. Finally, we aim to draw a conclusion of the potential and limitations of the PPG technique to provide a reliable measure of transmural pressure values.

10.1.1 Principles

Pressure-Volume (P-V) relationship is known to follow an exponential behaviour over a limited pressure range in the human circulation (Baker et al., 1997; Burkhoff et al., 2005) as noted in equation (10.1). Our assumption is that this practice is valid in the developed *in vitro* model which mimics the mechanics of the human circulation.

$$P = b\exp(nV) \tag{10.1}$$

Here b and n are parameters of the model.

When we apply PPG to an arterial model, total light intensity can be written as a function of fluid volume, given that the distance between the light sources and the photodetector is constant. The pulsatile volume is a combination of an oscillatory component $(\tilde{V}_o)$ and a steady component $(\bar{V}_s)$. Assuming that Lambert-Beer's Law holds, the following equation can express the relation between the total incident (I_o) and total transmitted light (I):

$$I = \exp(-\varepsilon_s c_s \bar{V}_s)\exp(-\varepsilon_o c_o \tilde{V}_o) I_0 \tag{10.2}$$

Where, c is the concentration of the light-absorbing substance in each component and ε is the absorbance coefficient. The subscripts, o and s, denote oscillatory and steady components respectively. Given that $(\bar{V}_s)$ is constant at the same pressure and wall elasticity, (10.3) holds for the steady volume component:

$$\bar{I} = \exp(-\varepsilon_s c_s \bar{V}_s) I_0 \tag{10.3}$$

Where, $(\bar{I})$ is constant light intensity obtained from the steady volume layer.

Hence, from (10.1) and (10.3), the following can be derived

$$\tilde{V}_o = (-\varepsilon_o c_o)^{-1}.\ln(\Delta I_{\lambda 1}/\overline{I}_{\lambda 1}) \tag{10.4}$$

Where $\Delta I_{\lambda 1}$ is the amplitude of the oscillatory optical signal, and $\overline{I}_{\lambda 1}$ is the level of the steady optical signal, at a particular wavelength ($\lambda 1$). It is noted that $\ln(I_{\lambda 1}/\overline{I}_{\lambda 1})$ is in direct proportion to the oscillatory component of the total fluid volume $(\tilde{V}_o)$, via the unknown constant term $(-\varepsilon_o c_o)$, presuming that both are constant. Hereafter, normalised pulse volume (NPV) is given by:

$$NVP = \ln(\Delta I_{\lambda 1}/\overline{I}_{\lambda 1}) \tag{10.5}$$

The reliance of the penetration depth on light wavelength is well documented (Stolik et al., 2000), and this concept is used in deriving the adjusted pulse volume (APV). The volume of steady flow layer is known to develop in the centre of the tube, where light with longer wavelength provides a better estimation, and the oscillatory flow occurs in layers closer to the wall, where shorter wavelengths provide a more accurate estimate, therefore:

$$\overline{I}_{\lambda 2} = \exp(-\varepsilon_s c_s \overline{V}_s) I_0 \tag{10.6}$$

Given that $\lambda_2 > \lambda_1$, (10.2) and (10.6) lead to

$$\tilde{V}_o = (-\varepsilon_o c_o)^{-1}.\ln(\Delta I_{\lambda 1}/\overline{I}_{\lambda 2}) \tag{10.7}$$

Given that $(-\varepsilon_o c_o)$ is constant. Hereafter, the adjusted pulse volume (APV) is referred to as

$$APV = -\ln(\Delta I_R/\overline{I}_{IR}) \tag{10.8}$$

Equation (10.1) is rewritten as:

$$\ln(P_s) = n\tilde{V}_o + \ln(b) \tag{10.9}$$

Where, P_s is the systolic pressure signal that drives the oscillatory fluid volume. It was previously noted that NPV and APV are in direct proportion to the oscillatory component of the fluid volume $(\tilde{V}_o)$ via the unknown constant term $(\varepsilon_o c_o)$. In this study, both parameters are kept constant in a controlled setup to validate the derived relationship. Therefore, (10.9) can be finally rewritten to give the following:

$$\ln(P_S) = n.NPV_R + \ln(b) \quad (10.10)$$

$$\ln(P_S) = n.NPV_{IR} + \ln(b) \quad (10.11)$$

$$\ln(P_S) = n.APV + \ln(b) \quad (10.12)$$

Finally, the effect of pumping frequencies and stroke volumes will be considered in the *in vitro* investigations. Both factors directly affect the pumping power which will be addressed in relation to PPG. Pumping power of a hydraulic pump can be expressed by the following equation (Cetinkunt, 2015):

$$W = \frac{f.SV.\Delta P_p}{\eta} \quad (10.13)$$

Where, W denotes power (W), f is stroke frequency (Hz), SV is stroke volume (m^3), ΔP_p is pressure difference over pump (Pa), η ,is the mechanical/hydraulic efficiency.

10.1.2 The Purpose of the Study

As briefly mentioned above this study aims to examine the relationship between both components (AC and DC) of R and IR PPG signals with pressure at different flow rates; controlled through pumping frequencies and stroke volume, in an *in vitro* setup.

We specifically target the following factors:

- The role of cross-sectional area in the generation of the PPG signal.
- The effect of changes in mean pressure values due to pumping frequency changes.
- The impact of changes in mean pressure values due to stroke volume changes.
- The validity of the derived relationship of NPV_R, $NPV_{IR,}$ and APV in providing a measure of systolic pressure values in models with the disparate cross-sectional area, at varied pumping rates and at different stroke volumes.

10.2 Protocol

The pump-arterial network setup described in **Chapter 8** and presented in **Figure 10-1** was used for this experiment. The setup was slightly adjusted by directing the flow to *Model 1* and *Model 3* simultaneously, using the stopcocks as illustrated in **Figure 10-1.**

The PPG reflectance sensors (described in Chapter 6) were fixed at the middle of each arterial model. The pressure was measured at the entrance of the tube, after the entrance range, using a catheter tip research grade pressure transducer (Harvard Apparatus, US). An Ultrasound Doppler (MD2, Huntleigh, UK) with an 8 MHz probe was fixed at a 60°

angle to the arterial model for further calculation of forward and backward flow using the Doppler effect. Data collection was performed at a sampling rate of 1000 Hz using the same data acquisition systems previously described (**Chapter 7**) and saved for further offline analysis.

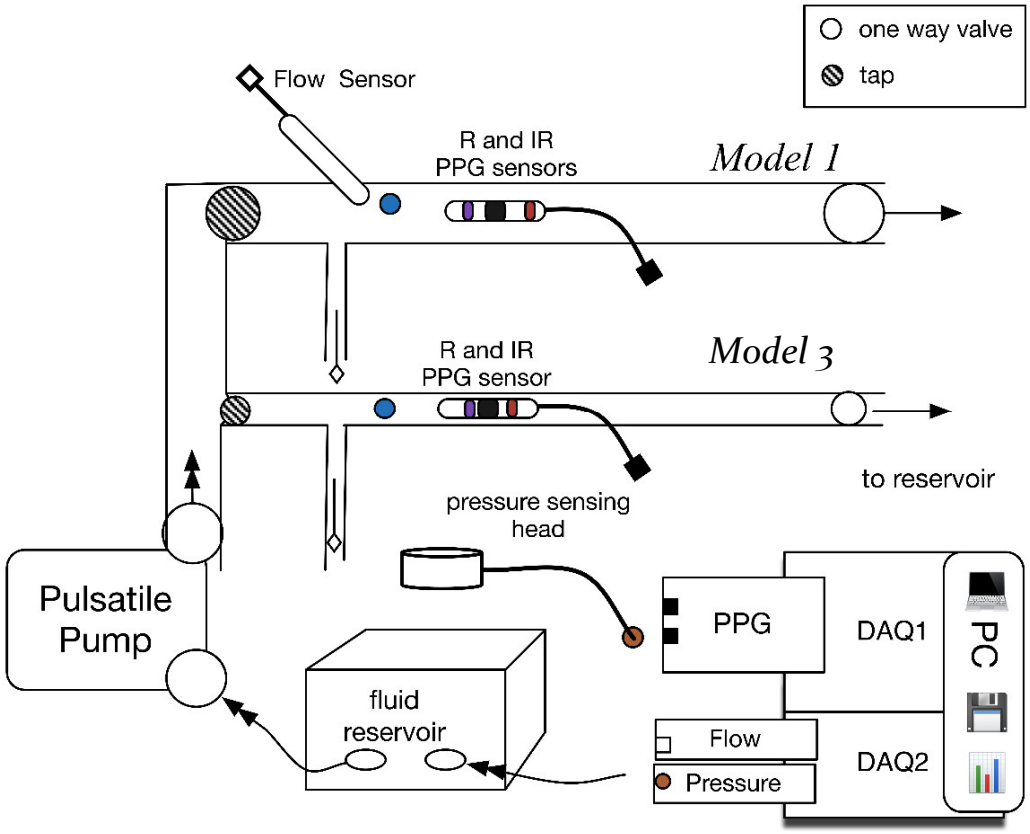

Figure 10-1
Schematic of the *in vitro* Pump Setup adjusted for this experiment.

A summary of the used parameters during the experiment can be seen in **Table *10-1***.

Table 10-1
Parameters used during the experiment

Parameter	Fluid 1 (*v1*)
Solution	Cobalt Nitrate in Saline Solution
Artery properties	*Model 1, Model 3*
Inside Diameter (ID) mm	16, 6
Outside Diameter (OD) mm	1.5, 1
Wall Elastic Modulus (MPa)	24, 17
Stroke volume (ml)	30 ,70 for each model
Density (g/ml)	1.0914
Concentration	0.6 M
Pulsating frequency (Hz)	f_1= 0.67 f_2= 1 f_3= 1.8
Speed (RPM)	40,60,108

The experiment was performed at the following steps:

1) Three litres of 0.6 M of Cobalt Nitrate (Co_2Ni_3) in saline solution were prepared.
2) The fluid optical spectrum was obtained using a sample of the solution in the visible and near infrared range using a spectrometer analyser (Lambda 1050, PerkinElmer).
3) The viscosity of the prepared fluid was measured at the three speeds (40, 60, 100 RPM) using the LVD3T rheometer (Brookfield, US).
4) Fluid pH and conductivity measurements were also obtained using the conductivity/pH meter (Jenway, UK). Both probes are shown in **Figure 10-2**.
5) The pump setup was cleaned and left to dry the previous day. Three litres of the prepared fluid were poured into the reservoir.
6) The pump was left to operate at the initial frequency 0.67 Hz and 30 ml of stroke volume, for 10 mins to assure bubble-

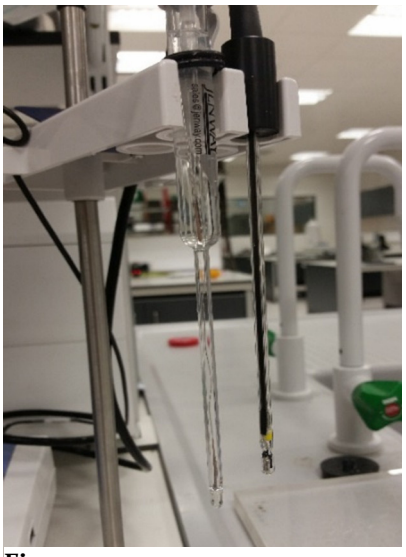

Figure 10-2
pH and conductivity Jenway probes.

free and fully developed flow in a closed loop.

7) Signal recording started after that period and continued for continuous two minutes for the following stages:

- **Stage 1:** Sensors are fixed on *Model 1* and the fluid is circulated under the varying pulsating frequencies at a stroke volume of 30 ml.
- **Stage 2:** Sensors are fixed on *Model 1* where the fluid is circulated under the varying pulsating frequencies at a stroke volume of 70 ml.
- **Stage 3:** Sensors are fixed on *Model 3* as seen in **Figure 10-3** and the fluid is circulated under varying pulsating frequencies at a stroke volume of 30 ml.
- **Stage 4:** Sensors are fixed on *Model 3* where the fluid is circulated under varying pulsating frequencies at a stroke volume of 70 ml.

8) The reservoir, tubes, and the pump were thoroughly cleaned and left to dry.

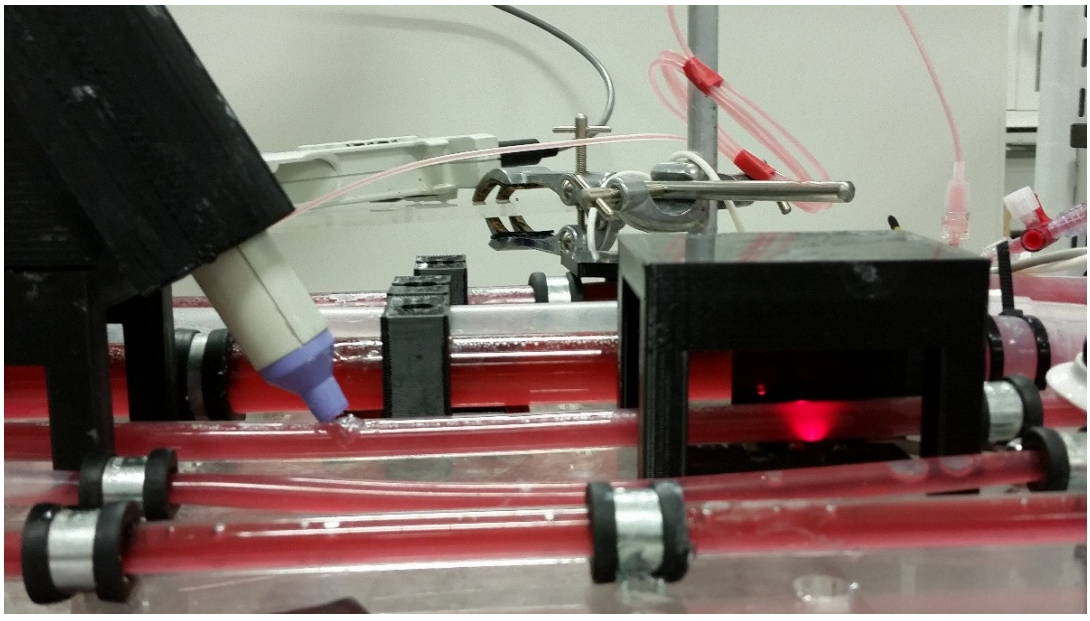

Figure 10-3
Pump Experimental Setup showing sensors connected to *Model 3* .

10.3 Data and Statistical Analysis

In this study, we observed DC and AC signals from the PPG signals, pressure signals, and forward and backwards flow signals. The collected data via the LabVIEW Virtual Software were analysed in the offline custom written script using Matlab. More details describing the script and methods of filtering and data extraction can be found in **Chapter 7**. The Data obtained were Infrared, Red AC and DC PPG signals, pressure signal and both forward and backward flow.

The data was grouped to include values at varying pulsating frequencies (0.67 Hz, 1 Hz, and 1.8 Hz) for each model (*Model 1* and *Model 3*), at both stroke volumes (30 ml and 70 ml). Statistical analysis was performed comparing values at the same pulsating frequency for both models at each stroke volume, and values at different pulsating frequencies for each model.

The data was confirmed to follow a Gaussian distribution by using the distribution fitting tool in Matlab on data samples. Therefore, the data qualified for one-way ANOVA test. This was followed by Sidak's multiple comparison tests to evaluate significance. A significant value is considered if the p-value is less than 0.05, with a 95% confidence interval.

In the case of model fitting, the goodness of the fitting was evaluated with the Sum Square Error (SSE), R-square (r^2) and the Root Mean Square Error (RMSE). Where SSE, shows variation from the mean and R-square is the percentage of the variable response variation.

10.4 Results

In this section, we present the measured values for fluid properties, including the optical spectra in the visible and near-infrared range, conductivity, pH, and viscosity measurements. We further, present visual data from the collected R and IR PPG_{AC} and PPG_{DC} signals; pressure, forward and backward flow, at both stroke volumes and varying pumping frequencies in both models. Furthermore, we present statistical analysis from the processed signals to draw average and standard variations of Infrared AC amplitudes, time ratios, Infrared DC levels, mean pressure values, peak forward and backward flow velocities. These values are tabulated and compared using the Sidak's multiple comparison tests, which compares values at each pumping frequency and different stroke volumes in both models. The statistical comparison shows mean differences, p-value, and summary of significance status. Finally, we present scattergrams of the three proposed methods APV, $NPV_{IR,}$ and NPV_R.

10.4.1 Fluid Properties

The optical spectra in the visible and near infrared region were obtained from the Spectrometer for the prepared fluid and can be seen in **Figure 10-4.** The solution had a conductivity of 77.4 mS and 3.6 pH levels at 22.7 °C. Viscosity measurement at varying shear rates are measured using the cone/plate viscometer for each fluid and are seen in **Figure 10-5**.

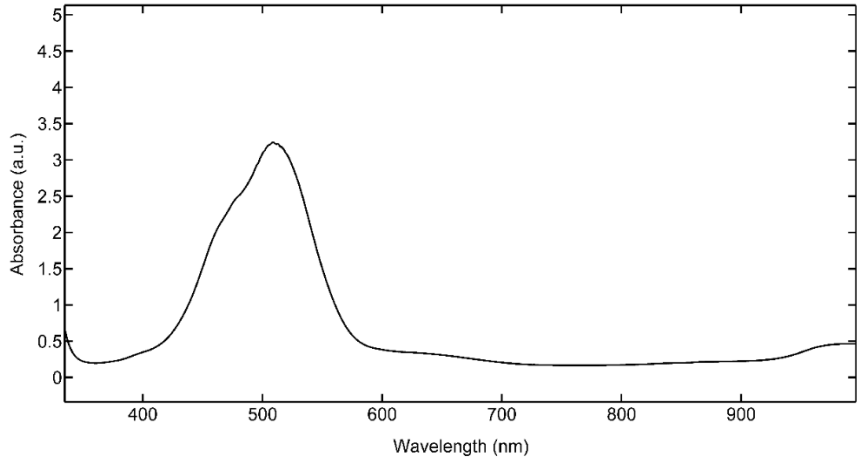

Figure 10-4
Absorption spectra for Cobalt Nitrate solution (Fluid 1) obtained from the spectrometer in the visible and near infrared range.

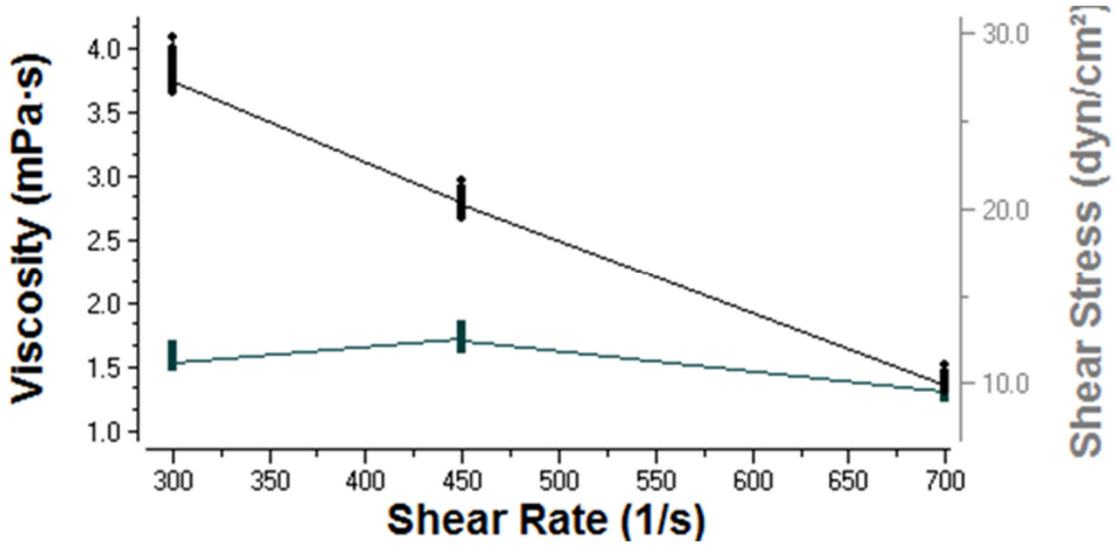

Figure 10-5
Viscosity measured for a 0.5 ml sample of Cobalt Nitrate in saline solution (0.6 M) in cone/plate rheometer at varying shear rates. Samples are collected for five mins (sampling rate 10 Hz) at each shear rate. Figure shows both shear stress values in grey and viscosity values in black.

10.4.2 Effect of Pulse Frequency and Stroke Volumes in *Model 1*

In this section, we observe how pressure, flow and PPG signals are affected by the change of stroke volumes from 30 ml to 70 ml. At each stroke volume, we further investigate the impact of pumping frequencies (0.67 Hz, 1 Hz, and 1.8 Hz).

We present visual results of the collected signals, at each stroke volume and varying pumping frequencies. **Figure 10-6** shows a five-second sample of the collected signal at a frequency of **0.67 Hz** for *Model 1* at both stroke volumes *(right, 30 ml and left, 70 ml).* Panel (a) shows infrared AC (IR_{AC}) and red AC (R_{AC}) signals, panel (b) shows IR_{DC} and

R_{DC} PPG signals. Panel (c) shows Pressure (P), where panel (d) presents forward (F1) and backwards (F2) flow velocities.

Figure 10-7 shows a five-second sample of the collected signal at a frequency of **1 Hz** for *Model 1* at both stroke volumes *(30 ml and 70 ml).* Panel (a) shows infrared AC (IR_{AC}) and red AC (R_{AC}) signals, panel (b) shows IR_{DC} and R_{DC} PPG signals. Panel (c) shows Pressure (P), where panel (d) presents forward (F1) and backwards (F2) flow velocities.

Figure 10-8 presents a five-second of the collected signals at a frequency of **1.8 Hz** for *Model 1* at both stroke volumes *(30 ml and 70 ml).* Panel (a) shows infrared AC (IR_{AC}) and red AC (R_{AC}) signals, panel (b) shows IR_{DC} and R_{DC} PPG signals. Panel (c) shows Pressure (P), where panel (d) presents forward (F1) and backwards (F2) flow velocities.

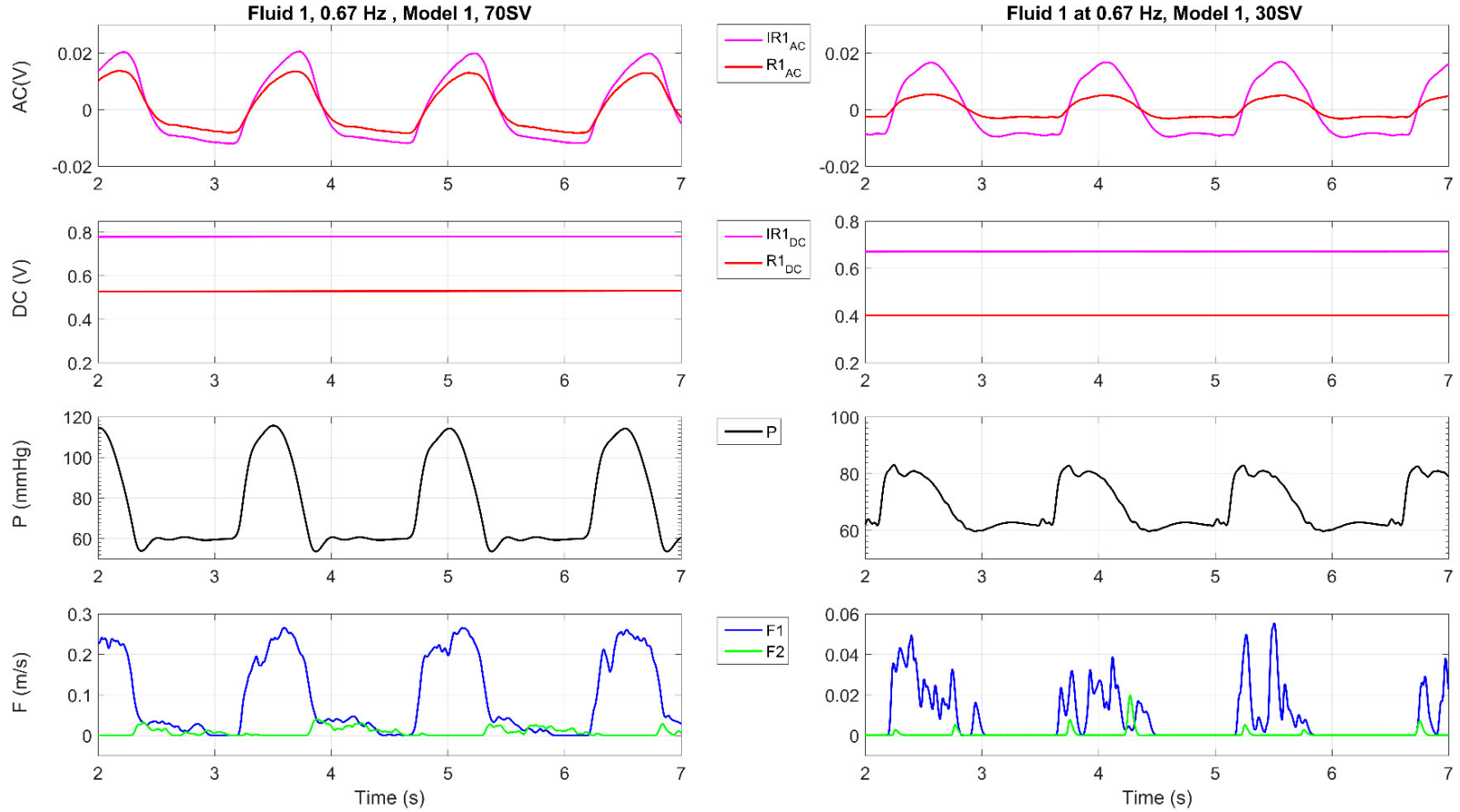

Figure 10-6
From the top, AC PPG signals for Red (R_{AC}) and Infrared (IR_{AC}), DC PPG signals for red (R_{DC}) and infrared (IR_{DC}), Pressure (P), Forward (F_1) and backward (F_2) flow velocities. Signals are obtained at a frequency of 0.67 Hz from Model 1. Signals are seen at a stroke volume of 70 ml (70SV) at left panels and for stroke volume of 30 ml at right panels (30SV).

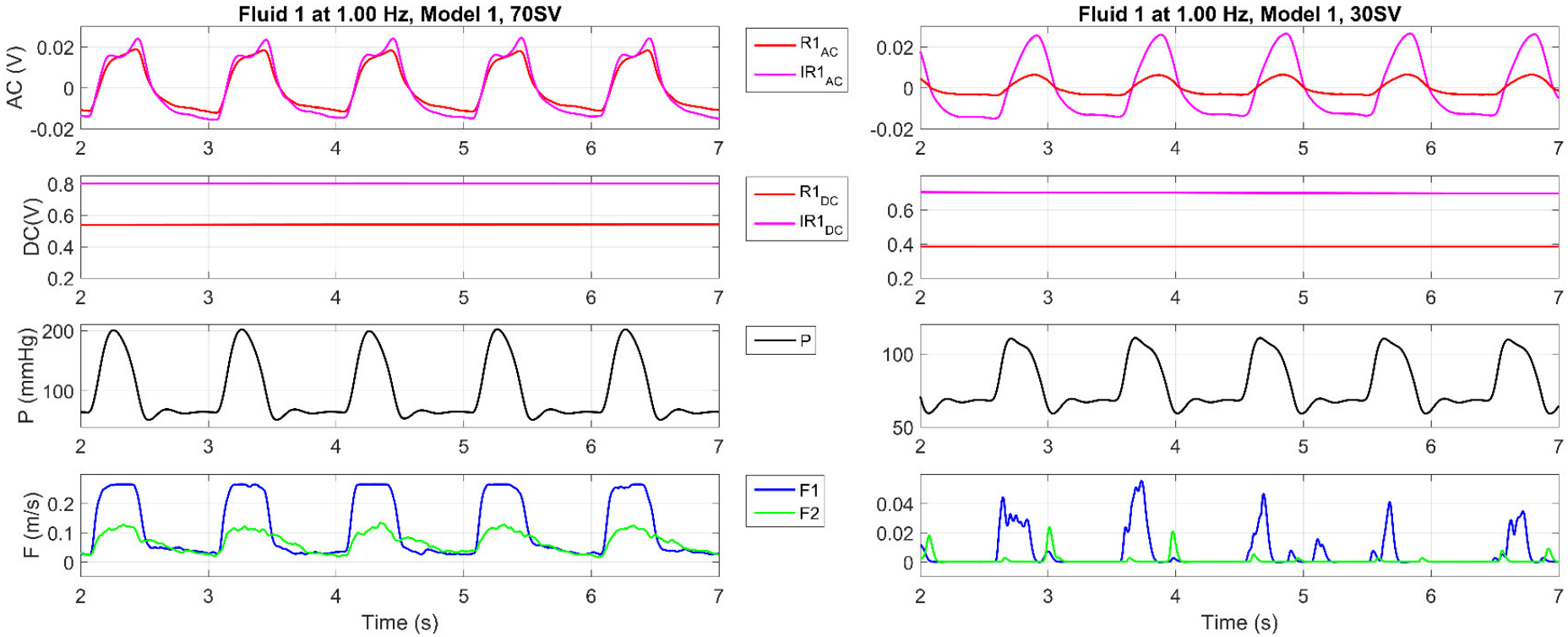

Figure 10-7
From the top, AC PPG signals for Red (R_{AC}) and Infrared (IR_{AC}), DC PPG signals for red (R_{DC}) and infrared (IR_{DC}), Pressure (P), Forward (F1) and backward (F2) flow velocities. Signals are obtained at a frequency of 1 Hz from *Model 1*. Signals are seen at a stroke volume of 70 ml (70SV) at left panels and for stroke volume of 30 ml at right panels (30SV).

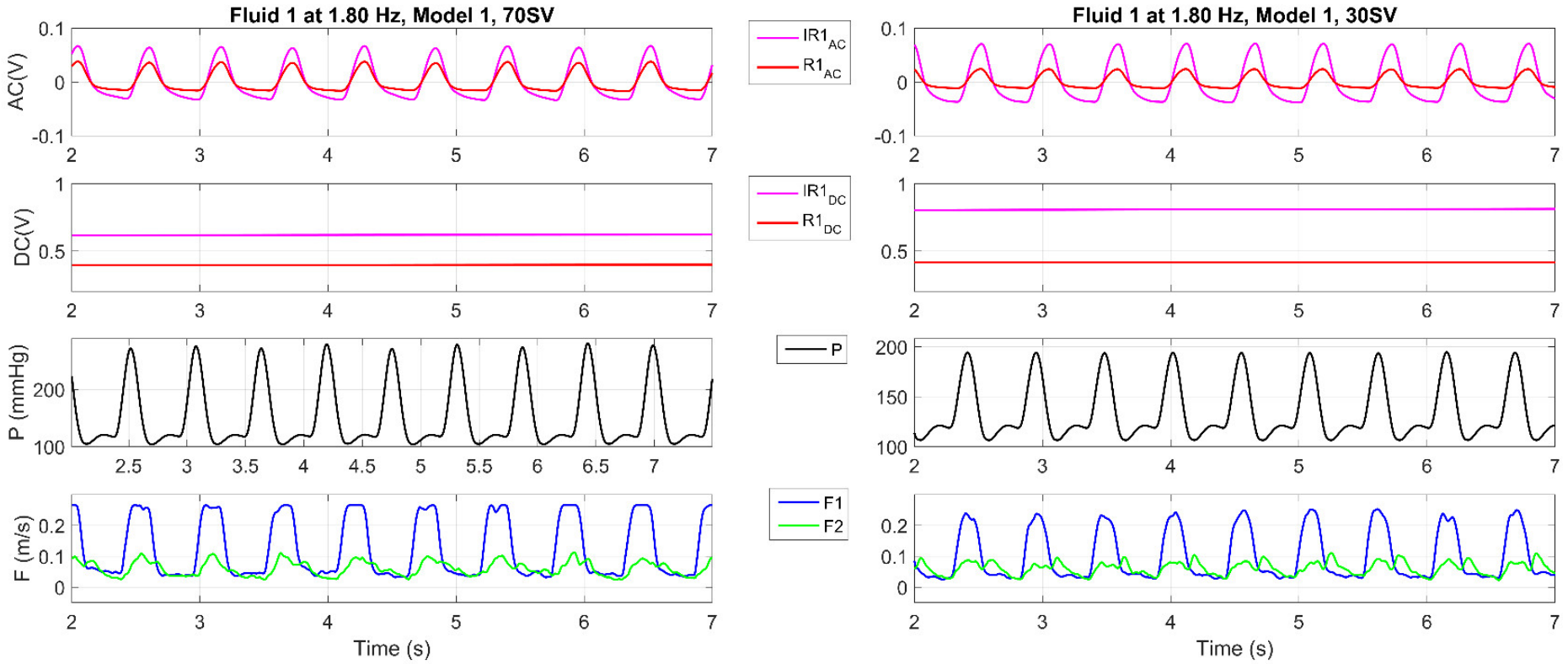

Figure 10-8
From the top, AC PPG signals for Red (R_{AC}) and Infrared (IR_{AC}), DC PPG signals for red (R_{DC}) and infrared (IR_{DC}), Pressure (P), Forward (F_1) and backward (F_2) flow velocities. Signals are obtained at a frequency of 1.8 Hz from *Model 1*. Signals are seen at a stroke volume of 70 ml (70SV) at left panels and for stroke volume of 30 ml at right panels (30SV).

10.4.3 Effect of Tube Diameter at Different Pumping Frequencies and Stroke Volumes

In this section, we observe how pressure, flow and PPG signals are affected by the change of tube diameter at distinct stroke volumes. In each arterial model, we further investigate the impact of pumping frequencies at the equivalent three set-points (0.67 Hz, 1 Hz, and 1.8 Hz).

We present visual results of the collected signals obtained from each arterial model at varying pumping frequencies. **Figure 10-9** shows a five-second sample of the collected signal at a frequency of **0.67 Hz** for *Model 3* at both stroke volumes *(right, 30 ml and left, 70 ml).* Panel (a) shows infrared AC (IR_{AC}) and red AC (R_{AC}) signals, panel (b) shows IR_{DC} and R_{DC} PPG signals. Panel (c) shows Pressure (P), where panel (d) presents forward (F1) and backwards (F2) flow velocities.

Figure 10-10 shows a five-second sample of the collected signal at a frequency of **1 Hz** for *Model 3* at both stroke volumes *(right, 30 ml and left, 70 ml).* Panel (a) shows infrared AC (IR_{AC}) and red AC (R_{AC}) signals, panel (b) shows IR_{DC} and R_{DC} PPG signals. Panel (c) shows Pressure (P), where panel (d) presents forward (F1) and backwards (F2) flow velocities.

Figure 10-11 shows a five-second sample of the collected signal at a frequency of **1.8 Hz** for *Model 3* at both stroke volumes *(right, 30 ml and left, 70 ml).* Panel (a) shows infrared AC (IR_{AC}) and red AC (R_{AC}) signals, panel (b) shows IR_{DC} and R_{DC} PPG signals. Panel (c) shows Pressure (P), where panel (d) presents forward (F1) and backwards (F2) flow velocities.

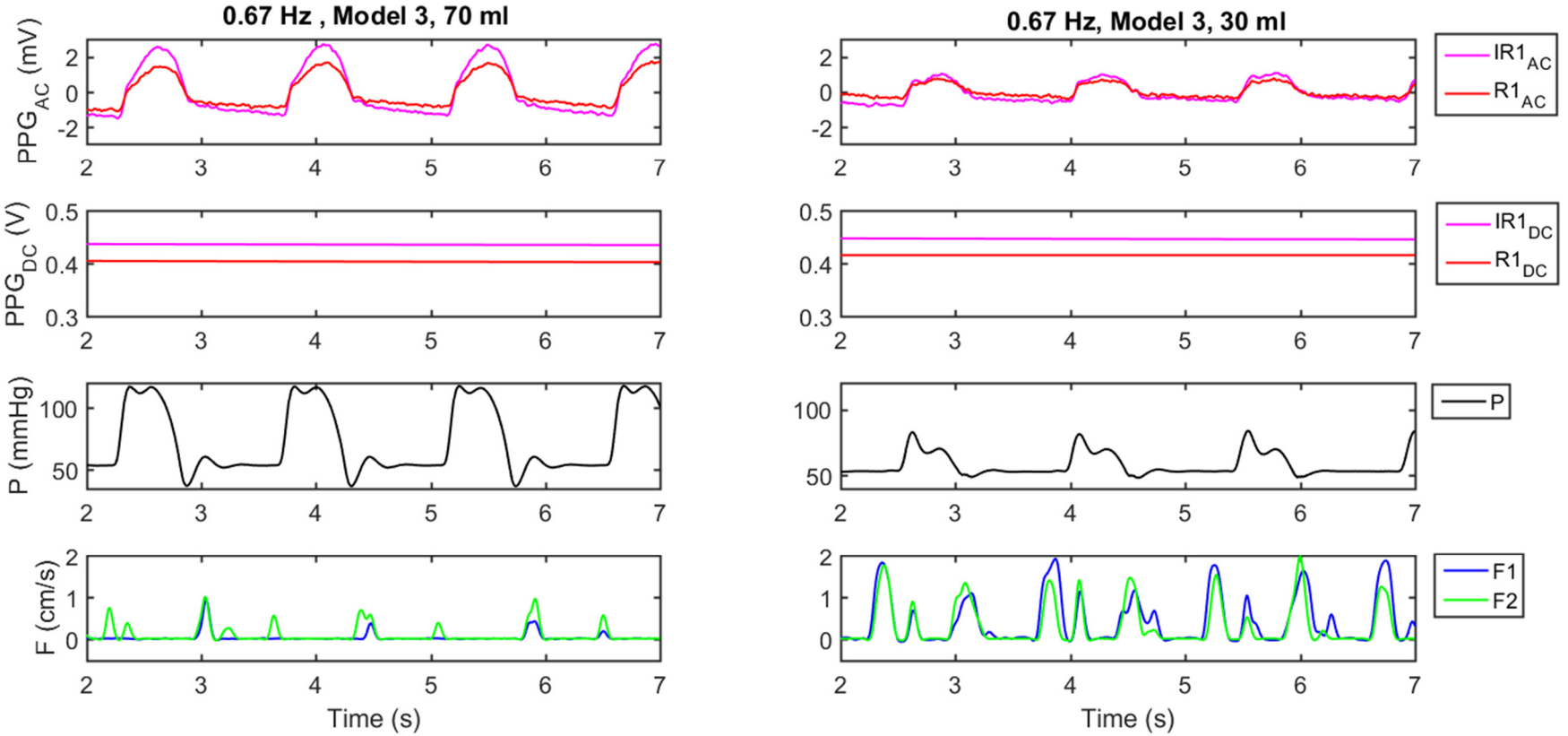

Figure 10-9
From the top, AC PPG signals for Red (R_{AC}) and Infrared (IR_{AC}), DC PPG signals for red (R_{DC}) and infrared (IR_{DC}), Pressure (P), Forward (F1) and backward (F2) flow velocities. Signals are obtained at a frequency of 0.67 Hz from *Model 3*. Signals are seen at a stroke volume of 70 ml (70SV) at left panels and for stroke volume of 30 ml at right panels (30SV).

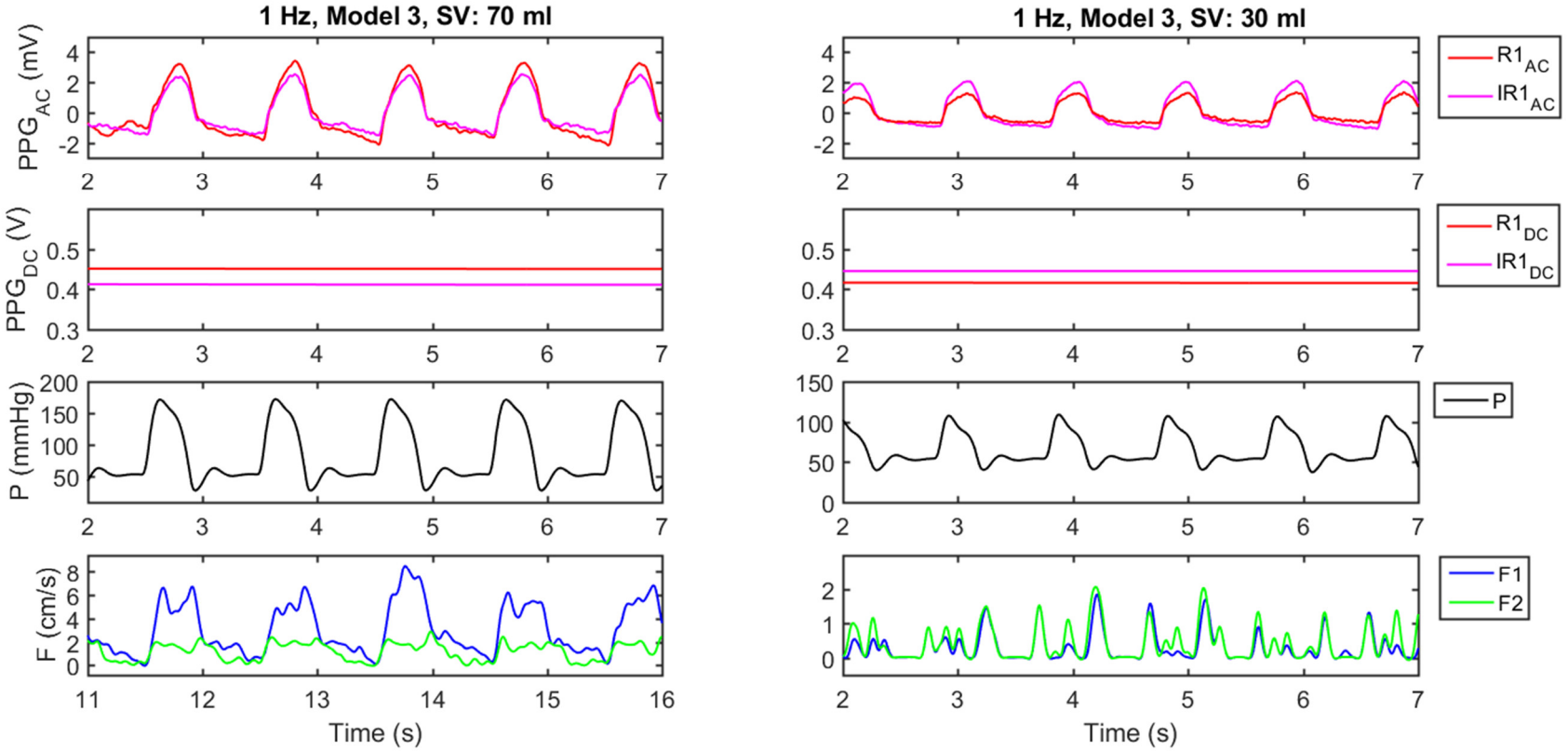

Figure 10-10
From the top, AC PPG signals for Red (R_{AC}) and Infrared (IR_{AC}), DC PPG signals for red (R_{DC}) and infrared (IR_{DC}), Pressure (P), Forward (F1) and backward (F2) flow velocities. Signals are obtained at a frequency of 1 Hz from *Model 3*. Signals are seen at a stroke volume of 70 ml (70SV) at left panels and for stroke volume of 30 ml at right panels (30SV).

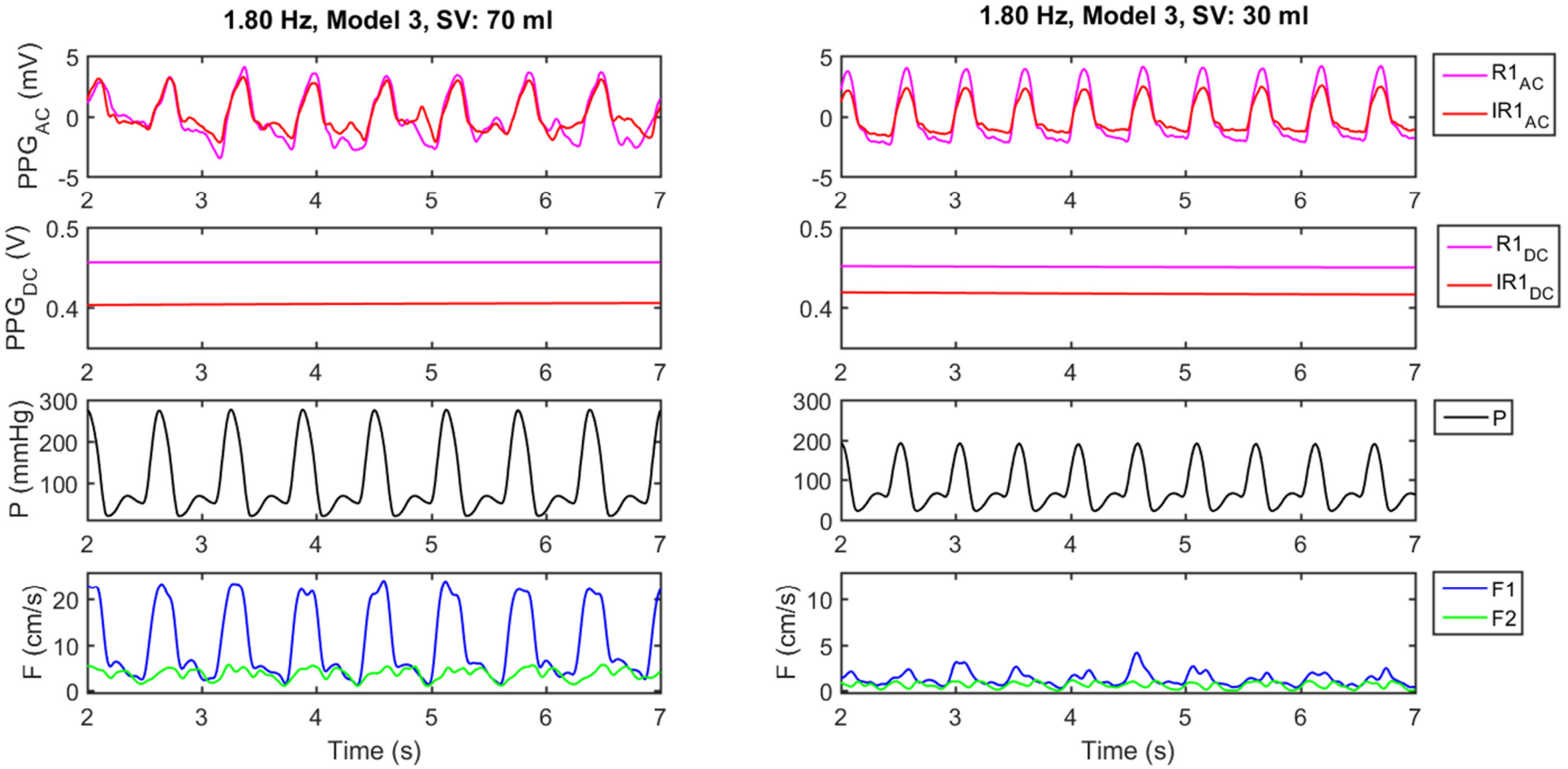

Figure 10-11
From the top, AC PPG signals for Red (R_{AC}) and Infrared (IR_{AC}), DC PPG signals for red (R_{DC}) and infrared (IR_{DC}), Pressure (P), Forward (F_1) and backward (F_2) flow velocities. Signals are obtained at a frequency of 1.8 Hz from *Model 3*. Signals are seen at a stroke volume of 70 ml (70SV) at left panels and for stroke volume of 30 ml at right panels (30SV).

10.4.4 Statistical Analyses

We present statistical analyses of the processed signals to draw average and standard variations of R and IR AC amplitudes, IR time ratio, R and IR DC levels, mean pressure values, peak forward and backward flow velocities. Moreover, we tabulate Sidak's multiple comparison tests, which compares values between both models at each pumping frequency and at fixed stroke volumes. We also draw comparisons between both stroke volumes at each pumping frequency for both models. Finally, comparisons are made between pumping frequencies at each stroke volume for both models separately. The statistical comparisons show mean differences, p-value, and summary of significance status using the 3-star system.

10.4.4.1 Mean pressure

The average ± SD of mean pressure values was calculated from two-minute recordings for both models and at both stroke volumes at varying pulsing frequencies (see **Figure 10-12**). Sidak's multiple comparison tests for significance are shown in **Table 10-2.** A clear and strong correlation is observed between mean pressure values and pumping frequencies. This relationship is observed in both models and at both stroke volumes. Mean pressure values were significantly higher in *Model 1* when compared to *Model 3.* In each model, mean pressure values were also significantly higher at higher stroke volumes when compared to lower stroke volumes.

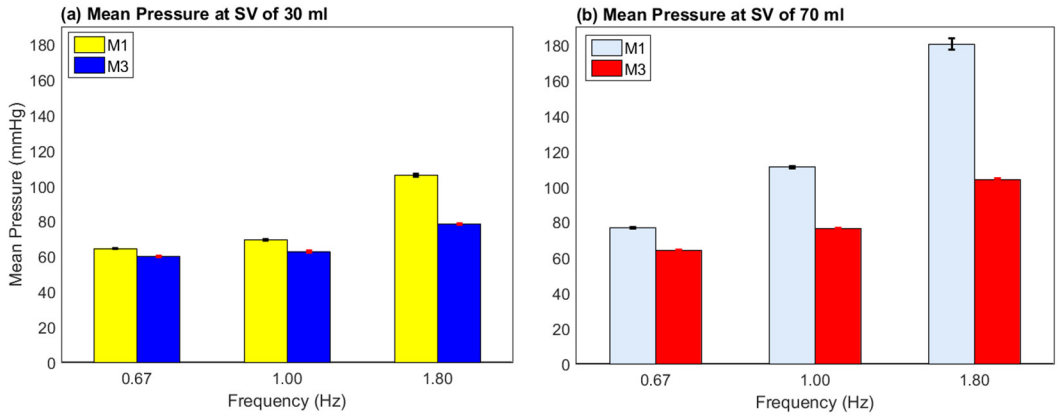

Figure 10-12
Average ± SD of mean pressure values at varying pumping frequencies for both models of different geometries, *Model 1* (M1) and *Model 3* (M3). Panel(a) showing values at a stroke volume of 30 ml and panle(b) showing values at a stroke volume of 70 ml.

Table 10-2
Mean Pressure Values Comparison using Sidak's multiple tests

Sidak's multiple comparisons test	Mean Diff.	Significant?	Summary	Adjusted P Value
Comparing values for *Model 1* and *Model 3* at each stroke volume and each pumping frequency				
30M3_f1 vs. 30M1_f1	-4.4919	Yes	***	< 0.0001
30M3_f2 vs. 30M1_f2	-6.7141	Yes	***	< 0.0001
30M3_f3 vs. 30M1_f3	-27.970	Yes	***	< 0.0001
70M3_f1 vs. 70M1_f1	-12.5550	Yes	***	< 0.0001
70M3_f2 vs. 70M1_f2	-35.0420	Yes	***	< 0.0001
70M3_f3 vs. 70M1_f3	-75.5860	Yes	***	< 0.0001
Comparing values for stroke volumes, 70 ml (70) and 30 ml (30) in each model at each rate				
70M1_f1 vs. 30M1_f1	12.1430	Yes	***	< 0.0001
70M1_f2 vs. 30M1_f2	41.9251	Yes	***	< 0.0001
70M1_f3 vs. 30M1_f3	73.9192	Yes	***	< 0.0001
70M3_f1 vs. 30M3_f1	4.0799	Yes	***	< 0.0001
70M3_f2 vs. 30M3_f2	13.5980	Yes	***	< 0.0001
70M3_f3 vs. 30M3_f3	26.3041	Yes	***	< 0.0001
Comparing values between pumping rates (f1,f2) and(f2,f3) in each model and stroke volume				
30M1_f2 vs. 30M1_f1	4.9232	Yes	***	< 0.0001
30M1_f3 vs. 30M1_f2	36.8680	Yes	***	< 0.0001
70M1_f2 vs. 70M1_f1	34.7050	Yes	***	< 0.0001
70M1_f3 vs. 70M1_f2	68.8620	Yes	***	< 0.0001
30M3_f2 vs. 30M3_f1	2.7010	Yes	***	< 0.0001
30M3_f3 vs. 30M3_f2	15.6121	Yes	***	< 0.0001
70M3_f2 vs. 70M3_f1	12.2193	Yes	***	< 0.0001
70M3_f3 vs. 70M3_f2	28.3181	Yes	***	< 0.0001

The correlation between mean pressure values and varying pumping frequencies for both stroke volumes and both models is shown in **Figure 10-13**, which presents scattergrams and curve fits with RMSE and r^2 values indicating the goodness of fit. Panel (a) presents values obtained at 30 ml SV for *Model 1*, panel (b) presents values obtained at 70 ml SV for *Model 1*, panel (c) presents values obtained at 30 ml SV for *Model 3*, and panel(d) presents values obtained at 70 ml SV for *Model 3*.

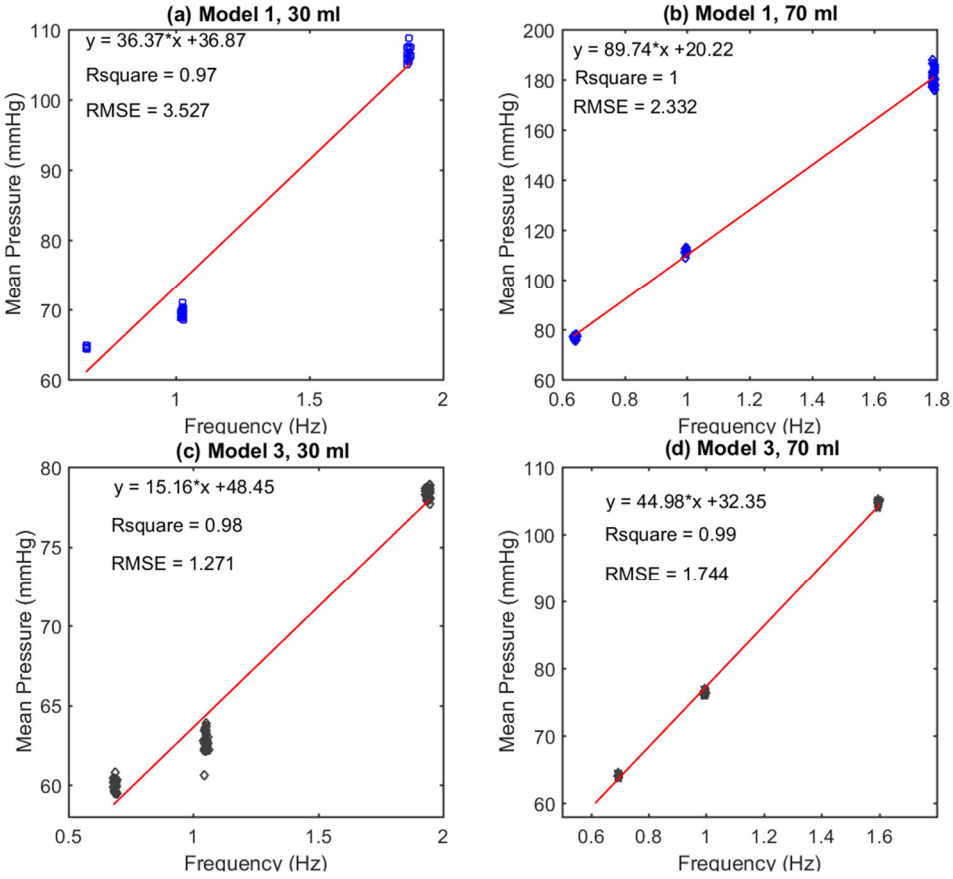

Figure 10-13
Scattergrams and first polynomial degree fittings for Mean pressure values versus pumping frequencies. Panel (a) presents values obtained from *Model 1* at 30 ml Stroke volume. Panel (b) presents values obtained from *Model 1* at 70 ml stroke volume. Panel(c) presents values obtained from *Model 3* at a stroke volume of 30 ml and panel (d) at a stroke volume of 70 ml.

10.4.4.2 Forward and backward flow velocities

Forward and backwards flow velocities for both models, at both stroke volumes and at varying pumping rates are presented in **Figure 10-14**. In general, forward flow velocities were significantly higher for *Model 1* when compared to *Model 3*. This pattern had one exception seen at 1.8 Hz and stroke volume of 70 ml, where *Model 3* showed significantly higher values than *Model 1*.

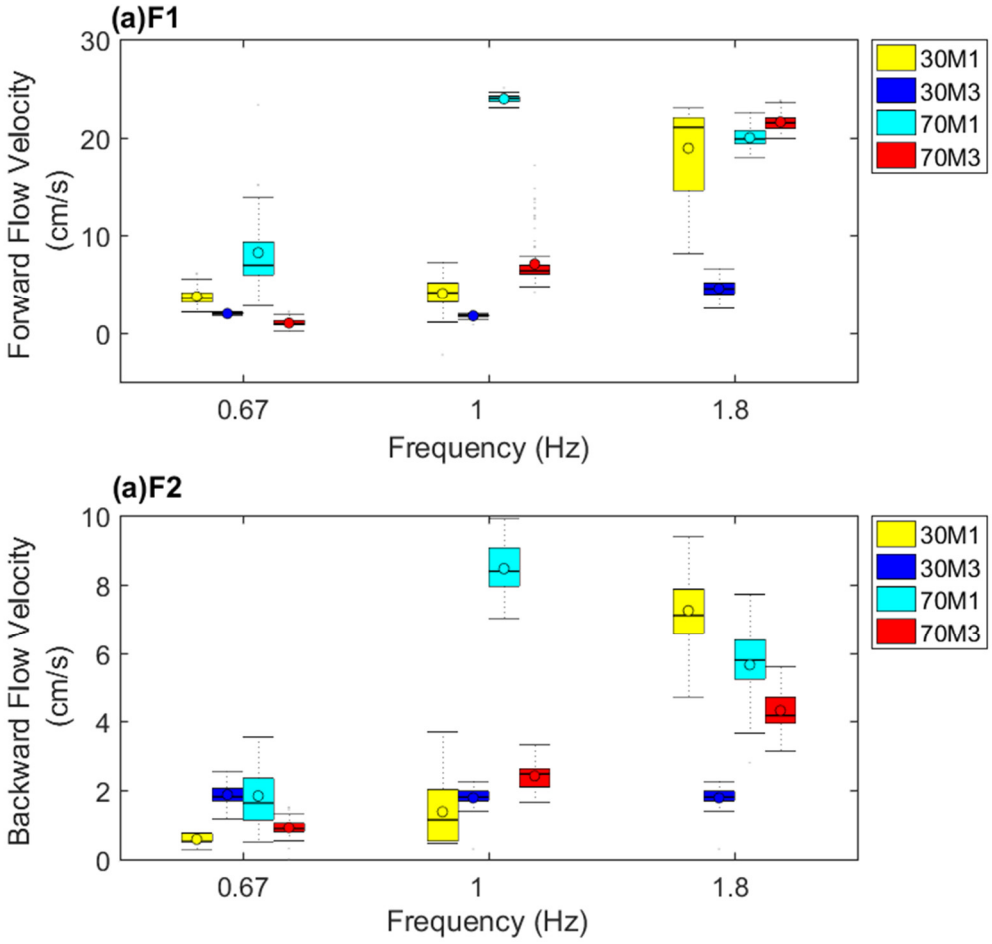

Figure 10-14
Boxplots showing flow velocities for both models at varying pumping frequencies at 30 and 70 ml stroke vlumes. Panel (a) forward flow velocities and panel(b) showing backwards flow velocities.

Sidak's multiple comparisons tests for significance comparing forward flow velocities in different models, at both stroke volumes, and at varying pumping frequencies are presented in **Table 10-3.**

Table 10-3
Forward flow velocities comparison table

Sidak's multiple comparisons test	Mean Diff.	Significant?	Summary	Adjusted P Value
Comparing values for *Model 1* and *Model 3* at each stroke volume and each pumping frequency				
30M3_*f1* vs. 30M1_*f1*	-0.0175	Yes	***	< 0.0001
30M3_*f2* vs. 30M1_*f2*	-0.0203	Yes	***	< 0.0001
30M3_*f3* vs. 30M1_*f3*	-0.1710	Yes	***	< 0.0001
70M3_*f1* vs. 70M1_*f1*	-0.2491	Yes	***	< 0.0001
70M3_*f2* vs. 70M1_*f2*	-0.1732	Yes	***	< 0.0001
70M3_*f3* vs. 70M1_*f3*	0.0143	Yes	***	< 0.0001
Comparing values for stroke volumes, 70 ml (70) and 30 ml (30) in each model at each rate				
70M1_*f1* vs. 30M1_*f1*	0.2221	Yes	***	< 0.0001
70M1_*f2* vs. 30M1_*f2*	0.2018	Yes	***	< 0.0001
70M1_*f3* vs. 30M1_*f3*	-0.0153	Yes	***	< 0.0001
70M3_*f1* vs. 30M3_*f1*	-0.0089	Yes	***	< 0.0001
70M3_*f2* vs. 30M3_*f2*	0.0496	Yes	***	< 0.0001
70M3_*f3* vs. 30M3_*f3*	0.1696	Yes	***	< 0.0001
Comparing values at different pumping rates for both models and both stroke volumes				
30M1_*f2* vs. 30M1_*f1*	0.0007	No	ns	> 0.9999
30M1_*f3* vs. 30M1_*f2*	0.1786	Yes	***	< 0.0001
30M3_*f2* vs. 30M3_*f1*	-0.0021	Yes	***	< 0.0001
30M3_*f3* vs. 30M3_*f2*	0.0283	Yes	***	< 0.0001
70M1_*f2* vs. 70M1_*f1*	0.1065	Yes	***	< 0.0001
70M1_*f3* vs. 70M1_*f2*	-0.0384	Yes	***	< 0.0001
70M3_*f2* vs. 70M3_*f1*	0.05631	Yes	***	< 0.0001
70M3_*f3* vs. 70M3_*f2*	0.1484	Yes	***	< 0.0001

Table 10-4
Backward flow velocities comparison tests

Sidak's multiple comparisons test	Mean Diff.	Significant?	Summary	Adjusted P Value
Comparing values for Model 1 and Model 3 at each stroke volume and each pumping frequency				
30M3_*f1* vs. 30M1_*f1*	0.0129	Yes	***	< 0.0001
30M3_*f2* vs. 30M1_*f2*	0.0040	No	Ns	0.1942
30M3_*f3* vs. 30M1_*f3*	-0.0545	Yes	***	< 0.0001
70M3_*f1* vs. 70M1_*f1*	-0.0092	Yes	***	< 0.0001
70M3_*f2* vs. 70M1_*f2*	-0.0604	Yes	***	< 0.0001
70M3_*f3* vs. 70M1_*f3*	-0.0133	Yes	***	< 0.0001
Comparing values for stroke volumes, 70 ml (70) and 30 ml (30) in each model at each rate				
70M1_*f1* vs. 30M1_*f1*	0.01259	Yes	***	< 0.0001
70M1_*f2* vs. 30M1_*f2*	0.07080	Yes	***	< 0.0001
70M1_*f3* vs. 30M1_*f3*	-0.0160	Yes	***	< 0.0001
70M3_*f1* vs. 30M3_*f1*	-0.0095	Yes	***	< 0.0001
70M3_*f2* vs. 30M3_*f2*	0.0064	Yes	**	0.0012
70M3_*f3* vs. 30M3_*f3*	0.0253	Yes	***	< 0.0001
Comparing values between pumping rates (*f1*,*f2*) and(f2,*f3*) in each model and stroke volume				
30M1_*f2* vs. 30M1_*f1*	0.0080	Yes	***	< 0.0001
30M1_*f3* vs. 30M1_*f2*	0.0586	Yes	***	< 0.0001
70M1_*f2* vs. 70M1_*f1*	0.0662	Yes	***	< 0.0001
70M1_*f3* vs. 70M1_*f2*	-0.0281	Yes	***	< 0.0001
30M3_*f2* vs. 30M3_*f1*	-0.0008	No	Ns	> 0.9999
30M3_*f3* vs. 30M3_*f2*	0.0000	No	Ns	> 0.9999
70M3_*f2* vs. 70M3_*f1*	0.01501	Yes	***	< 0.0001
70M3_*f3* vs. 70M3_*f2*	0.01893	Yes	***	< 0.0001

Finally, Reynold numbers are calculated from average forward flow velocities and presented in **Table 10-5** for both models at each stroke volume and varying pumping rates.

Table 10-5
Reynold numbers calculated for bot stroke volumes at varying pumping frequencies

Stroke volume (ml)	Model	f1	f2	f3
30l	*Model 1*	87.07	126.79	1186.29
	Model 3	45.38	53.70	286.65
70	*Model 1*	525.02	751.03	1253.38
	Model 3	22.76	222.17	1354.31

10.4.4.3 Analytics of AC amplitudes in both models at each stroke volume and varying pumping frequencies

In this section, analytics of the AC red and infrared PPG signals are presented. The average ± SD of AC amplitudes for R and IR PPG signals are displayed in **Figure 10-15** for *Model 1* and *Model 3* at stroke volumes of 30 ml and 70 ml (30M1, 30M3, 70M1, and 70M3) at varying pumping frequencies**.** Sidak's multiple comparison tests are presented in **Table 10-6** and **Table 10-7** for IR_{AC} and R_{AC} amplitudes, respectively.

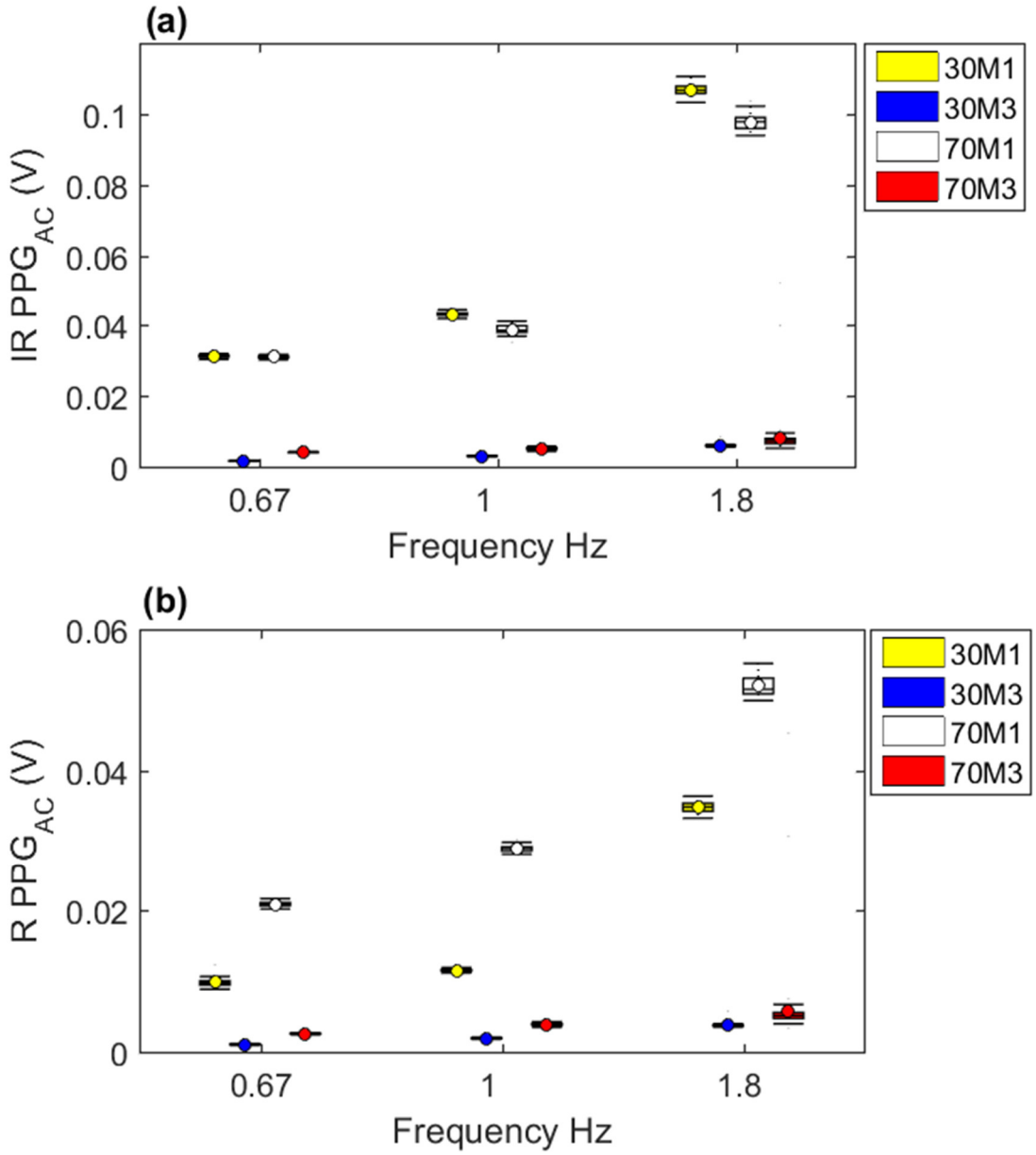

Figure 10-15
Box plot or AC amplitudes for *Model 1* (M1) and *Model 3* (M3) at 30 ml stroke volume (30 ml) and 70 ml stroke volume (70) at varying pumping frequencies. Panel (a) as obtained from IR PPGs and panel (b) as obtained from R PPGs.

Table 10-6
Infrared AC amplitudes compared to both Models, at both stroke volumes, and varying pumping frequencies

Sidak's multiple comparisons test	Mean Diff.	Significant?	Summary	Adjusted P Value
Comparing values for *Model 1* and *Model 3* at each stroke volume and each pumping frequency				
30M3_*f1* vs. 30M1_*f1*	-0.0242	Yes	***	< 0.0001
30M3_*f2* vs. 30M1_*f2*	-0.0381	Yes	***	< 0.0001
30M3_*f3* vs. 30M1_*f3*	-0.1007	Yes	***	< 0.0001
70M3_*f1* vs. 70M1_*f1*	-0.0268	Yes	***	< 0.0001
70M3_*f2* vs. 70M1_*f2*	-0.0338	Yes	***	< 0.0001
70M3_*f3* vs. 70M1_*f3*	-0.0904	Yes	***	< 0.0001
Comparing values for stroke volumes, 70 ml (70) and 30 ml (30) in each model at each rate				
70M1_*f1* vs. 30M1_*f1*	0.0052	Yes	***	< 0.0001
70M1_*f2* vs. 30M1_*f2*	-0.0022	Yes	***	< 0.0001
70M1_*f3* vs. 30M1_*f3*	-0.0087	Yes	***	< 0.0001
70M3_*f1* vs. 30M3_*f1*	0.0026	Yes	***	< 0.0001
70M3_*f2* vs. 30M3_*f2*	0.00211	Yes	***	< 0.0001
70M3_*f3* vs. 30M3_*f3*	0.00154	Yes	***	< 0.0001
Comparing values between pumping rates (*f1*,*f2*) and(f2,*f3*) in each model and stroke volume				
30M1_*f2* vs. 30M1_*f1*	0.0153	Yes	***	< 0.0001
30M1_*f3* vs. 30M1_*f2*	0.0656	Yes	***	< 0.0001
70M1_*f2* vs. 70M1_*f1*	0.0079	Yes	***	< 0.0001
70M1_*f3* vs. 70M1_*f2*	0.0592	Yes	***	< 0.0001
30M3_*f2* vs. 30M3_*f1*	0.0015	Yes	***	< 0.0001
30M3_*f3* vs. 30M3_*f2*	0.0031	Yes	***	< 0.0001
70M3_*f2* vs. 70M3_*f1*	0.0010	Yes	***	< 0.0001
70M3_*f3* vs. 70M3_*f2*	0.0025	Yes	***	< 0.0001

A clear observation is the highly significant increase in AC amplitudes for both R and IR PPG signals in *Model 1* when compared to *Model 3*. Another major observation is the highly significant increase in both R and IR AC amplitudes with increasing pumping frequencies. In regards to stroke volumes, however, only Red AC amplitudes showed a consistent and significant increase at 70 ml of stroke volumes when compared to 30 ml. IR AC amplitudes only showed this gap in favour of high stroke volumes at lower frequencies. At higher frequencies, a significant drop was observed in IR AC amplitudes when stroke volumes increased from 30 ml to 70 ml.

Table 10-7
Red AC amplitudes comparisons using Sidak;s multiple comparison tests

Sidak's multiple comparisons test	Mean Diff.	Significant?	Summary	Adjusted P Value
Comparing values for both Models ((M3) and M1) at each pumping rate and stroke volume				
30M3_*f1* vs. 30M1_*f1*	-0.0087	Yes	***	< 0.0001
30M3_*f2* vs. 30M1_*f2*	-0.0097	Yes	***	< 0.0001
30M3_*f3* vs. 30M1_*f3*	-0.0311	Yes	***	< 0.0001
70M3_*f1* vs. 70M1_*f1*	-0.0183	Yes	***	< 0.0001
70M3_*f2* vs. 70M1_*f2*	-0.0251	Yes	***	< 0.0001
70M3_*f3* vs. 70M1_*f3*	-0.0461	Yes	***	< 0.0001
Comparing values for stroke volumes, 70 ml (70) and 30 ml (30) in each model at each rate				
70M1_*f1* vs. 30M1_*f1*	0.0110	Yes	***	< 0.0001
70M1_*f2* vs. 30M1_*f2*	0.0174	Yes	***	< 0.0001
70M1_*f3* vs. 30M1_*f3*	0.0171	Yes	***	< 0.0001
70M3_*f1* vs. 30M3_*f1*	0.0015	Yes	***	0.0008
70M3_*f2* vs. 30M3_*f2*	0.0019	Yes	***	< 0.0001
70M3_*f3* vs. 30M3_*f3*	0.0020	Yes	***	< 0.0001
Comparing values between pumping rates (*f1*,*f2*) and(f2,*f3*) in each model and stroke volume				
30M1_*f2* vs. 30M1_*f1*	0.0017	Yes	***	0.0001
30M1_*f3* vs. 30M1_*f2*	0.0234	Yes	***	< 0.0001
70M1_*f2* vs. 70M1_*f1*	0.0081	Yes	***	< 0.0001
70M1_*f3* vs. 70M1_*f2*	0.0231	Yes	***	< 0.0001
30M3_*f2* vs. 30M3_*f1*	0.0009	Yes	*	0.02735
30M3_*f3* vs. 30M3_*f2*	0.0019	Yes	***	< 0.0001
70M3_*f2* vs. 70M3_*f1*	0.0013	Yes	**	0.0077
70M3_*f3* vs. 70M3_*f2*	0.0020	Yes	***	< 0.0001

Finally, mean pressure values are plotted versus IR AC amplitudes in **Figure 10-16** for 30 ml SV and 70 ml SV separately. Panel (a) values obtained from *Model 3* at 30 ml stroke volume (SV) (30M3). Panel(b) values obtained from *Model 3* at 70 ml SV (70M3). Panel(c) values obtained from *Model 1* at 30 ml SV (30M1). Panel(d) values obtained from *Model 1* at 70 ml SV (70M1).

Figure 10-17 presents mean pressure values plotted against AC amplitudes for both Red and infrared PPGs with both stroke volumes combined for each Model. Panel (a) shows values obtained from R PPGs from *Model 1* Panel (b) shows values obtained from IR PPGs from *Model 1* (c) shows values obtained from R PPGs from *Model 3* Panel(d) shows values

obtained from IR PPGs from *Model 3*. Variations in subplot (b) can be related to the mechanical movement of model 3 due to its high elasticity and the designed setup that does not restrict this movement.

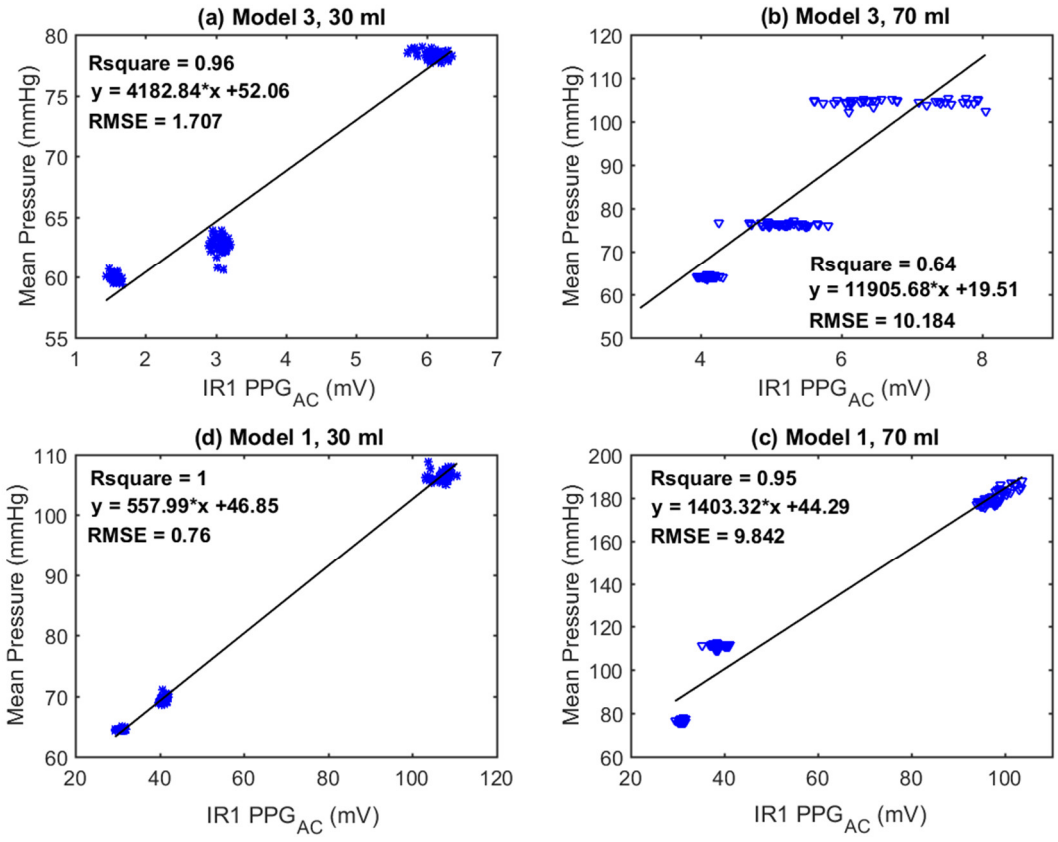

Figure 10-16
Linear fitting for mean pressure values versus IR AC amplitudes. Panel (a) values obtained from *Model 3* at 30 ml stroke volume (SV) (30M3) . Panel(b) values obtained from *Model 3* at 70 ml SV (70M3). Panel(c) values obtained from *Model 1* at 30 ml SV (30M1). Panel(d) values obtained from *Model 1* at 70 ml SV (70M1).

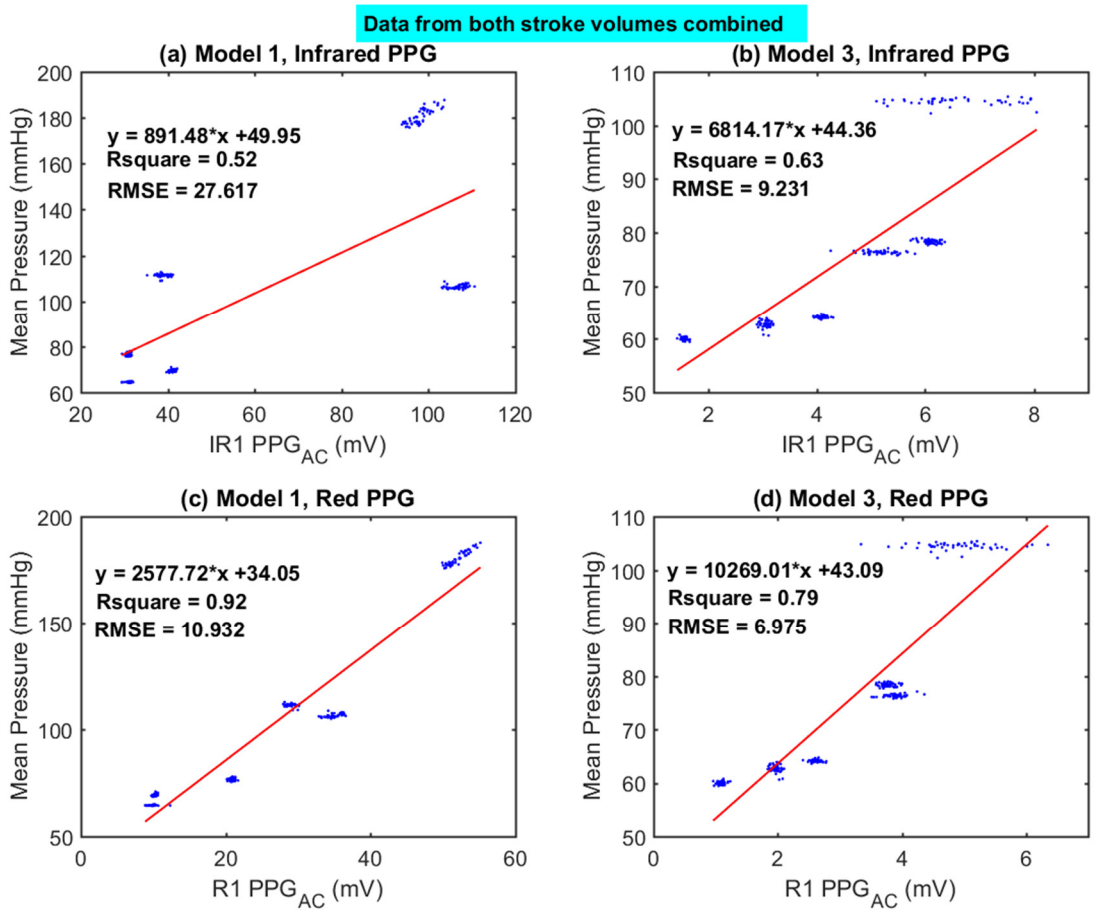

Figure 10-17
Linear fitting for mean pressure values versus AC amplitude. Panel (a) using IR AC amplitudes obtained from *Model 1* at 30 and 70 ml stroke volumes. Panel(b) using IR AC amplitudes obtained from *Model 3* at 30 and 70 ml stroke volumes. Panel(c) using R AC amplitudes obtained from *Model 1* at 30 and 70 ml stroke volumes. Panel(d) using R AC amplitudes obtained from *Model 3* at 30 and 70 ml stroke volumes

10.4.4.4 Time Ratio as obtained from IR PPG$_{AC}$

Time ratio is defined as the period of the falling slope in red AC signal divided by the whole length of the period cycle. It is estimated to reflect changes in flow efficiency, in relation to the amount of energy stored and consumed by the flow as a system (pumping powers, elastic walls and fluid properties). The values extracted from IR$_{AC}$ signal as described in **Chapter 7** are presented in a boxplot in **Figure 10-18**. Sidak's multiple comparisons tests are tabulated in **Table 10-8.** It is evident, that time ratios were significantly higher in *Model 3* when compared to *Model 1* at both stroke volumes and at all pumping frequencies. However, the effect of pumping frequencies and stroke volumes did not show much consistency. In *Model 3*, Time ratios showed a drop (mostly significant) with increasing frequencies. In *Model 1*, this pattern was not present, on the contrary, time ratios increased with pumping frequencies at a stroke volume of 70 ml. While, at stroke volumes of 30 ml, time ratios in *Model 1* dropped significantly at 1 Hz to

increase significantly at 1.8 Hz. In relation to time ratio changes at different stroke volumes, 4 out of the 6 cases showed significantly higher time ratios at low stroke volumes. While 2 cases, showed an increase in time ratios at higher stroke volumes.

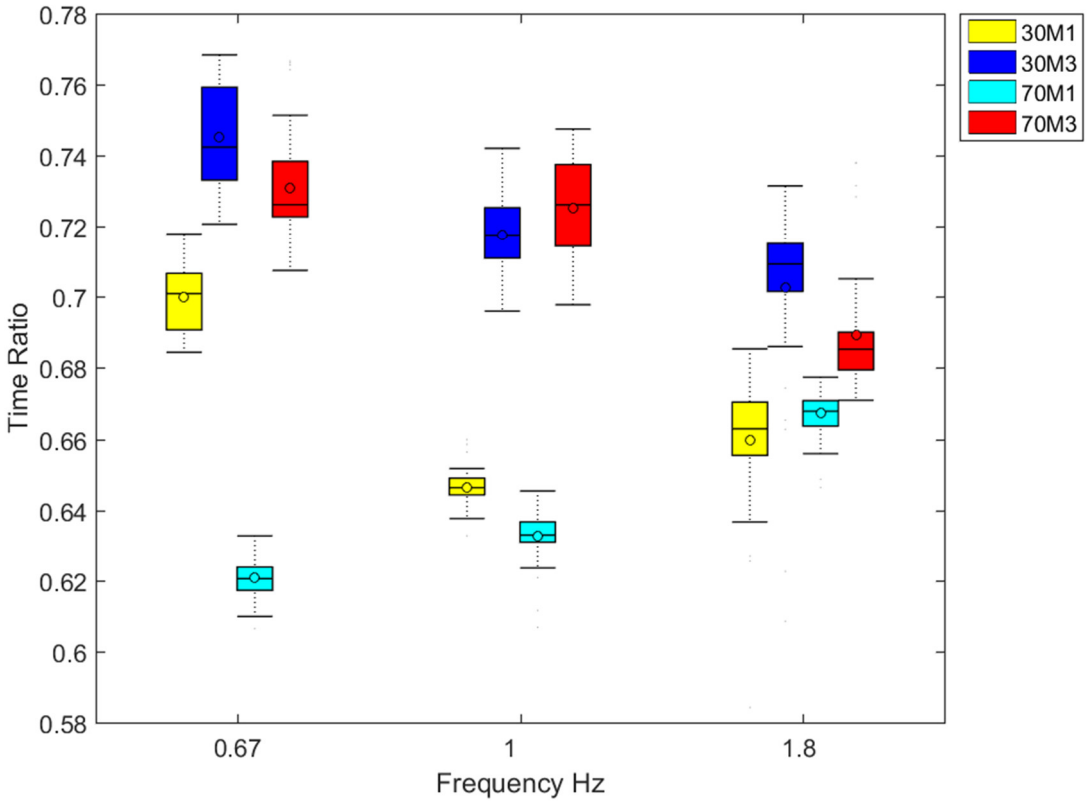

Figure 10-18
Box plot of IR time ratio for *Model 1* (M1) and *Model 3* (M3) at 30 ml stroke volume (30 ml) and 70 ml stroke volume (70) at varying pumping frequencies.

Table 10-8
Comparison of time ratios (obtained from Infrared PPG_{AC}).

Sidak's multiple comparisons test	Mean Diff.	Significant?	Summary	Adjusted P Value
Comparing values for *Model 1* and *Model 3* at each stroke volume and each pumping frequency				
30M3_*f1* vs. 30M1_*f1*	0.0408	Yes	***	0.0003
30M3_*f2* vs. 30M1_*f2*	0.0732	Yes	***	< 0.0001
30M3_*f3* vs. 30M1_*f3*	0.01713	Yes	*	0.0236
70M3_*f1* vs. 70M1_*f1*	0.1099	Yes	***	< 0.0001
70M3_*f2* vs. 70M1_*f2*	0.0926	Yes	***	< 0.0001
70M3_*f3* vs. 70M1_*f3*	0.0220	Yes	***	< 0.0001
Comparing values for stroke volumes, 70 ml (70) and 30 ml (30) in each model at each rate				
70M1_*f1* vs. 30M1_*f1*	-0.0834	Yes	***	< 0.0001
70M1_*f2* vs. 30M1_*f2*	-0.0117	Yes	*	0.04235
70M1_*f3* vs. 30M1_*f3*	0.0182	Yes	***	< 0.0001
70M3_*f1* vs. 30M3_*f1*	-0.0143	Yes	***	0.0006
70M3_*f2* vs. 30M3_*f2*	0.0077	No	ns	0.2251
70M3_*f3* vs. 30M3_*f3*	-0.0132	No	ns	0.1098
Comparing values between pumping rates (f1,f2) and(f2,f3) in each model and stroke volume				
30M1_*f2* vs. 30M1_*f1*	-0.0600	Yes	***	< 0.0001
30M1_*f3* vs. 30M1_*f2*	0.0412	Yes	***	< 0.0001
30M3_*f2* vs. 30M3_*f1*	-0.0277	Yes	***	< 0.0001
30M3_*f3* vs. 30M3_*f2*	-0.0148	Yes	**	0.0088
70M1_*f2* vs. 70M1_*f1*	0.0116	Yes	***	< 0.0001
70M1_*f3* vs. 70M1_*f2*	0.0347	Yes	***	< 0.0001
70M3_*f2* vs. 70M3_*f1*	-0.0056	No	ns	0.7824
70M3_*f3* vs. 70M3_*f2*	-0.0358	Yes	***	< 0.0001

10.4.4.5 DC levels in both models at different stroke volumes and at varying pumping frequencies

The average ± SD DC levels obtained from R and IR PPG signals are displayed in **Figure 10-19**. IR PPG_{DC} clearly shows a significant increase in *Model 1* when compared to *Model 3,* at both stroke volumes and at all pumping frequencies. Results from Sidak's multiple tests for IR PPG_{DC} are seen in **Table 10-9**. However, DC levels obtained from R_{PPG} as seen in **Figure 10-19(b)** fail to show a consistent pattern when *Model 1* and *Model 3* are compared. This behaviour will be further discussed in **Chapter 14**. Moreover, IR_{DC} tends to obtain significantly higher values at elevated stroke volumes when compared to lower stroke volumes in both models. This pattern was not consistent throughout all pumping

frequencies. At 0.67 Hz, *Model 3* showed significantly higher DC levels at stroke volumes of 30 ml. While at 1. Hz, *Model 1* showed significantly higher DC levels at 30 ml of stroke volume.

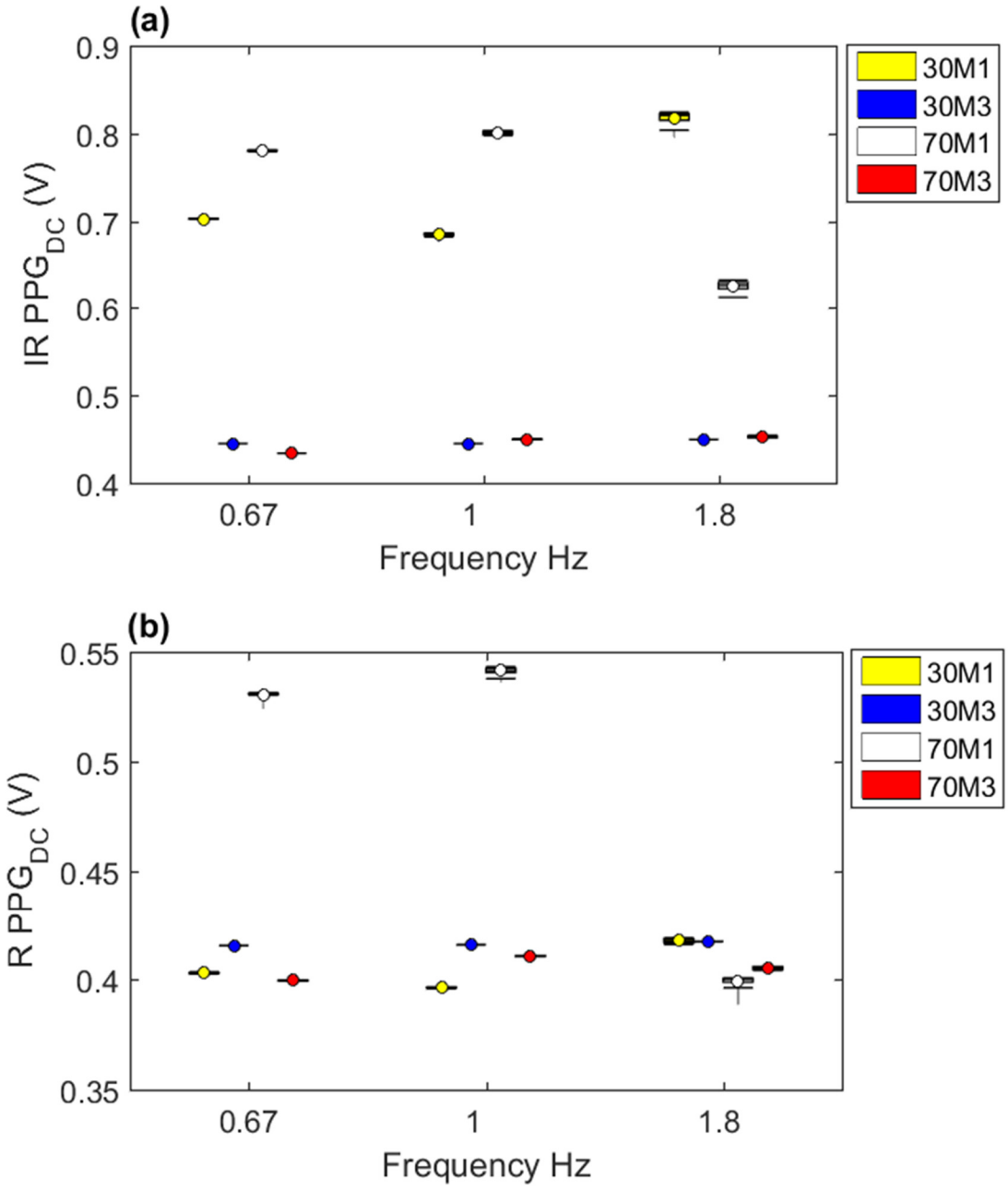

Figure 10-19
Box plot or DC levels for *Model 1* (M1) and *Model 3* (M3) at 30 ml stroke volume (30 ml) and 70 ml stroke volume (70) at varying pumping frequencies. Panel (a) as obtained from IR PPGs and panel (b) as obtained from R PPGs.

Table 10-9
Infrared DC levels compared using Sidak's multiple compairsons test

Sidak's multiple comparisons test	Mean Diff.	Significant?	Summary	Adjusted P Value
Comparing values for *Model 1* and *Model 3* at each stroke volume and each pumping frequency				
30M3_*f1* vs. 30M1_*f1*	-0.2575	Yes	***	< 0.0001
30M3_*f2* vs. 30M1_*f2*	-0.2575	Yes	***	< 0.0001
30M3_*f3* vs. 30M1_*f3*	-0.3732	Yes	***	< 0.0001
70M3_*f1* vs. 70M1_*f1*	-0.3469	Yes	***	< 0.0001
70M3_*f2* vs. 70M1_*f2*	-0.3494	Yes	***	< 0.0001
70M3_*f3* vs. 70M1_*f3*	-0.1777	Yes	***	< 0.0001
Comparing values for stroke volumes, 70 ml (70) and 30 ml (30) in each model at each rate				
70M1_*f1* vs. 30M1_*f1*	0.07830	Yes	***	< 0.0001
70M1_*f2* vs. 30M1_*f2*	0.0971	Yes	***	< 0.0001
70M1_*f3* vs. 30M1_*f3*	-0.1922	Yes	***	< 0.0001
70M3_*f1* vs. 30M3_*f1*	-0.0111	Yes	***	< 0.0001
70M3_*f2* vs. 30M3_*f2*	0.0053	Yes	***	< 0.0001
70M3_*f3* vs. 30M3_*f3*	0.0031	Yes	***	< 0.0001
Comparing values between pumping rates (*f1*,*f2*) and(f2,*f3*) in each model and stroke volume				
30M1_*f2* vs. 30M1_*f1*	0	No	ns	> 0.9999
30M1_*f3* vs. 30M1_*f2*	0.1203	Yes	***	< 0.0001
70M1_*f2* vs. 70M1_*f1*	0.0188	Yes	***	< 0.0001
70M1_*f3* vs. 70M1_*f2*	-0.169	Yes	***	< 0.0001
30M3_*f2* vs. 30M3_*f1*	0	No	ns	> 0.9999
30M3_*f3* vs. 30M3_*f2*	0.0046	Yes	***	< 0.0001
70M3_*f2* vs. 70M3_*f1*	0.0163	Yes	***	< 0.0001
70M3_*f3* vs. 70M3_*f2*	0.0024	Yes	***	< 0.0001

10.4.4.6 Normalised and Adjusted Pulse Volume

In **section 10.1.1**, a derived relationship from PPG intensities of the AC and DC PPG signals was obtained to provide a measure of volume changes using NPV_R, $NPV_{IR,}$ and APV. This is substituted in the assumed P-V exponential model to validate the potential of the PPG components to provide a measure of systolic pressure values non-invasively.

Scattergrams of the three different functions, $\ln(P_S)$-APV, $\ln(P_S)$-NPV_{IR} and $\ln(P_S)$-NPV_R are presented in (**Figure 10-20**) for *Model 1*, and in (**Figure 10-21**) for *Model 3*. Point-to-point measurements were obtained from 60 seconds at each pumping frequency (0.67, 1 and 1.8 Hz) at two stroke volumes (30 ml and 70 ml) for each panel.

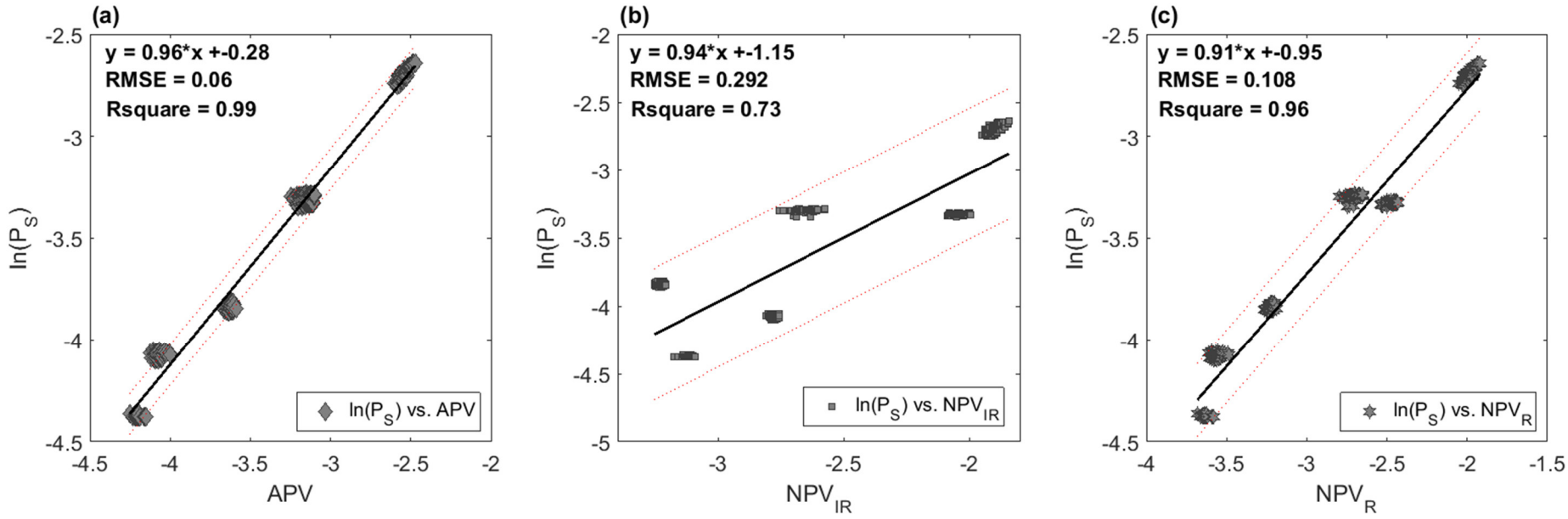

Figure 10-20
Scattergrams for ln(P_S)-V function for Model 1. Panel(a) V is estimated using Adjusted Pulse Volume method (APV).Panel(b) V is estimated using Infrared Normalized Pulse Volume (NPV_{IR}). Panel(c) V is estimated using Red NPV (NPV_R). Values present cycle-to-cycle measurements for 60 seconds at each stroke volume and at each varying pumping rate.

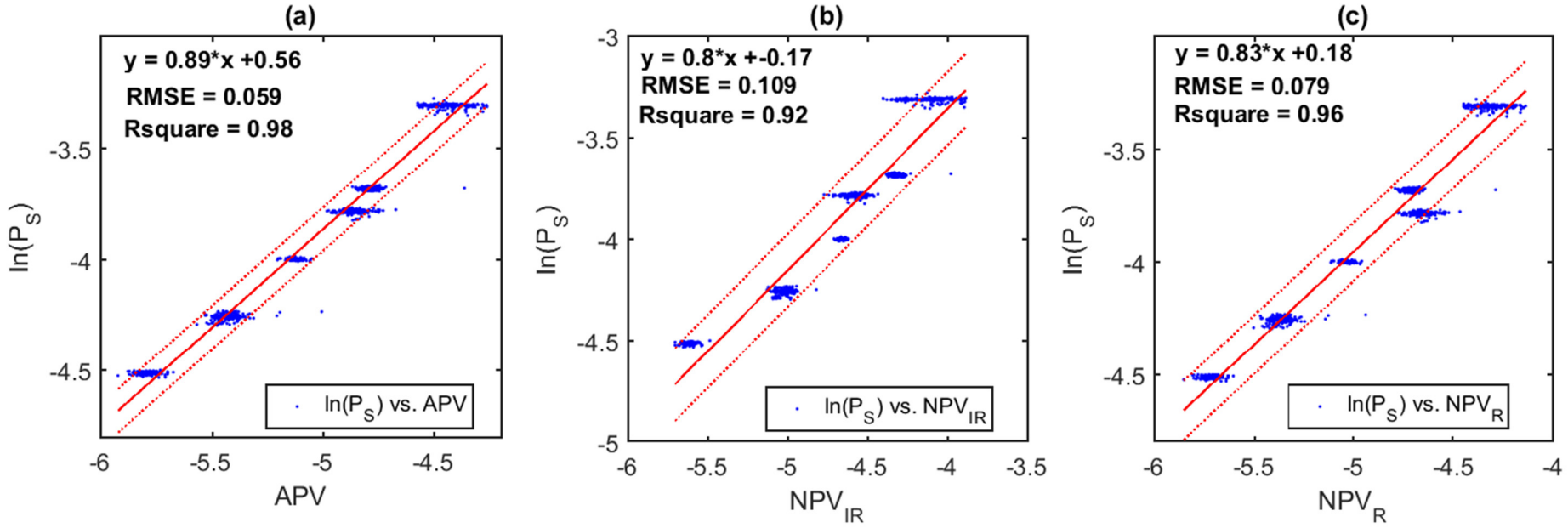

Figure 10-21
Scattergrams for ln(P_S)-V function for *Model 3*. Scattergrams for ln(P_S)-V function for Model Panel(a) V is estimated using Adjusted Pulse Volume method (APV).Panel(b) V is estimated using Infrared Normalized Pulse Volume (NPV_{IR}). Panel(c) V is estimated using Red NPV (NPV_R). Values present cycle-to-cycle measurements for 60 seconds at each stroke volume and at each varying pumping rate.

SUMMARY

The study investigated the effect of pumping frequencies, stroke volumes and cross-sectional area on the AC and DC components of the PPG signal. It is evident that both components are sensitive to the dynamics of the flow affected by the addressed factors.

The findings of this study highlight that PPG_{AC} represents the changes in the oscillatory flow. While, PPG_{DC} underwent significant changes with the variations in pumping speeds and stroke volumes, it is seen that it is also related to flow properties and not merely on constant variables, such as the arterial models' mechanical and optical properties . It might be related to changes in the steady flow; the flow layer that develops in the centre of the tube at the maximum possible speed. Further investigations using advanced flowmeters are required to establish this hypothesis. Nevertheless, It is also evident that both components of the flow interact in a way that maintains the maximum possible velocity of steady flow.

Raw AC amplitudes seem to correlate strongly and linearly with mean pressure values with increasing frequencies, yet this is only valid at constant stroke volumes and flow resistance. When either of these factors is altered, this relationship is weakened.

A primary finding indicates that AC and DC PPG signals can provide a measure of normalised pulse volume (NPV). A measure of NPV takes into account both flow components, which interact in a way that increases the efficiency of the flow. Similarly, the extracted parameter, the Adjusted Pulse Volume (APV) is defined concerning both wavelengths due to the depth of penetration of different wavelengths. NPV and APV correlate strongly with the assumed P-V relationship, with APV providing the best estimation and the most significant as validated in both models with different diameters.

This fundamental study highlights the potential of the PPG technique in clinical applications in providing a measurement of pressure. The proposed method is validated within a wide range of pressure values, low and high stroke volumes, three-set points pumping frequencies, and two arterial models with different cross-sectional areas. The results and the limitations of the method will be further discussed in **Chapter 14**.

The following chapter will address the effect of wall stiffness on both components of the PPG signal and validate a proposed method for measurement of arterial stiffness.

Chapter 11
VALIDATION OF PPG FOR VOLUME ELASTIC MODULUS QUANTIFICATION

11.1 Introduction

Previously in **Chapter 3**, we have highlighted the importance of arterial stiffness (AS) and its significance from a medical perspective as one of the earliest manifestations of adverse and functional changes in the vessel wall. The current understanding is that there is a disparity in the ability to measure AS using PPG techniques to predict future vascular events. This research has been primarily focused on the application of non-invasive PPG monitoring of AS considering the haemodynamic forces in order to provide a direct measurement of *arterial elastic modulus* for a quantification of AS. The *Volume Elastic modulus* E_v is estimated from the change in the regional stress–volumetric strain relationship. This parameter provides comprehensive information on the arterial wall properties regarding global effect of the circulation. A higher value of E_v indicates increased stiffness. We were unable to identify studies that reported methods for precise and direct measurement of the E_v of the arterial wall based on the stress–strain relationship using the PPG technique. Moreover, previous studies, have not investigated the complex mechanical interaction of the arterial wall constituents *in-vitro* under different scenarios of haemodynamic forces.

In this study, by using the PPG and pressure signals, we can provide a direct measure of the arterial *elastic modulus*. There is no doubt, that non-invasive methods used for the quantification of local vascular properties can bring many benefits to the clinical sector due to their fundamental role in the haemodynamic forces and their direct contribution to the biochemical control in health and disease. Such non-invasive approach can provide CVD and ATH patients with the ultimate device for reliable and continuous method for early detection, diagnosis, and control of pharmacological and non-pharmacological treatments.

11.1.1 Theoretical Method

Consider a circular tube with an initial volume (V_1), suppose the inner surfaces of the tube are exposed to transmural pressure (P); forces of radial stress are perpendicular to and act on all surfaces uniformly as seen in **Figure 11-1(a)**. The response of the object to this uniform stress is an expansion of volume to V_2. This behaviour can be characterised using the Volume Elastic modulus (E_v) which can be expressed with the following relationship:

$$(dV / V).E_v = dP \qquad (11.1)$$

Where *dP*, is the change in the transmural pressure signal, and *dV* is the change in the volume. In the presence of pulsatile flow conditions, the side view of the tube can be represented as seen in **Figure 11-1(b)** and the pulsatile transmural pressure (P) and Volume (V) signals are out of phase (∅), as seen in **Figure 11-1(d)**. This can be explained that pressure signals are the driving force for the change in volume and hence they occur first. Due to the time-dependency of the pulsatile flow, equation (1) can be derived with respect to time and expressed with eq (11.2). This is illustrated in the linear approximation in **Figure 11-1(c).**

$$E_v = d(dP / dt) / d((dV / dt) / V) \qquad (11.2)$$

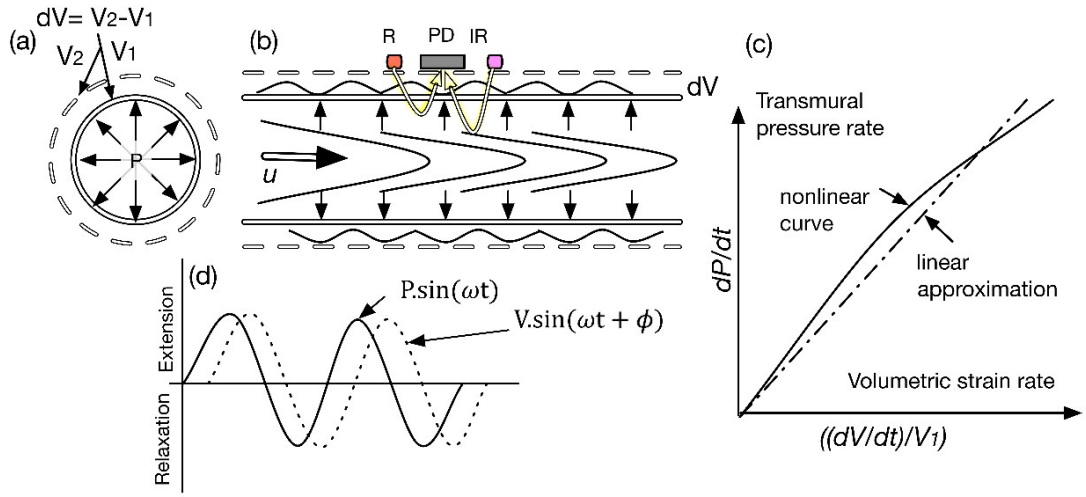

Figure 11-1
(a) A cross-sectional view of flow in a cylindrical model. (b) side view of flow in the model with a pulsatile pressure signal. (c) is a representation of the nonlinear curve and the linear approximation for measurement of Elastic Volume Modulus (d) the relationship between the pulsatile pressure and the pulsatile strain signals, where w, is the angular frequency and is the phase between both signals.

11.1.2 Measurement of Volumetric Strain

The volumetric strain in the arterial model was measured using the PPG signals. We considered the pulsatile flow to consist of an oscillatory component $(\tilde{V}_o)$ and a steady component $(\bar{V}_s)$ (Zamir, 2000). Assuming that the Beer-Lambert law holds in this model, by referring to subsection 10.1.1, Normalised Pulse Volume (NPV) can be given by equation (10.5).

As we are interested in the behaviour of a time-dependent signal, deriving (10.5) in respect to time and relying on the assumption that $(\varepsilon_o c_o)$ is an unknown constant term, the rate of change of NPV would be

$$(dNPV / dt) = -(dI / dt) / I \tag{11.1}$$

Finally, we introduce the rate of change of Normalised Volumetric Strain (NVS) as $dNPV / dt \big/ NPV$ which is given by the following equation:

$$dNVS / dt = (dI / dt) \big/ I.\ln(dI / \bar{I}) \tag{11.2}$$

And E_v from eq(11.2) can be expressed as in eq(11.9)

$$E_v = (dP / dt) \big/ (dNVS / dt) \tag{11.3}$$

11.1.3 Experimental Objectives

In order to investigate the plausibility of utilising the PPG components and pressure signals for the quantification of arterial mechanical properties, an *in-vitro* experiment was conducted with an aim to;

- Evaluate the feasibility of a new method for direct measurement of E_v in an *in vitro* model featuring a healthy artery and another affected with ATH. This is achieved by collecting PPG and pressure signals and validate the results with the gold standard E_v measurements.
- Investigate E_v values over a range of pressure values in normotensive, hypotensive and hypertensive conditions by controlling the stroke volume and pulse frequency.
- Contribute to the further understanding of the behaviour of the PPG in pulsatile flow considering the wall elastic properties and flow dynamic forces.

11.2 Protocol

The pump-arterial network setup described in **Chapter 8** was used for this experiment. The setup was slightly adjusted by directing the flow to *Model 1* and *Model 2* separately, using the stopcocks as illustrated in **Figure 10-1. The** PPG reflectance R and IR sensor (described in **Chapter 6**) was fixed at the middle of the targeted arterial model. The pressure was measured at the entrance of the tube, after the entrance range, using a catheter tip research grade pressure transducer (Harvard Apparatus, US). An Ultrasound Doppler (MD2, Huntleigh, UK) with an 8 MHz probe was fixed at a 60° angle with the arterial model for further calculation of forward and backward flow using the Doppler effect. Data collection was performed at a sampling rate of 1000 Hz using the same data acquisition systems previously described (**Chapter 7**) and saved for further offline analysis.

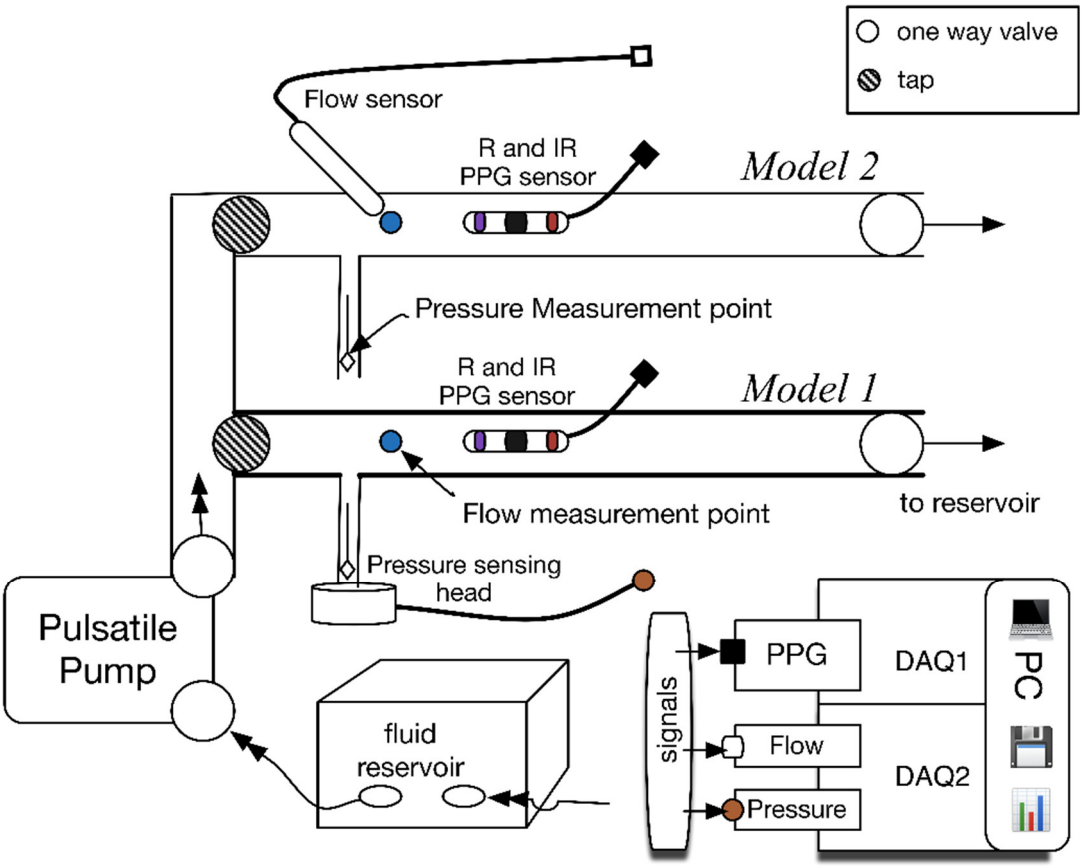

Figure 11-2
A schematic diagram of the flow loop used to impose mechanical stress at variable flow patterns.

A summary of the used parameters during the experiment can be seen in **Table 11-1**.

Table 11-1
Parameters used during the experiment

Parameter	Fluid 1 (v1)
Solution	Cobalt Nitrate in Saline Solution
Artery properties	*Model 1, Model 2*
Inside Diameter (ID) mm	16, 16
Wall thickness , mm	1.5, 0.6
Wall Elastic Modulus (MPa)	24, 8
Stroke volume (ml)	30 ,70 for each model
Density (g/ml)	1.0914
Concentration of $Co(NO_3)_2$	0.6 M
Pulsating frequency (Hz)	*f1= 0.67, f2= 1, f3= 1.8*

The experiment was performed at the following steps:

1. Three litres of 0.6 M of Cobalt Nitrate (Co_2Ni_3) in saline solution were prepared.

2. The fluid optical spectrum was obtained using a sample of the solution in the visible and near infrared range using a spectrometer analyser (Lambda 1050, PerkinElmer).
3. The viscosity of the prepared fluid was measured at the three speeds (40, 60, 100 RPM) using the LVD3T rheometer (Brookfield, US).
4. Fluid pH and conductivity measurements were also obtained using the conductivity/pH meter (Jenway, UK).
5. The pump setup was cleaned and left to dry the previous day. Three litres of the prepared fluid were poured into the reservoir.
6. The pump was left to operate at the initial frequency 0.67 Hz and 30 ml of stroke volume, for 10 mins to assure bubble-free and fully developed flow in a closed loop.
7. Signal recording started after that period and continued for continuous two minutes for the following stages:

- **Stage 1:** Sensors are fixed on *Model 1* and the fluid is circulated under the varying pulsating frequencies at a stroke volume of 30 ml.
- **Stage 2:** Sensors are fixed on *Model 1* where the fluid is circulated under the varying pulsating frequencies at a stroke volume of 70 ml.
- **Stage 3:** Sensors are fixed on *Model 2* and the fluid is circulated under varying pulsating frequencies at a stroke volume of 30 ml.
- **Stage 4:** Sensors are fixed on *Model 2* where the fluid is circulated under varying pulsating frequencies at a stroke volume of 70 ml.

8. The reservoir, tubes, and the pump were thoroughly cleaned and left to dry.

11.3 Data Analysis

11.3.1 Gold Standard Measurement of E

The *elastic modulus* (E) for both tube models was tested using the stress-strain curve from the gold standard method. The gold standard is a calibrated electromechanical system Instron (model 5900, Instron Co, USA). A 100 mm specimen from each tube was extended at a rate of 0.1 mm/s to obtain the stress-strain curve. E is calculated from the slope measurement of that curve. v is Poisson's ratio and is estimated from the traverse-longitudinal strain curve obtained using two external extensometers. E_v was calculated from the relationship $E = 3E_v(1-2v)$ and is shown in the section 11.4.5.

11.3.2 Proposed Method for Pulse Analyses for Measurement of E_v

The offline analysis was performed using an automated software developed in Matlab (Mathworks, Inc. Natick, MA). PPG signals were filtered accordingly to provide the AC

and DC components. Peaks and valleys of PPG and pressure signals were detected using a custom-made peak detector script using the first and second derivative. Pressure and optical rate of change in respect to time were performed on 30% of the signal in the systolic region as seen in **figure 11-3**, where CS is majorly present in a normal direction towards the wall. The change rate of NVS was obtained from the PPG signals as described in eq (11.2). To avoid inaccuracies, the measurement extended from 60% to 90% before the peak. In this region , the effect of wall stiffness is more visible than other regions where the fluid properties can affect the pattern of stresses towards the wall. Moreover, the slope of the signal varies from one region to another, taking an overall average can produce inaccuracies and hence, the 60-90% region was maintained throughout different signals. Finally, eq (11.3) can be rewritten as seen and E_v can be calculated as follows:

$$E_v = (\Delta P_{d,c} / \Delta t_{d,c}) \Big/ \left(\left((\Delta I_{b,a} / \Delta t_{b,a}) \Big/ \left(I_a . \ln(\Delta I_{pk-pk} / \bar{I}) \right) \right) . K \right) \qquad (11.4)$$

Where a,b,c,d are denoted as seen in **Figure 11-3** and ΔI_{pk-pk} is the peak to peak AC amplitude. K is the inverse of the total gain constant used in the PPG processing system.

Statistical analysis was performed using the statistical analysis package in Matlab (Mathworks, Inc. Natick, MA). The goodness of model fitting was evaluated with the Sum Square Error (SSE), R-square and the Root Mean Square Error (RMSE). Where SSE shows variation from the mean. R-square is the percentage of the response variable variation, and RMSE is the square root of the variance of the residuals and indicates the absolute fit of the model to the data. Correlation significance is stated with a p-value and t-value. PTT values were calculated as the difference between the location of the peak of the PPG_{AC} signal and the pressure peak. A statistical t-test was also performed with values of $p \leq 0.05$ considered to be significant and those where $p<0.001$ are highly significant. The slopes (E_v) of the measured and proposed methods were compared using the analysis of the covariance and the percent error values were also calculated with an accepted limit of 5%.

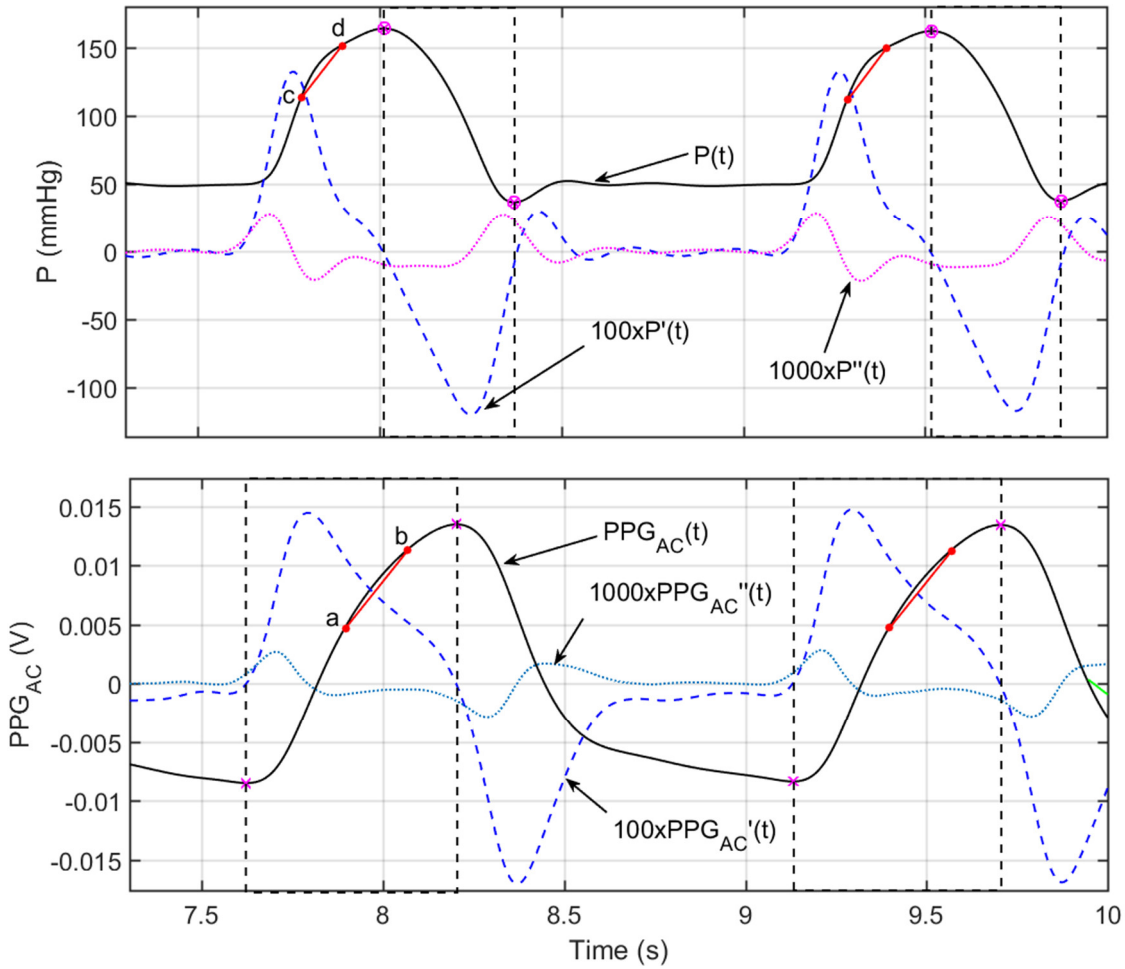

Figure 11-3
Three-second snap from the recorded data (stroke volume 70 ml, pump frequency: 0.6 Hz, *Model 1*) portraying the adopted pulse analytics method for pressure and pulsatile Infrared (IR_{AC}) PPG signal obtained by a custom made software using Matlab. The highlighted data points were used for calculation of slope measurements.

11.4 Results

In this section, we present the measured values for fluid properties, including the optical spectra in the visible and near-infrared range, conductivity, pH, and viscosity measurements. We further, present visual data from the collected R and IR PPG_{AC} and PPG_{DC} signals; pressure, forward and backward flow, at both stroke volumes and varying pumping frequencies in both models. Furthermore, we present statistical analysis from the processed signals to draw average and standard variations of Infrared AC amplitudes, time ratios, Infrared DC levels, mean pressure values, peak forward and backward flow velocities.

11.4.1 Fluid Properties

The prepared $Co(NO_3)_2$ solution had a conductivity of 68 mS and acidity of 4 pH. The optical spectrum is presented in **Figure 11-4.** and shows low absorption and high

transmission in the area of interest (660 – 860 nm). The measured viscosity at varying shear rates is shown in **Table 11-2**.

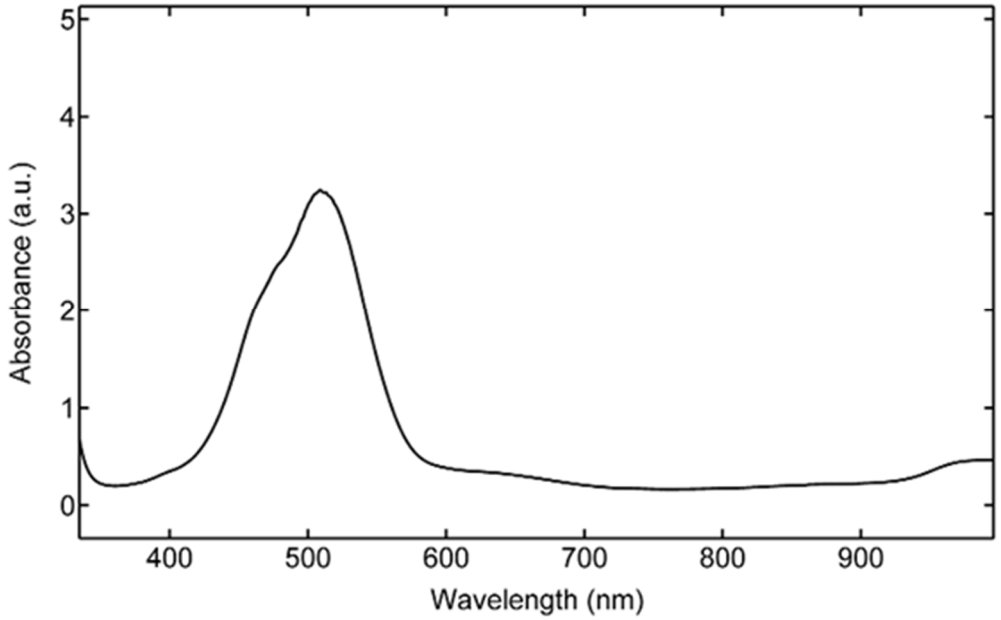

Figure 11-4
Optical Spectra for the prepared Co(NO3)2 solution.

Table 11-2
Fluid Viscosity Measurement

Shear rate (rpm)	Viscosity (mPa.s)
40	3.73
60	2.78
90	1.39

11.4.2 Data Collection

A 20 s sample of the recorded waveforms for both tube models is presented in **Figure 11-5**, at a stroke volume of 70 ml and pumping rate of 60 bpm. **Figure 11-5**(a) shows infrared PPG_{AC} signals, total flow and pressure signals obtained from *Model 1 (*a tube simulating an artery affected with ATH at a stroke volume of 70 ml and pumping rate of 40 bpm). **Figure 11-5**(b) shows infrared PPG_{AC} signals, total flow and pressure signals for *Model 2 (*at a stroke volume of 70 ml and pumping rate of 40 bpm).

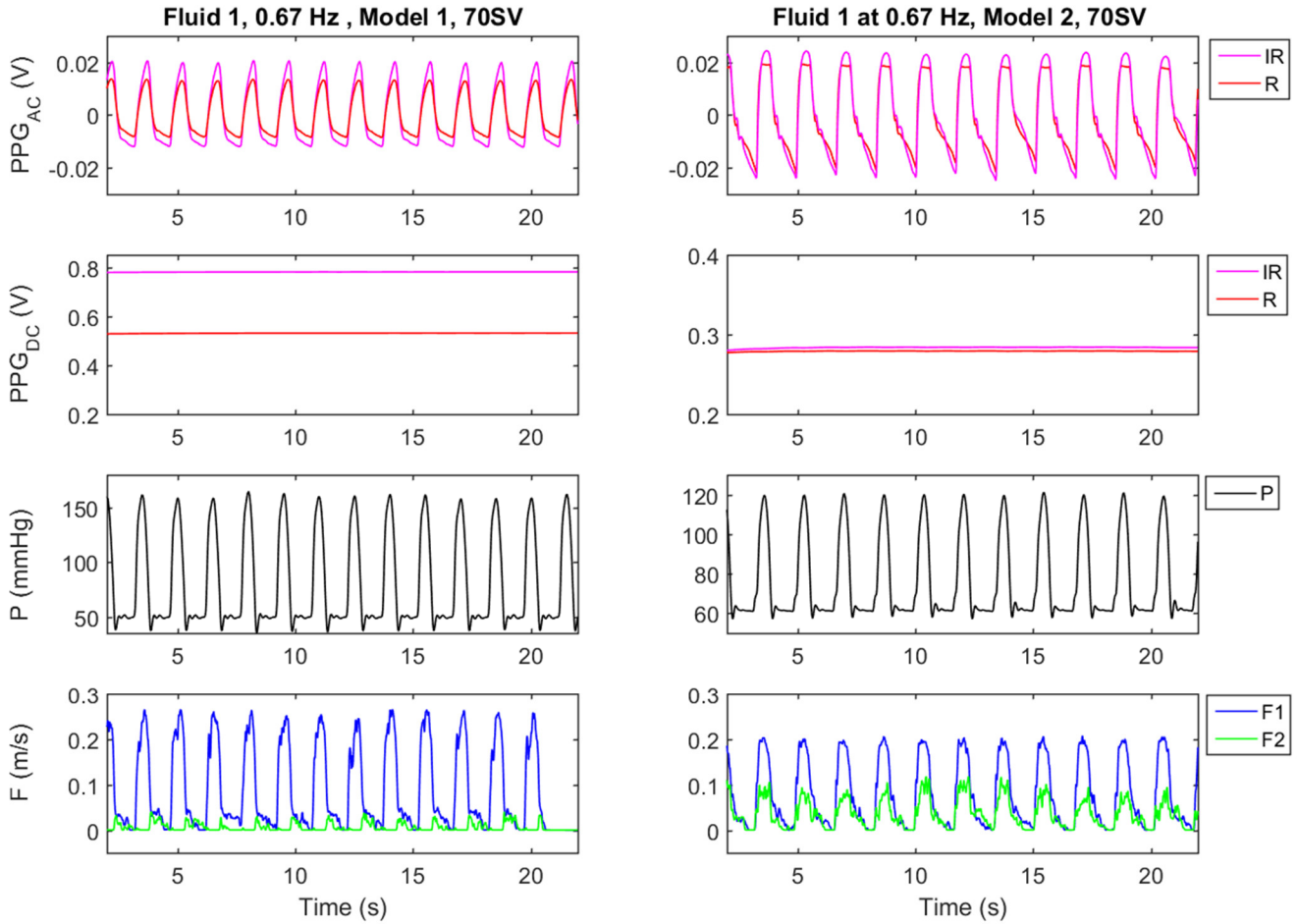

Figure 11-5
Presents a 20-second sample of all the recorded signals (from the top; PPG_{AC} for red (R) Infrared signals (IR), PPG_{DC} for red (R) Infrared signals (IR), pressure (P) and forward (F1) and backward (F2) flow velocities acquired at a frequency of 0.67 Hz , and a stroke volume of 70ml. (a) Left panels are acquired from Model 1, simulating an artery affected with ATH, while panels on the right side show signal acquired from Model 2, simulating a healthy artery.

11.4.2.1 Effect of Pulse Frequency on Optical and Pressure signals

The pump was set to operate at different pulsating frequencies. **Figure 11-6** shows a three-second sample of recorded infrared and red AC PPG signals at all operating pulse frequencies (*w1*=0.66 Hz, *w2*=1 Hz and *w3*=1.6 Hz) at a stroke volume of 70 ml from *Model 1* and *Model 2*.

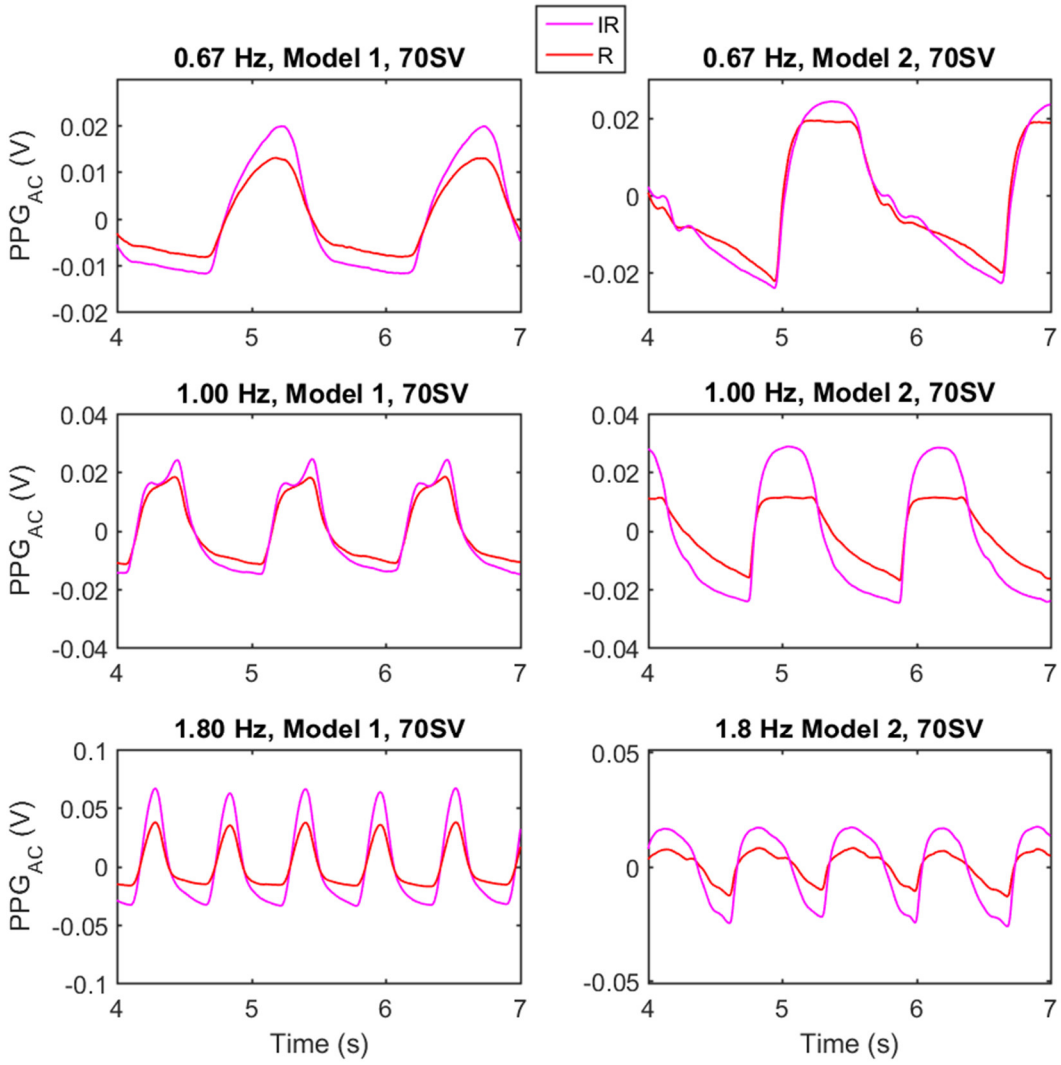

Figure 11-6
presents a 5 s sample for red (R) and Infrared (IR) PPG_{AC} signals acquired from *Model 1* and *Model 2*. This set of data is acquired at 70 ml of stroke volume at all operated pulse frequencies (w1: 0.6 Hz, w2: 1Hz and w3: 1.6 Hz).(a) Left panels present signals acquired from *Model 1*, simulating an artery affected with ATH, right panels show signals acquired from *Model 2*, simulating a healthy artery.

11.4.2.2 Effect of Stroke Volume on Optical and Pressure Signals

The pump parameters were altered to allow a stroke volume of 30 ml. **Figure 11-7** shows a three-second sample of recorded red and infrared AC PPG signals at all operating pulse

frequencies (w1=0.66 Hz, w2=1 Hz and w3=1.6 Hz) at a stroke volume of 30 ml from *Model 1* and *Model 2*.

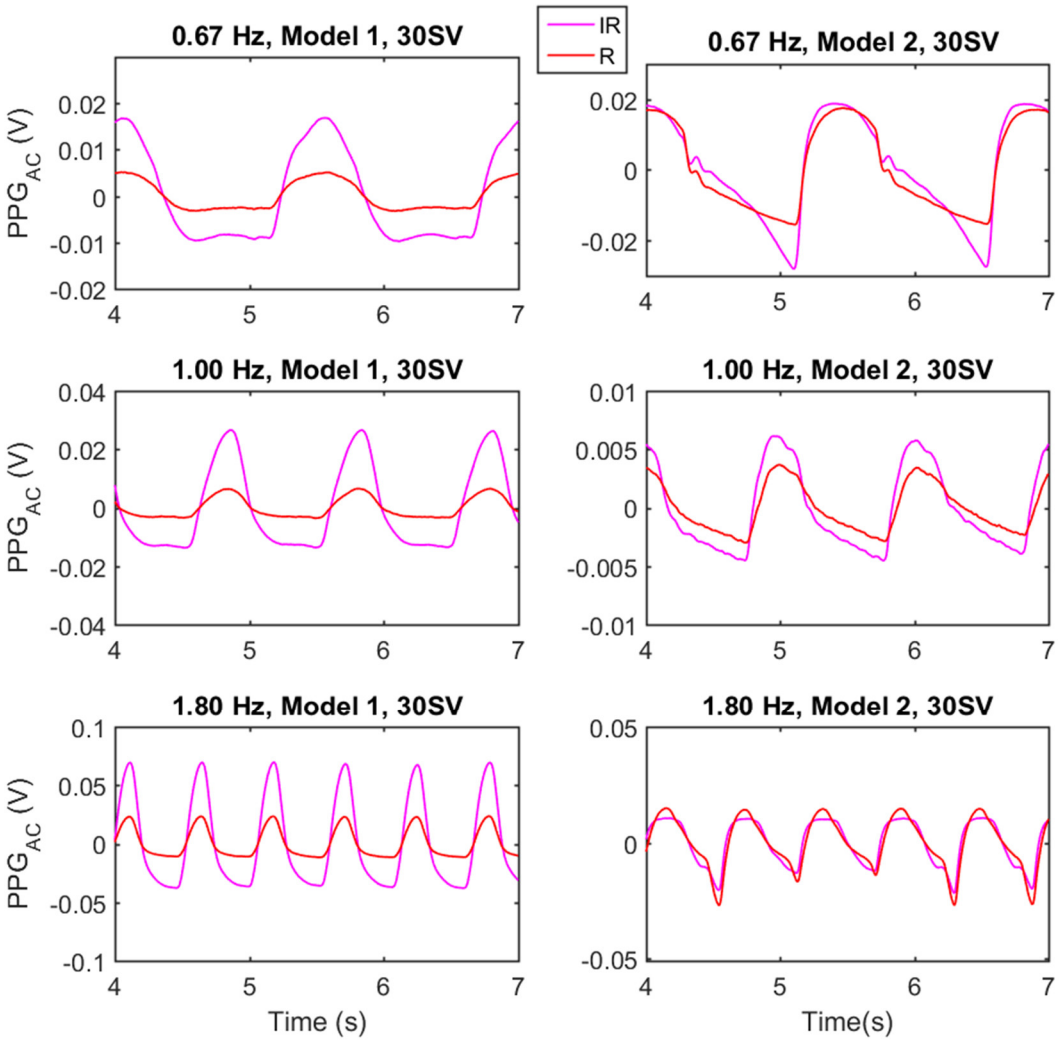

Figure 11-7
A 5-second sample for Red (R) and Infrared (IR) PPG_{AC} signals acquired from *Model 1* and *Model 2*. This set of data is acquired at 30 ml of stroke volume at all operated pulse frequencies . Left panels present signals acquired from *Model 1*, simulating an artery affected with ATH,right panels show signals acquired from *Model 2*, simulating a healthy artery.

11.4.3 Statistical Analyses Comparing *Model 1* and *Model 2* at Varying Pumping Frequencies and Different Stroke Volumes

Statistical summary of the systolic pressure values obtained from *Model 1* and *Model 2* at varying pumping frequencies and at low and high stroke volumes are presented in **Figure 11-8.** The data clearly shows an increase in pressure values with increasing frequencies in both models and at both stroke volumes. Another expected observation is that pressure

values are significantly higher in *Model 1* when compared to *Model 2* at each pumping frequency and at both stroke volumes. Since, *Model 1* is stiffer than *Model 2*.

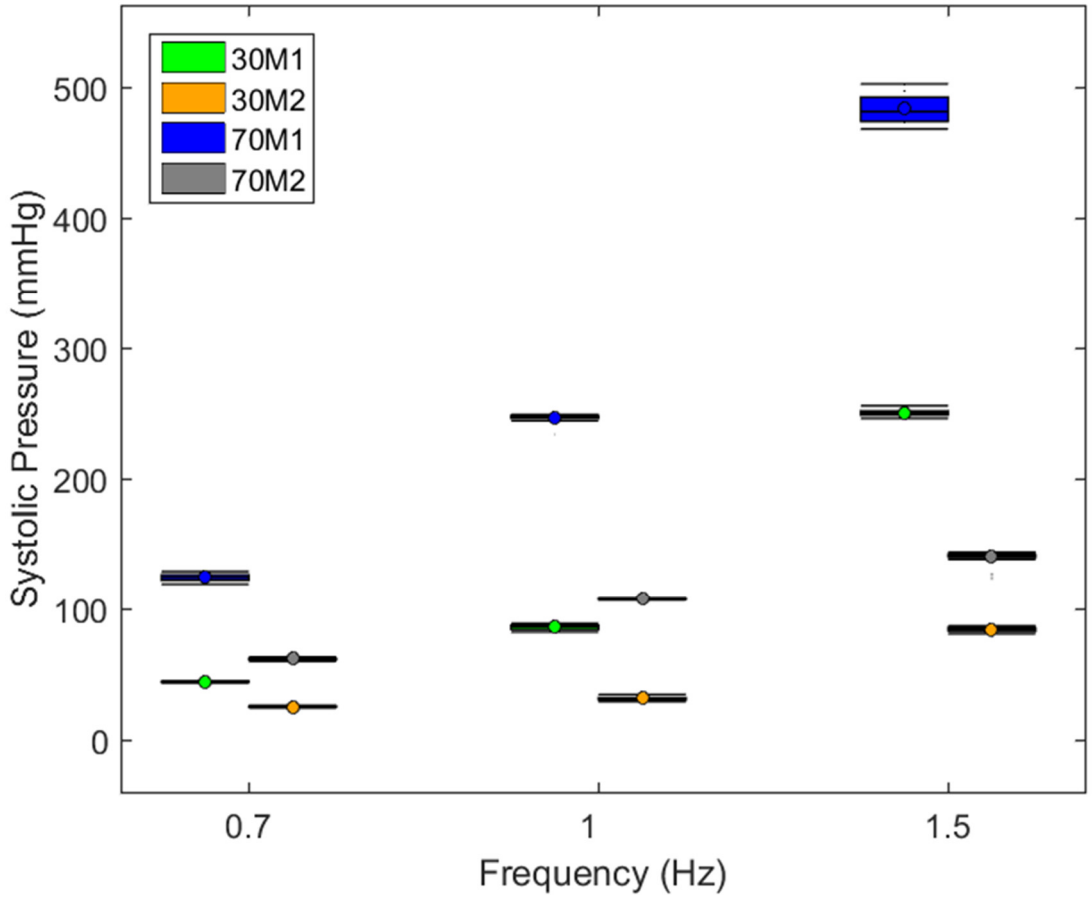

Figure 11-8
Systolic pressure values obtained from *Model 1* (M1) and *Model 2* (M2) at varying pumping frequencies and at stroke volumes of 30 ml (30) and 70 ml (70).

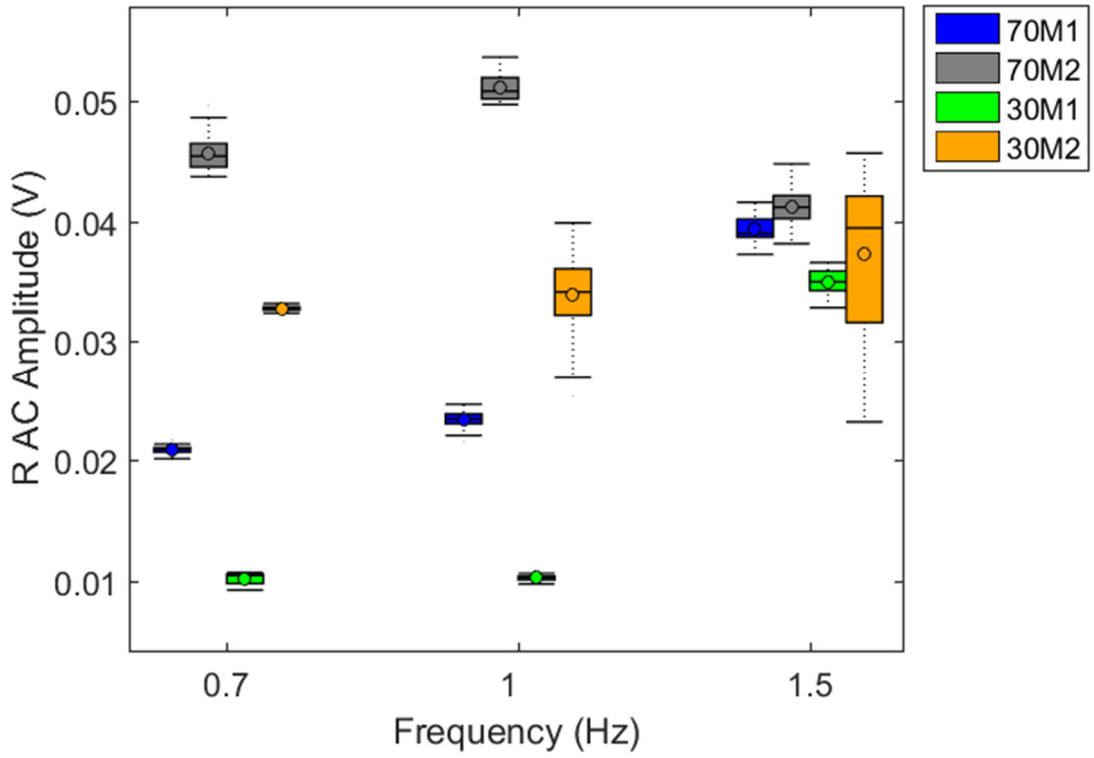

Figure 11-9
Red AC amplitudes obtained from *Model 1* (M1) and *Model 2* (M2) at varying pumping frequencies and at stroke volumes of 30 ml (30) and 70 ml (70).

A statistical summary of AC amplitudes obtained from red PPG AC signals from *Model 1* and *Model 2* and at stroke volumes of 30 ml and 70 ml are seen in **Figure 11-9.** *Model 2* had significantly elevated AC amplitudes when compared to *Model 1*, at both stroke volumes and at all pumping frequencies.

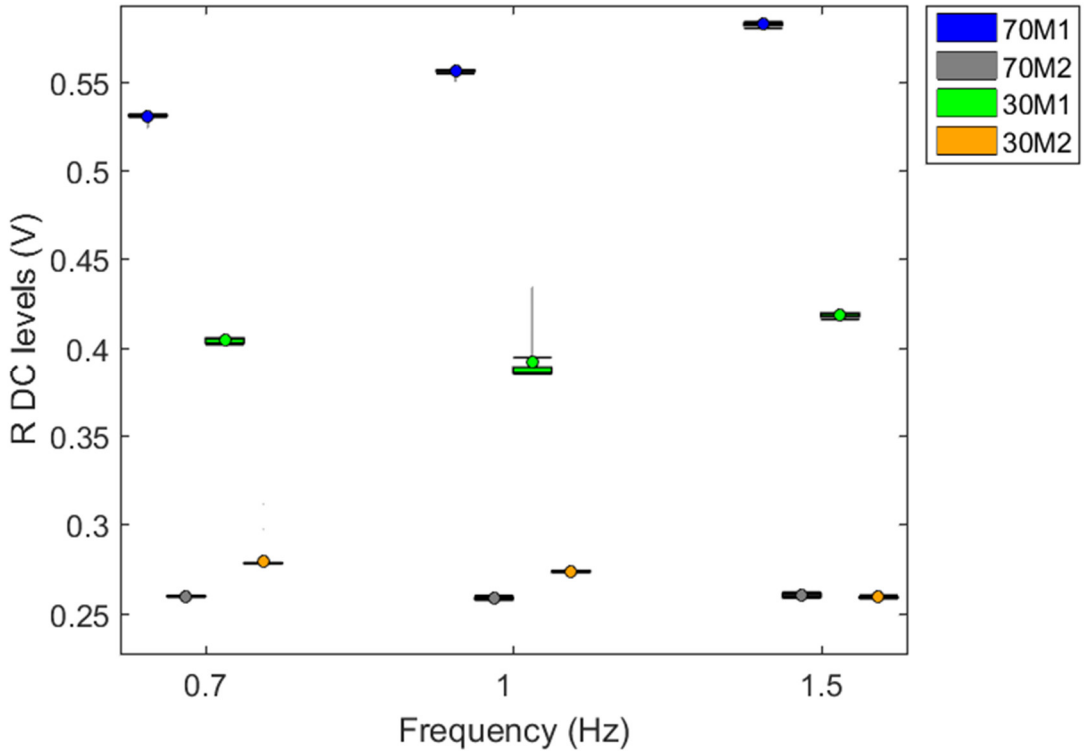

Figure 11-10
Red DC levels obtained from *Model 1* (M1) and *Model 2* (M2) at varying pumping frequencies and at stroke volumes of 30 ml (30) and 70 ml (70).

A statistical summary of Red DC levels obtained from *Model 1* and *Model 2* and at stroke volumes of 30 ml and 70 ml are seen in **Figure 11-10.** *Model 2* had significantly reduced DC levels when compared to *Model 1*, at both stroke volumes and at all pumping frequencies.

Statistical values for forward flow velocities are seen in **Figure 11-11** and those for backward flow velocities are seen in **Figure 11-12.** The main observation is that *Model 2* have significantly higher backward flow velocities when compared to *Model 1* at all pumping speeds and both stroke volumes. While, forward flow velocities seemed to generally increase with increasing pumping frequencies, this was not always the case. In the case of Model 1 at 70 ml stroke volume, forward flow velocities dropped at the highest pumping frequencies. These results will be further discussed in chapter 14.

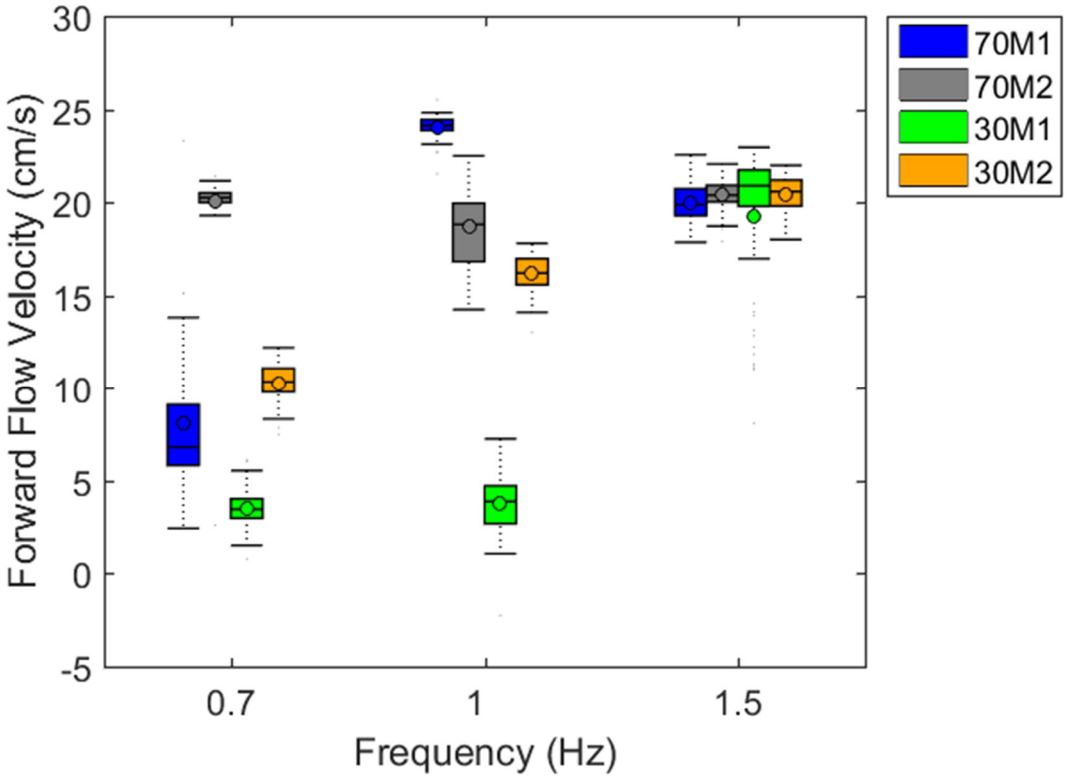

Figure 11-11
Forward flow velocities as obtained from *Model 1* (M1) and *Model 2* (M2) at varying pumping frequencies and at stroke volumes of 30 ml (30) and 70 ml (70).

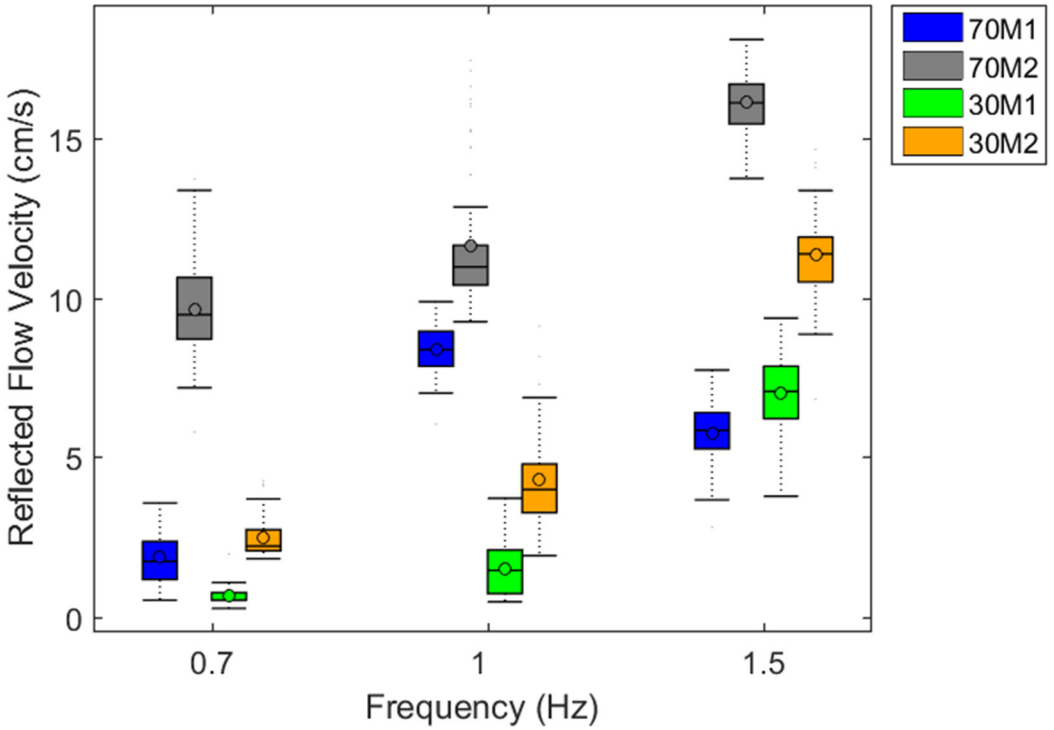

Figure 11-12
backward flow velocities as obtained from *Model 1* (M1) and *Model 2* (M2) at varying pumping frequencies and at stroke volumes of 30 ml (30) and 70 ml (70).

11.4.4 E_v Calculation

This section presents Ev values as calculated from the proposed method for both models. **Figure 11-13** presents the relationship seen in eq(11.10) for the rate of change of Pressure versus the change rate of NVS. Figure 11-13(a) shows values obtained from *Model 1* and **Figure 11-13(b)** shows values obtained from *Model 2*. SSE, R-square, and RMSE values indicate the goodness of the linear fit. Values are obtained from cycle-to-cycle measurements at both stroke volumes (30 ml and 70 ml) and at the three varying pulse frequencies. A plot of residuals versus lagged residuals is presented in **Figure 11-14** for *Model 1* and in **Figure 11-14(a)** and for *Model 2* in **Figure 11-14(b)**.

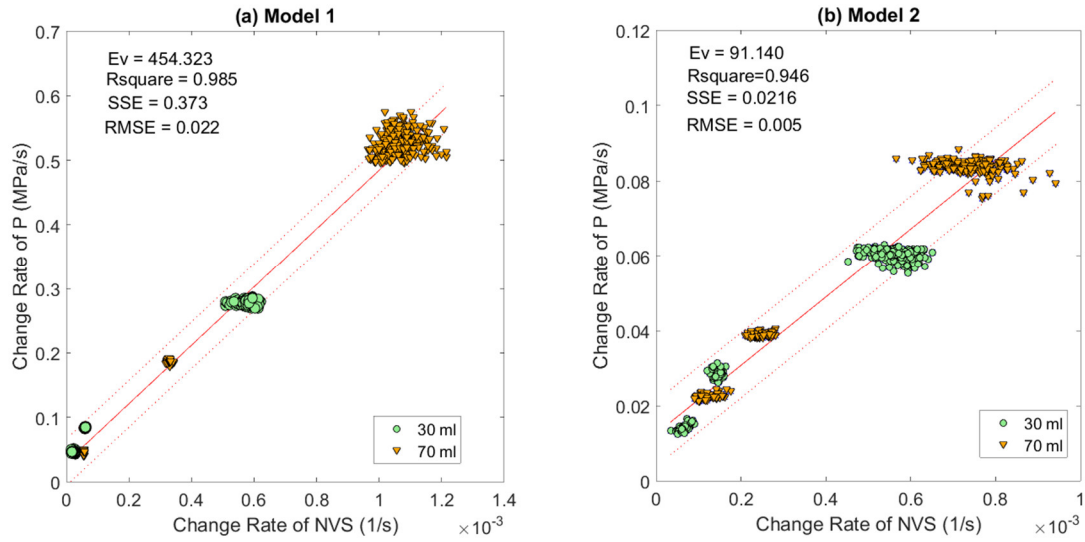

Figure 11-13
Scattergrams and linear regression models for the rate of change of Pressure versus the rate of change on Normalised Volumetric Strain. (a) Values obtained from *Model 1*, (b) values obtained from *Model 2*. Ev values are the slope of the fitting equation. R-square, SSE, and RMSE present the goodness of fit. Points are obtained from cycle-to-cycle measurements at both stroke volumes and at varying pumping frequencies.

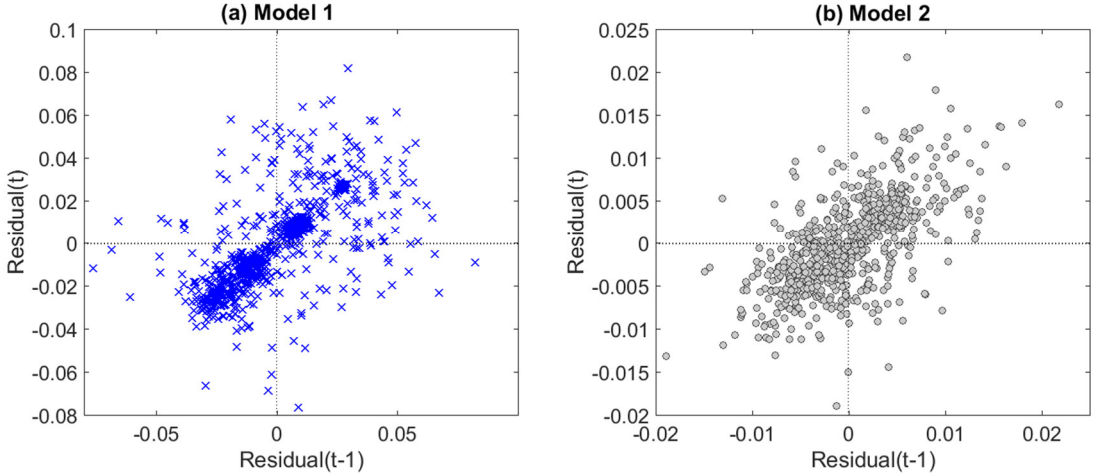

Figure 11-14
The plot of residuals versus lagged residuals (a) *Model 1* and (b) *Model 2*.

11.4.5 E_v Validation using the gold standard method

The stress-strain curves for both models as obtained from the gold standard elasticity measurement technique are presented in **Figure 11-15**. **Figure 11-15(a)** shows values obtained from *Model 1*, **Figure 11-15(b)** values obtained for *Model 2*. Elastic Modulus (E) is the slope value obtained using a 1st-degree polynomial fit and Ev is calculated for each model using the formula E/3(1-2v). Where v is the estimated Poisson's ratio from the longitudinal-transverse strain curve for each model and obtained the values, 0.4914 and 0.4884 for *Model 1* and *Model 2* respectively. SSE, R-square, and RMSE values indicate goodness of the linear approximation fit.

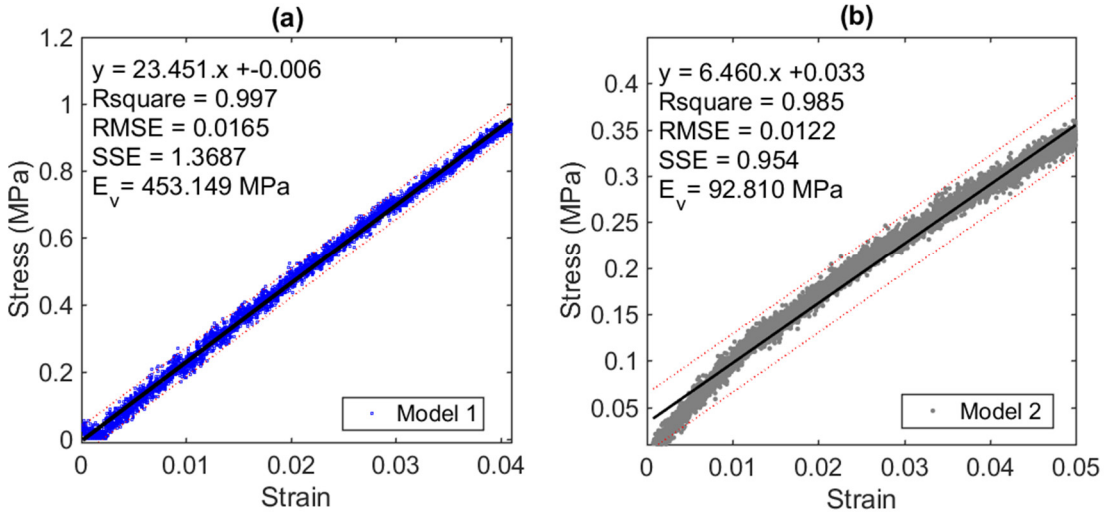

Figure 11-15
Stress-strain scattergrams as obtained using the gold standard method, Instron. A linear function is fitted to the data. (a) Measured Values for a sample of *Model 1*. (b) Measured values for a sample of *Model 2*.

The analysis of covariance was performed between the slope of the measured and the validated data, p-values are shown in **Table 11-3**.

Table 11-3
p-values, statistical significance and percent errors between the proposed E measurement method and the gold standard.

Model	p_value	Significant	Percent error
Model 1	0.409	No	0.258%
Model 2	0.080	No	1.85%

11.4.6 The Effect of Stroke Volume and Pumping Frequencies on E_v and PTT

Instantaneous E_v and PTT was calculated at different stroke volumes and at each pumping frequency. Instantaneous E_v was calculated as in equ(11.4) for each model at each frequency. PTT was calculated as the difference in time between the peaks of pressure and the foot of the infrared PPG signals. Boxplots for the instantaneous E_v and the pulse transit time methods calculated for both models are presented in **Figure 11-16**. **Figure 11-16(a)** shows values for E_v method and **Figure 11-16(b)** shows values for the PTT method. Values were estimated over 1 min of cycle-to-cycle data at each frequency and stroke volume 70 ml (70), 30 ml (30) and for both models, *Model 1* (M1) and *Model 2* (M2).

Bonferroni's multiple comparisons tests were able to detect a significant difference between *Model 1* and *Model 2* at both stroke volumes, and at all pumping frequencies from the PTT and E_v methods. However, the PTT method was not able to detect differences at increasing pumping frequencies in *Model 2* from 1 Hz to 1.8 Hz. At a frequency of 1 Hz, *Model 2* seemed to produce higher elasticity at higher stroke volumes from the PTT method. The E_v method showed a consistent significant drop in wall stiffness with increasing pumping frequencies. Moreover, a significant increase in wall stiffness was observed at higher stroke volumes. Nevertheless, this observation diminished at a frequency of 1.8 Hz with no significant difference in E_v values at both stroke volumes. The PTT method still detected significant differences between both stroke volumes at the highest operating frequency.

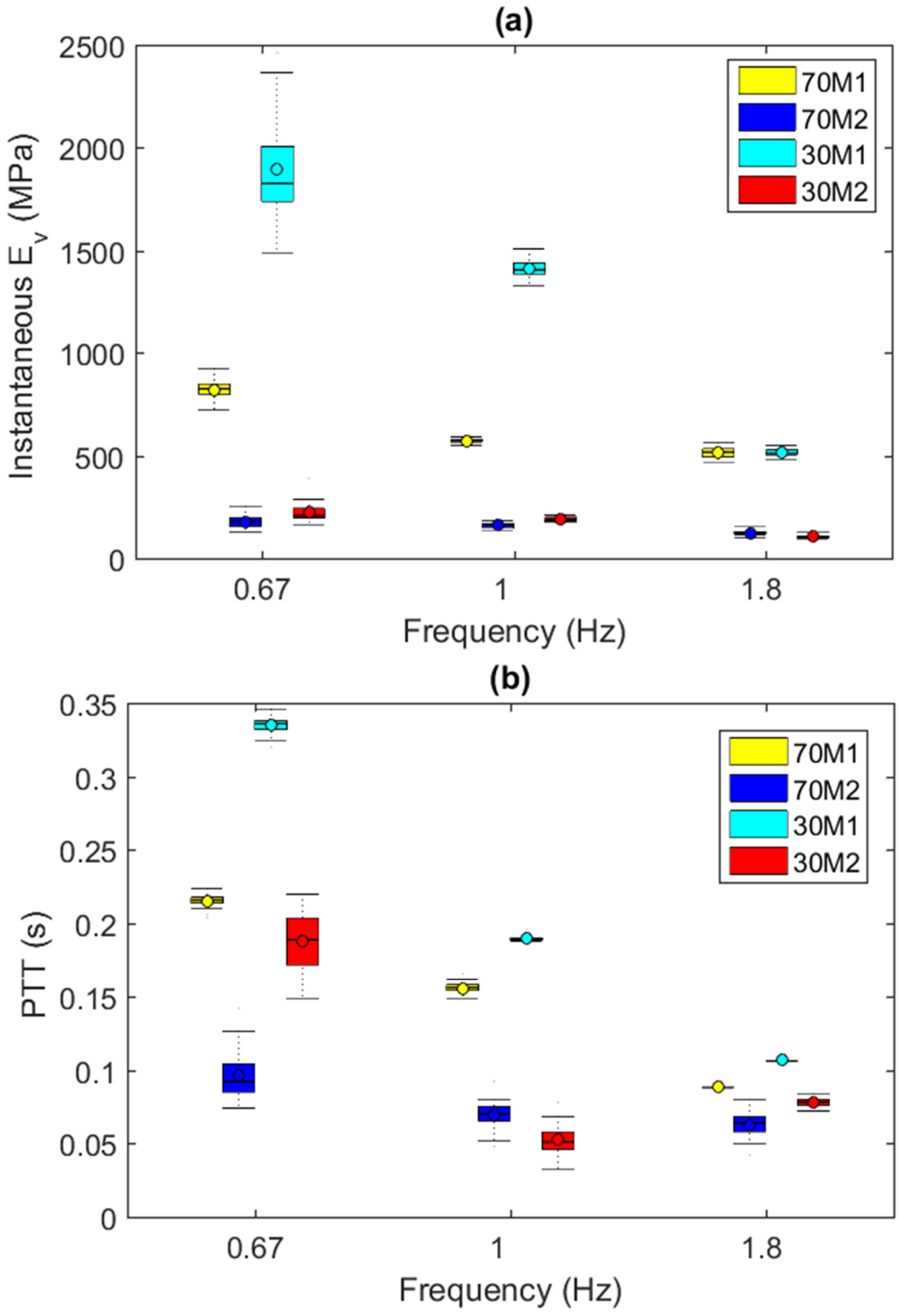

Figure 11-16
Boxplots for the instantaneous E_v and the pulse transit time methods calculated for both models at varying pumping frequency. Panel (a) shows values for E_v method and Panel (b) shows values for the PTT method. Values were estimated over 1 min of cycle-to-cycle data at each frequency and stroke volume, 70 ml (70), 30 ml (30) and for both models, *Model 1* (M1) and *Model 2* (M2).

SUMMARY

This chapter addressed the effect of wall stiffness on the AC and DC components of the PPG signal. It also presented a validation for a proposed method for measurement of volume elastic modulus (E_v) for quantification of arterial stiffness. Increased wall stiffness contributed to a drop in AC amplitudes and increase in DC levels, highlighting that wall stiffness is an important factor that alters the generated wave. The method of E_v measurement was validated and showed no significant difference against the gold standard method for E_v measurement. Observations and results will be further discussed in **Chapter 14**, however, this chapter highlighted that wall stiffness is an important factor that affects the morphology, AC amplitudes, and DC levels of the PPG signal.

Chapter 12
THE EFFECT OF FLUID VISCOSITY ON THE PPG SIGNALS

12.1 Introduction

Following the initial investigation of basic optical interaction with the pulsatile flow at different flow rates in the previous chapter, this chapter investigates the effect of fluid viscosity on both components (AC and DC) of the PPG signal under varied conditions of flow dynamics. The literature suggests that most investigators in the field of Photoplethysmography have overlooked the effect of blood viscosity and its contribution to the PPG signal.

It is possible to find abundant evidence throughout the literature that blood viscosity can be a significant indicator of cardiovascular disease as previously discussed in **Chapter 3**. Nonetheless, measurement of blood viscosity has been applied only for research purposes. Viscosity has never been adopted as one of the routine investigations during clinical blood tests for cardiovascular patients. This situation can be partly attributed to the lack of an appropriate instrument designed to measure blood viscosity suitable for considering the rheological properties of blood, specifically designed to meet clinical needs.

Consequently, a study investigating the potential of the PPG technique in detecting viscosity changes is especially justified, due to the following reasons:

(1) Previous *in vitro* studies reported on the potential of optical methods for measurement of blood viscosity (Keen et al., 2009; Muramoto and Nagasaka, 2011; Wang et al., 1995). This is further discussed in **Chapter 3**. Yet, these methods can only provide intermittent measurements, and were not taken further to

reach any clinical investigations. Therefore, such studies justify the possibility of PPG as an optical technique to detect viscosity changes.

(2) An increase in blood viscosity is known to increase the workload on the heart, and increase arterial pressure, and hence, affect flow patterns. PPG is a technique that proved to be sensitive to flow changes as seen in the previous chapter (Hertzman, 1938).

(3) Elevated blood viscosity is an established sign of increased cardiovascular risk and is linked with cardiovascular disease, whether at early or advanced stages, therefore, a non-invasive continuous approach utilising the PPG technique for viscosity measurements can be a convenient and affordable tool for clinical assessments.

This chapter aims to investigate the effect of fluid viscosity on the AC and DC components of the PPG signal in the *in vitro* experimental setup. The main focus of this study is to explore the concept of optical detection of fluid viscosity in pulsatile flow and establish the basis of the utility of the PPG technique for this purpose for further investigations. Using the previously described *in vitro* experimental setup (see **Chapter 9**), we evaluate the response of the AC and DC components of the PPG signal at distinctive fluid dynamic conditions by circulating fluids with different viscosities at varying flow rates.

12.2 Study Protocol

The pump-arterial network setup described in **Chapter 9** was used for this experiment. The setup was slightly adjusted by directing the flow to *Model 1* only, using the stopcocks as illustrated in **Figure 12-1**. The PPG reflectance R and IR sensor (described in Chapter 6) was fixed in the middle of the arterial model. The pressure was measured at the entrance of the tube, after the entrance range, using a research grade catheter-tip pressure transducer (Harvard Apparatus, US). An ultrasound Doppler (MD2, Huntleigh, UK) with an 8 MHz probe was fixed at a 60° angle with the arterial model for further calculation of forward and backward flow. Data collection was performed at a sampling rate of 1000 Hz using the same data-acquisition systems previously described (**Chapter 7**). All data collected in real time was archived for further offline analysis.

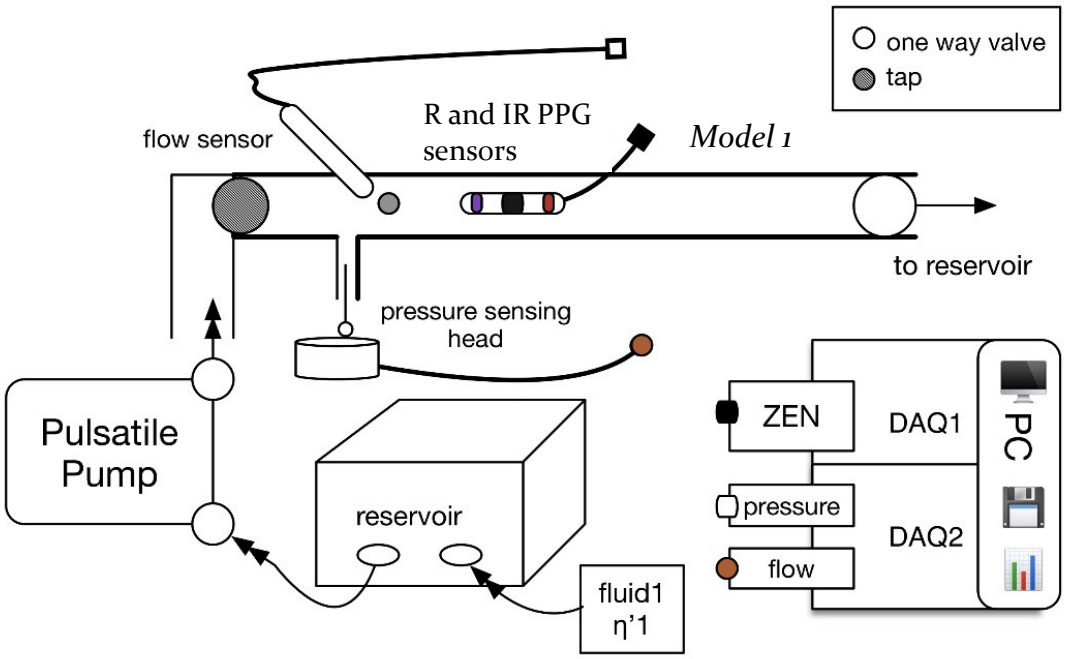

Figure 12-1
Schematic of Pump Setup modified for investigating the effect of fluid viscosity on PPG.

Throughout this investigation, the setup was designed to maintain its stability where all flow dynamics follow a controlled regime during the experiment. The experiment is divided into two stages, stage 1 where *fluid 1* is circulated under varying pulsating frequencies at a fixed stroke volume and stage 2, where *fluid 2* is circulated under varying pulsating frequencies at the same stroke volume. **Table 12-1** include all the parameters used during this experiment.

Table 12-1
Parameters used for the experiment.

Parameter	Fluid 1 (*v1*)	Fluid 2 (*v2*)
Artery properties	*Model 1*	*Model 1*
Wall Elastic Modulus (MPa)	24.00	24.00
Stroke volume (ml)	70.00	70.00
Density (g.ml)	1.0914	1.1102
Pulsating frequency (Hz)	f1= 0.67 f2= 1.00 f3= 1.80	f1= 0.67 f2= 1.00 f3= 1.80
Speed (RPM)	40,60,108	40,60,108
Resistance	Tube of interest only	Tube of interest only
Concentration	0.60 M	0.60 M
Solution	Saline	Saline
PEG concentration	-	66.00 g/L

The experiment was performed as follows:

1. Three litres of each fluid were prepared. Fluid 1 was ready to produce 0.6 M of Cobalt Nitrate $Co(NO_3)_2$ in saline solution (0.9%). Fluid 2 was produced with the same Cobalt Nitrate concentration in saline with added polyethene glycol (PEG) with a molecular weight of 6000, at a concentration of 66 g/L.
2. The optical absorption spectra were obtained using a sample of each solution in the visible and near infrared range using a spectrometer analyser (Lambda 1050, PerkinElmer). The viscosity of both fluids was measured at three speeds (40, 60, 100 Rpm) using the LVD3T rheometer (Brookfield, US). Fluid pH and conductivity were also obtained using the conductivity/pH metre (Jenway, UK). The experimental setup for testing mechanical and electrical characteristics of the fluids is shown in Figure 12-2.
3. The pump was cleaned and left to dry for one day. Three litres of fluid 1 were poured into the reservoir.
4. The pump was left to operate at the initial frequency 0.67 Hz for 20 minutes to ensure a bubble-free and fully developed flow.
5. Signal recording started after that period and continued for consecutive five minutes.

6. The pumping frequency was increased to one Hz, and the system was left to stabilise for ten minutes. The recording restarted after that period and continued for another five minutes. Finally, the pumping frequency was increased to 1.8 Hz. After the system was stabilised for ten minutes, the recording continued for another five minutes.
7. The reservoir, tubes, and the pump were thoroughly cleaned and left to dry.
8. Fluid 2 was poured into the reservoir and steps 4 to 6 were repeated.

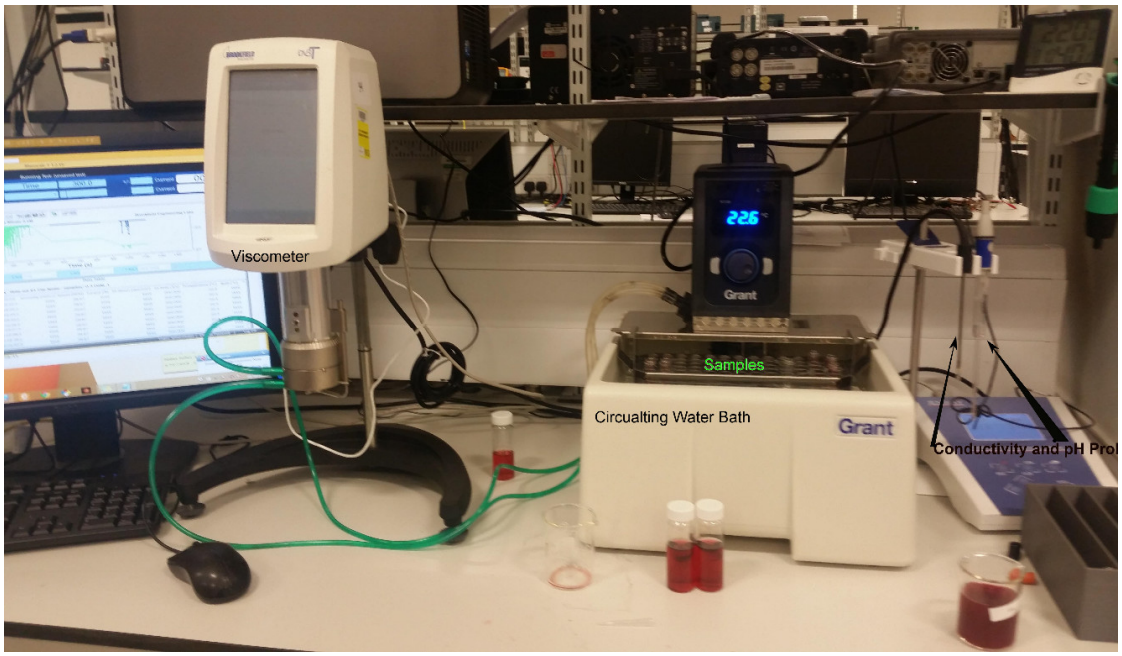

Figure 12-2
Experimental Setup for measurement of mechanical and electrical fluid properties. Showing temperature-controlled water bath containing fluid samples and the conductivity/pH probes. The water bath also circulates to the chamber of the cone/plate viscometer, where viscosity values are measured at varying shear rates.

12.3 Data and Statistical Analyses

The collected data via the LabVIEW software were analysed offline using Matlab. More details describing the script and methods of filtering and data extraction can be found in Chapter 8. The Data obtained are; Infrared and Red AC and DC PPG signals, pressure signal and both forward and backward flow signals.

The data fits Gaussian distribution as tested using the distribution fitting tool in Matlab. Therefore, the data qualified for one-way ANOVA test. This was followed by Sidak's multiple comparison tests to evaluate significance. A significant value was considered if the p-value is less than 0.05, with a 95% confidence interval.

12.4 Results

In this section, we present the measured values for fluid properties, including the optical spectra using the spectrophotometer in the red and near-infrared range, conductivity, pH, and viscosity measurements. We further, present visual data from the processed R and IR PPG_{AC} and PPG_{DC} signals; pressure, forward and backward flow. Furthermore, we present statistical analyses showing average and standard deviations of R and IR PP_{AC} amplitudes, R and IR PPG_{DC} levels, mean pressure values, peak forward and backward flow velocities. Moreover, we tabulate Sidak's multiple comparison tests, which compares both fluids at each pumping frequency, and each fluid separately at varying pumping frequency. The statistical comparison shows mean differences, p-value, and summary of significance status using the 3-star system.

12.4.1 Fluid Properties

The optical spectra in the visible and near infrared region were obtained from the Spectrometer for both fluids (*fluid 1* and *fluid 2*) and can be seen in **Figure 12-3**. Each fluid was tested for conductivity and pH values using a 20 ml sample, and the results are presented in **Table 12-2**. Viscosity values over varying shear rates were measured using the cone/plate viscometer for each fluid and are seen in **Table 12-3**. While both fluids have the same optical absorption peaks, fluid 1 is less viscous than fluid 2, and hence it is less absorbent and transmits more light than fluid 2 at the same frequency.

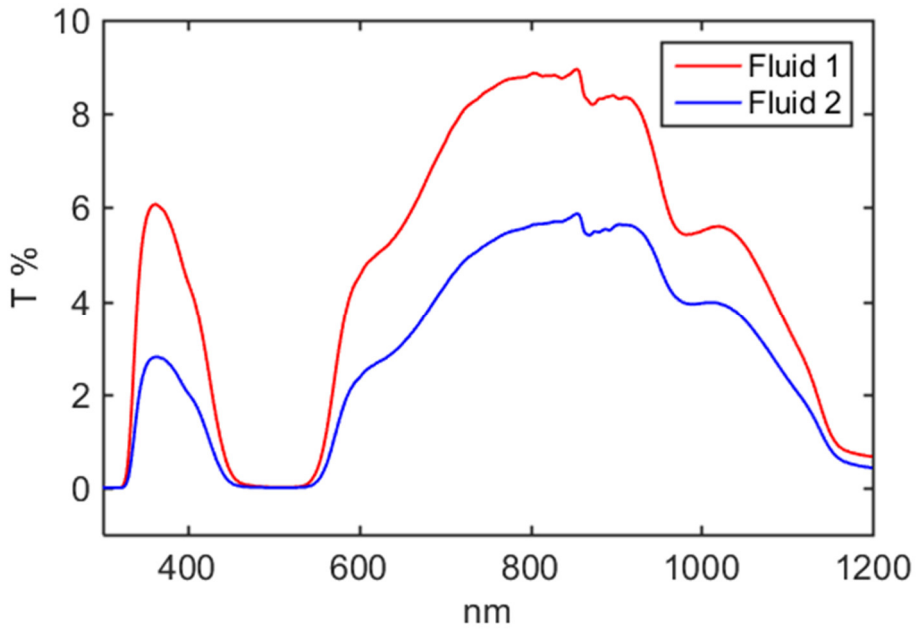

Figure 12-3
Transmission spectra in the visible and near infrared spectrum for fluid 1, cobalt nitrate in saline, and fluid 2 cobalt nitrate in PEG saline.

Table 12-2
Conductivity and pH levels

Material	Conductivity (mS)	pH	Temperature (°C)
Fluid 1 (v1)	77.40	3.60	22.70
Fluid 2 (v2)	60.20	3.10	22.70

Table 12-3
Viscosity values measured by DV3LT at varying shear rates

	Viscosity (mPa.s)	
Shear rate (RPM)	Fluid 1	Fluid 2
40	3.73	10.82
60	2.78	5.93
100	1.39	3.10

12.4.2 Data Collected from the Investigations of the Effect of Fluid Viscosity on the PPG Signals

In this section, we present visual results of the collected signals, for each fluid at different pumping frequencies. Signals were obtained at a fixed stroke volume of 70 ml. A five-second sample of the collected signals at a frequency of 0.67 Hz for *fluid 1* and *fluid 2* are shown in **Figure 12-4**. Panel(a) shows infrared AC (IR_{AC}) and red AC (R_{AC}) signals. Panel(b) showing DC (IR_{DC}) and DC (R_{DC}) PPG signals, panel(c) showing pressure (P) signals, and panel(d) forward (F1) and backward (F2) flow velocities.

Figure 12-5 presents five-second samples of IR and R AC PPG signals and DC PPG signals, pressure, forward and backward flow velocities at a frequency of one Hz for *fluid 1* and *fluid 2*. While **Figure 12-6** presents a five-second sample of IR and R AC and DC PPG signals, pressure and flow velocity signals at a pumping frequency of 1.8 Hz for both fluids. Flow velocities seem to saturate at the highest frequency showing a square-shape peak, this is due to technical limitation.

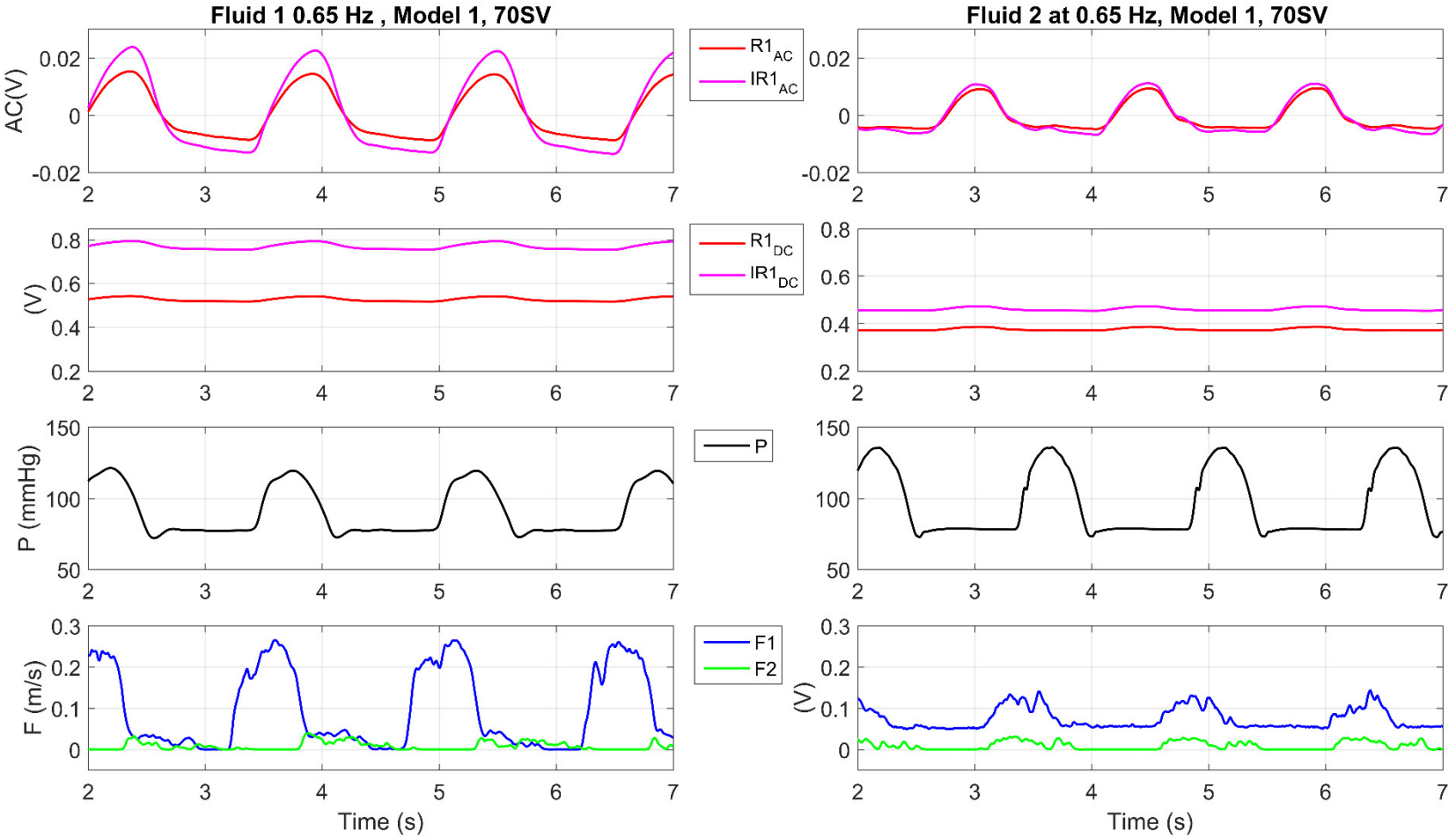

Figure 12-4
From the top, AC PPG signals for Red (R_{AC}) and Infrared (IR_{AC}), DC PPG signals for red (R_{DC}) and infrared (IR_{DC}), Pressure (P), Forward (F_1) and backward (F_2) flow velocities. Signals are obtained at a frequency of 0.67 Hz and a fixed stroke volume of 70 ml. Signals are seen for fluid 1 at left panels and fluid 2 at right panels.

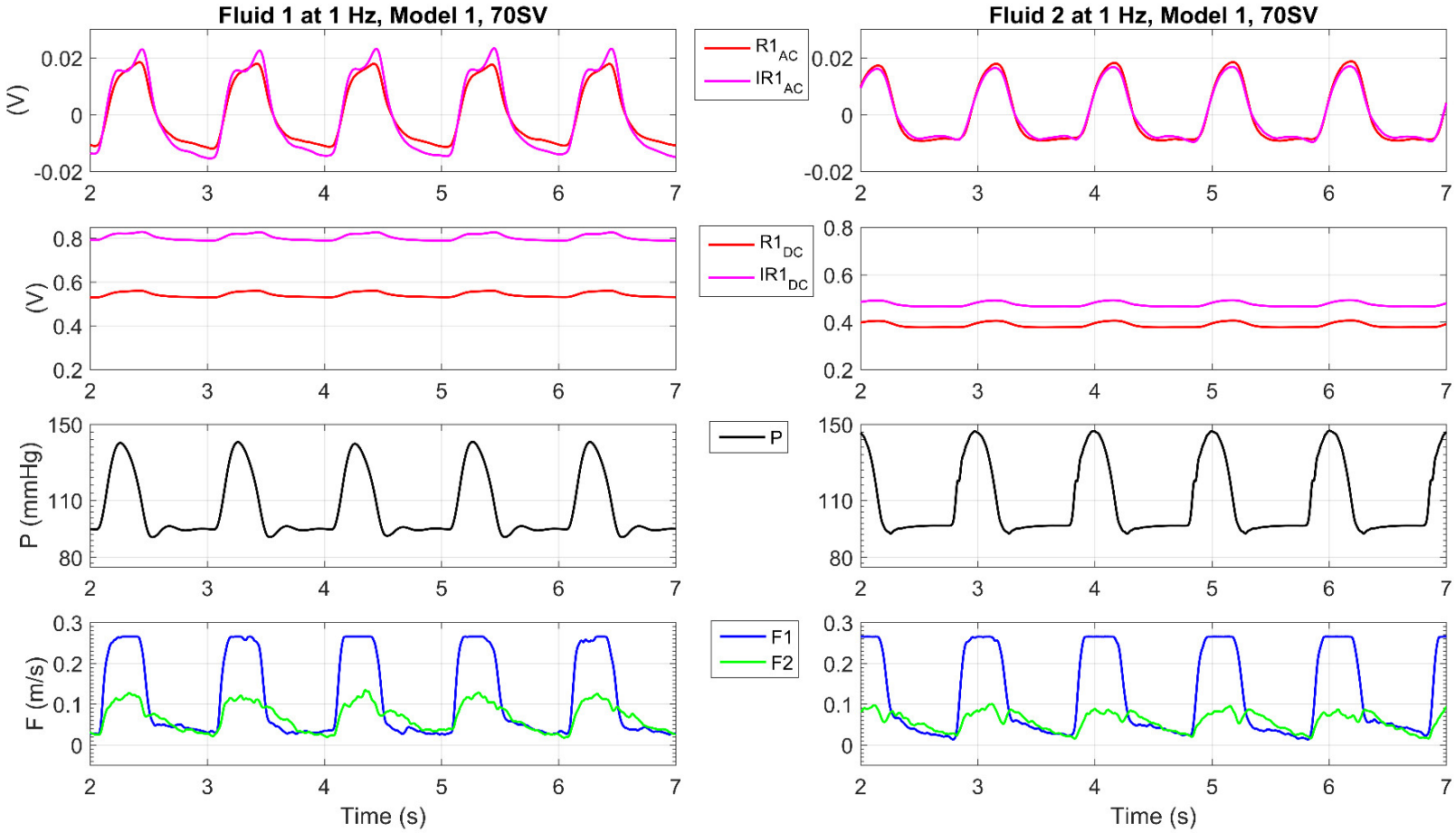

Figure 12-5
From the top, AC PPG signals for Red (R) and Infrared (IR), DC PPG signals for red (R) and infrared (IR), Pressure (P), Forward (F1) and backward (F2) flow velocities. Signals are obtained at a frequency of 1 Hz and a fixed stroke volume of 70 ml. Signals are seen for fluid 1 at left panels and for fluid 2 at right panels.

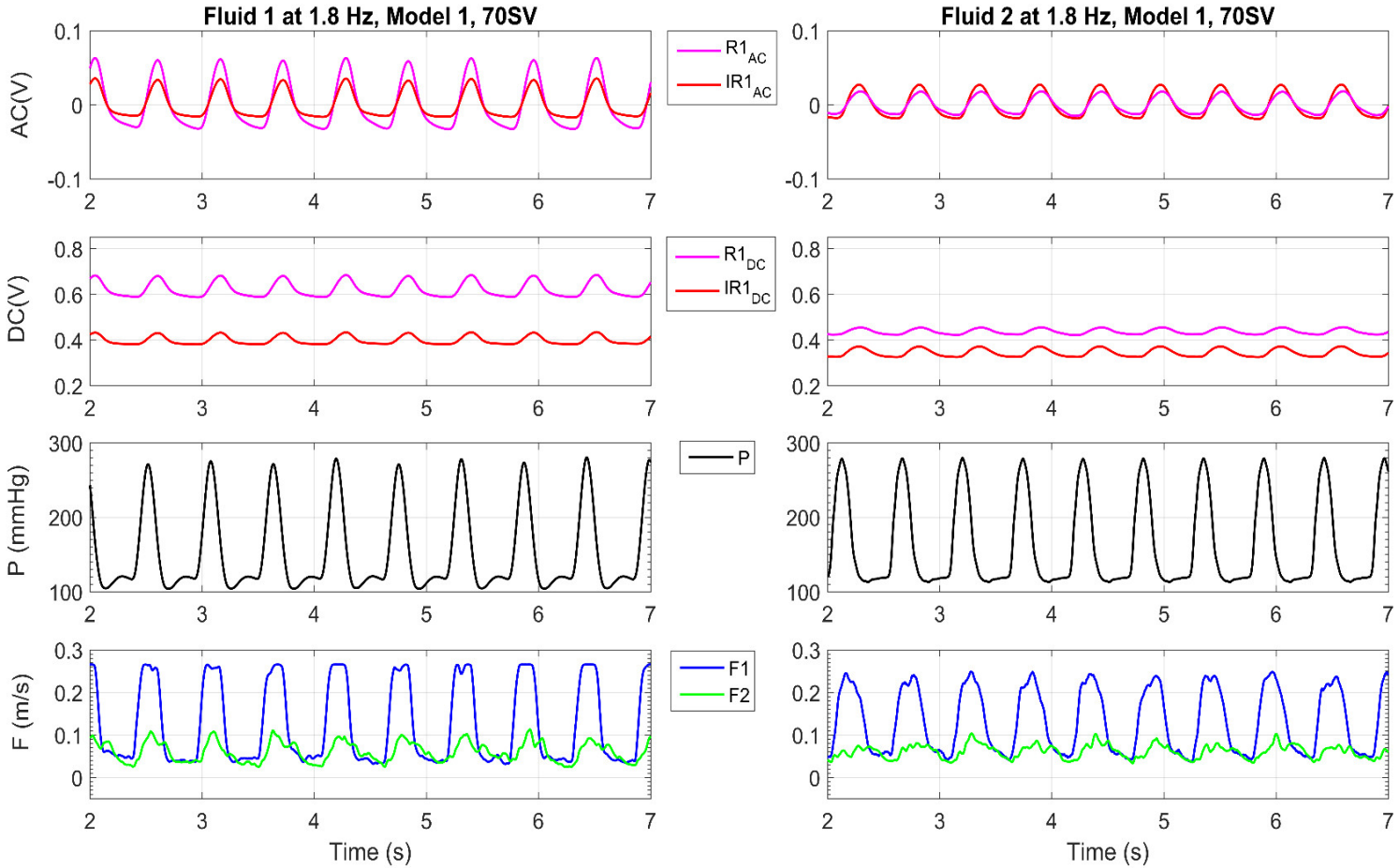

Figure 12-6
From the top, AC PPG signals for Red (R) and Infrared (IR), DC PPG signals for red (R) and infrared (IR), Pressure (P), Forward (F1) and backward (F2) flow velocities. Signals are obtained at a frequency of 1.8 Hz and a fixed stroke volume of 70 ml. Signals are seen for fluid 1 at left panels and for fluid 2 at right panels.

12.4.3 Statistical Analyses

One-way ANOVA tests were performed for each set of data, and Sidak's multiple comparison tests were performed to investigate the significance of the difference between the obtained measurements. Results are tabulated to include difference values, p-values, and significance summary. In this section, we presented the statistical analysis for pressure, forward and backward flow, R and IR AC amplitudes and DC levels for both fluids at varying pumping frequencies.

12.4.3.1 Mean Pressure values for both fluids at varying pumping frequencies

Mean pressure values are presented in **Figure 12-7**. Sidak's multiple comparison tests for significance are shown in **Table 12-4**.

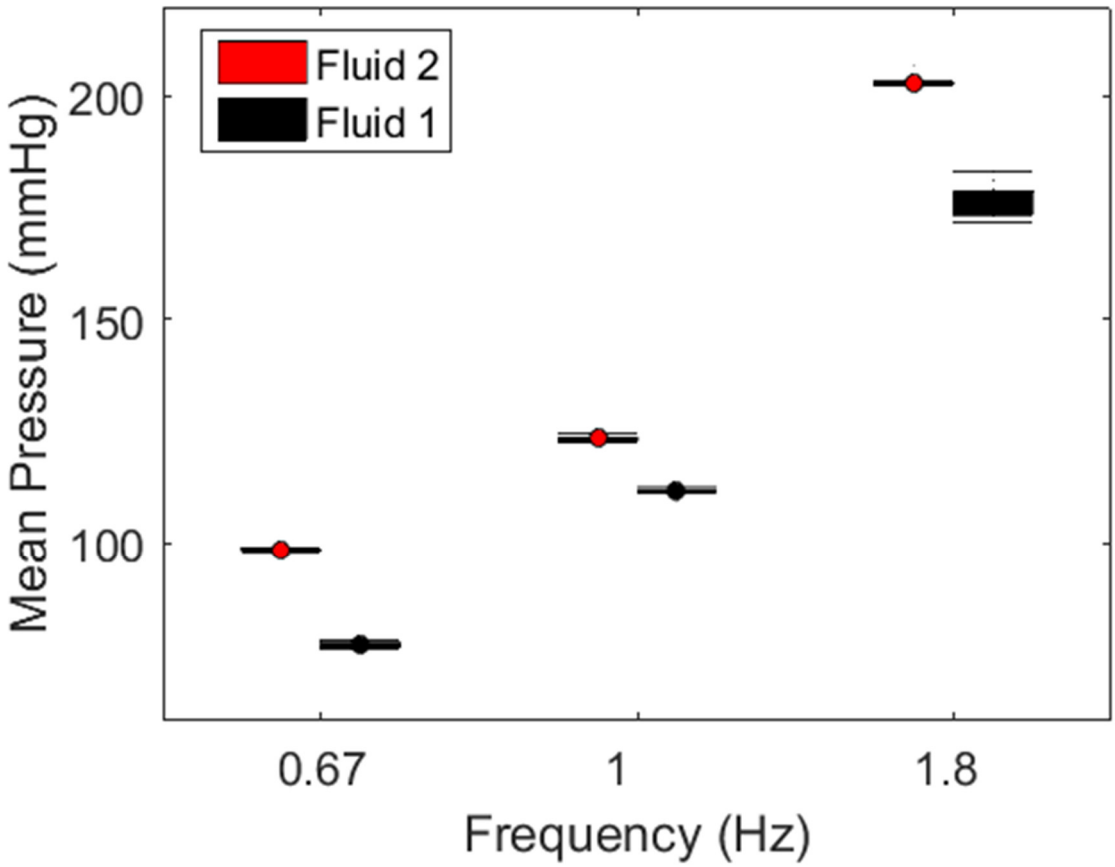

Figure 12-7
Average ± SD for mean pressure values at varying pumping frequencies while circulating fluids with different viscosity.

Table 12-4
Sidak's statistical test calculated for mean pressure values for multiple comparisons of both fluids at varying pumping frequencies

Comparing mean pressure values for fluid 1 (*v1*) and fluid 2(*v2*) at each pumping frequencies (*f1, f2, f3*)				
multiple comparisons test	Mean rank diff.	Significant?	Summary	Adjusted P Value
v1_f1 vs. v2_f1	-12.949	Yes	****	< 0.0001
v1_f3 vs. v2_f2	-11.662	Yes	****	< 0.0001
v1_f3 vs. v2_f3	-12.722	Yes	****	< 0.0001
Comparing mean pressure values at different pumping frequencies (*f1, f2, f3*) for each fluid (*v1* and *v2*)				
multiple comparisons test	Mean rank diff.	Significant?	Summary	Adjusted P Value
v2_f2 vs. v2_f1	32.369	Yes	****	< 0.0001
v1_f2 vs. v1_f1	33.656	Yes	****	< 0.0001
v2_f3 vs. v2_f2	64.636	Yes	****	< 0.0001
v1_f3 vs. v1_f2	63.575	Yes	****	< 0.0001

Mean pressure was significantly higher when the more viscous fluid (Fluid 2) was being circulated when compared to fluid 1. It is also clear that mean pressure values increased significantly with increasing pumping frequencies while circulating both fluids. **Figure 12-8** shows mean pressure values plotted against frequency for two minutes at each pumping frequency for each fluid. A first-degree polynomial model is fitted to each plot and the values for the goodness of fit are presented on the graph for both curves and shows the linear relationship.

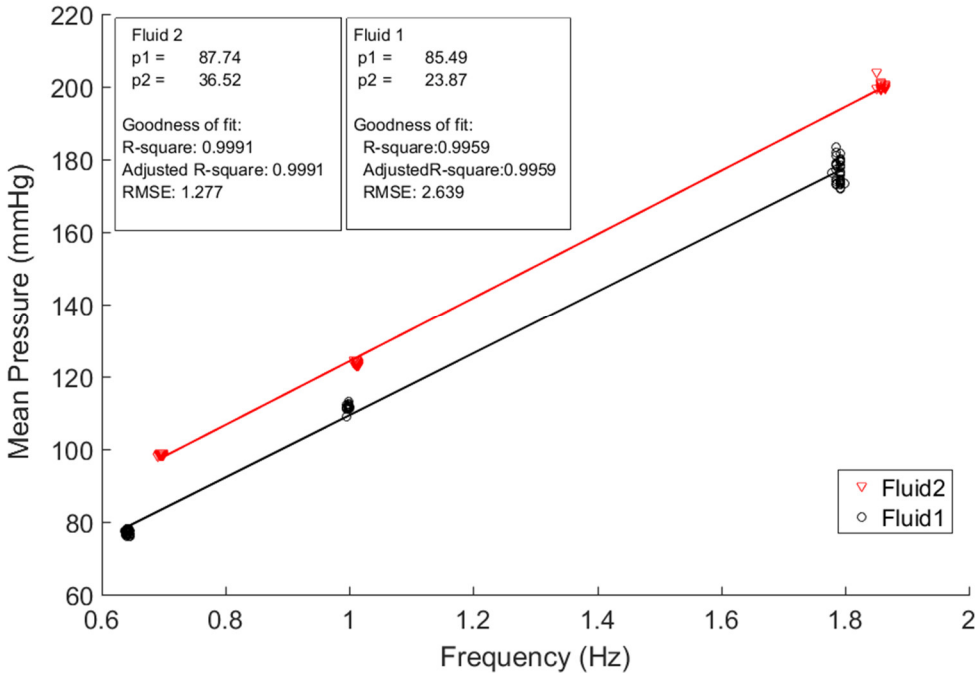

Figure 12-8
Mean pressure values at varying frequencies for both fluids at a stroke volume of 70 ml. The goodness of fit values for curve fitting using a first-degree polynomial model is also shown.

12.4.3.2 Forward and backward flow velocities for both fluids at varying pumping frequencies

The means ± SD of the peak forward flow velocity is presented in **Figure 12-9** Sidak's multiple comparison tests for significance are shown in **Table 12-5**.

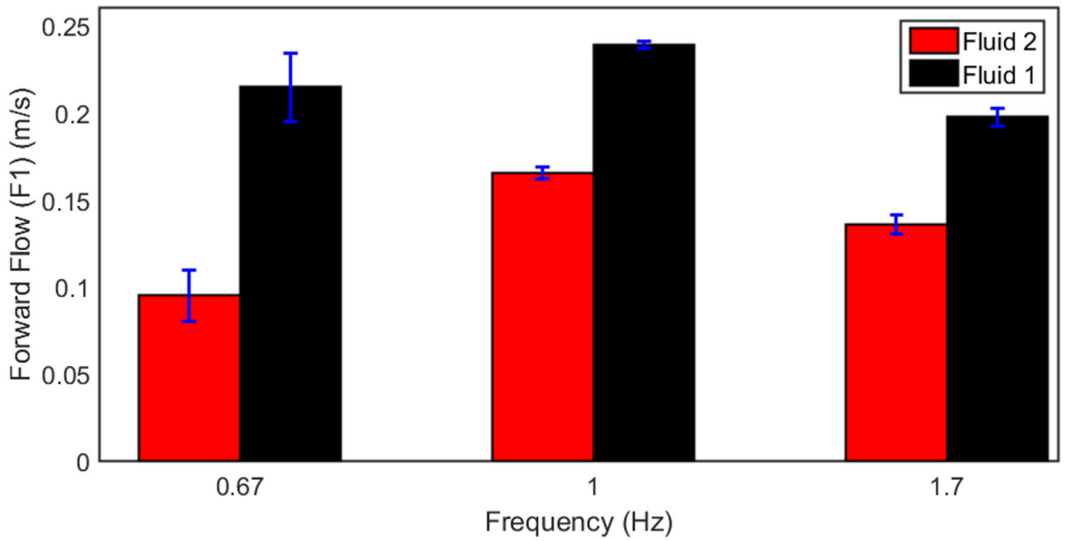

Figure 12-9
Maximum Forward flow velocities calculated over 1 min for both fluids at varying pulsating frequencies.

Table 12-5
Sidak's statistical test calculated for forward flow velocities for multiple comparisons of both fluids and varying pumping frequencies

Comparing values for both fluids (*v1* and *v2*) at each pumping frequency (*f1, f2, f3*)

Multiple Comparison Test	Mean Diff.	Significant?	Summary	Adjusted P Value
v1_f1 vs. v2_f1	0.1197	Yes	****	< 0.0001
v1_f2 vs. v2_f2	0.0732	Yes	****	< 0.0001
v1_f3 vs. v2_f3	0.0617	Yes	****	< 0.0001

Comparing values at different pumping frequencies (*f1, f2, f3*) for each fluid (*v1* and *v2*)

multiple comparisons test	Mean rank diff.	Significant?	Summary	Adjusted P Value
v2_f2 vs. v2_f1	0.0707	Yes	****	< 0.0001
v2_f3 vs. v2_f2	-0.0297	Yes	*	0.0140
v1_f2 vs. v1_f1	0.0240	No	ns	0.0689
v1_f3 vs. v1_f2	-0.0412	Yes	***	0.0002

The means ± SD of the maximum backward flow velocity values is presented in **Figure 12-10** Sidak's multiple comparison tests for significance are provided in **Table 12-6.**

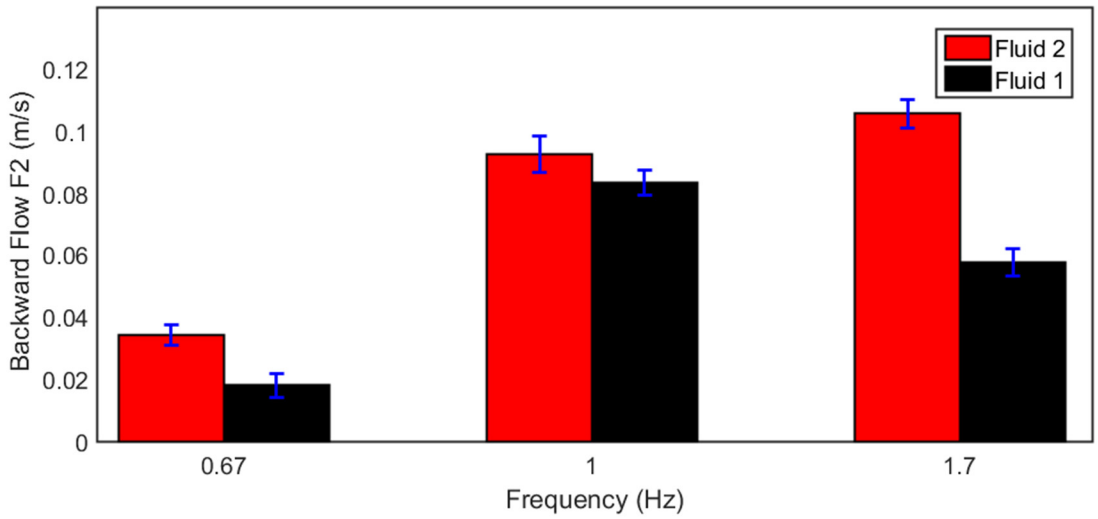

Figure 12-10
Mean and Standard variation bars calculated for backward flow velocity using the Ultrasound Doppler 8 MHz probe. The data is calculated over 1 min for each fluid at the varying.

Table 12-6
Sidak's statistical test calculated for backward flow velocities for multiple comparisons of both fluids and varying pulsating frequencies

Multiple comparisons test	Mean Diff.	Significant?	Summary	Adjusted P Value
Comparing values for fluid 1 (*v1*) and fluid 2(*v2*) at each pumping freequencies (*f1, f2, f3*)				
v1_f1 vs. v2_f1	-0.0160	Yes	****	< 0.0001
v1_f2 vs. v2_f2	-0.0090	Yes	****	< 0.0001
v1_f3 vs. v2_f3	-0.0479	Yes	****	< 0.0001
Comparing values at different pumping frequencies (*f1, f2, f3*) for each fluid (*v1* and *v2*)				
Multiple comparisons test	Mean Diff.	Significant?	Summary	Adjusted P Value
v2_f2 vs. v2_f1	0.0584	Yes	****	< 0.0001
v1_f2 vs. v1_f1	0.0655	Yes	****	< 0.0001
v2_f3 vs. v2_f2	0.0129	Yes	****	< 0.0001
v1_f3 vs. v1_f2	-0.025	Yes	****	< 0.0001

Table 12-7
Measured Total flow (TF) and Calculated Reynolds number (Re) of fluid 1 and fluid 2, at a stroke volume of 70 ml (SV) and varying pulsating frequencies (f).

SV (ml)	*f*(Hz)	Fluid 1		Fluid 2	
		TF (cm/s)	Re	TF (cm/s)	Re
70.00	0.67	26.22	613.76	10.28	84.42
	1.00	26.53	833.35	23.31	349.08
	1.80	23.03	1447.00	21.96	629.163

12.4.3.3 AC amplitudes, DC levels and time ratios for both fluids at varying pumping frequencies

The means ± SD of R and IR AC amplitude values are presented in **Figure 12-11** Sidak's multiple comparison tests for significance are shown in **Table 12-8.**

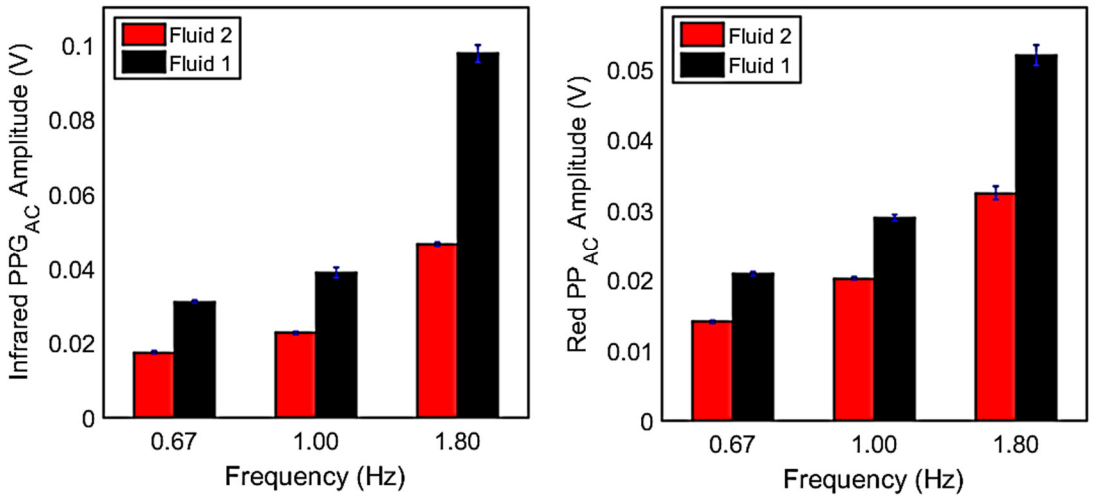

Figure 12-11
Red and Infrared AC mean and standard deviation bars calculated for each fluid, at varying pumping frequencies.

Table 12-8
Sidak's Statistical test calculated for IR AC levels, for multiple comparisons of both fluids and varying pumping frequencies

Sidak's multiple comparisons test	Mean Diff.	Significant?	Summary	Adjusted P-Value
Comparing values for fluid 1 (*v1*) and fluid 2(*v2*) at each pumping freequencies (*f1, f2, f3*)				
v1_f1 vs. f2_f1	0.0183	Yes	****	< 0.0001
v1_f2 vs. f2_f2	0.0118	Yes	****	< 0.0001
v1_f3 vs. f2_f3	0.0184	Yes	****	< 0.0001
Comparing values at different pumping frequencies (*f1, f2, f3*) for each fluid (*v1* and *v2*)				
Multiple comparisons test	Mean Diff.	Significant?	Summary	Adjusted P Value
v2_f2 vs. v2_f1	0.0084	Yes	****	< 0.0001
v1_f2 vs. v1_f1	0.0019	Yes	****	< 0.0001
v2_f3 vs. v2_f2	0.0052	Yes	****	< 0.0001
v1_f3 vs. v1_f2	0.0119	Yes	****	< 0.0001

Mean ± SD value for red and Infrared DC levels are presented in **Figure 12-12**. Sidak's multiple comparison tests for significance are shown in **Table 12-9**.

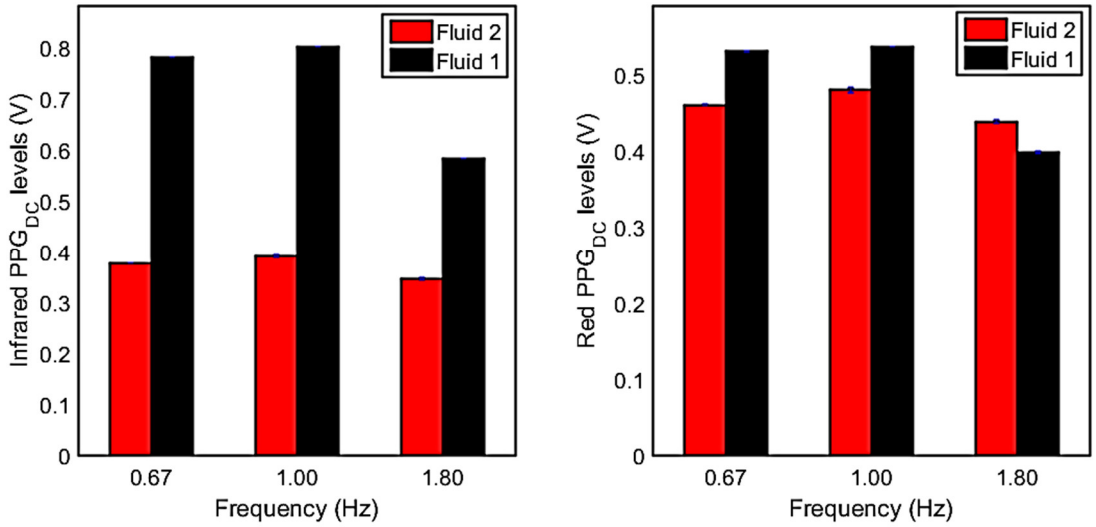

Figure 12-12
Mean and standard deviation values calculated from DC IR PPG signals for each fluid at varying pumping frequencies.

Table 12-9
Sidak's statistical test calculated for IR DC levels, for multiple comparisons of both fluids and varying pumping frequencies

Sidak's multiple comparisons test	Mean Diff.	Significant?	Summary	Adjusted P Value
Comparing values for fluid 1 (*v1*) and fluid 2(*v2*) at each pumping freequencies (*f1, f2, f3*)				
v1_f1 vs. v2_f1	0.3015	Yes	****	< 0.0001
v1_f2 vs. v2_f2	0.3158	Yes	****	< 0.0001
v1_f3 vs. v2_f3	0.1643	Yes	****	< 0.0001
Comparing values at different pumping frequencies (*f1, f2, f3*) for each fluid (*v1* and *v2*)				
Sidak's multiple comparisons test	Mean Diff.	Significant?	Summary	Adjusted P Value
v2_f2 vs. v2_f1	0.0163	Yes	****	< 0.0001
v2_f3 vs. v2_f2	-0.0449	Yes	****	< 0.0001
v1_f2 vs. v1_f1	0.0305	Yes	****	< 0.0001
v1_f3 vs. v1_f2	-0.1963	Yes	****	< 0.0001

The mean ± SD values of the time ratio for both fluids are presented **Figure 12-13**. Sidak's multiple comparison tests for significance are provided in **Table 12-8**.

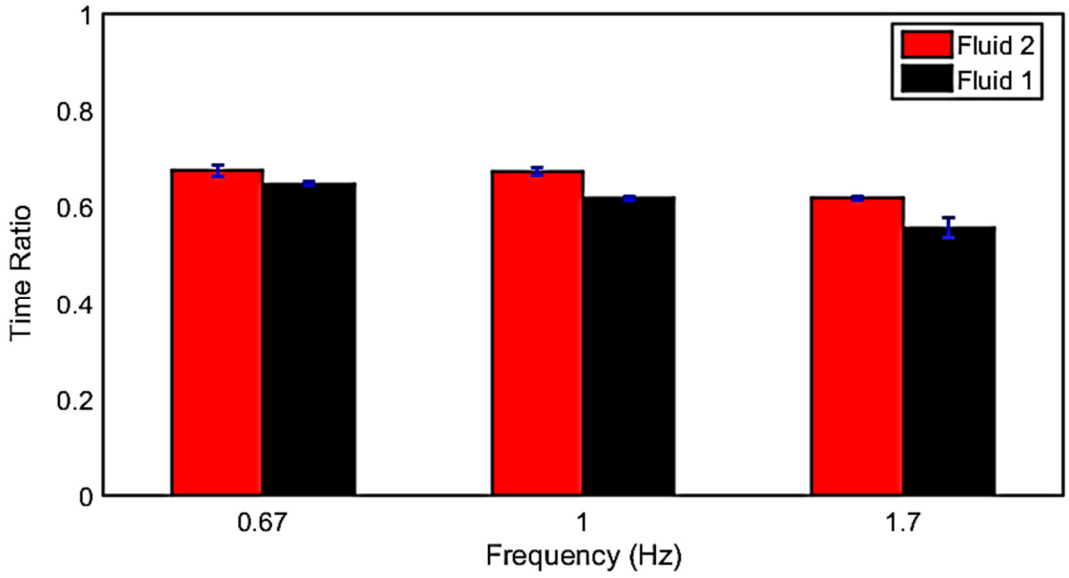

Figure 12-13
Mean and standard deviation values for the ratio of time fall to full cycle period calculated from AC IR PPG signals for each fluid at varying pulsating frequencies.

Table 12-10
Sidak's Statistical test calculated for ratio of time fall to cycle period from IR AC, for multiple comparisons of fluid 1 (v_1) and fluid 2 (v_2) and varying pumping frequencies (f_1,f_2, and f_3)

multiple comparisons test	Mean diff.	Significant?	Summary	Adjusted P Value
Comparing values for fluid 1 (v_1) and fluid 2(v_2) at each pumping freequencies (f_1, f_2, f_3)				
$v_1\_f_1$ vs. $v_2\_f_1$	-0.0259	Yes	****	< 0.0001
$v_1\_f_2$ vs. $v_2\_f_2$	-0.0575	Yes	****	< 0.0001
$v_1\_f_3$ vs. $v_2\_f_3$	-0.0618	Yes	****	< 0.0001
Comparing values at different pumping frequencies (f_1, f_2, f_3) for each fluid (v_1 and v_2)				
multiple comparisons test	Mean diff.	Significant?	Summary	Adjusted P Value
$v_2\_f_2$ vs. $v_2\_f_1$	0.0013	No	ns	0.9984
$v_2\_f_3$ vs. $v_2\_f_2$	-0.0572	Yes	****	< 0.0001
$v_1\_f_2$ vs. $v_1\_f_1$	-0.0302	Yes	****	< 0.0001
$v_1\_f_3$ vs. $v_1\_f_2$	-0.0617	Yes	****	< 0.0001

12.4.3.4 Normalised and Adjusted Pulse Volumes

In the previous chapter, we have proposed the adjusted and normalised pulse volume methods for a measure of the pulsatile volume. The method proved capable of providing a measure of transmural pressure. In this section, the mean ± SD values of adjusted pulse

volume (APV), R and IR normalised pulse volume (NPV_R and NPV_{IR}) are summarized in **Figure 12-14**. Finally, Scattergrams of ln(P_S)-APV, ln(P_S)-NPV_{IR}, and ln(P_S)-NPV_R for both fluids (Fluid 1 and Fluid 2) combined are presented in **Figure 12-15**. Points include cycle-to-cycle data of 60 seconds at each pumping frequencies (0.67 Hz, 1 Hz, and 1.8 Hz) obtained from both fluids at a fixed stroke volume of 70 ml.

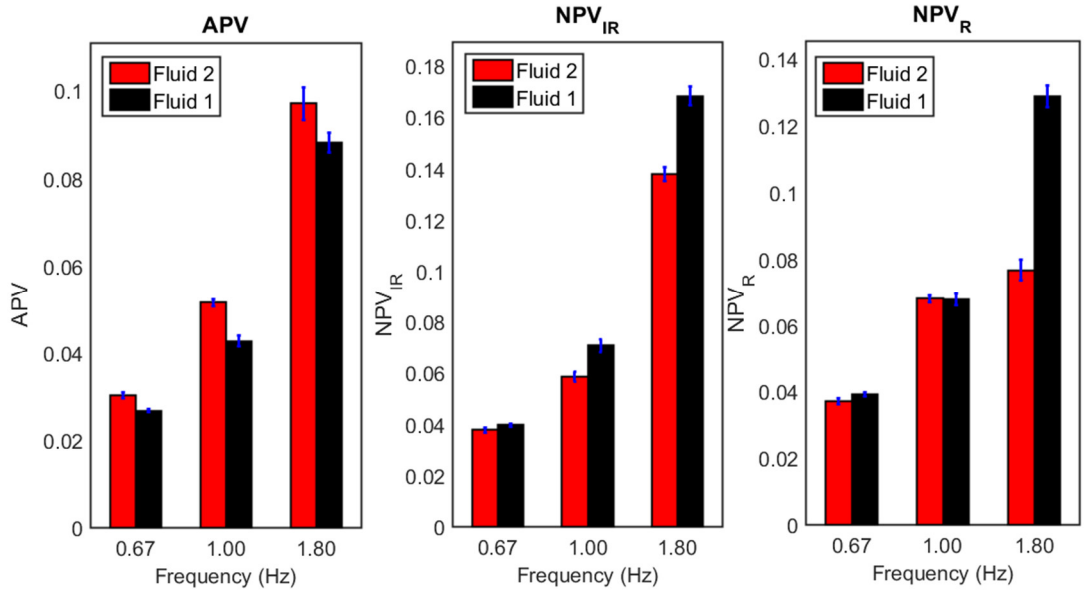

Figure 12-14
Mean ± SD values of red and infrared normalised pulse volume (NPV_R and NPV_{IR}) and Adjusted Pulse Volume (APV) for fluid 1 and fluid 2 at varying pumping frequencies.

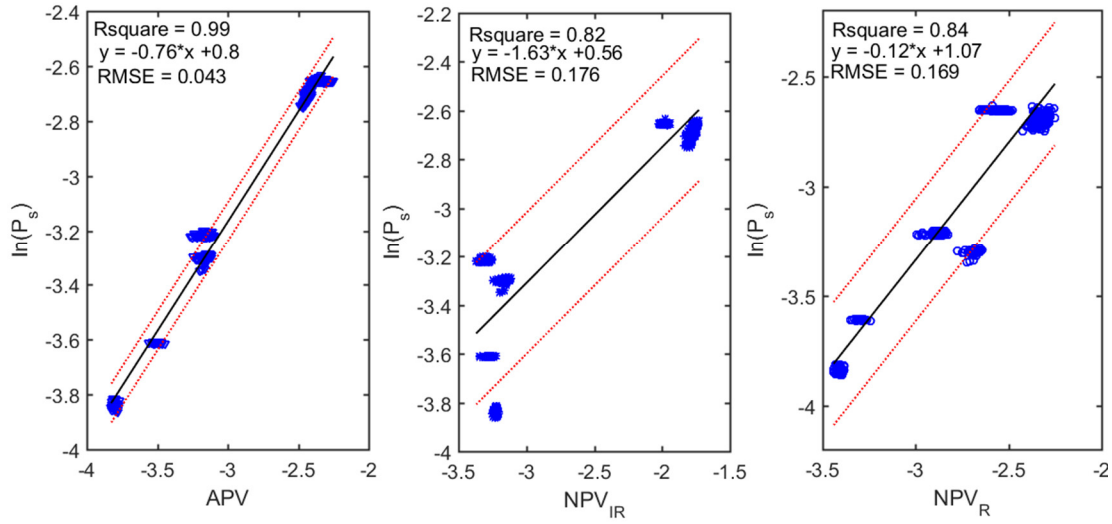

Figure 12-15
Typical scattergrams and curve fits for ln(P)-V function using different volume estimation methods. Points include cycle-to-cycle data of 60 seconds at each pumping frequencies from fluid 1 and fluid 2. Panel(a) shows ln(P_S)-Adjusted Pulse Volume (APV) function. Panel (b) shows ln(P_S)-infrared normalised pulse volume (NPV_{IR}) function. Panel(c) shows ln(P_S)-red normalised pulse volume (NPV_R) function. Values of the goodness of fit are presented in R-square(r) and Root Mean Square Error (RMSE). Dotted lines are 90% prediction bounds.

SUMMARY

In this chapter, the pulsatile pump/arterial network model described in **Chapter 9** was utilised to address the effect of fluid viscosity in pulsatile flow on the components of the PPG signal. Pressure signals, flow velocities, R and IR PPG signals were collected following a protocol that compares two circulating fluids with different viscosities. During the circulation of each fluid, the dynamics of the flow are altered by changing the pumping frequency.

We discern that AC amplitudes, DC levels and time ratio values of the PPG signal are sensitive to changes in fluid viscosity in the pulsatile flow. The ability of the PPG parameters to detect changes in fluid viscosity is not only due to the role of fluid viscosity in changes in mean pressure values and flow velocities, but also due to the changes in the optical properties of the fluid, which can be directly reflected in the PPG components and will be further discussed in **Chapter 14**.

Previously, we highlighted that the APV parameter, extracted from the PPG signal is strongly correlated with the natural logarithmic function of systolic pressure. Herein, we further underline that this relationship is still valid for different fluid viscosities, with APV again providing significantly better fit when compared to NPV_R and NPV_{IR}.

Finally, the literature confirms the importance of blood viscosity measurements and the link between hyperviscosity and cardiovascular diseases at early and advanced stages. It is evident that the components of the PPG signal are sensitive to changes in fluid viscosity in an *in vitro* controlled pulsatile flow which mimics the mechanics of the human circulation within a wide range of pressure values. We infer that further *in vitro* and *in vivo* investigations should address the utility of the PPG technique for non-invasive measurements of flow dynamics, including pressure values and possibly fluid rheological characteristics.

Chapter 13
THE EFFECT OF HAEMORHEOLOGY ON THE PPG SIGNALS

13.1 Introduction

In the previous chapter, we presented an overview of the effect of fluid viscosity on the components of the PPG signal at distinct flow conditions. Following the observed remarks that fluid viscosity is a factor that significantly affects the PPG signal, we herein use equine blood as the circulating fluid. We further explore the effect of the presence of red blood cells (RBCs) in whole blood, and thromboplastin activation on the PPG components, pressure and flow signals in the *in vitro* system at varied flow conditions.

Blood provides a suitable and important medium with which to study the influence of red blood cell morphology on the PPG signal. This is a highly desirable topic for the large community of scientists and engineers who are developing PPG applications for blood rheological and flow analysis *in vitro* as well as *in vivo* (e.g. to measure chemical content and derive quantitative information on blood analyses) as a diagnostic tool with a wide range of clinical applications.

Different shear rates applied to blood can readily induce variation in the shape, size, orientation, aggregate formation, and distribution of the erythrocytes. Thromboplastin activation is achieved using a chemical trigger.

This chapter will make an effort to answer some of the unanswered questions by addressing:

1. The effect of the presence of Red Blood Cells (RBCs) on the PPG signal.
2. The role of pumping frequency in altering blood cells morphology and how does that influence both the PPG components.
3. The effect of thromboplastin activation on cell rheology and the PPG components

13.2 Protocol

Equine blood (TCS Biosciences Ltd, UK) was used as test blood. The blood was pooled and treated with the anticoagulant ACD immediately after being collected from donors as advised by the supplier. Equine blood was chosen due to its properties that are similar to human blood. Equine red blood cells are biconcave discs of dimensions 6-7 μm diameter, 2.5 μm thick at the edge and 1 μm thick at the centre. An important feature is the ability of equine blood to form rouleaux, a property that is present in human blood and not in other species (i.e. Bovine).

The sample testing protocol was carried out as follows:

1. Haematocrit values were estimated using a centrifuge (Sorvall™ RX1 Thermo Scientific) to separate red blood cells from other components (speed: 13300, time: 8 mins).
2. Slide microscopy was prepared using the Wright-Giemsa staining method and microscopic images of whole equine blood samples were obtained (Microtec RM-1, TEC Microscopes LTD).
3. Thromboplastin activation was tested using calcium chloride (24 g/L $CaCl_2$) on 10 ml whole equine sample (Sibley et al., 1973). An Electron Microscopic image was obtained to confirm the activation. The image was obtained using the following protocol (Simpson, 1989):
    - Three drops of equine blood, 5 ml of 2.5% glutaraldehyde in 0.1 M cacodylate buffer at pH 7.4.
    - Fixation continued for overnight at room temperature.
    - Blood cells were washed twice with cacodylate buffer
    - The samples were dehydrated in ascending concentrations of ethanol up to absolute
    - Samples were transferred to pure, dry acetone and suspended in a final change of acetone-washed coverslip
    - The cells were gold-coated in a Polaron sputter coater

- The samples were photographed on fine grain film at x 5000 in the Autoscan electron microscopy at 20 kV.

4. The optical spectra are obtained using a sample of whole equine blood in the spectrometer (Lambda,1050).
5. Viscosity measurements are obtained using the cone/plate rheometer (Brookfield, LVDT3)
6. Blood conductivity and pH levels were measured using 10 ml blood sample.

Following sample testing, the *in vitro* setup described earlier (**Chapter 8**) was used in this experiment. Equine blood was circulated at ambient temperature (~23 ℃) through the arterial model described in Chapter 8. The flow was directed towards *Model 1* at varying pumping frequencies. The reservoir consisted of a magnetic stirrer spun at low speed to prevent sedimentation. The blood was pumped by the pulsatile pump (Harvard Apparatus, US) from the blood reservoir to the arterial model via disposable PVC tubing.

A summary of the parameters used during the protocol is listed in **Table 13-1**.The experiment follows the following protocol: -

1. The reservoir was filled with 2 Litres of equine blood. The blood is circulated at a stroke volume of 70 ml for two minutes to allow the system to stabilise.
2. Data collection started at a pumping frequency of 40 Bpm, and the recording continued for 10 minutes.
3. Pumping frequency was increased to 60 Bpm, 80 Bpm and 90 Bpm for 10 minutes at each speed.
4. The recording stopped, and the blood was left to regain rheological properties (in case of deformations due to shear stresses) for an average of 10 minutes while the magnetic stirrer is operating to prevent any sedimentation.
5. The pumping speed is set back to 1 Hz and the system resistance is increased, the recording started again for 10 minutes.
6. The clotting agent ($CaCl_2$ at a concentration of 24 g/L) was added and the pump was left to operate for 30 minutes while data collection continued.
7. The pump was emptied, washed, sterilised and left to dry.

Table 13-1
List of parameters used in each experimental stage

	Circulating fluid	Model	frequency (Hz)	Stroke Volume (ml)	Resistance
Stage 1	Equine blood Cobalt Nitrate Polymer	*Model 1*	f_2=1.00	70	High resistance
Stage 2	Equine Blood	*Model 1*	f_1 = 0.67 f_2 = 1.00 f_3 =1.50 f_4=1.90	30 and 70 each	Low resistance
Stage 3	Baseline equine blood, clotting blood	*Model 1*	f_2=1.00	70	High resistance

13.3 Data Collection and Statistical Analyses

The collected data via the LabVIEW Virtual Software were analysed in an offline custom written script using Matlab. More details describing the script and methods of filtering and data extraction can be found in **Chapter 7**. The Data obtained is Infrared and Red, AC and DC PPG signals, pressure signal and both forward and backward flow.

The data was grouped to include values at varying pulsating frequencies. Statistical analyses were performed to compare values at different pulsating frequencies for each model. The data was confirmed to follow a Gaussian distribution. Therefore, the data qualified for one-way ANOVA test. This was followed by Sidak's multiple comparison tests to evaluate significance.

In the case of model fitting, the goodness of the fitting was evaluated with the Sum Square Error (SSE), R-square (r2) and the Root Mean Square Error (RMSE). Where SSE, shows variation from the mean and R-square is the percentage of the variable response variation.

13.4 Results

In this section, we present the measured values for fluid properties, including the optical spectra in the visible and near-infrared range, conductivity, pH, and viscosity measurements. We further, present visual data from the collected signals; pressure, forward and backward flow, red and infrared PPG signals at both stroke volumes and

varying pumping frequencies in both models. Furthermore, we present statistical analysis from the processed signals to draw average and standard deviations of Infrared AC amplitudes, time ratios, Infrared DC levels, mean pressure values, peak forward and backward flow velocities. Moreover, we tabulate Sidak's multiple comparison tests, which compares values at each pumping frequency and different stroke volumes in both models. The statistical comparison shows mean differences, p-value, and summary of significance status. Finally, we present scattergrams of the three proposed methods APV, $NPV_{IR,}$ and NPV_{R}.

13.4.1 Fluid Properties

The haematocrit for 5 samples of the whole equine blood was estimated using the graded 1 ml cuvette. The samples were centrifuged to separate plasma, platelet, and red blood cells. The mark indicated a haematocrit of 0.45 in all samples as seen in **Figure 13-1.**

A blood microscopic image of a stained equine sample is shown in **Figure 13-2** at a magnification of 400. **Figure 13-3** shows Scanning Electron Microscopy (SEM) image of red blood cells after 10 mins of thromboplastin activation at a magnification of 5000.

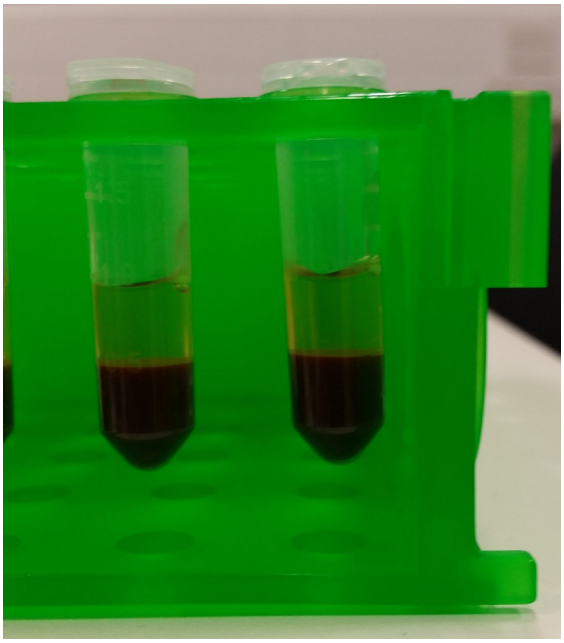

Figure 13-1
Centrifuged whole equine blood samples in marked micro tubes.

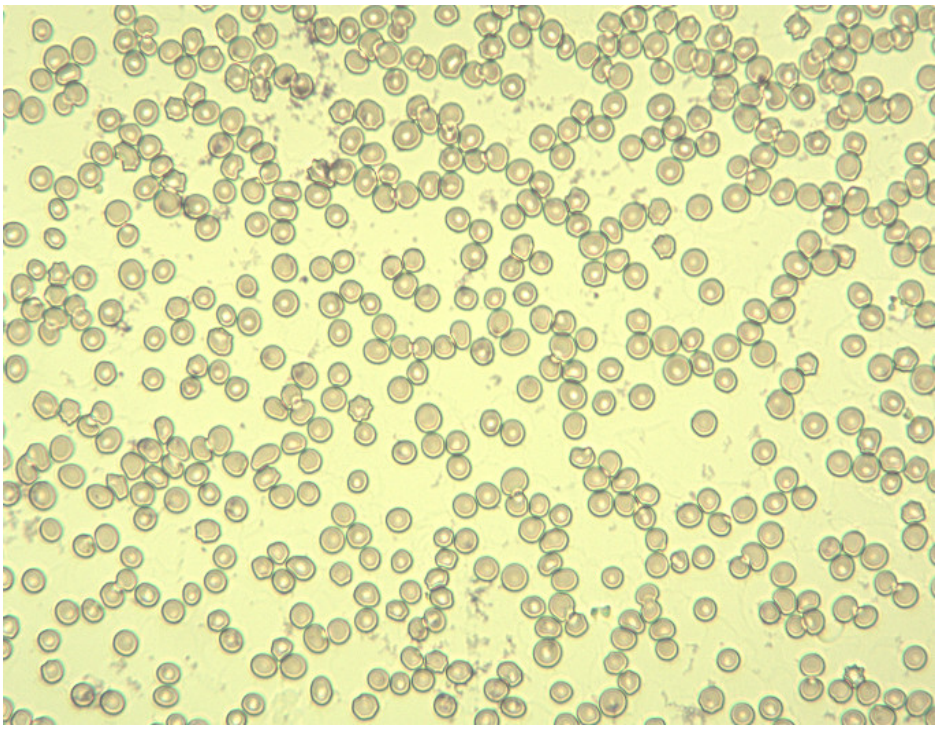

Figure 13-2
Microscopic image obtained from a prepared sample of whole Equine blood (Magnification 400x).

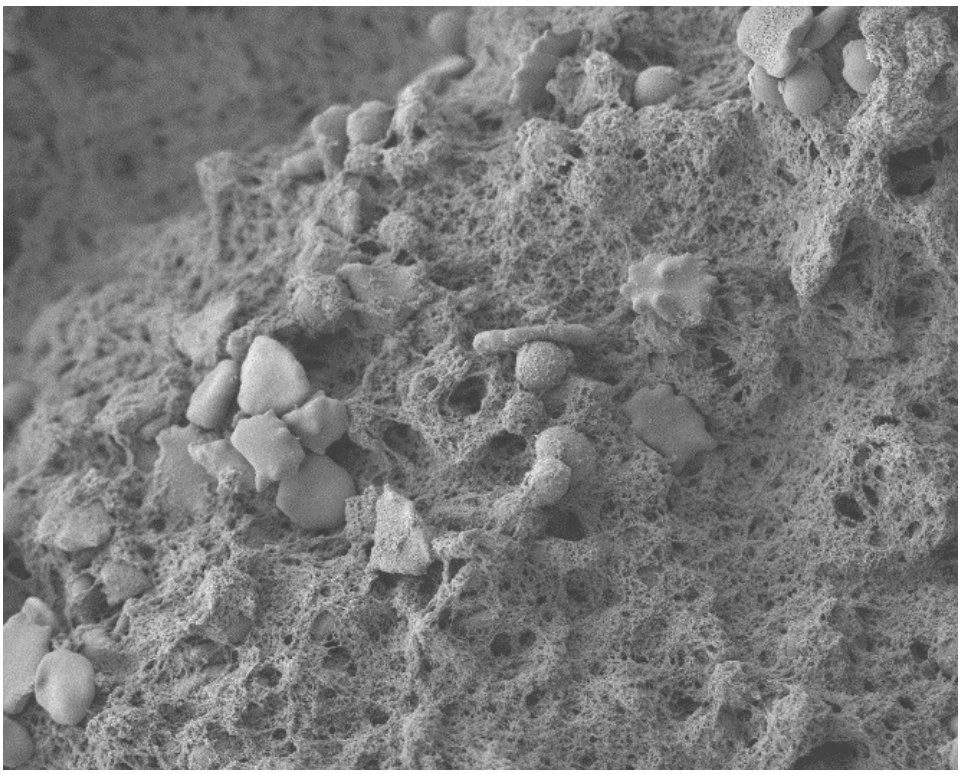

Figure 13-3
Electron microscopic image of of an equine blood sample treated with a chemical clotting trigger and fixed according to the described protocol (magnification 5000x). The image shows the formation of the fibrinous matrix.

pH and conductivity measurements are listed in **Table 13-2**.

Table 13-2
pH levels and conductivity measurement for fluids circulated during this experiment

	Whole blood sample	Cobalt Nitrate Polymer Solution
Conductivity mS	4.68 at 22.6°C	60.2 at 22.4°C
Ph levels	7.055 at 22.6°C	2.952 at 22.4°C

The optical spectra in the visible and near infrared region were obtained from the Spectrometer for whole equine blood samples and clotted blood samples as can be seen in **Figure 13-4.** Results obtained previously for Cobalt Nitrate Polymer solution of 0.6 M concentration are displayed for comparison purposes.

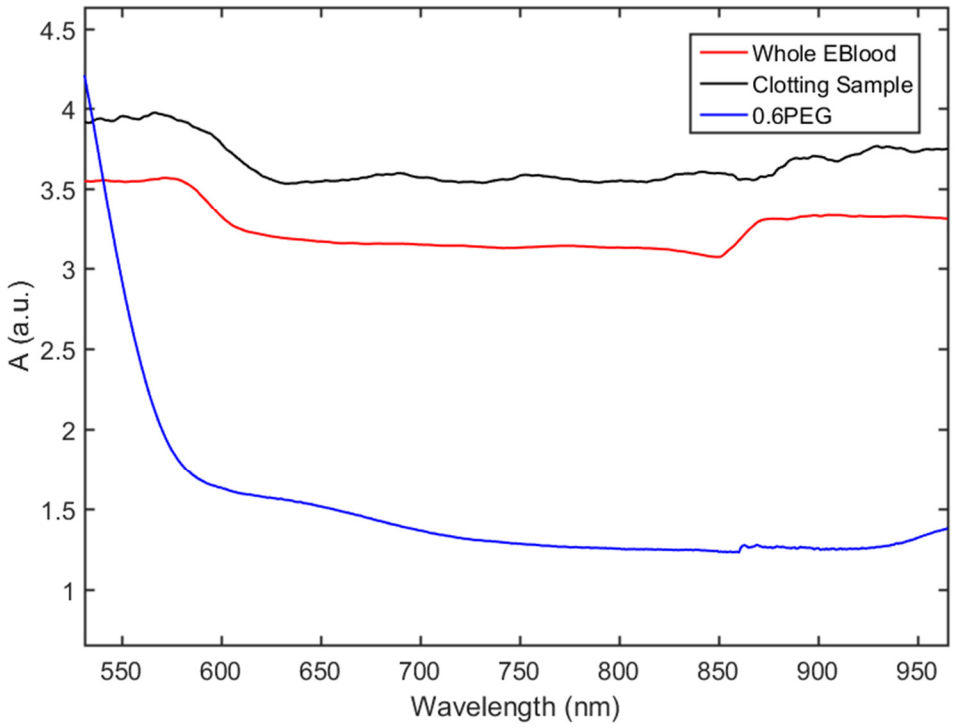

Figure 13-4
Optical Spectra for a sample of whole equine blood, a clotted equine samples, and Cobalt Nitrate solution with PEG 6000.

Viscosity measurement at varying shear rates are measured using the cone/plate viscometer for each fluid and are seen in **Figure 13-5**.

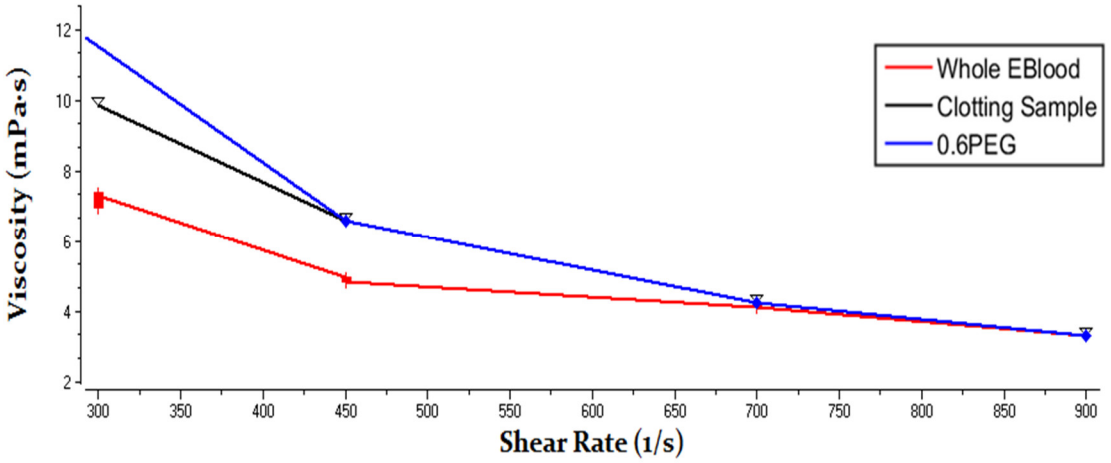

Figure 13-5
Shear controlled viscosity measurement for three samples. Blue data is Cobalt Nitrate solution with PEG 6000, red is whole equine blood, and black line is for a fully clotted equine blood sample with chemically triggered clotting function, measured after 28 minutes of start of clotting.

13.4.2 The Role of Red Blood Cells: Investigation of the Effect of RBCs on the PPG Signals

This section will present results comparing equine blood and cobalt nitrate PEG solution (0.6 M) circulating at a pumping frequency of 1 Hz and a stroke volume of 70 ml as described in the methods section. **Figure 13-6** shows a sample of the collected signals while circulating both fluids. **Figure 13-7** shows statistical analysis comparing whole equine blood and dye for AC amplitudes, DC levels for both R and IR signals, forward and backward flow velocities and mean pressure signals.

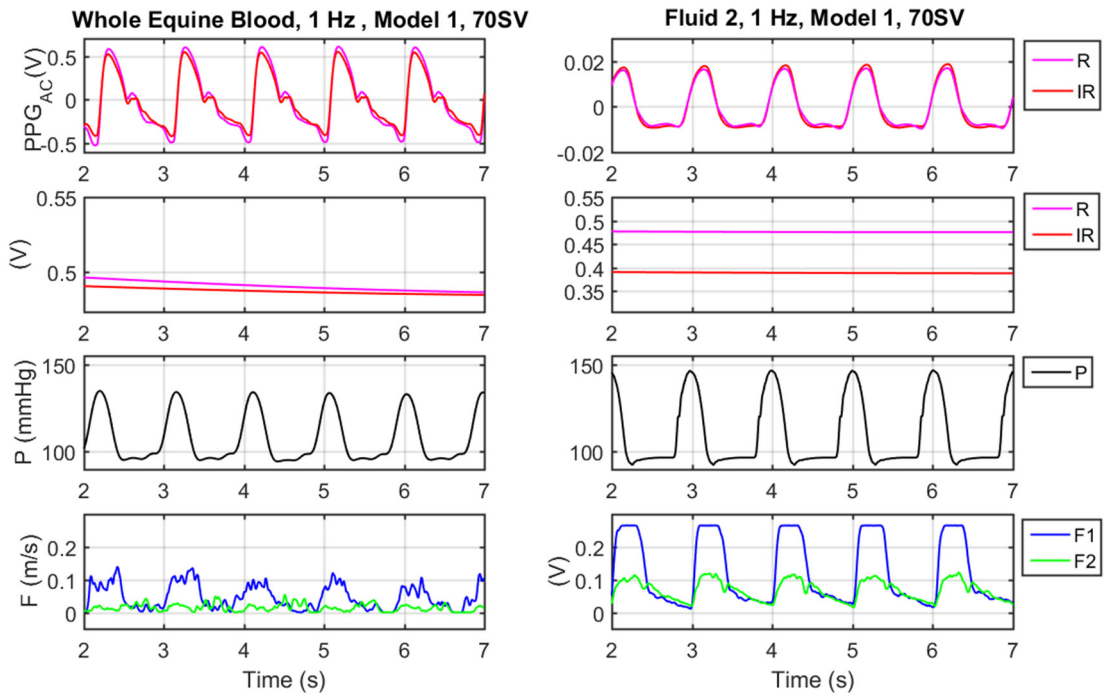

Figure 13-6
Five-second samples of the collected signals during the circulation of whole equine blood (left) and Cobalt Nitrate Polymer solution (right). From the top, AC waveforms for Red (R) and Infrared (IR) PPG signals, DC levels for R and IR PPG signals, Pressure (P), Forward (F1) and backward (F2) flow velocities. Signals are obtained at a frequency of 1 Hz and a fixed stroke volume of 70 ml from *Model 1*.

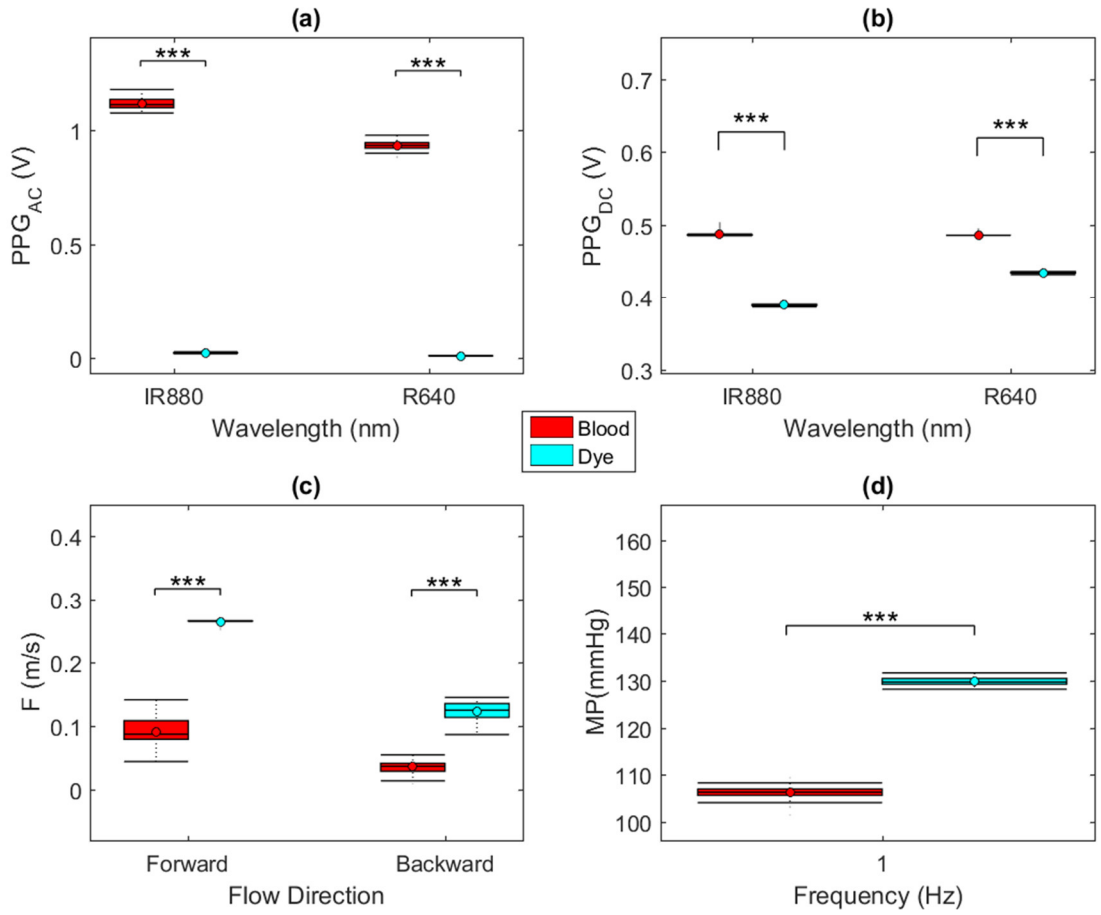

Figure 13-7
Comparing parameters obtained from circulating whole equine blood and cobalt nitrate polymer solution. Panel(a) compares Red and Infrared PPG_{AC} for both fluids, panel(b) compares R and IR PPG_{DC}, panel (c) shows forward and backward flow rates for both fluids and panel(d) compares mean pressure values obtained. Data collected at 1 Hz frequency and a stroke volume of 70 ml.

13.4.3 The Role of Red Blood Cells: Investigation of the Effect of Pumping Frequency on the PPG Signals

This section presents results obtained from circulating equine blood in the arterial model at varying pumping frequencies and stroke volumes. Visual representation of the collected data at varying pumping rates and a stroke volume of 70 ml are present in **Figure 13-8**. Panel(a) R and IR PPG_{AC} for 3 minutes at each pumping rate, panel(b) R and IR PPG_{DC} for 3 minutes at each pumping frequency, panel(c) Pressure signals showing data obtained for 3 minutes at each pumping frequency.

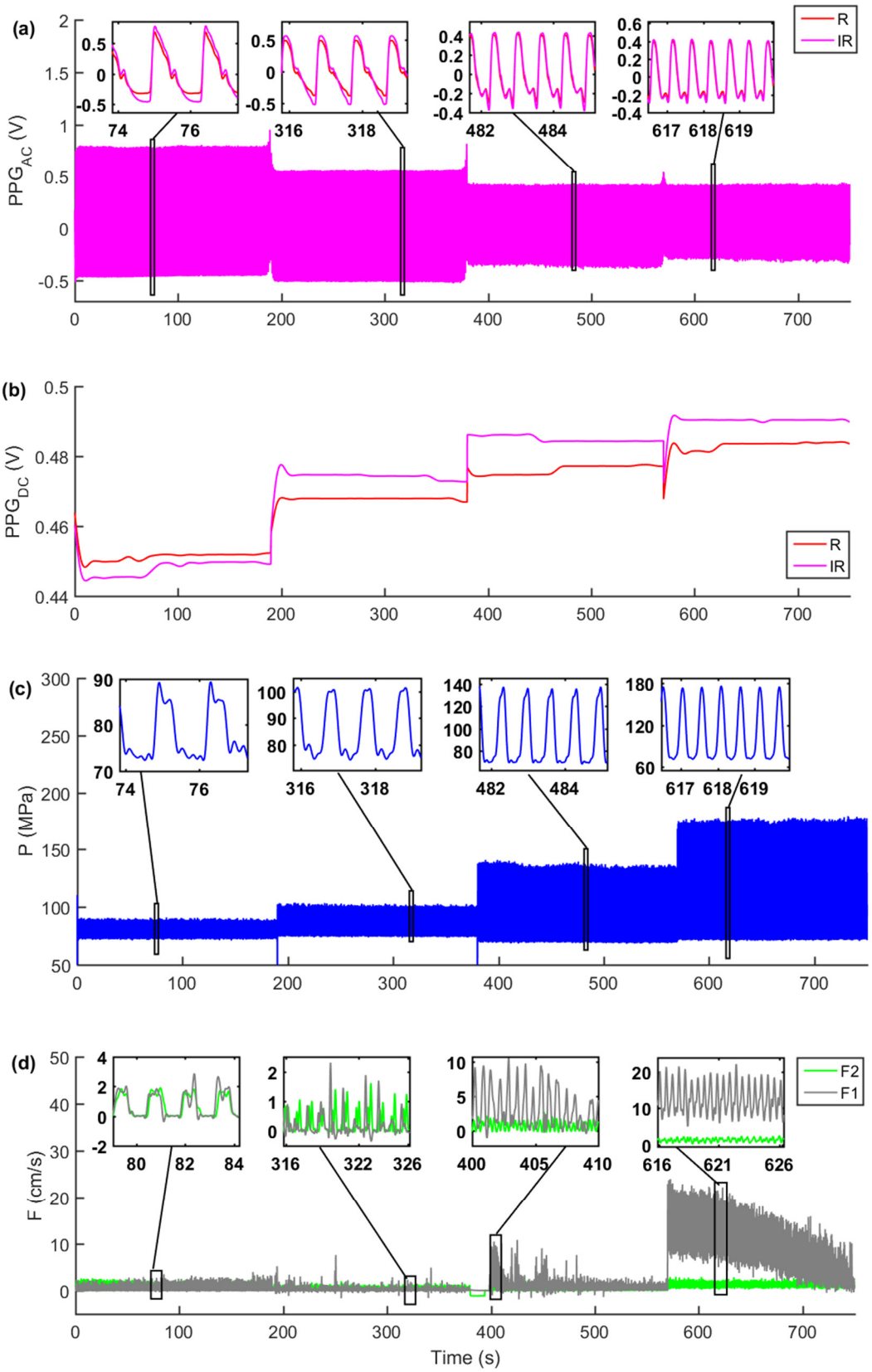

Figure 13-8
Signals collected during circulating whole equine blood at 190 seconds for each pumping frequency (0.7, 1, 1.5 and 1.8 Hz). (a) Red (R) and Infrared (IR) AC PPG signals. (b) R and IR DC levels. (c) Pressure (P) signals and (d) shows Forward (F1) and backward (F2) flow velocities.

13.4.3.1 Effect of pumping frequency on mean Pressure and flow velocities

Statistics for mean pressure values averaged over 190 seconds at four different pumping frequencies while circulating equine blood are presented in **Figure 13-9.** A highly significant increase was observed with increasing pumping frequencies as confirmed by the Sidak's multiple comparison tests as further displayed in **Table 13-3.**

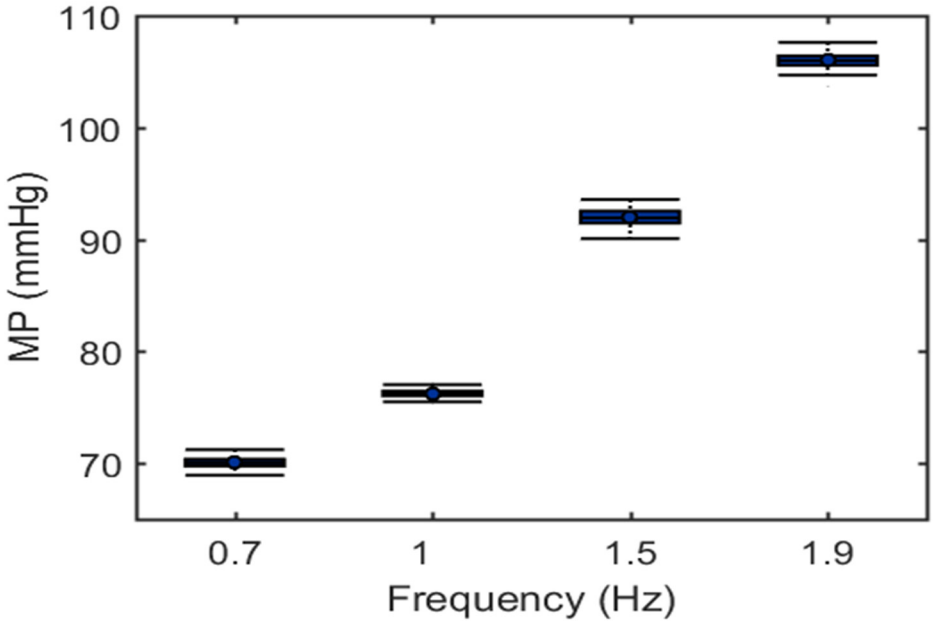

Figure 13-9
Mean Pressure values at varying pumping frequencies obtained while circulating Equine blood (B) in model 1 (M1) at 30 ml (30) and 70 ml (70) stroke volumes.

Statistics for Flow velocities are shown in **Figure 13-10**. Generally, forward and backward flow velocities increased significantly with increasing frequencies, with one exception. F1 and F2 dropped significantly when pumping frequencies increased from 0.7 to 1 Hz as further displayed in **Table 13-3**.

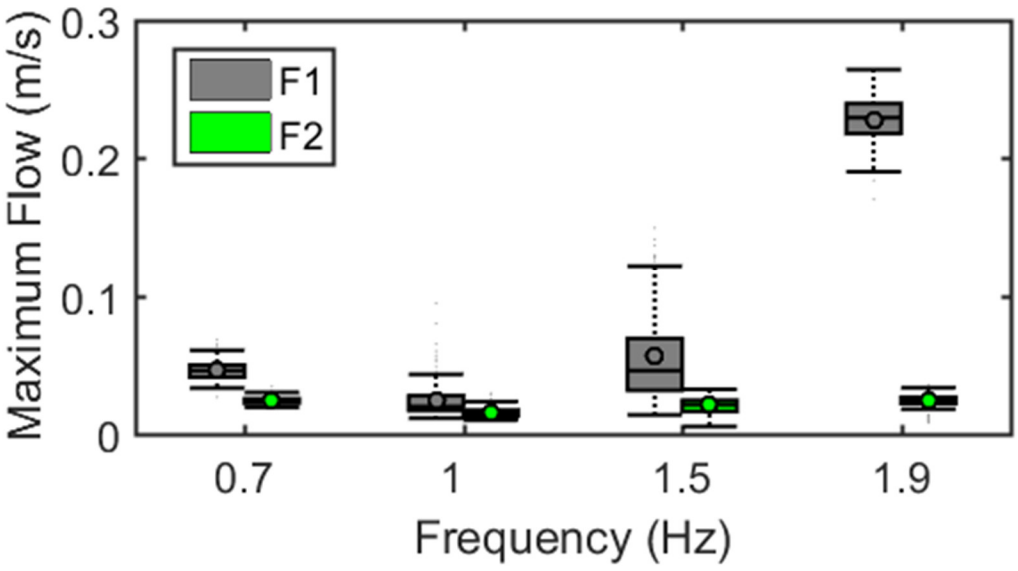

Figure 13-10
Maximum forward (F1) and backward (F2) flow velocities comparing values obtained in the in vitro setup while circulating equine blood at varying pumping frequencies.

Table 13-3
Comparison test for Mean pressure values, forward and backward flow velocities at different pumping frequencies (f1,f2,f3, and f4) and fixed stroke volume of 70 ml (70).

Sidak's multiple comparisons test	Mean Diff.	Significant ?	Summary	Adjusted P Value
Mean pressure comparisons				
70f2 vs. 70f1	6.2104	Yes	***	< 0.0001
70f3 vs. 70f2	15.7970	Yes	***	< 0.0001
70f4 vs. 70f3	13.9950	Yes	***	< 0.0001
Forward Velocities				
70f2 vs. 70f1	-0.0088	Yes	***	< 0.0001
70f3 vs. 70f2	0.0054	Yes	***	< 0.0001
70f4 vs. 70f3	0.0032	Yes	***	< 0.0001
Backward Flow velocities				
70f2 vs. 70f1	-0.0088	Yes	***	< 0.0001
70f3 vs. 70f2	0.0054	Yes	***	< 0.0001
70f4 vs. 70f3	0.0032	Yes	***	< 0.0001

13.4.3.2 Effect of pumping frequency on AC amplitudes and DC levels

Red (R) and Infrared (IR) PPG_{AC} amplitudes averaged over 190 seconds at four different pumping frequencies are presented in **Figure 13-11**. A highly significant drop was observed in AC amplitudes for both wavelengths with increasing pumping frequencies.

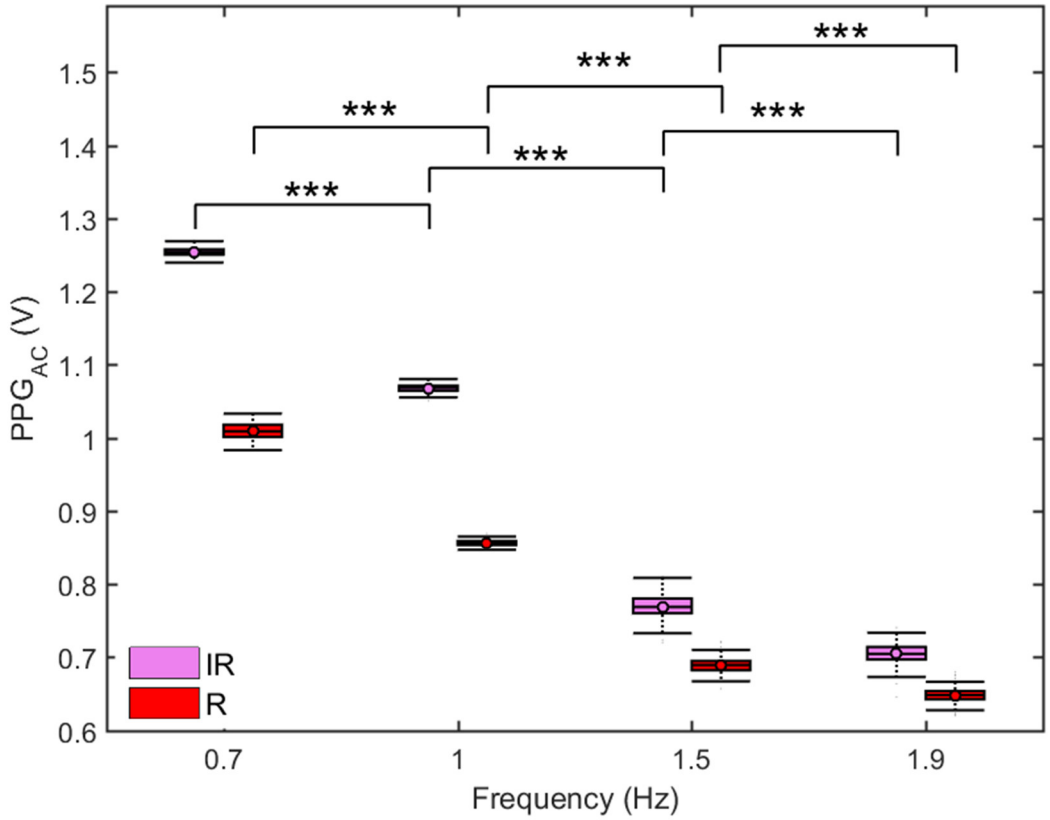

Figure 13-11
Red(R) and Infrared(IR) PPG_{AC} amplitudes at varying pumping frequencies obtained while circulating whole equine blood in model 1 (M1) at a stroke volume of 70.

Statistics for DC levels for R and IR PPG signals averaged over 190 seconds at four different pumping frequencies are presented in **Figure 13-12**. A highly significant increase was observed in DC levels for both wavelengths with increasing pumping frequencies.

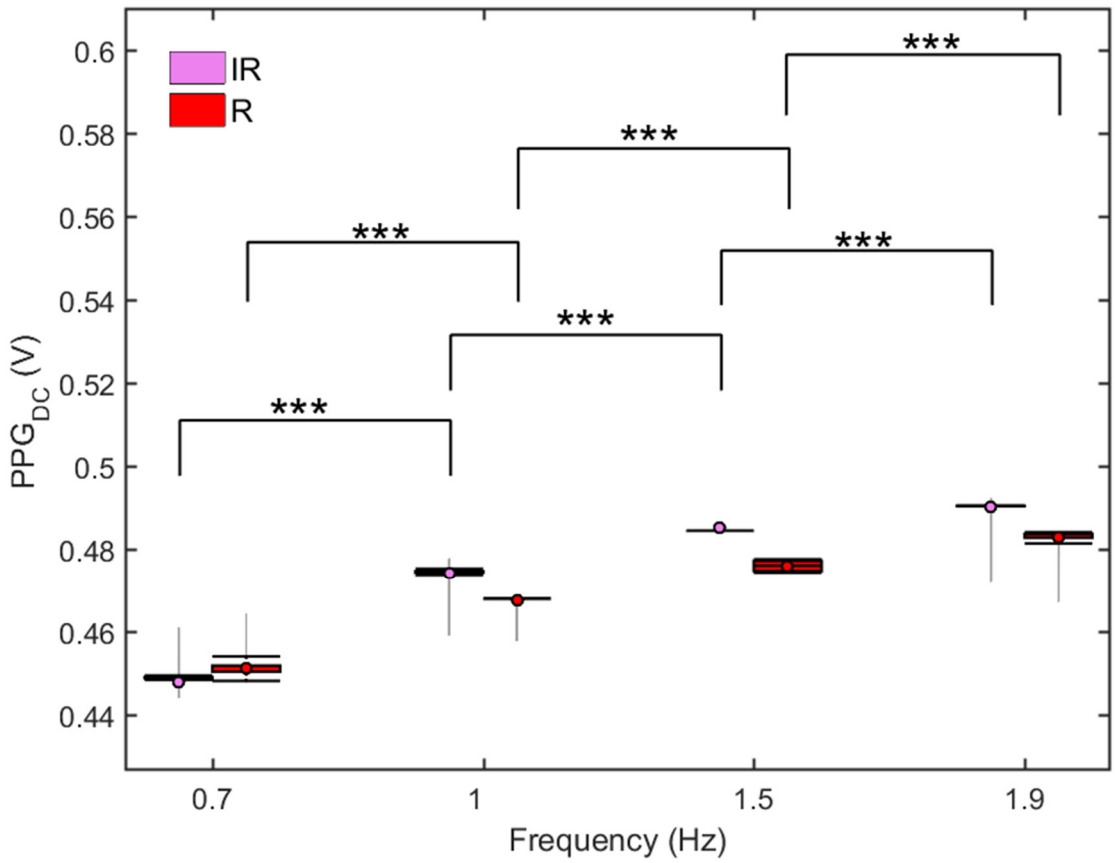

Figure 13-12
Red(R) and Infrared(IR) PPG_{DC} levels at varying pumping frequencies obtained while circulating whole equine blood in *Model 1* at a stroke volume of 70

13.4.3.3 APV, NPVR, and NPV IR validation while circulating equine whole blood

Scattergrams of $\ln(P_S)$-APV, $\ln(P_S)$-NPV_{IR}, and $\ln(P_S)$-NPV_R are presented in **Figure 13-13**. Points include cycle-to-cycle data of 190 seconds at each pumping frequencies (0.67 Hz, 1 Hz, 1.5 Hz and 1.8 Hz) obtained while circulating whole equine blood at a fixed stroke volume of 70 ml.

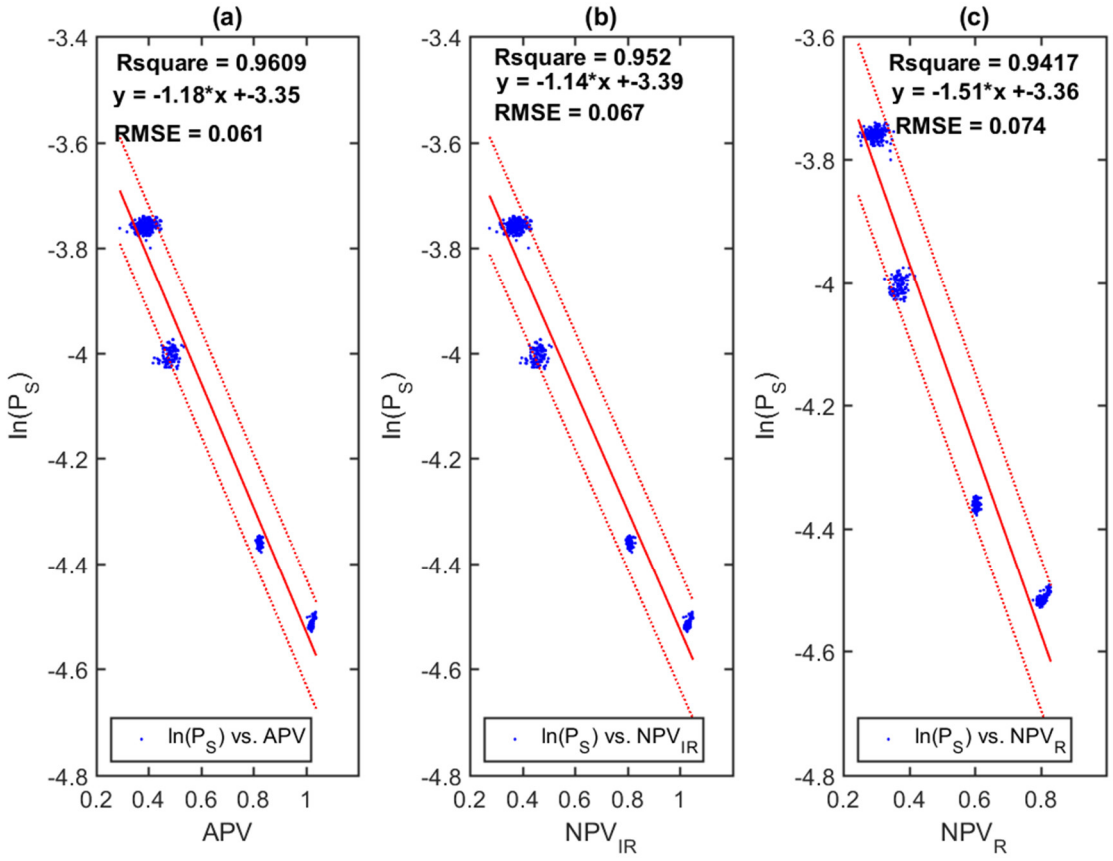

Figure 13-13
Typical scattergrams and curve fits for ln(P)-V function using different volume estimation methods. Points include cycle-to-cycle data of 190 seconds at each pumping frequencies (0.7, 1, 1.5 and 1.8 Hz) obtained while circulating whole equine blood Functions using the different methods are presented. Panel (a) shows the natural logarithmic systolic pressure ln(Ps)-Adjusted Pulse Volume (APV) function. Panel (b) shows ln(P_S)-IR normalised pulse volume (NPV_{IR}) function. Panel(c) shows ln(P_S)-R normalised pulse volume (NPV_R) function. Values of the goodness of fit are presented in R-square and RMSE. Dotted lines are 90% prediction bounds.

13.4.4 The Role of Platelets: Investigation of the effect of Thromboplastin Activation on the PPG Signals

In this section, we present results obtained at baseline pumping rate of 1 Hz at a stroke volume of 70 ml in *Model 1*. The recording continues for 20 mins after the clotting agent is added to the reservoir. The collected PPG and pressure signals are shown in **Figure 13-14**.

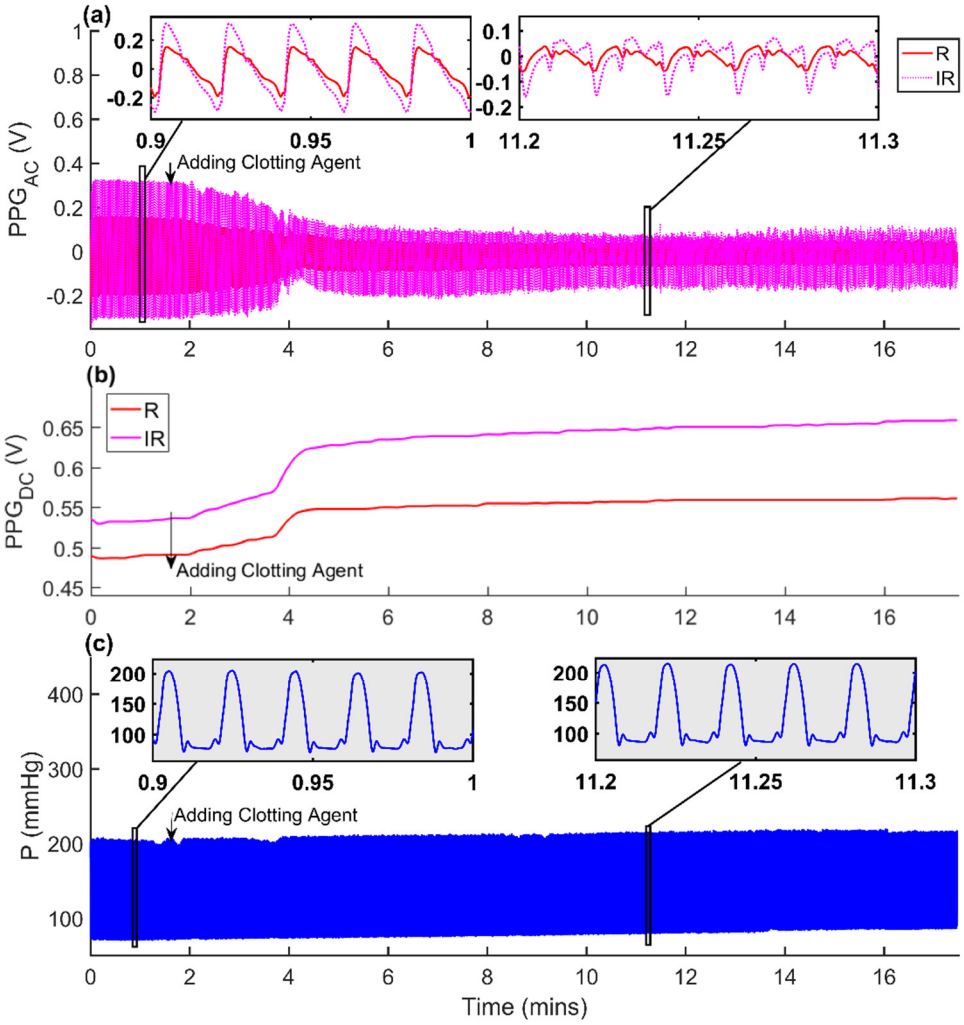

Figure 13-14
Collected signals from stage 2 experiment showing the signal behaviour after adding the clotting agent in the reservoir. Clotting agent was introduced to the reservoir after 80 seconds of baseline data collection. (a) InfraRed (IR) PPG_{AC}, (b) IR PPG_{DC}, (3) pressure signals. Data collected at 1 Hz, and 70 ml stroke volume in *Model 1*.

Figure 13-15 shows statistical comparisons of values obtained from the *in vitro* setup while circulating whole equine blood (WB) and after adding the clotting agent (Clot). Data obtained from 20 mins of baseline and 20 minutes after total clotting. Data obtained at a stroke volume of 70 ml and a frequency of 1 Hz. Panel(a) showing Red and Infrared PPG_{AC} amplitudes, panel(b) showing R and IR PPG_{DC} levels, panel(c) showing forward (F_1) and backward(F_2) flow velocities, and panel(d) showing mean pressure values. Statistical significance is presented using the 3-star system.

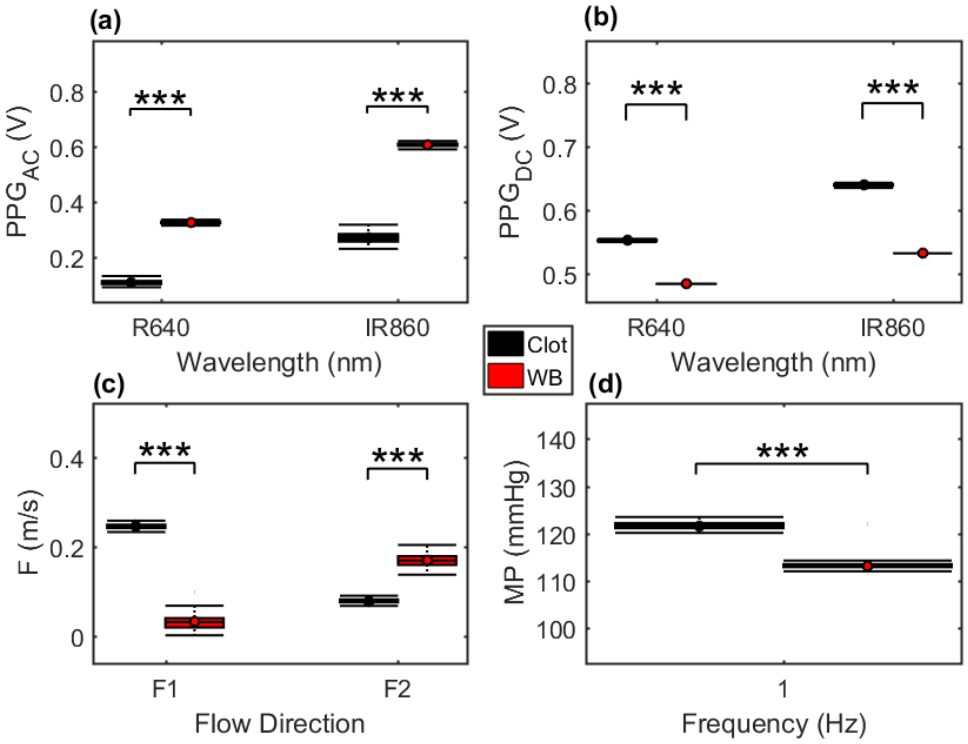

Figure 13-15
Comparing values obtained from the in vitro setup while circulating whole equine blood (WB) and after adding the clotting agent (Clot). Data obtained from 20 mins at each stage circulated at a stroke volume of 70ml and a frequency of 1 Hz. Panel(a) showing Red and Infrared PPG_{AC} amplitudes, panel(b) showing R and IR PPG_{DC} levels, panel(c) showing forward (F_1) and backward(F_2) flow velocities, and panel(d) showing mean pressure values. Statistical significance summary is displayed using the 3-star system.

SUMMARY

The focus of this chapter was to study the effect of blood rheology on the components of the PPG in the designed *in vitro* setup that mimics the mechanics of human circulation. We addressed the effect of the presence of red blood cells by comparing the collected signals while circulating whole equine blood (WEB) and a viscous solution (Cobalt Nitrate Polymer). We observed a highly significant increase in AC amplitudes while circulating WEB when compared to the cobalt solution. The only factor that can possibly contribute to this significant increase is the scattering properties of the vesicle-shaped red blood cells. This pattern was similarly observed in DC levels.

We also addressed the effect of different shear rates on the circulating WEB and observed an inverse pattern in AC amplitudes to that observed while circulating other solutions (Cobalt Nitrate or Cobalt Nitrate polymer solutions). A highly significant drop in AC levels was evident. This behaviour can only be attributed to flow migration and blood deformation. However, DC levels increased in the highly significant pattern, possibly, indicating axial migration and suggesting an increase in flow velocity at the middle of the tube.

Finally, the study addressed the effect of blood clotting on both components of the PPG signal. A highly significant drop in AC amplitudes was observed, highlighting the development of fibrous tissues and the disturbed shape of red blood cells. Both factors are believed to contribute to the reduced scattering and increased absorption in the pulsatile flow. DC levels significantly increased during and after the clot formation. This can be attributed to the medium losing its elastic properties and the significant increase in forward flow velocities.

Chapter 14
DISCUSSION AND CONCLUSIONS

Real-time cardiovascular assessment is vital for monitoring patients at an early stage of cardiovascular diseases (CVD), at risk of reoccurrence of heart attacks and strokes and during pharmacological and non-pharmacological treatments. Blood pressure (BP), arterial stiffness (AS) and blood viscosity (BV) are the three essential parameters that can provide a reliable assessment of hypertension, atherosclerosis, and hyperviscosity associated with the development and progression of cardiovascular pathologies to complex stages and occurrences of thrombosis. The currently available methods designed for the assessment of such parameters incur limitations and challenges that stand as an obstacle to the development of non-invasive, portable and reliable devices intended for personal use as previously discussed in **Chapter 3**. Moreover, the available methods are stand-alone devices and there is no available method or device that is capable of assessing BP, AS and BV in one all-inclusive device. Hence, this project aimed to investigate Photoplethysmography (PPG) as a technique intended for the development of a non-invasive and continuous monitoring device for the assessment of BP, AS, and BV. The project engaged in novel fundamental and rigorous *in vivo* and *in vitro* investigations in an effort to shed more light on the photoplethysmographic signals (AC and DC) during induced changes of BP, AS and BV. The underlying hypothesis is to show for the first time that PPG has the potential to non-invasively assess, in a qualifying and quantifying way, the above parameters. Positive outcomes from such an approach will establish universally the PPG technique as a preferential monitoring (screening and possible diagnosis) technique for the assessment of cardiovascular disease.

Prior to such investigations custom made reflectance finger and tube PPG probes (**Chapter 6**) operating at two wavelengths (R, 660 nm) and (IR, 880 nm) were designed, developed and successfully evaluated (see **Chapter 6** for further details). To pre-process and acquire the PPG signals, a dual-wavelength custom made PPG processing system was also developed and evaluated. ECG and temperature processing systems were designed and evaluated to be used during the *in vivo* investigation. The processing system was designed to operate in conjunction with a virtual data acquisition and control system developed in LabVIEW. The virtual instrument allowed the continuous acquisition,

display and recording of the signals during the investigations. An offline Matlab script was further developed to analyse the signals and perform statistical analysis after the investigations.

This project involved one *in vivo* and four *in vitro* investigations and several other performance verification experiments.

Following the evaluation of the finger sensors and the processing systems, a volunteer study commenced for investigating AC amplitudes and DC levels of the PPG signals during a cold pressor test (sympathetic stimulation). The City University Senate Research Ethics Committee has given the approval to conduct PPG measurements in 22 healthy volunteers undergoing a cold pressor test. R and IR PPG signals were acquired from the index finger from each hand, temperature signals from both fingers and ECG signals were continuously recorded for 2 minutes of baseline, 30 seconds of ice immersion of the right hand, and 10 minutes of rewarming at room temperature. Offline analyses were conducted on the acquired signals to examine the mean $\pm$ SD change in temperatures, PPG AC amplitudes, PPG DC levels and heart rates as measured from the ECG from all participants during the three periods. Statistical analyses were also performed to determine any significant difference between the three periods.

The results obtained from the *in vivo* investigation showed good quality R and IR PPG signals acquired from the index fingers using the custom built probe and processing system. During the immersion, the pattern of the signal morphology varied throughout different volunteers and different wavelengths and will be discussed further in the following pages. During the CPT, the change in skin temperatures can be seen in **Figure 8-6.** Skin temperatures in the right hand decreased significantly ($p<0.001$) during the immersion and increased significantly ($p<0.001$) during rewarming maintaining a significantly ($p<0.001$) lower temperature when compared to baseline. However, in the left hand, an unexpected temperature changes pattern was also observed, skin temperatures increased during the CPT and continued to increase during the rewarming. This change in temperature in the non-immersed hand was not previously documented in the literature. It indicates that the thermoregulation increase body metabolism and to compensate and ''fight'' the effect of temperature drop in the location undergoing local cooling. While this behaviour might not be visible in the cold hand due to the extreme temperature drop, it is marginally visible in the non-immersed hand with small increases in surface temperatures It further highlights that the sympathetic activation is of a more local nature and is more dominant in the immersed hand. In fact, as reported by Kellog,

a decrease in local skin temperatures with *local* cooling of the skin causes a *local*, temperature-dependent vasoconstriction (Kellogg, 2006). The local cooling vasoconstrictor response is dependent on intact noradrenergic cutaneous active vasoconstrictor nerves (Johnson et al., 2005; Pergola et al., 1993).

We further observe R and IR AC amplitudes during the CPT, both amplitudes showed a significant drop during the immersion in both hands with a percent changes tabulated in **Table 8-1** (left hand showing a drop of 45% and 53%, right hand showing a drop of 32% and 62% in R and IR AC amplitudes respectively). This response further highlights that that CPT incur systematic effects on blood flow regulation and haemodynamics in the human body. During the rewarming period, IR AC amplitudes in the right hand showed a significant increase ($p<0.001$), R AC amplitudes showed no significant increase ($p>0.05$) when compared to the immersion period. Both signals maintained significantly ($p<0.001$ in IR, and $p<0.01$ in R) lower amplitudes when compared to baseline. In the non-immersed (left) hand, however, AC amplitudes increased rapidly and significantly showing full recovery to baseline values with no significant ($p>0.05$) difference.

This pattern further confirms the expected vasoconstriction effects in the cold hand and suggests that the left hand which experiences a drop in AC amplitudes, an increase in skin temperatures and a fast full recovery, did not, in fact, experience a significant or any vasoconstriction effects. A question arises; what are the haemodynamics that caused the significant drop in AC amplitudes in the left hand during the immersion?

To answer this question, let us consider the signal morphology, DC levels and the expected effects of CPT on the systematic level. AC signals experienced a change in morphology during the immersion. In some volunteers, the signal lost its morphological character completely during the immersion. We were unable to detect a clear pattern of this behaviour. The morphology of the R or IR signals changes differently and the effects were observed with no clear pattern in both hands. Generally, red AC signals experienced the most disruptions which might indicate a change in the oxygen demand and consumption mechanisms during the immersion, and hence the change of oxygen affinities and bonds to haemoglobin molecules.

Looking at mean PPG DC levels (**Figure 8-10**) might provide a further insight into the thermal and blood flow regulation. During the CPT, DC levels increased in both hands. Furthermore, DC levels continued to increase in both hands during the rewarming period. This behaviour might be related to changes in red cell count and hence an

increase in backscattered light or can possibly be related to flow velocities in the steady layer, which are known to increase during CPT and due to the increase in heart rates. This increase in flow velocities can also possibly contribute to the increase in backscattered light.

The systematic effect of CPT has been previously investigated. There are contradictory opinions on the effect of CPT on blood pressure changes, while some studies highlighted that an increase in blood pressures can be observed and is correlated with CPT (Kalfon et al., 2015; Mourot et al., 2009), others have reported that mean blood pressure only experience a small increase (Korhonen, 2006). It was further reported that CPT significantly increases arterial stiffness (Kalfon et al., 2015). Furthermore, some studies highlighted that CPT has an effect on platelet function, increase in red cell count and increase in blood viscosity (Kawahara et al., 1989; Keatinge et al., 1984; Patterson et al., 1995; Takeshima et al., 1989). Hence, we conclude that there might be other factors that contribute to the drop in the AC amplitude in the left (non-immersed) hand in relation to the optical properties of the blood and the arterial wall. Such factors might be related to haemodynamics and the forces exerted on the inner surface of the vessels, such as arterial stiffness and haemorheological/viscosity changes. This conclusion has led us to further investigate the PPG from a fundamental point of view and study the effect of such factors on the PPG components in a controlled experimental environment.

The *in vitro* setup was designed and evaluated to mimic the human circulation under controlled flow conditions (**Chapter 9**). The model included the pulsatile pump, reservoir and an arterial model that includes three different models that simulate a flexible arterial model and a highly elastic arterial model with the same inner diameter (without extension) and another arterial model with 3/8 cross-sectional area of the other two models. Pressure and flow velocity signals were also acquired during the *in vitro* investigations. The protocol is designed to investigate the effect of fluid dynamics with the PPG signal, the effect of wall stiffness on the PPG signal, the sensitivity of the PPG components to fluid viscosity and effects of haemorheology on the PPG components under controlled conditions allowing control of tube models, circulating fluid, stroke volumes and pumping frequencies.

The **first** *in vitro* investigation (**Chapter 10**) highlights the relationship between the PPG signal and Pressure signals. The flow is directed towards *Model 1* and *Model 3*; *Model 1* is a flexible PVC transparent tube with a diameter of 16 mm that represents a large artery and *Model 3* is a flexible Tygon tube with a diameter of 6 mm that represents a small

artery. Flow patterns are controlled via two set-points of stroke volumes, 30 ml and 70 ml and three pumping frequencies f_1= 0.67, f_2= 1 and f_3= 1.8 Hz in each model. R and IR PPG signals, Doppler ultrasound flow, and pressure signals were recorded continuously for each stroke volume and pumping speed combination for 3 minutes each. The recorded signals, at varying pumping rates and each stroke volume from both models, were of high-quality. The processed signals obtained from *Model 1* are presented in (**Figure 10-6**, **Figure 10-7** and **Figure 10-8**) and those obtained from *Model 3* are shown in (**Figure 10-9**, **Figure 10-10** and **Figure 10-11**) for pumping frequencies (f_1, f_2, and f_3) respectively.

A noticeable observation is a linear increase in mean pressure values at the increasing pumping frequencies at each stroke volume in both models as seen from **Figure 10-13.** Strong correlations between both parameters can be observed (r^2=0.97, r^2=1) at SV of 30 ml and 70 ml, respectively for *Model 1,* and (r^2=0.98, r^2=0.99) at SV of 30 ml and 70 ml, respectively for *Model 3*. In fact, this pattern is expected due to the dependency of pumping powers on pumping frequencies (see equation (10.13)). Hence, we expect higher levels of energies to be delivered to the flow at higher pumping frequencies, and therefore, the increase in transmural pressure values. However, an important observation arises highlighting that this relationship varied significantly with different stroke volumes and different cross-sectional areas. A significantly higher slope at stroke volumes of 70 ml was also observed when compared to 30 ml stroke volumes, and at the larger tube diameter (*Model 1*) when compared to *Model 3* (see **Figure 10-13**). This trend can be foreseen. Higher stroke volumes and large cross-sectional areas are accompanied by an increase in pumping powers in the pulsatile pump and therefore, the increase in transmural pressure levels.

In addition, one can view in **Figure 10-12** the increase in mean pressure values in *Model 1* when compared to *Model 3* at both stroke volumes and at all pumping frequencies. While circulating the same fluid in both models with different diameters simultaneously, the flow will ''rush'' into *Model 1*, due to the increased resistance of *Model 3*. Moreover, at larger tube diameters, as in *Model 1*, higher fluid volume results in an increase in pressure towards the wall when compared to the model with smaller diameter, *Model 3*.

To further understand the effect of stroke volume, pumping rates and model cross-sectional area on the PPG signals recorded, let us take a closer look at both components of R and IR PPG signals. A prominent observation seen in **Figure 10-15** is the significant increase in AC amplitudes of R and IR signals in *Model 1* when compared to *Model 3*.

Another apparent observation is the increase in R and IR AC amplitudes at increasing pumping frequencies at both stroke volumes in each model. Both observations might indicate that the increase in AC amplitudes and mean pressure values (due to increasing pumping frequencies and increased cross-sectional area) might be representative of a direct relationship between AC amplitudes and pressure values. In order to investigate this assumption, let us discern **Figure 10-16** It is evident that there presents a strong correlation between AC amplitudes and mean pressure values (r^2=0.96, r^2=0.64, r^2=0.95, r^2=1) for *Model 3* at SV 30 ml, SV 70 ml and *Model 1* at SV 30 ml and 70 ml respectively. However, **Figure 10-17** shows that this correlation is strongly weakened when values of both stroke volumes are combined. Hence, our estimation is that raw AC amplitude is not the ideal method for pressure measurement. This due to the following reasons:

- The equation relating pressure and AC amplitudes differs significantly in both models at different stroke volumes. Hence, this assumption might be valid at constant diameters, elasticities and stroke volumes. However, it seems that this correlation can be only valid at varying pumping frequencies. All of the mentioned parameters differ in human subjects, from individual to another and in the same individuals according to sympathetic and parasympathetic events. Therefore, this method will incur errors that prevent it from providing a reliable tool for clinical devices.

To further understand and analyse this behaviour, let us consider changes in DC levels and how do they contribute to our understanding of the mechanics of pulsatile flow. AC and DC components are both products of pulsatile flow, and one cannot consider one but not the other. DC levels seem to be affected by changes in pumping speeds and stroke volumes, hence they seem to be related to flow of the steady component, which develops at the centre of the tube and obtains the maximum possible velocity in a straight line. The signal is independent of time and is related to the inertia of the fluid. A noticeable observation is that DC levels were also significantly higher in *Model 1* when compared to *Model 3* at both stroke volumes and at all pumping rates (see **Figure 10-19)**. The diameter of *Model 1* is 2.6 times that of *Model 3*, and, therefore, a higher fluid inertia was present in the larger tube resulting in increased scattering events due to the larger volume of the steady layer.

In *Model 1*, Infrared DC levels were substantially higher at higher stroke volumes at 0.67 and 1 Hz pumping rates and dropped significantly at 1.8 Hz to values lower than that observed at 30 ml SV. This behaviour mirrors that observed in forward flow velocities (**Figure 10-14**). Similarly, in *Model 3*, IR DC levels were significantly higher at higher

stroke volumes, with the exception of that obtained at 0.67 Hz. Again, this pattern mirrors that observed in forward flow velocities. At higher stroke volumes, the inertia of the fluid increases and the pumping power in the pulsatile pump. Although, such factors are usually expected to result in an increase in flow rates, a behaviour which was generally observed. However, the inertia of fluid might also increase the resistance of the flow and cause a reduction of flow efficiency, which has resulted in a drop in flow rates at 1.8 Hz. Therefore, DC levels can be also affected by the velocity of the flow in addition to the volume of the steady flow layer as noted in the former observation. Molecule-light interactions at steady flows moving at higher velocities are expected to have higher energy collisions. Due to the angle of interaction, such collisions are expected to casue the increase in backscattering events.

To further analyse the behaviour of both AC and DC components, let us observe time ratio results from **Figure 10-18.** Time ratio can be representative of energy consumption in the flow, where higher values might indicate that more energy has been transferred from the fluid to the wall allowing the oscillatory PPG component (AC) to peak in less time. A prominent observation is the significantly higher values observed in *Model 3* when compared to *Model 1*. Therefore, as previously discussed, the increase in fluid volume due to diameter increase will result in elevated fluid inertia levels, which can be a source of energy losses. The same pattern was generally observed when flow efficiency is compared at different stroke volumes. In both models, low stroke volumes obtained higher time ratio values, which might indicate more efficient flow patterns at low stroke volumes, due to the reduced inertia of the fluid and less energy required for fluid movement. In a few cases, the difference was not significant. Moreover, there was no clear pattern observed for time ratios at varying pumping frequencies. For example, time ratio in *Model 3* dropped significantly with increasing pumping frequencies at both stroke volumes. While, in *Model 1*, time ratios increased with increasing frequencies at 70 ml SV. Finally, at 30 ml SV, values for time ratio, dropped significantly at increasing frequency from 0.67 to 1 Hz to increase significantly again at 1.8 Hz.

Finally, as proposed in **section 10.1.1**, a derivation from the Beer-Lambert law allowed an estimation of pulsatile flow using normalised pulse volume (NPV) and Adjusted Pulse Volume (APV). NPV was defined in terms of red PPG signals (NPV_R) and infrared PPG (NPV_{IR}). APR was defined concerning both wavelengths to consider the different depth of light penetrations with pulsatile flow. We showed that our experimental data matched the assumed physiological Pressure-Volume exponential model. This is clear from the

significant correlations observed in both models as seen in **Figure 10-20** and **Figure 10-21**. NPV methods showed a significant fit to the assumed P-V model, NPV_R provided Rsquare, RMSE and correlation significance p-value as the following: (r^2=0.96, RMSE=0.108, p<0.001) for *Model 1* and (r^2=0.96, RMSE=0.079, p<0.001) in *Model 3*. NPV_{IR} provided values of (r^2=0.73, RMSE=0.292, p<0.001), (r^2=0.92, RMSE=0.109, p<0.001) for *Model 1* and *Model 3*, respectively. Moreover, APV showed a significant correlation (r^2=0.99, RMSE=0.06, p<0.001), (r^2=0.98, RMSE=0.059, p<0.001) for *Model 1* and *Model 3* respectively. In fact, APV had a significantly better fit as evaluated with z-score in both models. Z-scores for *Model 1* (z=21.1, p<0.001) and (z=12.5, p<0.001) when compared to both NPV_R and NPV_{IR}, respectively. In *Model 3*, z-scores and p-values were (z=11.1, p<0.001) and (z=5.5, p<0.001) when compared to both NPV_R and NPV_{IR}, respectively.

The P-V exponential model is the most commonly used physiological model for describing arterial flow with arterial pressure (Burkhoff et al., 2005). The modelled information computed from the PPG experimental data may provide the opportunity to estimate pressure values during haemodynamic instabilities, changes in stroke volumes, and pumping frequencies within the wide pressure range explored in this experiment regardless of cross-sectional areas, and possibly in human subjects.

The **second** *in vitro* investigation (**Chapter 11**) addresses the effect of arterial stiffness on the PPG signal. The chapter demonstrated the capability of the pulsatile component of the PPG as a measure of volumetric strain in monitoring and detecting changes in the volume *elastic modulus* (E_v) and hence its potential in the diagnosis of arterial stiffness. We have evaluated our method in the *in vitro* model of two arterial models, *Model 1*, a model of a healthy large artery and *Model 2*, a model of a large artery affected with atherosclerosis. In order to simulate symptoms of hypertension, we further explored our method under conditions of increased stroke volume and pulse frequency.

The linear regression was well fitted for dP/dt versus the rate of change of dNVS/dt. Correlation coefficients were highly significant (p<0.001) for both models as seen in the scattergrams in **figure 11-13**. Values from the proposed method for E_v measurement showed agreement with the gold standard (Instron) elasticity measurement with no significant difference as seen in **Table 11-3,** and percent errors were within the accepted 5% limit for both models. This finding highlights that PPG can provide a measure of volumetric strain via the proposed method and hence, using pressure values, an accurate measure of E_v.

It is observed that with increasing pumping frequencies, systolic pressure values and pressure rates increased significantly ($p<0.001$) in both models. Systolic pressure values and pressure rates also increased significantly at higher stroke volumes in both models. This is an expected behaviour that can be ascribed to the increase of pumping powers with increasing pumping frequencies and stroke volumes. When values are compared in both models, it is evident that systolic pressure values are significantly ($p<0.001$) higher in *Model 1*, when compared to *Model 2* at the same pumping frequency and stroke volume (see **figure 11-8**). This provides further confirmation of the effect of increased arterial stiffness and increased wall thickness on the functionality of the flow, where the affected model (*Model 1*) had a poor response to increased stroke volumes (inertial effects) and pulse frequency (fluid momentum) which caused a much larger increase in transmural pressure values against the wall interface. This also highlights the role of AS in hypertension patients which are linked with ATH and associated with a risk of lesion rupture (Bortolotto et al., 2000; Hollander, 1976; Laurent and Boutouyrie, 2012; Laurent et al., 2003) due to the increase in transmural pressures and circumferential stress. That is to say, the more elastic walls are capable of absorbing fluid energy delivered from the pump, where this energy is reflected back to the fluid and consumed as kinetic energy rather than being dissipated at the wall interface region, causing a significant increase in pressure values as seen in *Model 1*.

The instantaneous E_v values as seen in **figure 11-16(a)** highlight that an increase in pumping frequency can influence arterial distensibility. This observation is in agreement with previous studies that reported on the effect of heart rate on the stiffness of the ascending and descending aorta (Wilkinson et al., 2000) and the carotid and radial arteries (Giannattasio et al., 2003). Giannattasio et al (2003) highlighted that AS increase with increasing heart rate, Wilkinson et al (2000) also observed an inverse relationship between AIx and heart rates (Giannattasio et al., 2003; Wilkinson et al., 2000).

While these observations were consistent and significant in both models via the Instantaneous E_v method. The PTT method (seen in **figure 11-16 (b)**) was able to detect this behaviour in *Model 1*, nevertheless, there was no significant difference observed in *Model 2* when the frequency increased to 1.8 Hz at both stroke volumes. Though this behaviour is not clear, the change in flow velocity patterns limits the phase change between pressure and volumetric strain signals. At low pumping frequencies, the effect of stroke volume on AS seemed to be significant, with higher wall stiffness values observed at lower stroke volumes. The effect of stroke volume diminished at higher

pumping frequencies, where at 1.8 Hz, both Instantaneous E_v values had no significant difference. Yet, the PTT method was still able to detect a significant difference in values between both stroke volumes at the highest frequency. With increasing frequencies, fluid viscosity drops significantly (see **Table 11-2**), and hence fluid inertia becomes a less significant factor in the dynamics of the flow. However, the change of fluid characteristics might allow the pulsatile fluid signal to travel at a higher speed in the axial direction, and hence, the drop in phase between pressure and PPG signals might not be due to changes in wall stiffness. These findings highlight that as the E_v and the PTT methods were able to detect changes in arterial stiffness between both models, E_v provides a direct quantification of arterial stiffness and might provide better accuracy even at increased pumping frequency or stroke volume changes.

The **third** *in vitro* set of investigations are seen in **Chapter 12.** In this experiment PPG, pressure, and flow signals are collected in the *in vitro* setup of pulsatile flow while observing changes in flow dynamics in two fluids with different viscosities. The changes from all sensor outputs were investigated for a range of pumping frequencies at a fixed stroke volume. This work was primarily focused on understanding further the effect of fluid mechanical characteristics on the AC and DC components of the PPG signal.

Fluid 2 obtained higher viscosity values when compared to *fluid 1* as seen in **Table 12-3**. *Fluid 2* had lower conductivity levels and higher acidity when compared to *fluid 1* as seen in **Table 12-2**. This is due to the presence of PEG in *fluid 2* (Mei et al., 1995). The most obvious observation, seen in **Figure 12-7**, is that pressure values are significantly higher while *fluid 2* is circulating when compared to *fluid 1* at all pumping frequencies (see **Table 12-4***)*. As this is expected, it is an emphasis on the effect of fluid viscosity on flow resistance and, therefore, on pressure changes between the walls. These results suggest agreement with long-established studies stating that blood viscosity in the human circulation is an important factor in the development of cardiovascular diseases and especially in the early stages of hypertension (Letcher et al., 1983, 1981).

Another prominent observation is the significant increase in mean pressure values at increasing frequencies. We also observe the positive slope and linear relationship (r^2=0.99) between mean pressure values and pumping frequency while circulating both fluids, as demonstrated in **Figure 12-8**. This can be simply related to the pumping power equation, which draws a proportional relationship between pumping frequency and gradient pressure (see equation 10.13). It is also clear that both equations in **Figure 12-8** relating pumping frequency and mean pressure values have a different baseline, with a

higher baseline observed for *fluid 2*. There was no significant ($p>0.05$) difference between both slopes.

The effect of flow dynamics on the PPG AC, DC, time ratio, NPV_R, $NPV_{IR,}$ and APV is discussed herein. It was observed earlier in **Chapter 10** and **Chapter 11** that AC amplitudes augmented significantly at increasing pumping frequencies. This pattern was also detected in this investigation (**Figure 12-11** and **Table 12-8).** A striking observation is the significantly augmented AC amplitudes for *fluid 1* when compared to *fluid 2.* This relationship is valid at all pumping frequencies. More importantly, while *fluid 2* was circulating, mean pressure values were elevated when compared to *fluid 1*, and hence, AC values are expected to be greater, assuming that AC is linearly related to mean pressure values. Therefore, one is to conclude that raw AC amplitudes may provide an indication of fluid energy levels, which increase at higher frequencies, rather than a direct estimation of mean pressure values as discussed earlier. Moreover, this behaviour can be attributed to the optical density of the fluid. By referring to the spectra analysis for both media, seen in **Figure 12-4**. It is observed that *fluid 2* will allow lower light transmission in the range of interest and will experience higher absorption. Thereby, it appears that AC amplitudes are sensitive to changes in fluid viscosity in pulsatile flow.

From **Figure 12-13**, one can perceive that *fluid 1* holds significantly higher DC values when compared to *fluid 2*. As previously discussed, DC signals seem to reflect changes in the inertia of the steady flow, developed in the centre of the tube. This can be clearly observed again in **Table 12-9**. IR DC signals for *fluid 2* had significantly lower values when compared to *fluid 1* IR DC signals. The increased DC signals in *fluid 1* can be referred to the following:(1) The augmented forward flow velocities perceived for *fluid 1* may result in increased backscattering, hence the increase in DC levels. As these molecules are moving at an approximately perpendicular angle relative to the PPG sensor, the light is estimated to be scattered by this motion. (2) The lower absorption capability of *fluid 1* when compared to *fluid 2* due to its increased viscosity and density, as seen in **Figure 12-4**.

Finally, **Figure 12-13** presents mean $\pm$ SD values for time ratio. This ratio represents the relaxation (diastolic) time obtained from the AC PPG signal in relation to the full period cycle. It indicates the time the fluid requires to restore back to ''equilibrium'' state during the diastolic phase. Values were significantly elevated for *fluid 2* when compared to *fluid 1* at all pumping frequencies, as seen in **Table 12-10**. This is further evidence that the PPG can detect changes related to the mechanical properties of the circulating fluid, such as

fluid viscosity. As expected, *fluid 2* will obtain higher-energy exchange during the diastolic phase, and hence, a higher time ratio. This is referred to the increased amount of energy storage and dissipation when compared to *fluid 1*, which can be clearly observed from the time ratio. This observation was reinforced by higher backward flow velocities in *fluid 2* compared to *fluid 1 (***Figure 12-10** and **Table 12-6***)*.

The inability of AC amplitudes to detect the increase in mean pressure values in *fluid 2* led us to further analyse the described parameters in **Chapter 10**, NPV_R, $NPV_{IR,}$ and APV. The question was if the assumed exponential relationship of pressure and normalised volume is still valid for distinct fluid viscosities. The results discerned in **Figure 12-15** indicate a strong correlation of NPV_R, $NPV_{IR,}$ and APV with $\ln(P_S)$. Again, we note that APV provides a remarkable fit (r^2=0.99, $p<0.001$) compared to NPV_{IR} (r^2 = 0.82, z=20.99, $p<0.001$) and NPV_R (r^2= 0.84, z=20.03, $p<0.001$). This reinforces that APV-ln(P) function is the optimum method for detection of systolic pressure values, not only at different stroke volume as proved in **Chapter 10** but also at different fluid viscosities as seen in **Chapter 12**. Moreover, mean values were seen in **Figure 12-14** highlights that APV values were the only method that could detect a rise in volume at heightened mean pressure values in *fluid 2* when compared to raw AC amplitudes of NPV_R and NPV_{IR}.

The **fourth** *in vitro* set of investigations are seen in **Chapter 13** in an effort to finally address the effect of haemorheology on the PPG signal. Equine whole blood was circulated in the developed *in vitro* setup in order to observe the effect of RBC presence on the PPG components, the role of shear rates (pumping frequencies) on the PPG signal and finally the effect of platelet activation on the components of PPG signal.

To investigate the role of the presence RBCs on the PPG, we utilise the *in vitro* setup while circulating either blood or PEG Cobalt Nitrate solution (dye). Both fluids obtain similar viscosity values with PEG obtaining slightly higher values as seen in **Figure 13-5**.

Mean pressure values were significantly higher during the dye circulation when compared to whole equine blood, which can be due to the elevation of the fluid viscosity. Furthermore, we observe a significantly ($p<0.001$) higher values for R and IR AC amplitudes and DC levels when compared to the circulating dye. By observing optical spectra for both fluids, it is evident that equine blood samples have higher absorption levels when compared to the dye. Hence, the increase in AC amplitudes and DC levels reflect the importance of the scattering properties of red blood cells.

The second study in this set of investigations explores the effect of pumping rates (0.67, 1, 1.5, 1.9 Hz) on the PPG analytics. As previously observed, mean pressure values increase significantly with increasing pumping rates. However, whole equine blood circulating in the *in vitro* setup showed a drop in AC amplitudes of R and IR PPG signals with increasing frequencies (See **Figure 13-11**). Despite that, this behaviour is the inverse of that observed during the dye circulation as seen in **Chapter 10,** it is an expected behaviour. Shear rates are proportional to flow velocities, which increased with increasing pumping rates. Roggan et al. (1999), in their experiment showed that mean values of the absorption coefficient and reduced scattering versus shears at a haematocrit of 41% drops significantly with increasing shear rates, see **Figure 4-6**. Roggan suggested that it is not clear if this behaviour is due to cell deformation or axial migration (Roggan et al., 1999). Observing DC levels in **Figure 13-12** might give a further indication. There was a significant increase in DC levels with increasing shear rates. Our understanding is that the radial migration of the erythrocyte is an important factor in this behaviour due to the expected drop in blood viscosities with increasing shear rates and hence the drop in absorption. However, RBC deformation might also contribute to the reduced scattering.

Furthermore, the results discerned in **Figure 13-13** indicate a strong correlation of NPV_R, $NPV_{IR,}$ and APV with $\ln(P_S)$. Again, we note that APV provides a better fit (r^2=0.96, $p<0.001$) compared to NPV_{IR} (r^2= 0.95, $p<0.03$) and NPV_R (r^2=0.94, $p<0.02$). This reinforces that APV-ln(P) function is the optimum method for detection of systolic pressure values, not only at different stroke volume as proved in **Chapter 10** and not only at different fluid viscosities as seen in **Chapter 12,** but also it is valid while circulating whole equine blood.

Finally, we explored the effect of platelet activation on both optical and fluid dynamic signals. The chemically triggered platelet activation was achieved using calcium chloride powder. Mean pressure values increased significantly after the clotting activation (**Figure 13-15(d)**), which can be ascribed to the increase in viscosity of the clotting sample (**Figure 13-5**). The PPG_{AC} amplitude started to decrease as presented in **Figure 13-14(a)** few seconds after the clotting agent was added. At the time the clotting was complete, AC amplitudes stabilised with significantly lower AC amplitudes with disrupted morphology. This behaviour can be explained by observing the obtained spectra seen in **Figure 13-4**. The clotted blood sample had higher absorption than that observed in whole blood. We also observe a significant change in the morphology of PPG_{AC} signals indicating a significant change in the scattering properties of the medium. **Figure 13-3** shows a

scanning electronic image (5000 magnification) of the clotted sample after few minutes of the addition of the clotting trigger. The development of fibrinous matrix increases the absorptivity of whole blood (**Figure 13-4)** and shield the optical scattering of individual cells causing a significant disruption to the morphology of the PPG signal. R and IR DC levels increase significantly during the circulation of the clotting blood which might be related to the increase in forward flow velocities seen in **Figure 13-15(c).**

LIMITATIONS

The study incurs some limitations that need to be considered before it can be applied in an *in vivo* investigation.

- The basic assumption for the derivation of the Beer Lambert to measure volumetric strain and transmural pressure seen in **Chapter 10** considers the fluid as a non-scattering homogeneous medium. However, this presumption is known to be not valid for blood suspension because the light interaction through the suspension is caused by absorption, as well as scattering events (Friebel et al., 2006). Nonetheless, the evidence is accumulating that Beer-Lambert's law can be extended to a light scattering system (Kocsis et al., 2006). However, results applying the derived method to whole equine blood in **Chapter 13** and **Figure 13-13**, highlight that in fact the derived relationship is valid while circulating a scattering medium similar to human blood.

- The factors which can violate the directly proportional relationship between V_o and light intensity were not investigated experimentally in this study (concentration, c and absorption coefficient, ε). Yet, during an *in vivo* setup, ε is constant within and between subjects due to the fixed absorption coefficients of oxy and deoxyhaemoglobin at the specific wavelength. In respect to *c*, haematocrit changes are expected to be only a few percent due to changes in neurohormonal factors.

- The estimation of E and E_v was obtained using a fixed rate of extension in the instron (0.1 mm/s). By taking into account the rate of change of pressure and volumetric strain in the original equation of the proposed method, the effect of extension rate is eliminated as this might introduce an error in relating E_v estimation from both methods.

- It is known that the PPG signal behaves inversely in relation to blood pressure and it should be inverted to correlate positively with the blood volume. Recently Teplov et al reported the coexistence of two mutually inverted signals in adjacent locations (Teplov et al., 2014). This behaviour was also observed in this investigation as inverted signals

were observed along the same tube in different locations, and it is possibly related to the sensor contact pressure during the wall movement, or the direction of the flow. Nevertheless, this issue does not affect the amplitude or the morphology of the signal and is not the main concern of this work. To avoid any errors related to the inversion of the PPG signal, the signals were inverted to correlate with the blood pressure signals . As PPG and pressure signals were recorded simultaneously, the peak of the PPG signal was determined in relation to the pressure peak in each cycle.

Finally, future *in vivo* investigations are required to further validate the developed methods and findings for personal or clinical use. The studies need to be designed to address all the parameters combined and require comparisons between healthy subjects and cardiovascular patients for validation and calibration.

SUMMARY

In summary, this project investigated the potential of PPG as a monitoring device for blood pressure, arterial stiffness, fluid viscosity and haemorheology in an effort for the development of non-invasive, real-time screening of cardiovascular performance. In the *in vivo* investigation, finger PPG probes, skin thermistors and their processing systems with an ECG processing system were successfully designed and developed. Results obtained during a cold pressor test indicated that the local cooling has systemic effects on blood flow regulation mechanisms and haemodynamics. An *in vitro* controlled setup of the pulsatile pump, reservoir, and an arterial network were developed to address the effect of such factors on the PPG signal. The *in vitro* investigation allowed validation of the developed method for measurements of transmural pressure at different stroke volumes, cross-sectional areas and at varying pumping frequencies for a variety of fluids including equine blood under a wide range of pressure values. A measurement method for the volume elastic modulus was also proposed and validated in two arterial models. Moreover, the project presented results for the first time highlighting the effect of haemorheology on the AC and DC PPG components in relation to RBCs' deformation, axial migration and clotting. Such findings can aid researchers in the field to reach a better understanding of optical interaction with the pulsatile flow considering the haemodynamics and haemorheology of the circulation for the development of non-invasive monitoring of cardiovascular health and possibly early diagnosis of CVDs.

References

Aaronson, P.I., Ward, J.P.T., Connolly, M.J., 2012. The Cardiovascular System at a Glance. John Wiley & Sons.

Adler, J.N., Hughes, L.A., Vtvilecchia, R., Jr., C.A.C., 1998. Effect of Skin Pigmentation on Pulse Oximetry Accuracy in the Emergency Department. Academic Emergency Medicine 5, 965–970. doi:10.1111/j.1553-2712.1998.tb02772.x

Ahlstrom, C., Johansson, A., Uhlin, F., Länne, T., Ask, P., 2005. Noninvasive investigation of blood pressure changes using the pulse wave transit time: a novel approach in the monitoring of hemodialysis patients. J Artif Organs 8, 192–197. doi:10.1007/s10047-005-0301-4

Alvim, R. de O., Santos, P.C.J.L., Musso, M.M., Cunha, R. de S., Krieger, J.E., Mill, J.G., Pereira, A.C., 2013. Impact of diabetes mellitus on arterial stiffness in a representative sample of an urban Brazilian population. Diabetology & Metabolic Syndrome 5, 45. doi:10.1186/1758-5996-5-45

Alzahrani, A., Hu, S., Azorin-Peris, V., Barrett, L., Esliger, D., Hayes, M., Akbare, S., Achart, J., Kuoch, S., 2015. A Multi-Channel Opto-Electronic Sensor to Accurately Monitor Heart Rate against Motion Artefact during Exercise. Sensors 15, 25681–25702. doi:10.3390/s151025681

Anderson, R.R., Parrish, J.A., 1981. The Optics of Human Skin. Journal of Investigative Dermatology 77, 13–19. doi:10.1111/1523-1747.ep12479191

Aoyagi, T., 2003. Pulse oximetry: its invention, theory, and future. J Anesth 17, 259–266. doi:10.1007/s00540-003-0192-6

Aravind Krishnaswamy, Baranoski, G.V.G., 2004. A Study on Skin Optics. CiteSeerX.

Asakura, T., Karino, T., 1990. Flow patterns and spatial distribution of atherosclerotic lesions in human coronary arteries. Circulation Research 66, 1045–1066. doi:10.1161/01.RES.66.4.1045

Asif-Ul-Hoque, M., Ahsan, M.S., Mohajan, B., 2011. Measurement of Blood Pressure Using Photoplethysmography, in: 2011 UkSim 13th International Conference on Computer Modelling and Simulation (UKSim). Presented at the 2011 UkSim 13th International Conference on Computer Modelling and Simulation (UKSim), pp. 32–35. doi:10.1109/UKSIM.2011.16

Awad, A.A., Ghobashy, M.A.M., Ouda, W., Stout, R.G., Silverman, D.G., Shelley, K.H., 2001. Different Responses of Ear and Finger Pulse Oximeter Wave Form to Cold Pressor Test. Anesth Analg 92, 1483–1486.

Azabji Kenfack, M., Lador, F., Licker, M., Moia, C., Tam, E., Capelli, C., Morel, D., Ferretti, G., 2004. Cardiac output by Modelflow method from intra-arterial and fingertip pulse pressure profiles. Clin. Sci. 106, 365–369. doi:10.1042/CS20030303

Baker, E.H., 2000. Ion channels and the control of blood pressure. Br J Clin Pharmacol 49, 185–198. doi:10.1046/j.1365-2125.2000.00159.x

Baker, P.D., Westenskow, D.R., Kück, K., 1997. Theoretical analysis of non-invasive oscillometric maximum amplitude algorithm for estimating mean blood pressure. Medical and Biological Engineering and Computing 35, 271–8. doi:http://0-dx.doi.org.wam.city.ac.uk/10.1007/BF02530049

Ball, D.W., 2001. The Basics of Spectroscopy. SPIE Press.

Barac, A., Campia, U., Panza, J.A., 2007. Methods for Evaluating Endothelial Function in Humans. Hypertension 49, 748–760. doi:10.1161/01.HYP.0000259601.38807.a6

Baskurt, O., Neu, B., Meiselman, H.J., 2011. Red Blood Cell Aggregation. CRC Press.

Baskurt, O.K., 2007. Handbook of Hemorheology and Hemodynamics: Texte Imprimé. IOS Press.

Ben-Shlomo, Y., Spears, M., Boustred, C., May, M., Anderson, S.G., Benjamin, E.J., Boutouyrie, P., Cameron, J., Chen, C.-H., Cruickshank, J.K., Hwang, S.-J., Lakatta, E.G., Laurent, S., Maldonado, J., Mitchell, G.F., Najjar, S.S., Newman, A.B., Ohishi, M., Pannier, B., Pereira, T., Vasan, R.S., Shokawa, T., Sutton-Tyrell, K., Verbeke, F., Wang, K.-L., Webb, D.J., Willum Hansen, T., Zoungas, S., McEniery, C.M., Cockcroft, J.R., Wilkinson, I.B., 2014. Aortic Pulse Wave Velocity Improves Cardiovascular Event Prediction: An Individual Participant Meta-Analysis of Prospective Observational Data From 17,635 Subjects. Journal of the American College of Cardiology 63, 636–646. doi:10.1016/j.jacc.2013.09.063

Beulen, B.W.A.M.M., Bijnens, N., Koutsouridis, G.G., Brands, P.J., Rutten, M.C.M., Vosse, F.N. van de, 2011. Toward Noninvasive Blood Pressure Assessment in Arteries by Using Ultrasound. Ultrasound in Medicine and Biology 37, 788–797. doi:10.1016/j.ultrasmedbio.2011.01.020

Bitbol, M., 1986. Red blood cell orientation in orbit C = 0. Biophys J 49, 1055–1068.

Björn, L.O., 2007. Photobiology: The Science of Life and Light. Springer.

Blacher, J., Asmar, R., Djane, S., London, G.M., Safar, M.E., 1999. Aortic Pulse Wave Velocity as a Marker of Cardiovascular Risk in Hypertensive Patients. Hypertension 33, 1111–1117. doi:10.1161/01.HYP.33.5.1111

Blacher, J., Guerin, A.P., Pannier, B., Marchais, S.J., Safar, M.E., London, G.M., 1999. Impact of Aortic Stiffness on Survival in End-Stage Renal Disease. Circulation 99, 2434–2439. doi:10.1161/01.CIR.99.18.2434

Bohren, C.F., Huffman, D.R., 2007. Absorption and Scattering of Light by Small Particles.

Bortolotto, L.A., Blacher, J., Kondo, T., Takazawa, K., Safar, M.E., 2000. Assessment of vascular aging and atherosclerosis in hypertensive subjects: second derivative of photoplethysmogram versus pulse wave velocity. Am. J. Hypertens. 13, 165–171.

Boutouyrie, P., Bussy, C., Lacolley, P., Girerd, X., Laloux, B., Laurent, S., 1999. Association Between Local Pulse Pressure, Mean Blood Pressure, and Large-Artery Remodeling. Circulation 100, 1387–1393. doi:10.1161/01.CIR.100.13.1387

Brahme, A., 2014. Comprehensive biomedical physics.

Bramwell, J.C., Hill, A.., 1922. VELOCITY OF TRANSMISSION OF THE PULSE-WAVE. The Lancet 199, 891–892. doi:10.1016/S0140-6736(00)95580-6

Broome, I.J., Mills, G.H., Spiers, P., Reilly, C.S., 1993. An evaluation of the effect of vasodilatation on oxygen saturations measured by pulse oximetry and venous blood gas analysis. Anaesthesia 48, 415–416. doi:10.1111/j.1365-2044.1993.tb07017.x

Burkhoff, D., Mirsky, I., Suga, H., 2005. Assessment of systolic and diastolic ventricular properties via pressure-volume analysis: a guide for clinical, translational, and basic researchers. American Journal of Physiology - Heart and Circulatory Physiology 289, H501–H512. doi:10.1152/ajpheart.00138.2005

Caro, C.G., 2012. The Mechanics of the Circulation. Cambridge University Press.

Catalano, M., Scandale, G., Dimitrov, G., 2013. Arterial Stiffness: A Review in Type 2 Diabetes, in: Masuo, K. (Ed.), Type 2 Diabetes. InTech.

Cetinkunt, S., 2015. Mechatronics with Experiments. John Wiley & Sons.

Challoner, A.V.J., Ramsay, C.A., 1974. A photoelectric plethysmograph for the measurement of cutaneous blood flow. Physics in Medicine and Biology 19, 317–328. doi:10.1088/0031-9155/19/3/003

Chan, F.C.D., Hayes, M.J., Smith, P.R., 2007. VENOUS PULSE OXIMETRY. EP1469773.

Chee, Y.L., Crawford, J.C., Watson, H.G., Greaves, M., 2008. Guidelines on the assessment of bleeding risk prior to surgery or invasive procedures. British Committee for Standards in Haematology. Br. J. Haematol. 140, 496–504. doi:10.1111/j.1365-2141.2007.06968.x

Chien, S., Usami, S., Dellenback, R.J., Gregersen, M.I., 1967. Blood viscosity: influence of erythrocyte deformation. Science 157, 827–829. doi:10.1126/science.157.3790.827

Cho, Y.I., Cho, D.J., Rosenson, R.S., 2014. Endothelial Shear Stress and Blood Viscosity in Peripheral Arterial Disease. Curr Atheroscler Rep 16, 1–10. doi:10.1007/s11883-014-0404-6

Chobanian AV, Bakris GL, Black HR, et al, 2003. The seventh report of the joint national committee on prevention, detection, evaluation, and treatment of high blood pressure: The jnc 7 report. JAMA 289, 2560–2571. doi:10.1001/jama.289.19.2560

Chowienczyk, P.J., Kelly, R.P., MacCallum, H., Millasseau, S.C., Andersson, T.L., Gosling, R.G., Ritter, J.M., Anggård, E.E., 1999. Photoplethysmographic assessment of pulse wave reflection: blunted response to endothelium-dependent beta2-adrenergic vasodilation in type II diabetes mellitus. J. Am. Coll. Cardiol. 34, 2007–2014.

Chung, E., Chen, G., Alexander, B., Cannesson, M., 2013. Non-invasive continuous blood pressure monitoring: a review of current applications. Front Med 7, 91–101. doi:10.1007/s11684-013-0239-5

Cokelet, G., 2011. Hemorheology and Hemodynamics. Morgan & Claypool Publishers.

Cone and Plate Chamber, 2008. Retrieved from http://soft-matter.seas.harvard.edu/index.php/File:Cone_and_plate.jpg.

Cooke, E.D., Bowcock, S.A., Smith, A.T., 1985. Photoplethysmography of the distal pulp in the assessment of the vasospastic hand. Angiology 36, 33–40.

Coull, B.M., Beamer, N., de Garmo, P., Sexton, G., Nordt, F., Knox, R., Seaman, G.V., 1991. Chronic blood hyperviscosity in subjects with acute stroke, transient ischemic attack, and risk factors for stroke. Stroke 22, 162–168.

Courneya et al., 2010. Cardiovascular Physiology: A Clinical Approach. Lippincott Williams & Wilkins.

Crowley, J.P., Metzger, J., Assaf, A., Carleton, R.C., Merrill, E., Valeri, C.R., 1994. Low density lipoprotein cholesterol and whole blood viscosity. Ann. Clin. Lab. Sci. 24, 533–541.

D'Agrosa, L.S., Hertzman, A.B., 1967. Opacity pulse of individual minute arteries. J Appl Physiol 23, 613–620.

D'Agrosa, L.S., Hertzman, A.B., 1967. Opacity pulse of individual minute arteries. J Appl Physiol 23, 613–620.

de Trafford, J., Lafferty, K., 1984. What does photoplethysmography measure? Med Biol Eng Comput 22, 479–480.

Delfino, A., Moore, J.E., Meister, J.J., 1994. Lateral deformation and movement effects on flow through distensible tube models of blood vessels. Biorheology 31, 533–547.

Delpy, D.T., Cope, M., Zee, P. van der, Arridge, S., Wray, S., Wyatt, J., 1988. Estimation of optical pathlength through tissue from direct time of flight measurement. Physics in Medicine and Biology 33, 1433–1442. doi:10.1088/0031-9155/33/12/008

Dintenfass, L., 1964. Viscosity and Clotting of Blood in Venous Thrombosis and Coronary Occlusions. Circulation Research 14, 1–16. doi:10.1161/01.RES.14.1.1

Ercan, M., Koksal, C., 2003. The Relationship Between Shear Rate and Vessel Diameter. Anesth Analg 96, 307–308. doi:10.1213/01.ANE.0000035798.98613.56

Ethier, C.R., Simmons, C.A., 2007. Introductory Biomechanics: From Cells to Organisms. Cambridge University Press.

Expert Panel on Detection, Evaluation, and Treatment of High Blood Cholesterol in Adults, 2001. Executive Summary of The Third Report of The National Cholesterol Education Program (NCEP) Expert Panel on Detection, Evaluation, And Treatment of High Blood Cholesterol In Adults (Adult Treatment Panel III). JAMA 285, 2486–2497.

Feireisl, E., 2003. Dynamics of Viscous Compressible Fluids. Oxford University Press.

Fischer, T.M., 2007. Tank-tread frequency of the red cell membrane: dependence on the viscosity of the suspending medium. Biophys. J. 93, 2553–2561. doi:10.1529/biophysj.107.104505

Foo, J.Y.A., Lim, C.S., 2006. Pulse transit time as an indirect marker for variations in cardiovascular related reactivity. Technol Health Care 14, 97–108.

Forsyth, A.M., Wan, J., Owrutsky, P.D., Abkarian, M., Stone, H.A., 2011. Multiscale approach to link red blood cell dynamics, shear viscosity, and ATP release. Proc. Natl. Acad. Sci. U.S.A. 108, 10986–10991. doi:10.1073/pnas.1101315108

Fossum, E., Høieggen, A., Moan, A., Nordby, G., Velund, T.L., Kjeldsen, S.E., 1997. Whole blood viscosity, blood pressure and cardiovascular risk factors in healthy blood donors. Blood Press. 6, 161–165.

Franklin, S.S., Gustin, W., Wong, N.D., Larson, M.G., Weber, M.A., Kannel, W.B., Levy, D., 1997. Hemodynamic patterns of age-related changes in blood pressure. The Framingham Heart Study. Circulation 96, 308–315.

Friebel, M., Roggan, A., Müller, G., Meinke, M., 2006. Determination of optical properties of human blood in the spectral range 250 to 1100 nm using Monte Carlo simulations with hematocrit-dependent effective scattering phase functions. Journal of Biomedical Optics 11, 34021. doi:10.1117/1.2203659

Fujii, M., Nakajima, K., Sakamoto, K., Kanai, H., 1999. Orientation and Deformation of Erythrocytes in Flowing Blood. Annals of the New York Academy of Sciences 873, 245–261. doi:10.1111/j.1749-6632.1999.tb09473.x

Fung, Y.C., Zweifach, B.W., Intaglietta, M., 1966. Elastic environment of the capillary bed. Circ. Res. 19, 441–461.

Gatzka, C.D., Cameron, J.D., Kingwell, B.A., Dart, A.M., 1998. Relation between coronary artery disease, aortic stiffness, and left ventricular structure in a population sample. Hypertension 32, 575–578.

GBS, 2015. The desired interaction of these ablative lasers is to precisely remove a thin layer. GBS. Retrieved from http://www.gbslaser.com/ablative-lasers-skin-refurfacing/.

Gesche, H., Grosskurth, D., Küchler, G., Patzak, A., 2012. Continuous blood pressure measurement by using the pulse transit time: comparison to a cuff-based method. Eur. J. Appl. Physiol. 112, 309–315. doi:10.1007/s00421-011-1983-3

Giannattasio, C., Vincenti, A., Failla, M., Capra, A., Cirò, A., De Ceglia, S., Gentile, G., Brambilla, R., Mancia, G., 2003. Effects of heart rate changes on arterial distensibility in humans. Hypertension 42, 253–256. doi:10.1161/01.HYP.0000085199.33254.15

Grabovskis, A., Kviesis-Kipge, E., Marcinkevics, Z., Lusa, V., Volceka, K., Greve, M., 2011. Reliability of Hemodynamic Parameters Measured by a Novel Photoplethysmography Device, in: Dremstrup, K., Rees, S., Jensen, M.Ø. (Eds.), 15th Nordic-Baltic Conference on Biomedical Engineering and Medical Physics (NBC 2011), IFMBE Proceedings. Springer Berlin Heidelberg, pp. 199–202.

Grahamfield, 2016. ADVANCED UPPER ARM BLOOD PRESSURE MONITOR.Retrieved from http://www.grahamfield.com/nosync/productimagesV2/400/InventoryItem10449_400.jpg.

Gusev, E.I., Petukhov, E.B., Martynov, M.I., Kolesnikova, T.I., Iasamanova, A.N., Makarov, A.N., Berezov, V.P., Serdiuk, I.E., Nikonov, A.A., 2008. [The circadian changes of plasma and blood viscosity and hematocrit in patients with ischemic stroke]. Zh Nevrol Psikhiatr Im S S Korsakova Suppl 22, 61–65.

Hale, J.F., McDonald, D.A., Womersley, J.R., 1955. Velocity profiles of oscillating arterial flow, with some calculations of viscous drag and the Reynolds number. The Journal of Physiology 128, 629–640. doi:10.1113/jphysiol.1955.sp005330

Hamunen, K., Kontinen, V., Hakala, E., Talke, P., Paloheimo, M., Kalso, E., 2012. Effect of pain on autonomic nervous system indices derived from photoplethysmography in healthy volunteers. Br. J. Anaesth. aes001. doi:10.1093/bja/aes001

Hamunen, K., Kontinen, V., Hakala, E., Talke, P., Paloheimo, M., Kalso, E., 2012. Effect of pain on autonomic nervous system indices derived from photoplethysmography in healthy volunteers. Br J Anaesth 108, 838–844. doi:10.1093/bja/aes001

Hansen, T.W., Staessen, J.A., Torp-Pedersen, C., Rasmussen, S., Li, Y., Dolan, E., Thijs, L., Wang, J.-G., O'Brien, E., Ibsen, H., Jeppesen, J., 2006. Ambulatory arterial stiffness index predicts stroke in a general population: Journal of Hypertension 24, 2247–2253. doi:10.1097/01.hjh.0000249703.57478.78

He, X., Ku, D.N., 1994. Unsteady entrance flow development in a straight tube. J Biomech Eng 116, 355–360.

Hecht, E., 2002. Optics. Addison-Wesley.

Hermeling, E., Reesink, K.D., Reneman, R.S., Hoeks, A.P.G., 2008. Confluence of incident and reflected waves interferes with systolic foot detection of the carotid artery distension waveform. J. Hypertens. 26, 2374–2380. doi:10.1097/HJH.0b013e328311cdd5

Hertzman, A.B., 1938. The Blood Supply of Various Skin Areas as Estimated by the Photoelectric Plethysmograph. American Journal of Physiology -- Legacy Content 124, 328–340.

Hertzman, A.B., Randall, W.C., Jochim, K.E., 1946. The Estimation of the Cutaneous Blood Flow with the Photoelectric Plethysmograph. American Journal of Physiology -- Legacy Content 145, 716–726.

Hertzman, A.B., Roth, L.W., 1942. The Vasomotor Components in the Vascular Reactions in the Finger to Cold. Am J Physiol 136, 669–679.

Hertzman, Spealman, 1937. Observations on the finger volume pulse recorded photoelectrically [WWW Document]. URL http://aqwave.reflexwireless.com/?q=node/15 (accessed 12.10.12).

Higgins, J.L., Fronek, A., 1986. Photoplethysmographic evaluation of the relationship between skin reflectance and skin blood volume. J Biomed Eng 8, 130–136.

Hinkelbein, J., Genzwuerker, H.V., Sogl, R., Fiedler, F., 2007. Effect of nail polish on oxygen saturation determined by pulse oximetry in critically ill patients. Resuscitation 72, 82–91. doi:10.1016/j.resuscitation.2006.06.024

Hirai, T., Sasayama, S., Kawasaki, T., Yagi, S., 1989. Stiffness of systemic arteries in patients with myocardial infarction. A noninvasive method to predict severity of coronary atherosclerosis. Circulation 80, 78–86. doi:10.1161/01.CIR.80.1.78

Hocherman, S., Palti, Y., 1967. Correlation between blood volume and opacity changes in the finger. J Appl Physiol 23, 157–162.

Hollander, W., 1976. Role of hypertension in atherosclerosis and cardiovascular disease. Am. J. Cardiol. 38, 786–800.

How, T.V., 1996. Advances in Hemodynamics and Hemorheology. Elsevier.

Hulley, S.B., Walsh, J.M., Newman, T.B., 1992. Health policy on blood cholesterol. Time to change directions. Circulation 86, 1026–1029. doi:10.1161/01.CIR.86.3.1026

Iaizzo, P.A., 2010. Handbook of Cardiac Anatomy, Physiology, and Devices. Springer Science & Business Media.

Ilies, C., Bauer, M., Berg, P., Rosenberg, J., Hedderich, J., Bein, B., Hinz, J., Hanss, R., 2012. Investigation of the agreement of a continuous non-invasive arterial pressure device in comparison with invasive radial artery measurement. Br. J. Anaesth. 108, 202–210. doi:10.1093/bja/aer394

Irace, C., Carallo, C., Scavelli, F., Franceschi, M.S.D., Esposito, T., Gnasso, A., 2013. Blood viscosity in subjects with normoglycemia and prediabetes. Dia Care DC_131374. doi:10.2337/dc13-1374

Isii, Y., Matsukawa, K., Tsuchimochi, H., Nakamoto, T., 2007. Ice-Water Hand Immersion Causes a Reflex Decrease in Skin Temperature in the Contralateral Hand. The Journal of Physiological Sciences 57, 241–248.

Jan, K.M., Chien, S., Bigger, J.T., 1975. Observations on blood viscosity changes after acute myocardial infarction. Circulation 51, 1079–1084.

Jay, G.D., Hughes, L., Renzi, F.P., 1994. Pulse oximetry is accurate in acute anemia from hemorrhage. Ann Emerg Med 24, 32–35.

Jeleazcov, C., Krajinovic, L., Münster, T., Birkholz, T., Fried, R., Schüttler, J., Fechner, J., 2010. Precision and accuracy of a new device (CNAPTM) for continuous non-invasive arterial pressure monitoring: assessment during general anaesthesia. Br J Anaesth 105, 264–272. doi:10.1093/bja/aeq143

Jerrard-Dunne, P., Mahmud, A., Feely, J., 2008. Ambulatory arterial stiffness index, pulse wave velocity and augmentation index – interchangeable or mutually exclusive measures?: Journal of Hypertension 26, 529–534. doi:10.1097/HJH.0b013e3282f35265

Jespersen, L.T., Pedersen, O.L., 1986. The quantitative aspect of photoplethysmography revised. Heart Vessels 2, 186–190.

Jha, A.K., 2009. A Textbook of Applied Physics. I. K. International Pvt Ltd.

Joely Kaufman, M.D., Jeremy Green, M.D., Elizabeth R. Geddes, M.D., 2012. Melanin measurement tool can increase safety, efficacy of light-based devices [WWW Document]. Dermatology Times. URL http://www.modernmedicine.com/modernmedicine/article/articleDetail.jsp?id=771702 (accessed 12.3.12).

Johansson, A., Öberg, P.P.Å., 1999. Estimation of respiratory volumes from the photoplethysmographic signal. Part I: experimental results. Med. Biol. Eng. Comput. 37, 42–47. doi:10.1007/BF02513264

Johnson, J.M., Yen, T.C., Zhao, K., Kosiba, W.A., 2005. Sympathetic, sensory, and nonneuronal contributions to the cutaneous vasoconstrictor response to local cooling. American Journal of Physiology - Heart and Circulatory Physiology 288, H1573–H1579. doi:10.1152/ajpheart.00849.2004

Kalfon, R., Campbell, J., Alvarez-Alvarado, S., Figueroa, A., 2015. Aortic Hemodynamics and Arterial Stiffness Responses to Muscle Metaboreflex Activation With Concurrent Cold Pressor Test. American Journal of Hypertension 28, 1332–1338. doi:10.1093/ajh/hpv043

Kamal, A.A.R., Harness, J.B., Irving, G., Mearns, A.J., 1989. Skin photoplethysmography — a review. Computer Methods and Programs in Biomedicine 28, 257–269. doi:10.1016/0169-2607(89)90159-4

Kamshilin, A.A., Nippolainen, E., Sidorov, I.S., Vasilev, P.V., Erofeev, N.P., Podolian, N.P., Romashko, R.V., 2015. A new look at the essence of the imaging photoplethysmography. Sci. Rep. 5. doi:10.1038/srep10494

Kass, D.A., Saeki, A., Tunin, R.S., Recchia, F.A., 1996. Adverse influence of systemic vascular stiffening on cardiac dysfunction and adaptation to acute coronary occlusion. Circulation 93, 1533–1541.

Kawahara, J., Sano, H., Fukuzaki, H., Saito, K., Hiroucht, H., 1989. Acute Effects of Exposure to Cold on Blood Pressure, Platelet Function and Sympathetic Nervous Activity in Humans. Am J Hypertens 2, 724–726. doi:10.1093/ajh/2.9.724

Keatinge, W.R., Coleshaw, S.R., Cotter, F., Mattock, M., Murphy, M., Chelliah, R., 1984. Increases in platelet and red cell counts, blood viscosity, and arterial pressure during mild surface cooling: factors in mortality from coronary and cerebral thrombosis in winter. Br Med J (Clin Res Ed) 289, 1405–1408.

Kellogg, D.L., 2006. In vivo mechanisms of cutaneous vasodilation and vasoconstriction in humans during thermoregulatory challenges. Journal of Applied Physiology 100, 1709–1718. doi:10.1152/japplphysiol.01071.2005

King, L.V., 1916. XXXVII. *Theory and experiments relating to the establishment of turbulent flow in pipes and channels*. Philosophical Magazine Series 6 31, 322–338. doi:10.1080/14786440408635504

Kocica, M.J., Corno, A.F., Carreras-Costa, F., Ballester-Rodes, M., Moghbel, M.C., Cueva, C.N.C., Lackovic, V., Kanjuh, V.I., Torrent-Guasp, F., 2006. The helical ventricular myocardial band: global, three-dimensional, functional architecture of the ventricular myocardium☆. European Journal of Cardio-Thoracic Surgery 29, S21–S40. doi:10.1016/j.ejcts.2006.03.011

Kocsis, L., Herman, P., Eke, A., 2006. The modified Beer–Lambert law revisited. Physics in Medicine and Biology 51, N91–N98. doi:10.1088/0031-9155/51/5/N02

Korhonen, I., 2006. Blood pressure and heart rate responses in men exposed to arm and leg cold pressor tests and whole-body cold exposure. Int J Circumpolar Health 65, 178–184.

Korteweg, D., 1878. Ueber die Fortpflanzungsgeschwindigkeit des Schalles in elastischen Röhren. Annalen der Physik 525–542.

Ku, D.N., 1997. Blood Flow in Arteries. Annual Review of Fluid Mechanics 29, 399–434. doi:10.1146/annurev.fluid.29.1.399

Kwak, B.R., Bäck, M., Bochaton-Piallat, M.-L., Caligiuri, G., Daemen, M.J.A.P., Davies, P.F., Hoefer, I.E., Holvoet, P., Jo, H., Krams, R., Lehoux, S., Monaco, C., Steffens, S., Virmani, R., Weber, C., Wentzel, J.J., Evans, P.C., 2014. Biomechanical factors in atherosclerosis: mechanisms and clinical implications. Eur. Heart J. 35, 3013–3020, 3020a–3020d. doi:10.1093/eurheartj/ehu353

Kyriacou, P.A., 2006. Pulse Oximetry in the oesphagus.

Kyriacou, P.A., 2013. Direct Pulse Oximetry Within the Esophagus, on the Surface of Abdominal Viscera, and on Free Flaps: Anesthesia & Analgesia 117, 824–833. doi:10.1213/ANE.0b013e3182a1bef6

Laslett, L.J., Alagona Jr, P., Clark III, B.A., Drozda Jr, J.P., Saldivar, F., Wilson, S.R., Poe, C., Hart, M., 2012. The Worldwide Environment of Cardiovascular Disease: Prevalence, Diagnosis, Therapy, and Policy Issues: A Report From the American College of Cardiology. Journal of the American College of Cardiology, The Worldwide Environment of Cardiovascular Disease: Diagnostic and Treatment Options, Policy ConsiderationsA Report From the American College of Cardiology 60, S1–S49. doi:10.1016/j.jacc.2012.11.002

Lauda GmbH, 2016. Capillary Viscometers.

Laurent, D.S., Boutouyrie, P., 2012. Arterial Stiffness and Stroke in Hypertension. CNS Drugs 19, 1–11. doi:10.2165/00023210-200519010-00001

Laurent, S., Katsahian, S., Fassot, C., Tropeano, A.-I., Gautier, I., Laloux, B., Boutouyrie, P., 2003. Aortic Stiffness Is an Independent Predictor of Fatal Stroke in Essential Hypertension. Stroke 34, 1203–1206. doi:10.1161/01.STR.0000065428.03209.64

Lee, C., Sik Shin, H., Lee, M., 2011. Relations between ac-dc components and optical path length in photoplethysmography. Journal of Biomedical Optics 16, 077012-077012-4. doi:10.1117/1.3600769

Lee, R.T., Richardson, S.G., Loree, H.M., Grodzinsky, A.J., Gharib, S.A., Schoen, F.J., Pandian, N., 1992. Prediction of mechanical properties of human atherosclerotic tissue by high-frequency intravascular ultrasound imaging. An in vitro study. Arterioscler Thromb Vasc Biol 12, 1–5. doi:10.1161/01.ATV.12.1.1

Letcher, R.L., Chien, S., Pickering, T.G., Laragh, J.H., 1983. Elevated blood viscosity in patients with borderline essential hypertension. Hypertension 5, 757–762. doi:10.1161/01.HYP.5.5.757

Letcher, R.L., Chien, S., Pickering, T.G., Sealey, J.E., Laragh, J.H., 1981. Direct relationship between blood pressure and blood viscosity in normal and hypertensive subjects: Role of fibrinogen and concentration. The American Journal of Medicine 70, 1195–1202. doi:10.1016/0002-9343(81)90827-5

Lipowsky, H.H., 2005. Microvascular rheology and hemodynamics. Microcirculation (New York, N.Y.: 1994) 12, 5–15.

Loukogeorgakis, S., Dawson, R., Phillips, N., Martyn, C.N., Greenwald, S.E., 2002. Validation of a device to measure arterial pulse wave velocity by a photoplethysmographic method. Physiol Meas 23, 581–596.

Lowe, G.D.O., Lee, A.J., Rumley, A., Price, J.F., Fowkes, F.G.R., 1997. Blood viscosity and risk of cardiovascular events: the Edinburgh Artery Study. British Journal of Haematology 96, 168–173. doi:10.1046/j.1365-2141.1997.8532481.x

Lu, S., Zhao, H., Ju, K., Shin, K., Lee, M., Shelley, K., Chon, K.H., 2008. Can photoplethysmography variability serve as an alternative approach to obtain heart rate variability information? J Clin Monit Comput 22, 23–29. doi:10.1007/s10877-007-9103-y

Mackenzie, I.S., Wilkinson, I.B., Cockcroft, J.R., 2002. Assessment of arterial stiffness in clinical practice. QJM 95, 67–74. doi:10.1093/qjmed/95.2.67

Mancia, G., De Backer, G., Dominiczak, A., Cifkova, R., Fagard, R., Germano, G., Grassi, G., Heagerty, A.M., Kjeldsen, S.E., Laurent, S., Narkiewicz, K., Ruilope, L., Rynkiewicz, A., Schmieder, R.E., Boudier, H.A.S., Zanchetti, A., 2007. 2007 ESH-ESC Practice Guidelines for the Management of Arterial Hypertension: ESH-ESC Task Force on the Management of Arterial Hypertension. Journal of Hypertension 25, 1751–1762. doi:10.1097/HJH.0b013e3282f0580f

Mannheimer, P.D., 2007. The Light–Tissue Interaction of Pulse Oximetry. Anesth Analg 105, S10–S17. doi:10.1213/01.ane.0000269522.84942.54

Marieb, E.N., 2000. Human Anatomy and Physiology: Cat Version. Pearson College Division.

Marini, J.J., Wheeler, A.P., 2012. Critical Care Medicine: The Essentials. Lippincott Williams & Wilkins.

Martelli, F., Del Bianco, S., Ismaelli, A., Zacanti, G., 2010. Light Propagation through Biological Tissue. SPIE Press.

Matsushima, Y., Kawano, H., Koide, Y., Baba, T., Toda, G., Seto, S., Yano, K., 2004. Relationship of carotid intima-media thickness, pulse wave velocity, and ankle brachial index to the severity of coronary artery atherosclerosis. Clin Cardiol 27, 629–634. doi:10.1002/clc.4960271110

Mattace-Raso, F.U.S., Cammen, T.J.M. van der, Hofman, A., Popele, N.M. van, Bos, M.L., Schalekamp, M.A.D.H., Asmar, R., Reneman, R.S., Hoeks, A.P.G., Breteler, M.M.B., Witteman, J.C.M., 2006. Arterial Stiffness and Risk of Coronary Heart Disease and Stroke The Rotterdam Study. Circulation 113, 657–663. doi:10.1161/CIRCULATIONAHA.105.555235

May, J.M., Kyriacou, P.A., Honsel, M., Petros, A.J., 2014. Investigation of photoplethysmographs from the anterior fontanelle of neonates. Physiol Meas 35, 1961–1973. doi:10.1088/0967-3334/35/10/1961

McArdle, W.D., Katch, F.I., Katch, V.L., 2006. Essentials of Exercise Physiology. Lippincott Williams & Wilkins.

McDonald, D.A., 1960. Blood flow in arteries. E. Arnold.

McGill, H.C., McMahan, C.A., Gidding, S.S., 2008. Preventing Heart Disease in the 21st Century Implications of the Pathobiological Determinants of Atherosclerosis in Youth (PDAY) Study. Circulation 117, 1216–1227. doi:10.1161/CIRCULATIONAHA.107.717033

Mei, L.-H., Lin, D.-Q., Zhu, Z.-Q., Han, Z.-X., 1995. Densities and Viscosities of Polyethylene Glycol + Salt + Water Systems at 20 .degree.C. J. Chem. Eng. Data 40, 1168–1171. doi:10.1021/je00022a002

Members, A.F., Mancia, G., Fagard, R., Narkiewicz, K., Redon, J., Zanchetti, A., Böhm, M., Christiaens, T., Cifkova, R., Backer, G.D., Dominiczak, A., Galderisi, M., Grobbee, D.E., Jaarsma, T., Kirchhof, P., Kjeldsen, S.E., Laurent, S., Manolis, A.J., Nilsson, P.M., Ruilope, L.M., Schmieder, R.E., Sirnes, P.A., Sleight, P., Viigimaa, M., Waeber, B., Zannad, F., Council, E.S., Redon, J., Dominiczak, A., Narkiewicz, K., Nilsson, P.M., Burnier, M., Viigimaa, M., Ambrosioni, E., Caufield, M., Coca, A., Olsen, M.H., Schmieder, R.E., Tsioufis, C., Borne, P. van de, (cpg), E.C. for P.G., Zamorano, J.L., Achenbach, S., Baumgartner, H., Bax, J.J., Bueno, H., Dean, V., Deaton, C., Erol, C., Fagard, R., Ferrari, R., Hasdai, D., Hoes, A.W., Kirchhof, P., Knuuti, J., Kolh, P., Lancellotti, P., Linhart, A., Nihoyannopoulos, P., Piepoli, M.F., Ponikowski, P., Sirnes, P.A., Tamargo, J.L., Tendera, M., Torbicki, A., Wijns, W., Windecker, S., Reviewers, D., Clement, D.L., Coca, A., Gillebert, T.C., Tendera, M., Rosei, E.A., Ambrosioni, E., Anker, S.D., Bauersachs, J., Hitij, J.B., Caulfield, M., Buyzere, M.D., Geest, S.D., Derumeaux, G.A., Erdine, S., Farsang, C., Funck-Brentano, C., Gerc, V., Germano, G., Gielen, S., Haller, H., Hoes, A.W., Jordan, J., Kahan, T., Komajda, M., Lovic, D., Mahrholdt, H., Olsen, M.H., Ostergren, J., Parati, G., Perk, J., Polonia, J., Popescu, B.A., Reiner, Ž., Rydén, L., Sirenko, Y., Stanton, A., Struijker-Boudier, H., Tsioufis, C., Borne, P. van de, Vlachopoulos, C., Volpe, M., Wood, D.A., 2013. 2013 ESH/ESC Guidelines for the management of arterial hypertension. European Heart Journal 34, 2159–2219. doi:10.1093/eurheartj/eht151

Members, A.F., Perk, J., Backer, G.D., Gohlke, H., Graham, I., Reiner, Ž., Verschuren, M., Albus, C., Benlian, P., Boysen, G., Cifkova, R., Deaton, C., Ebrahim, S., Fisher, M., Germano, G., Hobbs, R., Hoes, A., Karadeniz, S., Mezzani, A., Prescott, E., Ryden, L., Scherer, M., Syvänne, M., Reimer, W.J.M.S.O., Vrints, C., Wood, D., Zamorano, J.L., Zannad, F., Guidelines, O. experts who contributed to parts of the, Cooney, M.T., (cpg), E.C. for P.G., Bax, J., Baumgartner, H., Ceconi, C., Dean, V., Deaton, C., Fagard, R., Funck-Brentano, C., Hasdai, D., Hoes, A., Kirchhof, P., Knuuti, J., Kolh, P., McDonagh, T., Moulin, C., Popescu, B.A., Reiner, Ž., Sechtem, U., Sirnes, P.A., Tendera, M., Torbicki, A., Vahanian, A., Windecker, S., Reviewers, D., Funck-Brentano, C., Sirnes, P.A., Aboyans, V., Ezquerra, E.A., Baigent, C., Brotons, C., Burell, G., Ceriello, A., Sutter, J.D., Deckers, J., Prato, S.D., Diener, H.-C., Fitzsimons, D., Fras, Z., Hambrecht, R., Jankowski, P., Keil, U., Kirby, M., Larsen, M.L., Mancia, G., Manolis, A.J., McMurray, J., Pająk, A., Parkhomenko, A., Rallidis, L., Rigo, F., Rocha, E., Ruilope, L.M., Velde, E. van der, Vanuzzo, D., Viigimaa, M., Volpe, M., Wiklund, O., Wolpert, C., 2012. European Guidelines on cardiovascular disease prevention in clinical practice (version 2012). European Heart Journal 33, 1635–1701. doi:10.1093/eurheartj/ehs092

Meredith, D.J., Clifton, D., Charlton, P., Brooks, J., Pugh, C.W., Tarassenko, L., 2012. Photoplethysmographic derivation of respiratory rate: a review of relevant physiology. Journal of Medical Engineering & Technology 36, 1–7. doi:10.3109/03091902.2011.638965

Millasseau, S.C., Guigui, F.G., Kelly, R.P., Prasad, K., Cockcroft, J.R., Ritter, J.M., Chowienczyk, P.J., 2000. Noninvasive Assessment of the Digital Volume Pulse Comparison With the Peripheral Pressure Pulse. Hypertension 36, 952–956. doi:10.1161/01.HYP.36.6.952

Miller, R.D., Jones, T.B., 1993. Electro-orientation of ellipsoidal erythrocytes. Theory and experiment. Biophys. J. 64, 1588–1595. doi:10.1016/S0006-3495(93)81529-7

Moens, A., 1878. Die Pulsekurve. Leiden. E. J. Brill.

Mofrad, M.R.K., Kamm, R.D., 2006. Cytoskeletal Mechanics: Models and Measurements in Cell Mechanics. Cambridge University Press.

Mohiaddin, R.H., Underwood, S.R., Bogren, H.G., Firmin, D.N., Klipstein, R.H., Rees, R.S., Longmore, D.B., 1989. Regional aortic compliance studied by magnetic resonance imaging: the effects of age, training, and coronary artery disease. Br Heart J 62, 90–96. doi:10.1136/hrt.62.2.90

Molitor, H., Knalzuk, M., 1936. A New Bloodless Method for Continous Recording of Peripheral Circulatory Changes.pdf.

Mourot, L., Bouhaddi, M., Regnard, J., 2009. Effects of the cold pressor test on cardiac autonomic control in normal subjects. Physiol Res 58, 83–91.

Muramoto, Y., Nagasaka, Y., 2011. High-speed sensing of microliter-order whole-blood viscosity using laser-induced capillary wave. J Biorheol 25, 43–51. doi:10.1007/s12573-011-0037-0

Naghavi, M., 2010. Asymptomatic Atherosclerosis: Pathophysiology, Detection and Treatment. Springer Science & Business Media.

Naidu, M.U.R., Reddy, B.M., Yashmaina, S., Patnaik, A.N., Rani, P.U., 2005. Validity and reproducibility of arterial pulse wave velocity measurement using new device with oscillometric technique: A pilot study. Biomed Eng Online 4, 49. doi:10.1186/1475-925X-4-49

Nakajima, K., Tamura, T., Miike, H., 1996. Monitoring of heart and respiratory rates by photoplethysmography using a digital filtering technique. Medical Engineering & Physics 18, 365–372. doi:10.1016/1350-4533(95)00066-6

Nemati, M., Presura, C.N., Urbach, H.P., Bhattacharya, N., 2014. Dynamic light scattering from pulsatile flow in the presence of induced motion artifacts. Biomed. Opt. Express 5, 2145–2156. doi:10.1364/BOE.5.002145

Nichols, W.W., M.D, M.F.O., 2011. McDonald's Blood Flow in Arteries: Theoretical, Experimental, and Clinical Principles. CRC Press.

Nielsen, K., Zhao, L., Stamnes, J., Stamnes, K., Moan, J., 2008. The Optics of Human Skin: Aspects Important for Human Health. Solar Radiation and Human Health.

Nijboer, J.A., Dorlas, J.C., Mahieu, H.F., 1981. Photoelectric plethysmography--some fundamental aspects of the reflection and transmission method. Clin Phys Physiol Meas 2, 205–215.

Nm, G., Dr, L., Ja, D., 1991. The accuracy of Finapres noninvasive mean arterial pressure measurements in anesthetized patients. Anesthesiology 74, 647–652.

O'Rourke, M.F., Pauca, A., Jiang, X.-J., 2001. Pulse wave analysis. Br J Clin Pharmacol 51, 507–522. doi:10.1046/j.0306-5251.2001.01400.x

O'Rourke, M.F., Vlachopoulos, C., Graham, R.M., 2000. Spurious systolic hypertension in youth. Vasc Med 5, 141–145. doi:10.1177/1358836X0000500303

Ochoa, W., Ohara, I., 1980. The effect of hematocrit on photoelectric plethysmogram. Tohoku J. Exp. Med. 132, 413–419.

Ortiz, F.O., Aldrich, T.K., Nagel, R.L., Benjamin, L.J., 1999. Accuracy of pulse oximetry in sickle cell disease. Am. J. Respir. Crit. Care Med. 159, 447–451. doi:10.1164/ajrccm.159.2.9806108

Packard, C.J., Rader, D.J., 2005. Lipids and Atherosclerosis. CRC Press.

Packard, R.R.S., Libby, P., 2008. Inflammation in Atherosclerosis: From Vascular Biology to Biomarker Discovery and Risk Prediction. Clinical Chemistry 54, 24–38. doi:10.1373/clinchem.2007.097360

Padilla, J.M., Berjano, E.J., Saiz, J., Facila, L., Diaz, P., Merce, S., 2006. Assessment of relationships between blood pressure, pulse wave velocity and digital volume pulse, in: Computers in Cardiology, 2006. Presented at the Computers in Cardiology, 2006, pp. 893–896.

Patterson, S.M., Krantz, D.S., Gottdiener, J.S., Hecht, G., Vargot, S., Goldstein, D.S., 1995. Prothrombotic effects of environmental stress: changes in platelet function, hematocrit, and total plasma protein. Psychosom Med 57, 592–599.

Pauca, A.L., Wallenhaupt, S.L., Kon, N.D., Tucker, W.Y., 1992. Does radial artery pressure accurately reflect aortic pressure? Chest 102, 1193–1198.

Payne, R.A., Symeonides, C.N., Webb, D.J., Maxwell, S.R.J., 2006. Pulse transit time measured from the ECG: an unreliable marker of beat-to-beat blood pressure. Journal of Applied Physiology 100, 136–141. doi:10.1152/japplphysiol.00657.2005

Pedrizzetti, G., Martiniello, A.R., Bianchi, V., D'Onofrio, A., Caso, P., Tonti, G., 2015. Cardiac fluid dynamics anticipates heart adaptation. J Biomech 48, 388–391. doi:10.1016/j.jbiomech.2014.11.049

Pereira, T., Correia, C., Cardoso, J., 2015. Novel Methods for Pulse Wave Velocity Measurement. J Med Biol Eng 35, 555–565. doi:10.1007/s40846-015-0086-8

Pergola, P.E., Kellogg, D.L., Johnson, J.M., Kosiba, W.A., Solomon, D.E., 1993. Role of sympathetic nerves in the vascular effects of local temperature in human forearm skin. American Journal of Physiology - Heart and Circulatory Physiology 265, H785–H792.

Peskin, C.S., McQueen, D.M., 1992. Cardiac fluid dynamics. Crit Rev Biomed Eng 20, 451–459.

Pianosi, P., Charge, T.D., Esseltine, D.W., Coates, A.L., 1993. Pulse oximetry in sickle cell disease. Arch Dis Child 68, 735–738.

Pop, G.A.M., Bisschops, L.L.A., Iliev, B., Struijk, P.C., Hoeven, J.G. van der, Hoedemaekers, C.W.E., 2013. On-line blood viscosity monitoring in vivo with a central venous catheter, using electrical impedance technique. Biosensors and Bioelectronics 41, 595–601. doi:10.1016/j.bios.2012.09.033

Pop, G.A.M., Duncker, D.J., Gardien, M., Vranckx, P., Versluis, S., Hasan, D., Slager, C.J., 2002. The clinical significance of whole blood viscosity in (cardio)vascular medicine. Neth Heart J 10, 512–516.

Popele, N.M. van, Bos, W.J.W., Beer, N.A.M. de, Kuip, D.A.M. van der, Hofman, A., Grobbee, D.E., Witteman, J.C.M., 2000. Arterial Stiffness as Underlying Mechanism of Disagreement Between an Oscillometric Blood Pressure Monitor and a Sphygmomanometer. Hypertension 36, 484–488. doi:10.1161/01.HYP.36.4.484

Pressman, G.L., Newgard, P.M., 1963. A Transducer for the Continuous External Measurement of Arterial Blood Pressure. IEEE Transactions on Bio-medical Electronics 10, 73–81. doi:10.1109/TBMEL.1963.4322794

© Primal Pictures. All rights reserved. Primal Pictures, an informa business www.primalpictures.com www.anatomy.tv

Reims, H.M., Sevre, K., Høieggen, A., Fossum, E., Eide, I., Kjeldsen, S.E., 2005. Blood viscosity: effects of mental stress and relations to autonomic nervous system function and insulin sensitivity. Blood Press. 14, 159–169. doi:10.1080/08037050510034176

Reims, H.M., Sevre, K., Høieggen, A., Fossum, E., Eide, I., Kjeldsen, S.E., 2004. OR 32: Whole-blood viscosity, autonomic nervous system, and effects of mental stress in borderline hypertensive and normotensive subjects. American Journal of Hypertension 17, 14A–15A. doi:10.1016/j.amjhyper.2004.03.031

Resnick, L.M., Militianu, D., Cunnings, A.J., Pipe, J.G., Evelhoch, J.L., Soulen, R.L., 1997. Direct Magnetic Resonance Determination of Aortic Distensibility in Essential Hypertension Relation to Age, Abdominal Visceral Fat, and In Situ Intracellular Free Magnesium. Hypertension 30, 654–659. doi:10.1161/01.HYP.30.3.654

Reynolds, L., Johnson, C., Ishimaru, A., 1976. Diffuse reflectance from a finite blood medium: applications to the modeling of fiber optic catheters. Applied Optics 15, 2059. doi:10.1364/AO.15.002059

Rhoades, R.A., Bell, D.R., 2012. Medical Phisiology: Principles for Clinical Medicine. Lippincott Williams & Wilkins.

Rietzschel, E.-R., Boeykens, E., Buyzere, M.L.D., Duprez, D.A., Clement, D.L., 2001. A Comparison Between Systolic and Diastolic Pulse Contour Analysis in the Evaluation of Arterial Stiffness. Hypertension 37, e15–e22. doi:10.1161/01.HYP.37.6.e15

Roach, R.C., Wagner, P.D., Hackett, P.H., 2002. Hypoxia: From Genes to the Bedside. Springer Science & Business Media.

Roggan, A., Friebel, M., Do¨rschel, K., Hahn, A., Mu¨ller, G., 1999. Optical Properties of Circulating Human Blood in the Wavelength Range 400–2500 nm. J. Biomed. Opt 4, 36–46. doi:10.1117/1.429919

Rolfe, P., 1979. Non-invasive physiological measurements / edited by Peter Rolfe, Medical physics series. Academic Press, London ; New York :

Safar, M.E., Czernichow, S., Blacher, J., 2006. Obesity, Arterial Stiffness, and Cardiovascular Risk. JASN 17, S109–S111. doi:10.1681/ASN.2005121321

Safar, M.E., O'Rourke, M., Frohlich, E.D., 2014. Blood Pressure and Arterial Wall Mechanics in Cardiovascular Diseases. Springer.

Sandell, J.L., Zhu, T.C., 2011. A review of in-vivo optical properties of human tissues and its impact on PDT. J Biophotonics 4, 773–787.

Sawada, Y., Tanaka, G., Yamakoshi, K., 2001. Normalized pulse volume (NPV) derived photo-plethysmographically as a more valid measure of the finger vascular tone. International Journal of Psychophysiology 41, 1–10. doi:10.1016/S0167-8760(00)00162-8

Schmitt, J.M., Meindl, J.D., Mihm, F.G., 1986. An Integrated Circuit-Based Optical Sensor for In Vivo Measurement of Blood Oxygenation. IEEE Transactions on Biomedical Engineering BME-33, 98–107. doi:10.1109/TBME.1986.325883

Secker, C., Spiers, P., 1997. Accuracy of pulse oximetry in patients with low systemic vascular resistance. Anaesthesia 52, 127–130.

Seidler, J., Vondráček, J., Saxl, I., 2000. The life and work of Zbyněk Šidák (1933–1999). Applications of Mathematics 45, 321–336. doi:10.1023/A:1022238410461

Selvaraj, N., Jaryal, A., Santhosh, J., Deepak, K.K., Anand, S., 2008. Monitoring of Cardiovascular Reactivity During Cold Pressor Test Using Photoplethysmography, in: International Conference on Signal Processing, Communications and Networking, 2008. ICSCN '08. Presented at the International Conference on Signal Processing, Communications and Networking, 2008. ICSCN '08, pp. 363–367. doi:10.1109/ICSCN.2008.4447220

Severinghaus, J.W., 2007. Takuo Aoyagi: Discovery of Pulse Oximetry. Anesth Analg 105, S1–S4. doi:10.1213/01.ane.0000269514.31660.09

Severinghaus, J.W., Kelleher, J.F., 1992. Recent developments in pulse oximetry. Anesthesiology 76, 1018–1038.

Severinghaus, J.W., Koh, S.O., 1990. Effect of anemia on pulse oximeter accuracy at low saturation. J Clin Monit 6, 85–88.

Shelley, K.H., 2007. Photoplethysmography: beyond the calculation of arterial oxygen saturation and heart rate. Anesth. Analg. 105, S31–36, tables of contents. doi:10.1213/01.ane.0000269512.82836.c9

Shimada, S., Hasegawa, K., Wada, H., Terashima, S., Satoh-Asahara, N., Yamakage, H., Kitaoka, S., Akao, M., Shimatsu, A., Takahashi, Y., 2011. High blood viscosity is closely associated with cigarette smoking and markedly reduced by smoking cessation. Circ. J. 75, 185–189.

Shoenfeld, Y., Harats, D., Wick, G., 2001. Atherosclerosis and Autoimmunity. Elsevier.

Shusterman, V., Barnea, O., 2005. Sympathetic nervous system activity in stress and biofeedback relaxation. IEEE Engineering in Medicine and Biology Magazine 24, 52–57. doi:10.1109/MEMB.2005.1411349

Sinex, J.E., 1999. Pulse oximetry: Principles and limitations. The American Journal of Emergency Medicine 17, 59–66. doi:10.1016/S0735-6757(99)90019-0

Sliwa, K., Stewart, S., Gersh, B.J., 2011. Hypertension A Global Perspective. Circulation 123, 2892–2896. doi:10.1161/CIRCULATIONAHA.110.992362

Solá, E., Vayá, A., Simó, M., Hernández-Mijares, A., Morillas, C., España, F., Estellés, A., Corella, D., 2007. Fibrinogen, plasma viscosity and blood viscosity in obesity. Relationship with insulin resistance. Clin. Hemorheol. Microcirc. 37, 309–318.

Somer, T., Meiselman, H.J., 1993. Disorders of blood viscosity. Ann. Med. 25, 31–39.

Splinter, R., Hooper, B.A., 2007. An Introduction to Biomedical Optics. Taylor & Francis Group.

Stefanadis, C., Dernellis, J., Tsiamis, E., Stratos, C., Diamantopoulos, L., Michaelides, A., Toutouzas, P., 2000. Aortic stiffness as a risk factor for recurrent acute coronary events in patients with ischaemic heart disease. Eur. Heart J. 21, 390–396. doi:10.1053/euhj.1999.1756

Steinke, J.M., Shepherd, A.P., 1988. Diffusion model of the optical absorbance of whole blood. Journal of the Optical Society of America A 5, 813. doi:10.1364/JOSAA.5.000813

Stokes, D.N., Clutton-Brock, T., Patil, C., Thompson, J.M., Hutton, P., 1991. Comparison of Invasive and Non-Invasive Measurement of Continuous Arterial Pressure Using the Finapres. Br. J. Anaesth. 67, 26–35. doi:10.1093/bja/67.1.26

Stone, M.J., 2009. Waldenstrom's Macroglobulinemia: Hyperviscosity Syndrome and Cryoglobulinemia. Clin. Lymphoma Myeloma 9, 97–99. doi:10.3816/CLM.2009.n.026

Stone, M.J., Bogen, S.A., 2012. Evidence-based focused review of management of hyperviscosity syndrome. Blood 119, 2205–2208. doi:10.1182/blood-2011-04-347690

Sutton-Tyrrell, K., Najjar, S.S., Boudreau, R.M., Venkitachalam, L., Kupelian, V., Simonsick, E.M., Havlik, R., Lakatta, E.G., Spurgeon, H., Kritchevsky, S., Pahor, M., Bauer, D., Newman, A., Health ABC Study, 2005. Elevated aortic pulse wave velocity, a marker of arterial stiffness, predicts cardiovascular events in well-functioning older adults. Circulation 111, 3384–3390. doi:10.1161/CIRCULATIONAHA.104.483628

Sutton-Tyrrell, K., Najjar, S.S., Boudreau, R.M., Venkitachalam, L., Kupelian, V., Simonsick, E.M., Havlik, R., Lakatta, E.G., Spurgeon, H., Kritchevsky, S., Pahor, M., Bauer, D., Newman, A., Health ABC Study, 2005. Elevated aortic pulse wave velocity, a marker of arterial stiffness, predicts cardiovascular events in well-functioning older adults. Circulation 111, 3384–3390. doi:10.1161/CIRCULATIONAHA.104.483628

Takashima, N., Turin, T.C., Matsui, K., Rumana, N., Nakamura, Y., Kadota, A., Saito, Y., Sugihara, H., Morita, Y., Ichikawa, M., Hirose, K., Kawakani, K., Hamajima, N., Miura, K., Ueshima, H., Kita, Y., 2014. The relationship of brachial-ankle pulse wave velocity to future cardiovascular disease events in the general Japanese population: the Takashima Study. J Hum Hypertens 28, 323–327. doi:10.1038/jhh.2013.103

Takeshima, T., Takao, Y., Urakami, K., Nishikawa, S., Takahashi, K., 1989. Muscle Contraction Headache and Migraine: Platelet Activation and Plasma Norepinephrine during the Cold Pressor Test. Cephalalgia 9, 7–13. doi:10.1046/j.1468-2982.1989.901007.x

Tamura, T., Maeda, Y., Sekine, M., Yoshida, M., 2014. Wearable Photoplethysmographic Sensors—Past and Present. Electronics 3, 282–302. doi:10.3390/electronics3020282

Tanaka, G., Yamakoshi, K., Sawada, Y., Matsumura, K., Maeda, K., Kato, Y., Horiguchi, M., Ohguro, H., 2011. A novel photoplethysmography technique to derive normalized arterial stiffness as a blood pressure independent measure in the finger vascular bed. Physiol. Meas. 32, 1869. doi:10.1088/0967-3334/32/11/003

Taniguchi, T., Nakamura, T., Sawada, T., 2014. Arterial stiffness, endothelial dysfunction and recurrent angina post-chemotherapy. QJM hcu184. doi:10.1093/qjmed/hcu184

Tank, J., Diedrich, A., Hale, N., Niaz, F.E., Furlan, R., Robertson, R.M., Mosqueda-Garcia, R., 2003. Relationship between blood pressure, sleep K-complexes, and muscle sympathetic nerve activity in humans. Am. J. Physiol. Regul. Integr. Comp. Physiol. 285, R208-214. doi:10.1152/ajpregu.00013.2003

Teplov, V., Nippolainen, E., Makarenko, A.A., Giniatullin, R., Kamshilin, A.A., 2014. Ambiguity of mapping the relative phase of blood pulsations. Biomedical Optics Express 5, 3123. doi:10.1364/BOE.5.003123

Tortora, G.J., Derrickson, B.H., 2008. Principles of Anatomy and Physiology. John Wiley & Sons.

Townsend N, Williams J, Bhatnagar P, et al. Cardiovascular disease statistics 2014. London: British Heart Foundation, 2014

Tuchin, V.V. (Valeriĭ V., 2007. Tissue Optics: Light Scattering Methods and Instruments for Medical Diagnosis. SPIE Press.

Turczyński, B., Słowińska, L., Szczesny, S., Baschton, M., Bartosik-Baschton, A., Szyguła, J., Wodniecki, J., Spyra, J., 2002. [The whole blood and plasma viscosity changes in course of acute myocardial infarction]. Pol. Arch. Med. Wewn. 108, 971–978.

Valant, A.Z., Žiberna, L., Papaharilaou, Y., Anayiotos, A., Georgiou, G.C., 2011. The influence of temperature on rheological properties of blood mixtures with different volume expanders—implications in numerical arterial hemodynamics simulations. Rheol Acta 50, 389–402. doi:10.1007/s00397-010-0518-x

van Veen, R.L.P., Sterenborg, H.J.C.M., Pifferi, A., Torricelli, A., Chikoidze, E., Cubeddu, R., 2005. Determination of visible near-IR absorption coefficients of mammalian fat using time- and spatially resolved diffuse reflectance and transmission spectroscopy. J Biomed Opt 10, 54004. doi:10.1117/1.2085149

Viscopedia, 2016. Fallin Ball Principle.Retrieved from http://www.viscopedia.com/methods/measuring-principles/.

Viswanath, D.S., Ghosh, T., Prasad, D.H.L., Dutt, N.V.K., Rani, K.Y., 2007. Viscosity of Liquids: Theory, Estimation, Experiment, and Data. Springer Science & Business Media.

Vo, D.T., 2003. Biomedical photonics: handbook. CRC Press.

Volgyesi, G.A., Spahr-Schopfer, I., 1991. Does skin pigmentation affect the accuracy of pulse oximetry? an in vitro study: Anesthesiology 75, A406. doi:10.1097/00000542-199109001-00406

Waite, L., AccessEngineering, 2007. Applied biofluid mechanics. McGraw-Hill, New York.

Waldenström, J., 1944. Incipient myelomatosis or «essential« hyperglobulinemia with fibrinogenopenia — a new syndrome? Acta Medica Scandinavica 117, 216–247. doi:10.1111/j.0954-6820.1944.tb03955.x

Wang, T., Palucci, D., Law, K., Yanagawa, B., Yam, J., Butany, J., 2012. Atherosclerosis: pathogenesis and pathology. Diagnostic Histopathology 18, 461–467. doi:10.1016/j.mpdhp.2012.09.004

Webster, J.G., 1997. Design of Pulse Oximeters. CRC Press.

Weiss, E., Gayat, E., Dumans-Nizard, V., Le Guen, M., Fischler, M., 2014. Use of the Nexfin™ device to detect acute arterial pressure variations during anaesthesia induction. Br J Anaesth 113, 52–60. doi:10.1093/bja/aeu055

Wilkinson, I.B., MacCallum, H., Flint, L., Cockcroft, J.R., Newby, D.E., Webb, D.J., 2000. The influence of heart rate on augmentation index and central arterial pressure in humans. J Physiol 525, 263–270. doi:10.1111/j.1469-7793.2000.t01-1-00263.x

Wilson, B.J., Cowan, H.J., Lord, J.A., Zuege, D.J., Zygun, D.A., 2010. The accuracy of pulse oximetry in emergency department patients with severe sepsis and septic shock: a retrospective cohort study. BMC Emergency Medicine 10, 9. doi:10.1186/1471-227X-10-9

Windberger, U., Bartholovitsch, A., Plasenzotti, R., Korak, K.J., Heinze, G., 2003. Whole blood viscosity, plasma viscosity and erythrocyte aggregation in nine mammalian species: reference values and comparison of data. Exp. Physiol. 88, 431–440.

Wolbarsht, M.L., Walsh, A.W., George, G., 1981. Melanin, a unique biological absorber. Appl. Opt. 20, 2184–2186. doi:10.1364/AO.20.002184

Womersley, J.R., 1955. Oscillatory Motion of a Viscous Liquid in a Thin-walled Elastic Tube: I. The Linear Approximation for Long Waves.

Wong, K.K.L., Kelso, R.M., Worthley, S.G., Sanders, P., Mazumdar, J., Abbott, D., 2008. The characterisation of blood rotation in a human heart chamber based on statistical analysis of vorticity maps</title>, in: Nicolau, D.V., Metcalfe, G. (Eds.), . p. 72700W–72700W–10. doi:10.1117/12.810703

Wowern, E., Östling, G., Nilsson, P.M., Olofsson, P., 2015. Digital Photoplethysmography for Assessment of Arterial Stiffness: Repeatability and Comparison with Applanation Tonometry. PLoS One 10. doi:10.1371/journal.pone.0135659

Yamashina, A., Tomiyama, H., Takeda, K., Tsuda, H., Arai, T., Hirose, K., Koji, Y., Hori, S., Yamamoto, Y., 2002. <B>Validity, Reproducibility, and Clinical Significance of Noninvasive Brachial-Ankle Pulse Wave Velocity Measurement</B>. Hypertension Research 25, 359–364. doi:10.1291/hypres.25.359

Yoneda, S., Kako, T., Kohketsu, M., Fujinami, T., 1989. Changes in blood viscosity following nifedipine administration and its relation to the contents of adenosine triphosphate and 2,3-diphosphoglyceric acid in red blood cells in patients with angina pectoris. Arzneimittelforschung 39, 504–506.

Zaman, T., Kyriacou, P.A., Pal, S.K., 2013. Free flap pulse oximetry utilizing reflectance photoplethysmography. Conf Proc IEEE Eng Med Biol Soc 2013, 4046–4049. doi:10.1109/EMBC.2013.6610433

Zamir, M., 2000. The physics of pulsatile flow. Springer.

Zamir, M., 2005. The Physics of Coronary Blood Flow. Springer.

Zijlstra, W.G., Buursma, A., Assendelft, O.W.V., 2000. Visible and Near Infrared Absorption Spectra of Human and Animal Haemoglobin: Determination and Application. VSP.

Zijlstra, W.G., Buursma, A., Assendelft, O.W.V., 2000. Visible and Near Infrared Absorption Spectra of Human and Animal Haemoglobin: Determination and Application. VSP.

Zureik, M., Temmar, M., Adamopoulos, C., Bureau, J.-M., Courbon, D., Thomas, F., Bean, K., Touboul, P.-J., Ducimetière, P., Benetos, A., 2002. Carotid plaques, but not common carotid intima-media thickness, are independently associated with aortic stiffness. J. Hypertens. 20, 85–93.